

University of Strathclyde

Department of Mechanical & Aerospace Engineering

# **An Open-Source Hybrid CFD-DSMC Solver for High-Speed Flows**

Daniel Espinoza

A thesis presented in fulfilment of the requirements  
for the degree of Doctor of Philosophy

2018

## **Declaration of author's rights**

This thesis is the result of the author's original research. It has been composed by the author and has not been previously submitted for examination which has led to the award of a degree.

The copyright of this thesis belongs to the author under the terms of the United Kingdom Copyright Acts as qualified by University of Strathclyde Regulation 3.50. Due acknowledgement must always be made of the use of any material contained in, or derived from, this thesis.

Daniel Espinoza

August 2018

# Abstract

A new open-source hybrid CFD-DSMC solver, called *hyperFoam*, has been implemented within the OpenFOAM framework. The capabilities of the OpenFOAM computational fluid dynamics (CFD) solver *rhoCentralFoam* for supersonic simulations were analysed, showing good agreement with state-of-the-art solvers such as DLR-Tau, and then enhanced, by incorporating the local time stepping (LTS) and adaptive mesh refinement (AMR) techniques. These aspects would later be used for the development of the hypersonic CFD code *hy2Foam*.

*hyperFoam* relies on *hy2Foam* and the direct direct simulation Monte Carlo (DSMC) code *dsmcFoam* to be able to resolve the flow physics while under the slip-transition regime. Using a mixture of Boyd's Gradient-Length-Local Knudsen number and a generalised modified Chapman-Enskog parameter, *hyperFoam* is capable of identifying the continuum and rarefied zones within the computational domain and solve each with its respective CFD or DSMC solver. *hyperFoam* has been used to simulate several Couette flow with heat transfer test cases, each of different complexity. Good agreement was shown between the DSMC and hybrid results for these simulations. The hybrid code was then used to analyse a hypersonic cylinder. Reasonably similar accuracy was found between the DSMC and hybrid results for vibrationless  $N_2$  and  $N_2 - O_2$ . However, for  $O_2$  important discrepancies were found due to an inconsistency between continuum and rarefied vibrational modelling.

# Contents

<b>Abstract</b>	<b>ii</b>
<b>List of Figures</b>	<b>v</b>
<b>List of Tables</b>	<b>xi</b>
<b>Acknowledgements</b>	<b>xiii</b>
<b>1 Introduction</b>	<b>1</b>
1.1 Motivation . . . . .	1
1.2 Previous work . . . . .	4
1.2.1 CFD . . . . .	4
1.2.2 DSMC . . . . .	6
1.2.3 Hybrid solvers . . . . .	8
1.3 Objectives . . . . .	13
1.4 Thesis Overview . . . . .	14
<b>2 Validation of <i>rhoCentralFoam</i> and Convergence Acceleration Techniques</b>	<b>16</b>
2.1 Hollow cylinder . . . . .	17
2.2 Tools to accelerate convergence . . . . .	32
2.2.1 Local time stepping . . . . .	32
2.2.2 Adaptive mesh refinement . . . . .	43

## Contents

<b>3 OpenFOAM solvers for the hybrid code</b>	<b>53</b>
3.1 CFD and <i>hy2Foam</i> . . . . .	53
3.1.1 Two-temperature model . . . . .	54
3.1.2 Multispecies . . . . .	57
3.2 DSMC and <i>dsmcFoam</i> . . . . .	61
3.2.1 Boundary Conditions . . . . .	63
3.2.2 Collisions . . . . .	63
3.2.3 Chemical reactions . . . . .	65
3.2.4 Distribution functions . . . . .	66
<b>4 <i>hyperFoam</i></b>	<b>73</b>
4.1 Characteristics . . . . .	73
4.1.1 Determination of the continuum and rarefied domains . . . . .	76
4.1.2 Progression of the solution using the DSMC solver . . . . .	78
4.1.3 Progression of the solution using the CFD solver . . . . .	79
4.1.4 Check for final time . . . . .	81
4.2 Validation with a Couette Flow . . . . .	81
4.2.1 Argon . . . . .	82
4.2.2 Vibrationless Nitrogen . . . . .	84
4.2.3 Molecular Nitrogen . . . . .	87
4.2.4 Argon mixture . . . . .	93
4.2.5 Atomic Nitrogen and Oxygen . . . . .	93
4.2.6 Vibrationless Nitrogen and Oxygen . . . . .	99
4.2.7 Molecular Nitrogen and Oxygen . . . . .	99
<b>5 Hypersonic cylinder</b>	<b>105</b>
5.1 Computational domain . . . . .	105
5.2 Vibrationless $N_2$ . . . . .	106
5.3 Vibrationless $N_2 - O_2$ . . . . .	120
5.4 Molecular $O_2$ . . . . .	133

Contents

<b>6 Conclusions</b>	<b>148</b>
6.1 Future work . . . . .	149
<b>A Derivation of the temperature-jump conditions</b>	<b>151</b>
<b>Bibliography</b>	<b>168</b>

# List of Figures

1.1	Flow-field features encountered during the Earth atmosphere reentry . . . . .	3
1.2	Flow regimes depending on $Kn$ . . . . .	3
1.3	Typical hybrid coupling procedures . . . . .	9
2.1	Hollowed cylinder . . . . .	18
2.2	Mesh blocks near the cylinder for the $AoA = 0^\circ$ case . . . . .	20
2.3	Pressure contour plot in $Pa$ for the $AoA = 0^\circ$ case . . . . .	22
2.4	Temperature contour plot in $K$ for the $AoA = 0^\circ$ case, in K . . . . .	22
2.5	Velocity magnitude contour plot in $m/s$ for the $AoA = 0^\circ$ case . . . . .	23
2.6	Mach number contour plot for the $AoA = 0^\circ$ case . . . . .	23
2.7	Schlieren visualization of the shock structure inside the cylinder . . . . .	24
2.8	Recirculation bubble in the region of interest from Figure 2.7, with the background colour for contrast. . . . .	24
2.9	Flow features of a laminar shock impingement configuration. . . . .	25
2.10	Pressure contour plots for the $AoA = 90^\circ$ case . . . . .	26
2.11	Temperature contour plots for the $AoA = 90^\circ$ case . . . . .	27
2.12	Velocity magnitude contour plots for the $AoA = 90^\circ$ case . . . . .	28
2.13	Recirculating flow inside the cylinder for the $AoA = 90^\circ$ case, with velocity magnitude contour plot, in $m/s$ . . . . .	29
2.14	Comparison of axial force coefficients . . . . .	30
2.15	Comparison of normal force coefficients . . . . .	30
2.16	Comparison of heat fluxes . . . . .	31

## List of Figures

2.17	Mesh for the Couette flow test case . . . . .	34
2.18	Results from the unmodified and the LTS solvers for temperature . . . . .	36
2.19	Results from the unmodified and the LTS solvers for $x$ -velocity . . . . .	36
2.20	Results from the unmodified and the LTS solvers for $y$ -velocity . . . . .	37
2.21	Mesh for the flat plate test case . . . . .	39
2.22	Results from the unmodified and the LTS solvers for pressure . . . . .	41
2.23	Results from the unmodified and the LTS solvers for temperature . . . . .	41
2.24	Results from the unmodified and the LTS solvers for $y$ -velocity . . . . .	42
2.25	Results from the unmodified and the LTS solvers for $x$ -velocity . . . . .	42
2.26	Example of a refinement/coarsening sequence . . . . .	45
2.27	Flow chart for the AMR algorithm . . . . .	46
2.28	Initial mesh for the supersonic wedge test case . . . . .	46
2.29	Mach number contour plots for different refinement levels . . . . .	47
2.30	Comparison between Mach contour plots and analytical position (line in black) of the shock wave for different refinement levels . . . . .	48
2.31	Solution comparison for the initial and refined meshes . . . . .	49
2.32	Initial mesh for the shock tube test case . . . . .	49
2.33	Density contour plots for the different refinement criteria. . . . .	51
2.34	Solution comparison for initial and refined meshes. . . . .	52
3.1	Maxwell-Boltzmann (Max), Chapman-Enskog (CE), and Generalised Chapman-Enskog (GCE) distribution functions comparison . . . . .	71
3.2	Maxwell-Boltzmann (Max), Chapman-Enskog (CE), and Generalised Chapman-Enskog (GCE) perturbation functions comparison . . . . .	72
4.1	Determination of the different domains for the hybrid solver. . . . .	78
4.2	Particle progression with the DSMC solver. . . . .	80
4.3	Boundary conditions and zones for the Couette flow . . . . .	83
4.4	Translational temperature comparison, for $Ar$ . . . . .	84
4.5	Velocity comparison, for $Ar$ . . . . .	85
4.6	Influence of different distributions in the translational temperature, for $Ar$	85

## List of Figures

4.7	Influence of different distributions in the velocity, for $Ar$ . . . . .	86
4.8	Transrotational temperature comparison, for vibrationless $N_2$ . . . . .	87
4.9	Velocity comparison, for vibrationless $N_2$ . . . . .	88
4.10	Influence of different distributions in the transrotational temperature, for vibrationless $N_2$ . . . . .	88
4.11	Influence of different distributions in the velocity, for vibrationless $N_2$ .	89
4.12	Transrotational temperature comparison, for $N_2$ . . . . .	90
4.13	Vibrational temperature comparison, for $N_2$ . . . . .	90
4.14	Velocity comparison, for $N_2$ . . . . .	91
4.15	Influence of different distributions in the transrotational temperature, for $N_2$ . . . . .	91
4.16	Influence of different distributions in the vibrational temperature, for $N_2$	92
4.17	Influence of different distributions in the velocity, for $N_2$ . . . . .	92
4.18	Translational temperature comparison, for an $Ar - Ar$ mixture . . . . .	94
4.19	Velocity comparison, for an $Ar - Ar$ mixture . . . . .	94
4.20	Number density comparison, for an $Ar - Ar$ mixture, $Ar_1$ . . . . .	95
4.21	Number density comparison, for an $Ar - Ar$ mixture, $Ar_2$ . . . . .	95
4.22	Comparison between $Ar$ and $Ar - Ar$ gas mixture, for translational temperature . . . . .	96
4.23	Comparison between $Ar$ and $Ar - Ar$ gas mixture, for velocity . . . . .	96
4.24	Translational temperature comparison, for a $N - O$ mixture . . . . .	97
4.25	Velocity comparison, for a $N - O$ mixture . . . . .	97
4.26	Number density comparison, for a $N - O$ mixture, $N$ . . . . .	98
4.27	Number density comparison, for a $N - O$ mixture, $O$ . . . . .	98
4.28	Transrotational temperature comparison, for a vibrationless $N_2 - O_2$ mixture . . . . .	99
4.29	Velocity comparison, for a vibrationless $N_2 - O_2$ mixture . . . . .	100
4.30	Number density comparison, for a vibrationless $N_2 - O_2$ mixture, $N_2$ . .	100
4.31	Number density comparison, for a vibrationless $N_2 - O_2$ mixture, $O_2$ . .	101
4.32	Transrotational temperature comparison, for a $N_2 - O_2$ mixture . . . . .	102

## List of Figures

4.33	Vibrational temperature comparison, for a $N_2 - O_2$ mixture, $N_2$	102
4.34	Vibrational temperature comparison, for a $N_2 - O_2$ mixture, $O_2$	103
4.35	Velocity comparison, for a $N_2 - O_2$ mixture	103
4.36	Number density comparison, for a $N_2 - O_2$ mixture, $N_2$	104
4.37	Number density comparison, for a $N_2 - O_2$ mixture, $O_2$	104
5.1	Hypersonic cylinder domain and boundary conditions	106
5.2	Hypersonic cylinder CFD and DSMC zones for different criteria, $N_2$ case.	108
5.3	Pressure contour comparison, in $Pa$ , between the DSMC solver and other solvers, $N_2$ case.	109
5.4	Transrotational temperature contour comparison, in $K$ , between the DSMC solver and other solvers, $N_2$ case.	110
5.5	Velocity magnitude contour comparison, in $m/s$ , between the DSMC solver and other solvers, $N_2$ case.	111
5.6	Density plot along the stagnation line, $N_2$ case.	112
5.7	Transrotational temperature plot along the stagnation line, $N_2$ case.	113
5.8	Velocity plot along the stagnation line, $N_2$ case.	113
5.9	Density plot along the symmetry plane, in the wake. $N_2$ case.	114
5.10	Transrotational temperature plot along the symmetry plane, in the wake. $N_2$ case.	115
5.11	Velocity plot along the symmetry plane, in the wake. $N_2$ case.	115
5.12	Transrotational temperature plot along the cylinder surface, $N_2$ case.	116
5.13	Slip velocity plot along the cylinder surface, $N_2$ case.	117
5.14	Pressure coefficient plot along the cylinder surface, $N_2$ case.	118
5.15	Friction coefficient plot along the cylinder surface, $N_2$ case.	118
5.16	Heat transfer coefficient plot along the cylinder surface, $N_2$ case.	119
5.17	Hypersonic cylinder zones using $Kn_{GLL}$ (top) and $Kn_{breakdown}$ (bottom) as criteria, $N_2 - O_2$ case.	121
5.18	Pressure contour comparison, in $Pa$ , between the DSMC solver and other solvers, $N_2 - O_2$ case.	122

## List of Figures

5.19 Transrotational temperature contour comparison, in $K$ , between the DSMC solver and other solvers, $N_2 - O_2$ case. . . . .	123
5.20 Velocity magnitude contour comparison, in $m/s$ , between the DSMC solver and other solvers, $N_2 - O_2$ case. . . . .	124
5.21 $N_2$ density plot along the stagnation line, $N_2 - O_2$ case. . . . .	125
5.22 $O_2$ density plot along the stagnation line, $N_2 - O_2$ case. . . . .	125
5.23 Transrotational temperature plot along the stagnation line, $N_2 - O_2$ case. . . . .	126
5.24 Velocity plot along the stagnation line. . . . .	126
5.25 $N_2$ density plot along the symmetry plane, in the wake. $N_2 - O_2$ case. . . . .	127
5.26 $O_2$ density plot along the symmetry plane, in the wake. $N_2 - O_2$ case. . . . .	128
5.27 Transrotational temperature plot along the symmetry plane, in the wake. $N_2 - O_2$ case. . . . .	128
5.28 Velocity plot along the symmetry plane, in the wake. $N_2 - O_2$ case. . . . .	129
5.29 Transrotational temperature plot along the cylinder surface, $N_2 - O_2$ case. . . . .	129
5.30 Slip velocity plot along the cylinder surface, $N_2 - O_2$ case. . . . .	130
5.31 Pressure coefficient plot along the cylinder surface, $N_2 - O_2$ case. . . . .	130
5.32 Friction coefficient plot along the cylinder surface, $N_2 - O_2$ case. . . . .	131
5.33 Heat transfer coefficient plot along the cylinder surface, $N_2 - O_2$ case. . . . .	131
5.34 Hypersonic cylinder CFD and DSMC zones using different criteria, $O_2$ case. . . . .	134
5.35 Pressure contour comparison, in $Pa$ , between the DSMC solver and other solvers. $O_2$ case. . . . .	136
5.36 Transrotational temperature contour comparison, in $K$ , between the DSMC solver and other solvers, $O_2$ case. . . . .	137
5.37 Vibrational temperature contour comparison, in $K$ , between the DSMC solver and other solvers, $O_2$ case. . . . .	138
5.38 Velocity magnitude contour comparison, in $m/s$ , between the DSMC solver and other solvers, $O_2$ case. . . . .	139
5.39 Density plot along the stagnation line, $O_2$ case. . . . .	140
5.40 Transrotational temperature plot along the stagnation line, $O_2$ case. . . . .	140

## List of Figures

5.41 Vibrational temperature plot along the stagnation line, $O_2$ case. . . . .	141
5.42 Velocity plot along the stagnation line, $O_2$ case. . . . .	141
5.43 Density plot along the symmetry plane, in the wake. $O_2$ case. . . . .	142
5.44 Transrotational temperature plot along the symmetry plane, in the wake. $O_2$ case . . . . .	142
5.45 Vibrational temperature plot along the symmetry plane, in the wake. $O_2$ case . . . . .	143
5.46 Velocity plot along the symmetry plane, in the wake. $O_2$ case. . . . .	143
5.47 Transrotational temperature plot along the cylinder surface, $O_2$ case. . .	144
5.48 Vibrational temperature plot along the cylinder surface, $O_2$ case. . . . .	145
5.49 Slip velocity plot along the cylinder surface, $O_2$ case. . . . .	145
5.50 Pressure coefficient plot along the cylinder surface, $O_2$ case. . . . .	146
5.51 Friction coefficient plot along the cylinder surface, $O_2$ case. . . . .	146
5.52 Heat transfer coefficient plot along the cylinder surface, $O_2$ case. . . . .	147

# List of Tables

2.1	Forces and heat flux results . . . . .	21
2.2	Initial and boundary conditions for the Couette flow test case . . . . .	35
2.3	Simulation time-step in each iteration level, for the unmodified and LTS solvers . . . . .	37
2.4	Computational time required to reach each iteration level, for the unmodified and LTS solvers . . . . .	38
2.5	Computational time required to reach each iteration level, for the unmodified and LTS solvers . . . . .	40
5.1	Time comparison among the different solvers, $N_2$ case . . . . .	119
5.2	Time comparison among the different solvers, $N_2 - O_2$ case . . . . .	132
5.3	Time comparison among the different solvers, $O_2$ case . . . . .	147

# Acknowledgements

I cannot start this thesis without first thanking the people who helped making it possible. First of all, I would like to express my gratitude to Dr Tom Scanlon and Prof. Richard Brown, for their continuous support throughout the years, as well as Dr Matt Stickland, who took over my project after Dr Scanlon retired. I appreciate the guidance, knowledge and insight they have provided all this time.

A sincere thank you to Dr Rodrigo Palharini (Instituto de Aeronáutica e Espaço, São José dos Campos, Brazil), Dr Vincent Casseau, Dr Javier Herrera, Dr Alessandro Mogavero and everyone else at the Future Air-Space Transportation Technology Laboratory (University of Strathclyde, Glasgow, UK), and Ferdin Don Bosco (James Weir Fluids Laboratory, University of Strathclyde, Glasgow, UK) for the advice and fruitful discussions regarding different aspects of this thesis.

A warm thanks to my family, for their constant love and support. Specially my late brother Diego, for our sibling rivalry that helped encourage me to pursue a PhD in the first place, I wish you could see it finished. To you all I dedicate this thesis.

To Montana Aeberhardt, Elisabeth Fraczek, and Ela Šifnerová, among many of the aforementioned people, I am indebted to you for helping me through difficult times. To many friends who believed in me and inspired me, from Glasgow, Madrid, and other parts of world, thank you.

Finally, I would like to thank the Engineering and Physical Sciences Research Council (EPSRC) for funding this PhD thesis, and the travel awards from both the University of Strathclyde and the Mechanical and Aerospace Engineering Department which allowed me to present my research at different conferences all over the world.

# Nomenclature

## Acronyms

AMAR	Adaptive Mesh and Algorithm Refinement
AMR	Adaptive Mesh Refinement
CE	Chapman-Enskog
CFD	Computational Fluid Dynamics
DAC	DSMC Analysis Code
DLR	German Aerospace Center (Deutsches Zentrum für Luft- und Raumfahrt)
DPLR	Data-Parallel Line Relaxation
DSMC	Direct Simulation Monte Carlo
FAST20XX	Future high-Altitude high-Speed Transport 20XX
GCE	Generalised Chapman-Enskog
HARA	High-Temperature Air Radiation
HIKARI	HIgh speed Key technologies for future Air transport - Research & Innovation cooperation scheme
IP	Information Preservation
L-B	Larsen-Borgnakke

## Nomenclature

LAURA	Langley Aerothermodynamic Upwind Relaxation Algorithm
LTS	Local Time Stepping
MPC	Modular Particle-Continuum
NASA	National Aeronautics and Space Administration
NEQAIR	Non-Equilibrium Air Radiation
NTC	No Time Counter
OpenFOAM	Open source Field Operation And Manipulation
PIC	Particle-In-Cell
PVD	Physical Vapour Deposition
Q-K	Quantum-Kinetic
SARA	Satélite de Reentrada Atmosférica
SCEBD	Self Consistent Effective Binary Diffusion
SIMPLE	Semi-Implicit Method for Pressure Linked Equations
STS	Space Transportation System
TCE	Total Collision Energy
VDF	Velocity Distribution Function
VHS	Variable Hard Sphere

## Greek Symbols

$\alpha$	Thermal-accommodation coefficient
$\beta_s$	Inverse of the most probable speed of species $s$
$\delta$	Mean molecular spacing

## Nomenclature

$\Gamma$	Gamma function
$\gamma$	Ratio of specific heats
$\kappa$	Thermal conductivity
$\lambda$	Mean free path; second coefficient of viscosity
$\mu$	Dynamic viscosity
$\omega$	Temperature exponent of the coefficient of viscosity
$\Omega_{s,r}^{(m,n)}$	Collision integral
$\rho$	Density
$\sigma$	Tangential-momentum-accommodation coefficient
$\hat{\tau}$	Non-dimensional viscous stress tensor
$\tau$	Viscous stress tensor
$\theta_d$	Characteristic dissociation temperature
$\theta_{vib}$	Characteristic vibrational temperature
$\zeta$	Degrees of freedom

## Symbols

$a$	Speed of sound
$AoA$	Angle of attack
$\vec{c}$	Non-dimensional thermal velocity
$\vec{c}$	Thermal velocity
$\vec{c}_p$	Particle velocity
$C$	Courant number

## Nomenclature

$c_f$	Skin friction coefficient
$c_p$	Pressure coefficient
$c_q$	Heat transfer coefficient
$C_v$	Heat capacity at constant volume
$\mathcal{D}_s$	Effective diffusion coefficient of species s
$\mathcal{D}_{s,r}$	Binary diffusion coefficient of species s and r
$\vec{\mathcal{D}}$	Non-dimensional diffusive flux
$d$	Effective molecular diameter
$d_{ref}$	Reference molecular diameter
$e$	Energy per unit mass
$e_a$	Activation energy of an exchange reaction
$e_{coll}$	Collision energy
$e_{tot}$	Total energy per unit mass
$h_{tot}$	Total enthalpy per unit mass
$\vec{\mathcal{J}}$	Diffusive flux
$k_B$	Boltzmann constant
$Kn$	Knudsen number
$\mathcal{M}$	Molecular weight
$M$	Mach number
$m_{s,r}^*$	Reduced mass of molecules s and r
$m_s$	Mass of one particle of species s

## Nomenclature

$N$	Number of samples
$n$	Number density
$p$	Pressure
$Pr$	Prandtl number
$\hat{\vec{q}}$	Non-dimensional heat flux vector
$\vec{q}$	Heat flux vector
$Q_{v-c}$	Vibrational energy addition or removal due to chemical reactions
$Q_{v-t}$	Vibrational-translational energy transfer
$Q_{v-v}$	Vibrational-vibrational energy transfer
$R_g$	Specific gas constant
$Re$	Reynolds number
$T$	Temperature
$t_{hybrid}$	Hybrid simulation time
$u$	Flow speed in the $x$ -direction
$\vec{v}$	Velocity vector
$v$	Flow speed in the $y$ -direction
$t$	time
$w$	Flow speed in the $z$ -direction
$X_s$	Molar fraction of species $s$
$Y_s$	Mass fraction of species $s$
$Z$	Collision number

## Nomenclature

### Superscripts

$T$  Transpose

### Subscripts

$GLL$  Gradient-Length-Local

$\infty$  Upstream

$max$  Maximum

$min$  Minimum

$r$  Species r

$ref$  Reference values

$rot$  Rotational properties

$s$  Species s

$t - r$  Transrotational properties

$tra$  Translational properties

$vib$  Vibrational properties

### Other Symbols

$\Delta t$  Time-step

$\Delta t_{CFD}$  Time-step for the CFD solver

$\Delta t_{DSMC}$  Time-step for the DSMC solver

$\Delta t_{hybrid}$  Time interval between CFD-DSMC coupling in the hybrid solver

$f^{(0)}(\vec{c})$  Maxwellian distribution

$f^{(0)}(\vec{c}, \epsilon_{rot}, \epsilon_{vib})$  Maxwell-Boltzmann distribution

## Nomenclature

$f^{(1)}(\vec{c})$  Chapman-Enskog distribution

$f^{(1)}(\vec{c}, \epsilon_{rot}, \epsilon_{vib})$  Generalised Chapman-Enskog distribution

$\Gamma_{CE}(\vec{c})$  Chapman-Enskog perturbation function

$\Gamma_{CE}(\vec{c}, \epsilon_{rot}, \epsilon_{vib})$  Generalised Chapman-Enskog perturbation function

# Chapter 1

## Introduction

### 1.1 Motivation

Since time immemorial, mankind has looked up in wonder, marvelling at the sky, trying to understand and reach the heavens. Even after having reached the stage of space exploration our interest has not diminished. The current interest lies on different fronts.

On one hand, present and future developments in air transport technologies are aimed at achieving hypersonic commercial flight. Projects such as HIKARI (HIgh speed Key technologies for future Air transport - Research & Innovation cooperation scheme) [1] and FAST20XX (Future high-Altitude high-Speed Transport 20XX) [2] have focused on the research and development of the elements needed to achieve these goal within 35 years. This research has generated concepts like the SpaceLiner [3], designed to be able to travel from Europe to Australia in 90 minutes, reaching speeds up to 7 km/s. Another interesting focus of research is that of reusable launchers. There is quite an enthusiasm for SpaceX and its capabilities of landing the first stage of their launcher. However, current research is also focused on reusable Single-Stage-To-Orbit (SSTO) vehicles, with concepts such as the cFASTT-1 [4], designed at the University of Strathclyde.

Finally, it is impossible to talk about these topics without mentioning space itself. Plans for many future space missions involve spacecraft entering a planetary atmosphere. The

## Chapter 1. Introduction

Orion Crew Module [5–7] has been designed for both Martian landing and Earth reentry.

All of these fields require in-depth studies of the flow around the vehicles. A fault on the design of the vehicles or a problem during flight could cause damage to the spacecraft, or worse, the loss of human life. For this reason, exhaustive computational analysis should be performed on all of these scenarios.

The complexity of the physics involved has to be taken into account when dealing with these problems numerically. The hypersonic regime leads to strong shock waves that generate a dramatic increase in the temperature after the shock. These high temperatures activate the vibrational modes of the molecules that comprises air. Whereas all exchange between the energy modes require certain number of collisions to reach an equilibrium, it is usually the vibrational and electronic energy modes the ones that require the most. This leads to situations where, even though they are enough collisions during the characteristic time of the flow for the translational and rotational temperatures to be in equilibrium, this number of collisions is insufficient for the vibrational temperature. In addition, chemical reactions start occurring once the gas reaches characteristic temperatures that depend on the species involved. These chemical reactions are of special importance due to their endothermic nature, thus absorbing energy that would otherwise lead to increasing surface heating. Figure 1.1 shows the typical ranges in terms of altitude and speed for which thermal non-equilibrium and chemical reactions occur during reentry. For these reasons, considering thermal and chemical non-equilibrium can drastically improve the accuracy of a numerical simulation.

Not only that, but the high altitudes that these applications usually occur at, can even change the physical models altogether. High altitudes in the atmosphere are characterised by low density, which means high values for the mean free path,  $\lambda$ , that is the average distance a molecule has to travel before colliding with another. If the Knudsen number,  $Kn$ , defined as the ratio between the mean free path and a characteristic length of the problem, increases too much, the continuum hypothesis of the Navier-Stokes equations of fluid dynamics could break down, and rarefied gas dynamics

models would be used instead (see Figure 1.2). In this situation, different numerical methods other than conventional continuum solvers would need to be employed to be able to characterise the flow field correctly.

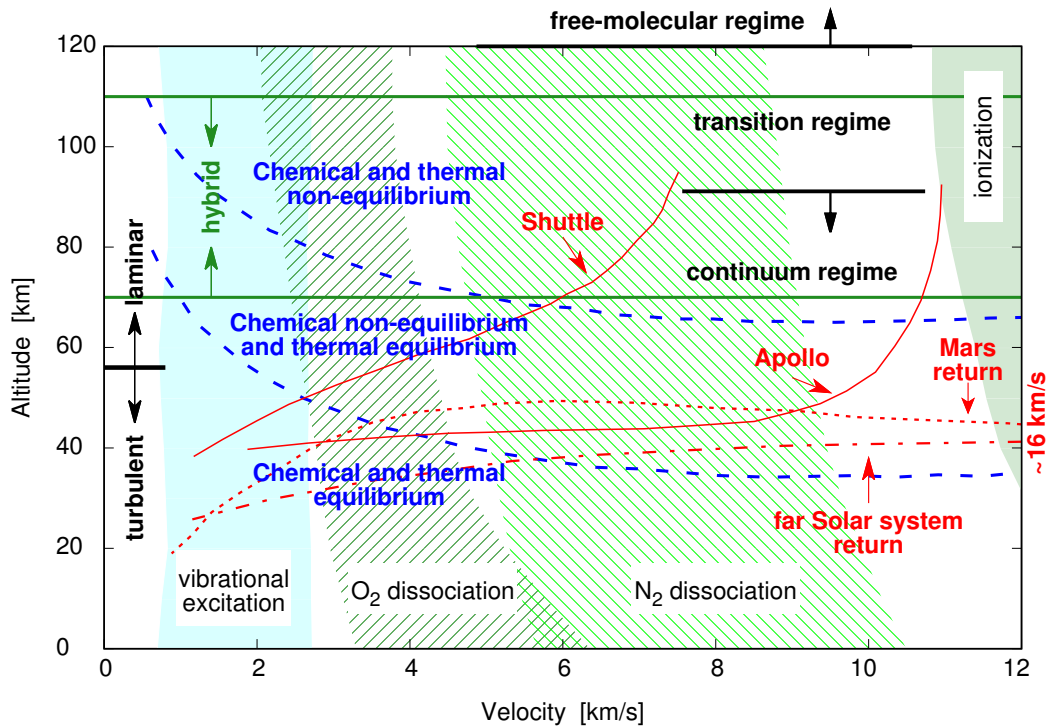


Figure 1.1: Flow-field features encountered during the Earth atmosphere reentry (adapted from [8]). A qualitative altitude interval at which the hybrid solver would be more efficient is indicated in green.

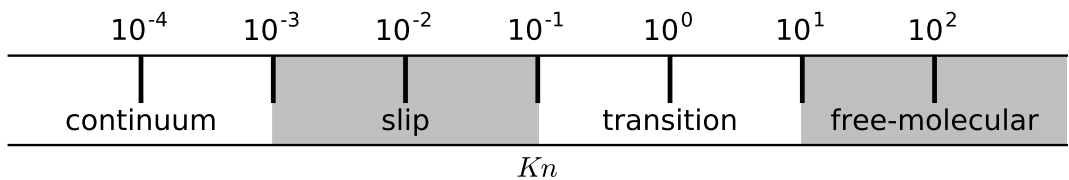


Figure 1.2: Flow regimes depending on  $Kn$

Such situation is of significance during reentry, as the spacecraft would pass through the full range of  $Kn$  (see Figure 1.1). While high up in the atmosphere, the gas around the spacecraft would be rarefied, and a possible method to use would be the direct

## Chapter 1. Introduction

simulation Monte Carlo (DSMC) method. The DSMC method, developed by Bird [9], can be used efficiently for high values of the Knudsen number, and its use is widely extended, especially among academic research groups and space agencies.

At sea level, the continuum assumption holds, and so conventional Computational Fluid Dynamics (CFD) can be used to solve the Navier-Stokes equations, valid at these altitudes. There is a  $Kn$  range, however, for which the flow around the spacecraft would not be completely rarefied nor continuum. For these conditions, the selection of the solver is anything but trivial. On one hand, the continuum hypothesis would stop being valid in the rarefied regions, so a CFD solver would not obtain accurate results in them. On the other hand, the computational cost of a DSMC simulation scales with  $Kn^{-4}$  [10], which could render the simulation impractical.

A possible solution to this conundrum is the use of both type of solvers, each acting in the portions of the domain where they are best suited for. This is called a hybrid solver. A qualitative representation of the altitude interval at which the hybrid solver would be more effective is shown in Figure 1.1.

## 1.2 Previous work

### 1.2.1 CFD

There is a wide range of computational codes that can be used for aerothermodynamics simulations. NASA has years of expertise, with both the LAURA [11] and DPLR [12] solvers. The DLR-TAU solver from the German Aerospace Center (Deutsches Zentrum für Luft- und Raumfahrt DLR) has also been used for hypersonic applications [13, 14]. Some universities have developed their own codes as well, like LeMANS [15, 16] from the University of Michigan. In the next paragraphs, some of these solvers are described in detail, together with an open-source code.

## LAURA

LAURA (Langley Aerothermodynamic Upwind Relaxation Algorithm) is a computational aerothermodynamics code developed at NASA Langley Research Center. It has a variety of chemical models [17], uses the High-Temperature Air Radiation (HARA) [18, 19] code for coupled radiation calculations, and can perform coupled and uncoupled ablation calculations.

LAURA has been used to simulate a variety of reentry vehicles, from Space Transportation System (STS) 2 [20], to perform, together with other CFD codes, the numerical analysis on STS-107 (Space Shuttle Columbia) accident [21]. In addition, the Orion Crew Module, has been simulated for different altitudes, comparing the results with DSMC simulations, to be able to predict at which altitude CFD cannot be used any longer [5].

## DPLR

DPLR (Data-Parallel Line Relaxation) is a CFD solver developed at NASA Ames Research Center. It includes different physical models, such as finite-rate reaction kinetics, chemical non-equilibrium processes, and ionised flow physics, and it allows for the simulation of ablation [22]. Although DPLR doesn't include a radiation code, it permits loose coupling with external codes, and has been used with the Non-Equilibrium Air Radiation (NEQAIR) [23, 24] code.

DPLR has been used several times for hypersonic simulations, such as the afterbody flow of the Project Fire II ballistic reentry [25], as well as the afterbody heating rates of the Apollo AS-202 Command Module reentry [26] and the Orion Crew Module [6]. As a case worth mentioning, DPLR was also used to calculate the effects a protruding gap filler will cause during reentry for STS-114, resulting in an additional extravehicular activity to remove the gap filler and avoid an accident similar to that of the Space Shuttle Columbia [27].

### ***rhoCentralFoam* and *hy2Foam***

*rhoCentralFoam* is an open-source CFD solver developed within the OpenFOAM (Open Field Operation and Manipulation) platform [28]. Whereas the solver is suited for high-speed simulations [29–31], it can only simulate single-species flow in thermal equilibrium. To extend the OpenFOAM’s CFD capabilities, *hy2Foam* was developed at the University of Strathclyde [32,33]. Based on *rhoCentralFoam* numerical schemes, *hy2Foam* adds a two-temperature model, by considering both translational-rotational and vibrational-electronic energy pools. In addition, multiple species can now be included in the simulation, also incorporating chemical reactions, based on different models. *hy2Foam* has been tested on the Mach 11.3 flow of non-reacting nitrogen over a blunted cone, and the Mach 20 flow of reacting nitrogen over a cylinder [34].

#### **1.2.2 DSMC**

DSMC includes by default quite a number of pre-requisites for aerothermodynamics simulations, therefore there are few differences between a standard DSMC code and one suitable for hypersonics. The following paragraphs describe some of these codes.

#### **MONACO**

MONACO is a DSMC code from the University of Michigan first developed by Dietrich and Boyd [35,36]. It has multi-species capabilities, allows for arbitrary 2D and 3D geometries, can calculate gas-surface interaction, and uses the No Time Counter (NTC) [37] collision method and the Total Collision Energy (TCE) chemical reaction model [38]. The code can only be used from within the United States.

MONACO has been used on a wide variety of test cases, ranging from hypersonic flow [39–42] to nonequilibrium flow around spacecraft [43,44]. In addition, the code has been successfully merged with a Particle-In-Cell (PIC) technique [45] for the sim-

## Chapter 1. Introduction

ulation of plasmas [46], and with CFD for the simulation of hypersonic flow with both continuum and rarefied regions [47–50].

### DAC

DAC (DSMC Analysis Code) is a code from NASA Johnson Space Flight Center. Developed by LeBeau [51], DAC is capable of multi-species simulations, can adapt the grid used for collision automatically, and uses the Larsen-Borgnakke energy redistribution [52], and the TCE model, with the Quantum-Kinetic (Q-K) chemistry model [53] having been recently implemented [54].

DAC has been used to simulate the reentry of NASA’s X-38 test vehicle [51], the aerothermodynamic of the Mars Pathfinder [55] and of the Mars Global Surveyor [56], the effect of the Reaction Control System (RCS) plumes on both the flowfield near the Space Shuttle and on the aerodynamic loads on the Mir Space Station [57], and the reentry of the Orion Crew Module [6].

### *dsmcFoam* and *dsmcFoam+*

*dsmcFoam* is an open-source DSMC solver developed within the OpenFOAM framework at the University of Strathclyde [58, 59]. It can deal with arbitrary 2D/3D geometries, can be used for multi-species simulations, employs a quantum version of the Larsen-Borgnakke procedure for energy redistribution, and uses the Quantum-Kinetic method for the chemical reactions present in the flow. Recently, electronic energy has been added to the solver [60, 61], with this new solver being called *dsmcFoam+*.

*dsmcFoam* has been used to simulate the flow past the Orion Crew Module [62], and the SARA capsule [63], as well as the demise of a satellite [64], and the interaction between a rocket plume and a surface, in the same conditions as on Phobos [65].

### 1.2.3 Hybrid solvers

Two main issues need to be taken into account before elaborating on hybrid solvers: the criterion to determine the different regions (and thus the interface between them), and the method used to transmit the information from one region to the other.

To distinguish between separation from equilibrium, different parameters have been proposed, all of them calculated using macroscopic flow properties. The most notable of these parameters are Bird's parameter [66], Garcia's Chapman-Enskog parameter [67], and Boyd's Gradient-Length-Local Knudsen number ( $Kn_{GLL}$ ) [68]. The definition of these parameters will be further explored in Chapter 4.

Regarding the information transfer between regions, two methods are typically used (see Figure 1.3). Flux-base coupling consists on the calculation of mass, momentum, and energy fluxes at the interface, according to both the rarefied and continuum solvers. In general, these two fluxes will be different, and therefore a modified one must be calculated to maintain the conservativeness of the resulting code. The modified flux will then be used to create a particle distribution for the rarefied region at the interface, and employed as boundary condition for the continuum region as well.

In state-based coupling, each region is extended past the interface, and the macroscopic properties of each are calculated in these cells, called buffer cells. The particle average of the rarefied region will be used as the macroscopic values in the buffer cells of the continuum region, while the macroscopic properties of the continuum region will be used to generate particles in the buffer cells of the rarefied region. Using this method each solver will handle the fluxes through the interface themselves, making them inherently conservative. In general, the statistical scatter on the calculation of fluxes for the flux-based coupling has been shown to scale as  $error_{flux} \sim error_{state}/Kn$  [69]. As the error in the cell average scales with the number of samples with a factor of  $1/\sqrt{Kn}$ , to obtain  $error_{flux} \approx error_{state}$ , the required number of samples will scale as  $1/Kn^2$ . As the interface is usually in near-equilibrium conditions ( $Kn \sim 0.01$ ) [70], flux-based coupling finds itself at a clear disadvantage.

In addition, three types of coupling can be distinguished depending on the frequency of information transfer. A decoupled solver will pass information only after the solvers have reached steady state, whereas a fully-coupled solver will do so at every time step. A loosely-coupled solver stands in between, the information transfer occurring more frequently than for decoupled solvers, but not as often as for fully-coupled.

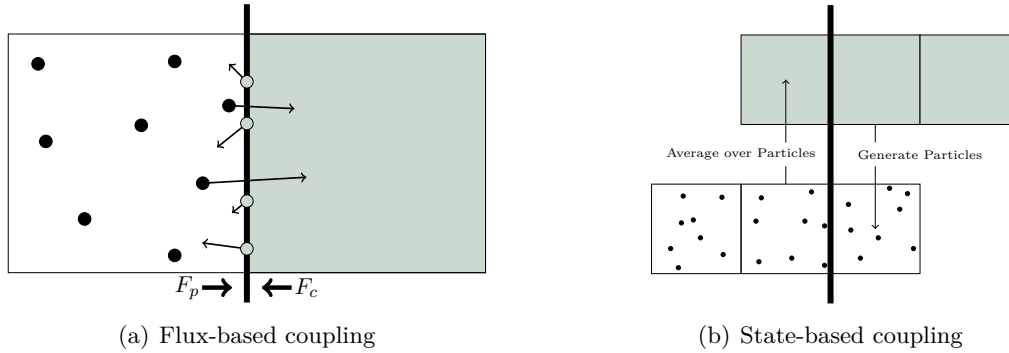


Figure 1.3: Typical hybrid coupling procedures (adapted from [70])

Despite the initial disadvantage of flux-based coupling regarding statistical scatter, numerous hybrid codes have been developed using this coupling method. Within flux-based coupling, Hash and Hassan employed a decoupled solver for the study of a rarefied flow over a blunted cone at Mach 10.3 [71]. The solver used results from a previous continuum simulation to generate the  $Kn_{GLL}$ , and used both the Maxwellian and the Chapman-Enskog distributions to generate the particles at the interface. A loosely-coupled implementation was used on the study of a Couette flow [72]. A decoupled solver was also applied to a plume flow through a high speed nozzle into hard vacuum by George and Boyd [73]. Their solver used the Chapman-Enskog parameter for region determination, and it was observed that the DSMC results greatly improved the accuracy of the solution when compared with the original CFD simulation. Finally, decoupled methods have also used the DSMC results to correct the CFD solution on near-wall regions. Bourgat *et al.* simulated a near-rarefied flat plate using CFD through the entire domain, but overlapping the DSMC solver near wall boundaries. This was shown to capture the friction forces more accurately than the generic slip boundary

## Chapter 1. Introduction

conditions used by the CFD solver itself [74].

Wadsworth and Erwin, developed a strongly coupled hybrid solver that used Maxwellian distributions to generate the particles at the interface. The solver was used to simulate 1D shocks [75], and a 2D rarefied slit flow [76].

Stephani modified and coupled NASA's DPLR and DAC code, resulting in a hybrid solver capable of dealing with multi-species flows [77]. The CFD and DSMC regions are defined by a modified form of Garcia's Chapman-Enskog Parameter, and the DSMC particles are initialised from the CFD results by using modified Chapman-Enskog distributions, that take into account rotational and vibrational internal degrees of freedom, as well as diffusion. This distribution reduces to the classic Chapman-Enskog distribution for a single-species flow with no internal degrees of freedom. The solver was used to examine a boundary layer flow, and the region in proximity to a normal shock, for a five-species gas mixture. The solver was then used to analyse hypersonic boundary layer flow over a discrete surface roughness element, with regard to the STS-119 flight experiment. Results from the hybrid were compared to DPLR, showing the importance of including non-equilibrium effects on these calculations.

On the other hand, many efforts have also been devoted to the implementation of state-based coupling hybrid solvers. Roveda *et al.* developed a strongly coupled code that uses Euler and DSMC solvers. Time-accurate 1D shock waves [78] and unsteady 2D slit flow [79] were simulated using this solver. Having implemented the Euler equations into the CFD portion of the code, which do not consider non-equilibrium phenomena, allows for the use of Maxwellian distributions to generate the particles on the buffer region.

In addition, dealing with a cell-based transfer of information between continuum and rarefied regions allowed for the implementation of different techniques that rely on cell properties. Garcia *et al.* extended adaptive mesh refinement (AMR) to use a particle method on regions requiring microscopic resolution, and a continuum method for

## Chapter 1. Introduction

larger scales, with different levels of refinement. This method, the adaptive mesh and algorithm refinement (AMAR), was designed to simulate flows with length scales that span several orders of magnitude. AMAR was then used to simulate thermodynamic equilibrium, an impulsive piston, a Rayleigh problem, and the flow past a sphere, showing good agreement with pure particle methods while reducing the number of particles required [80].

Following the creation of the AMAR method, Wijesinghe *et al.* modified it to implemented a time-adaptive technique to use with hybrid solvers. After an initial CFD solution is obtained and stored, using a suitable time step, the DSMC regions are calculated, using smaller steps. As such, the amount of iterations for the CFD solver is reduced, while maintaining accuracy in the DSMC region. It was validated for different test cases, including thermodynamic equilibrium and shock waves [81].

Carlson *et al.* employed the Information Preservation (IP) methodology to simulate a shock tube filled with argon [82]. This method reduced the statistical scatter in the buffer region by tracking the macroscopic flow properties of the DSMC domain. Whereas the results showed good agreement with experiments, the computational resources spent by the hybrid were higher than a pure DSMC simulation. Simulations over a flat plate and a micro aerofoil were later performed by Sun *et al.* [83], and showed lower computational expenses by larger percentage of CFD cells, as the additional macroscopic calculations needed in the DSMC domain are reduced in number.

Schwartzentruber and Boyd developed the Modular Particle-Continuum (MPC) method, combining the CFD code LeMANS and the DSMC code MONACO, and used it to simulate 1D shocks [70], with  $Kn_{GLL} = 0.05$  as the breakdown parameter. Posterior work on this code has improved the breakdown parameter to include thermal non-equilibrium, defining a new parameter  $Kn_{tra-rot}$ , where the subscripts *tra* and *rot* stand for translational and rotational respectively. This MPC solver was then be used on a 2D hypersonic cylinder, with  $\max(Kn_{GLL}, Kn_{tra-rot}) = 0.05$  as the breakdown parameter [47]. The MPC method has been used for different test cases [48–50], and

## Chapter 1. Introduction

extended to model rotational [84] and vibrational [85] non-equilibrium, as well as multi-species flows [86].

Abbate *et al.* developed both a steady-state and an unsteady solver. For the steady-state solver, the different regions are identified using  $Kn_{GLL}$  as breakdown parameter, and the overlapping region is determined by a variations of  $Kn$ . CFD and DSMC are then calculated independently in their subdomains until steady-state is achieved. At this point, the breakdown parameter is recalculated and the domain is once again split. This process is repeated until the  $Kn_{GLL}$  exceeds the breakdown criterion only in the DSMC region. A similar process is followed by the unsteady solver, except that the coupling is reapplied when a preset coupling time-step is reached, such that  $\Delta t_{coupling} >> \Delta t_{CFD}, \Delta t_{DSMC}$ . The method was applied to a 1D shock tube and a 2D expanding jet, showing that the accuracy of the solution is greater than the one obtained by purely CFD methods [10]. Later work focused on a supersonic expansion, showing the validity of this methodology for high-speed applications [87].

A scheme suitable for unstructured meshes was developed by Wu *et al.*, and it was validated using 2D supersonic flow over a wedge and 3D flow of parallel orifice jets [88]. Using a different CFD solver, the code was modified for parallel computations, and used to simulate the hypersonic flow over a square cylinder, and the same wedge from the previous work, for comparison [89].

Concerning open-source solvers, Darbandi and Roohi developed a hybrid cycle within OpenFOAM , using the *rhoCentralFoam* and *dsmcFoam* as the respective CFD and DSMC solvers [90]. The cycle involved manual manipulations of the results from each solver, instead of a full hybrid code. The breakdown parameter is calculated using the CFD solution, which in turn allows for the determination of the DSMC region including the buffer cells. The results obtained are then compared to a convergence criterion, which is dependent on either a full DSMC solution, or experimental results. If the simulation is yet to converge, the DSMC region is extended, and the particle solver

continues until the criterion is met. The hybrid cycle was validated using a hypersonic flow over a microcylinder and a hypersonic flow over a nanoscale flat plate as test cases. The results proved satisfactory, and showed that the CFD/DSMC interface should be situated at a location that can be described by both models.

Gott [91] went a step further, and developed an open source full hybrid solver within OpenFOAM, using *rhoCentralFoam* and *birdFoam*, a modified version of *dsmcFoam* that makes it more suitable for the simulation of physical vapour deposition (PVD). The solver was designed specifically for PVD, taking advantage of phenomena like the one-way motion of vapour from dense to rarefied conditions.

### 1.3 Objectives

The aim of this project is to provide the fundamentals for an open-source hybrid solver capable of providing in a time-efficient manner accurate results for the full range of Knudsen numbers, which a spacecraft would encounter during a planetary atmosphere entry. This solver would require methods to handle both rarefied and continuum conditions, and to be able to behave like its respective solver when only one type of these conditions are found within the domain.

At the rarefied regime found in high altitudes, *dsmcFoam* becomes a natural candidate to form part of the hybrid solver. First, the University of Strathclyde has extensive experience with this code, since its development and posterior improvements. Additionally, the capabilities of the solver itself made it one of the few open-source DSMC codes capable of accurately describe Earth atmospheric re-entry back when this project was started in 2014. Finally, the OpenFOAM framework is commonly used in academia and some industrial research, which grants the code with good exposure to the community.

For the continuum regime found at low altitudes, many possible CFD codes can be taken into account. However, using a continuum solver within OpenFOAM would sim-

plify the communication efforts with *dsmcFoam*. When the project started, the solver that most complied with the needed requirements was *rhoCentralFoam*. However, this compliance was still far from ideal, both in terms of physical modelling capabilities as well as time efficiency. Parallel to this work, the research by Casseau *et al.* [32–34] contributed to the development of the required new physical models into what would become the *hy2Foam* solver, and thus a new objective for this project was the implementation of some convergence acceleration tools, originally for *rhoCentralFoam*, but that could be also adopted by *hy2Foam*.

In addition, a suitable criterion should be identified for the definition of the continuum and rarefied domains. The  $Kn_{GLL}$  and  $B$  parameters seem to be the ones that could best represent the continuum-rarefied transition. Finally, the transfer of information between the two types of domains needs to be carefully implemented. State-based coupling matches the hybrid requirements quite well for the applications of interest.

With all of this, the thesis would have achieved its novelty contribution, which is the development of the first open-source hybrid particle-continuum solver for high-speed, high-altitude flows.

## 1.4 Thesis Overview

Chapter 2 focuses on the verification and developments on the OpenFOAM solver *rhoCentralFoam*. Two techniques to accelerate the convergence of high speed simulations were incorporated and analysed, showing good agreement and time reduction. At the time, *rhoCentralFoam* was OpenFOAM’s most accurate solver for high-speed flows, but this analysis contributed to the creation of *hy2Foam*, the solver adopted for the hybrid code.

Chapter 3 deals with an in-depth analysis of the physics behind high-speed flows, and the equations behind the continuum and rarefied formulations. In particular, this

## Chapter 1. Introduction

chapter focuses on the incorporation of said physics into *hy2Foam* and *dsmcFoam*, the continuum and rarefied solvers used for the creation of *hyperFoam*.

Chapter 4 describes the development of the hybrid solver, *hyperFoam*, detailing its characteristics. A Couette flow with heat transfer is used to analyse the behaviour and accuracy of *hyperFoam* when compared to a pure DSMC simulation.

Chapter 5 continues with the validation of *hyperFoam* by simulating a more complex hypersonic cylinder, comparing both its accuracy and the computational resources used with those from *dsmcFoam*.

Chapter 6 reports the most important findings of this research, together with future areas of work.

## Chapter 2

# Validation of *rhoCentralFoam* and Convergence Acceleration Techniques

OpenFOAM provides different alternatives for compressible solvers. Some of the solvers are compressible versions of normally incompressible schemes, such as *rhoSimpleFoam*, the compressible version of the Semi-Implicit Method for Pressure Linked Equations (SIMPLE) [92]. However, to better capture shock waves and other characteristics of high-speed flows, density-based methods (Riemann solvers [93]) have historically been preferred over pressure-based methods (such as SIMPLE, mentioned above). OpenFOAM includes that type of solver, *rhoCentralFoam* [29], an unsteady solver that uses semi-discrete, non-staggered, Godunov-type central [94] and upwind-central [95] schemes. These schemes can be considered more as a process of *interpolation*, rather than the *reconstruction - evolution - projection* process of other Godunov-type methods [29] (such as AUSM [96], HLLC [97] or Roe [98], to cite a few) due to their simplicity, achieved by avoiding the need to solve the Riemann problem at each cell interface, effectively integrating the solution over the Riemann fan instead [95]. The absence of a Riemann solver contributes to the schemes' stability by eliminating the presence of the carbuncle phenomenon [99, 100], as this instability appears when solving the Rie-

mann problem using a contact-resolving Riemann solver [101]. This increased stability ensures the suitability of these schemes, and therefore *rhoCentralFoam*, for high-speed flows.

*rhoCentralFoam* has been successfully used for the simulation of high-speed flow simulations [29, 30]. However, some of these test cases have been rather simplistic. For this reason, further studies on the capabilities of the solver have been performed. Section 2.1 analyses a Mach 9 flow over a hollow cylinder for different angles of attack, comparing the results obtained with other from different state-of-the-art CFD codes. Due to the huge computational results spent on these simulations, some techniques are incorporated into *rhoCentralFoam* aiming to reduce the computational time required to achieve convergence. This is the focus of section 2.2, with an analysis on local time stepping and adaptive mesh refinement on subsections 2.2.1 and 2.2.2, respectively.

## 2.1 Hollow cylinder

Some hypersonic test cases were proposed for the 1<sup>st</sup> Spacecraft Demise Workshop, that sat within the 8<sup>th</sup> European Symposium on Aerothermodynamics for Space Vehicles, that took place in March 2015. The cases consisted of a 1 m long, 1 m diameter cylinder, with different thicknesses (see Figure 2.1), angles of attack, and sideslip angles. The flow properties were also case dependent, including both continuum and rarefied free-stream conditions.

Two of those test cases were analysed using *rhoCentralFoam*. The flow properties are the same for both, these conditions being  $M_\infty = 9$ ,  $T_\infty = 256.26$  K,  $p_\infty = 272.72$  Pa,  $T_W = 700$  K, where  $M$  is the Mach number,  $T$  the temperature,  $p$  the pressure, the subscript  $W$  refers to the conditions at the wall, and the subscript  $\infty$  refers to upstream conditions. The gas used is air, considered a non-reacting, perfect gas, with a dynamic viscosity ( $\mu$ ) that follows Sutherland's law [102] using the following coeffi-

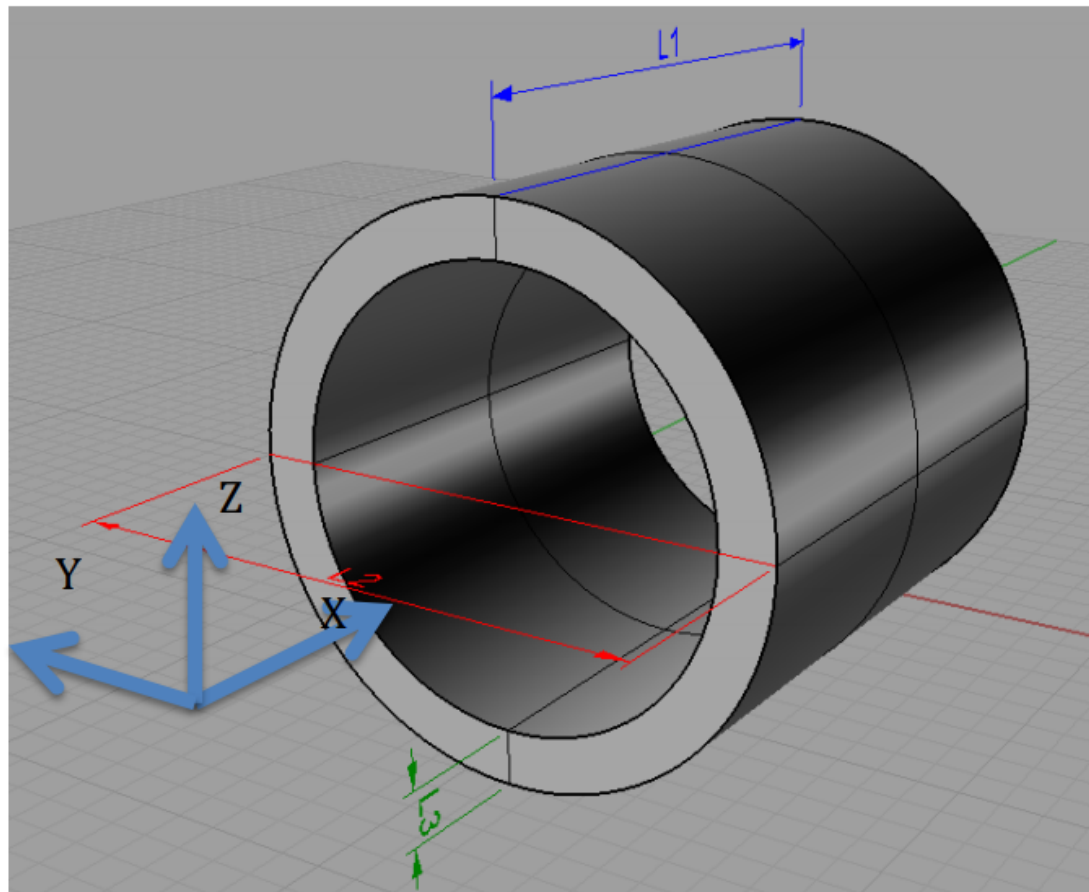


Figure 2.1: Hollowed cylinder (from [31])

cients:  $A_S = 1.458 \cdot 10^{-6}$  Pa·s/ $\sqrt{\text{K}}$ ,  $T_S = 110.4$  K. Both of the test cases also share a cylinder thickness of 25 cm, the only difference between them being the angle of attack ( $AoA$ ): a configuration with  $AoA = 0^\circ$  (flow parallel to the cylinder axis, case M001) and a second one with  $AoA = 90^\circ$  (flow perpendicular to the cylinder axis, case M003).

For the  $AoA = 0^\circ$  case, an axisymmetric mesh could be used for the whole domain instead of a 3D mesh, thus saving computational time. This structured mesh, created with the open source mesh generator gmsh [103], was modified twice after creation for two different reasons. First of all, to capture the heat transfer between the flow and the cylinder as accurately as possible, the mesh should be aligned with the shock wave [104]. This required the results from a first simulation to estimate the position of the shock. After the first alignment procedure and refinement of cells near the shock to increase accuracy on its location, the new mesh returned a solution that was no longer aligned. After the second time this methodology was applied, the shock remained aligned with the mesh and thus no further iterations were required. The second reason was the refinement of the mesh on the near-wall and near-symmetry-axis regions. The first mesh couldn't capture all the relevant details in these areas, with 1 mm cell resolution near the boundary (resulting in  $y^+ = 30$ ). However, these results were still mandatory to be able to identify those regions that required higher resolution, resulting in a wall distance of 0.1 mm ( $y^+ = 3$ ) on the third mesh. The mesh size experience *sym33%* increase in these modifications, from around 200000 cells to 265970 cells in the third mesh. A sketch of the blocks used for the final mesh can be seen in Figure 2.2.

For the  $AoA = 90^\circ$  case, quarter symmetry could be used, but even the coarse initial mesh had almost 1.5 million cells with a wall distance of 1 mm ( $y^+ = 30$ ). For this case, no further refinement nor alignment were implemented. It is important to note that this lack of modifications will result in a less accurate solution, from a smeared shock profile to less-than-optimal boundary measurements.

Figures 2.3-2.6 show the different contour plots obtained for the  $AoA = 0^\circ$  case,

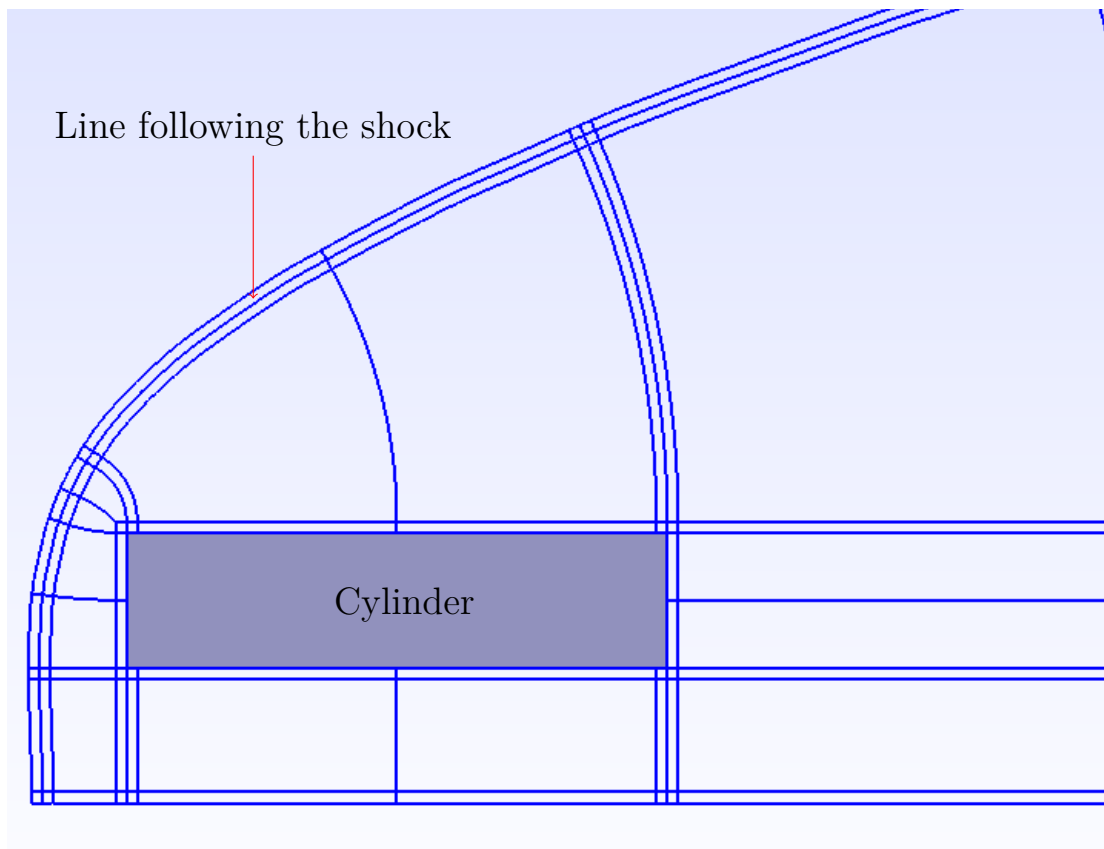


Figure 2.2: Mesh blocks near the cylinder for the  $AoA = 0^\circ$  case

Case	Angle	Axial force (N)	Normal force (N)	Heat flux (W)
M001	$0^\circ$	$1.567 \times 10^4$	0.0	$4.077 \times 10^5$
M003	$90^\circ$	0.0	$1.826 \times 10^4$	$3.575 \times 10^5$

Table 2.1: Forces and heat flux results

showing that, after the oblique shock waves generated from the first Mach disk reflect on the cylinder inner walls, more than one wave is generated. This can be better observed in Figure 2.7, and is caused by the interaction between the shock wave and the boundary layer [105]. The shock caused a separation of the boundary layer at the inner wall of the cylinder, which can be observed from the recirculation bubble on Figure 2.8. This separation creates a first set of compression waves near the separation point that coalesce into a shock wave not further away from the cylinder wall. A similar set of compression waves is also formed at the reattachment point, later coalescing into a shock wave. An schematic of this can be seen on Figure 2.9. Due to the need of a well refined mesh to properly capture the boundary layer, only two simulations on the workshop showed this phenomenon.

Figures 2.10-2.12 show the contour plots for the  $AoA = 90^\circ$  case. Figure 2.13 show flow recirculation happening inside the cylinder, moved due to shear by the flow travelling at high speeds on the cylinder sides.

The global forces and heat flux can be seen in Table 2.1. The comparison between the current results and those obtained with other state-of-the-art codes can be seen in Figures 2.14-2.16 (from Ref. [31]), where it can be seen that *rhoCentralFoam* compares quite well with other CFD codes such as DLR-TAU.

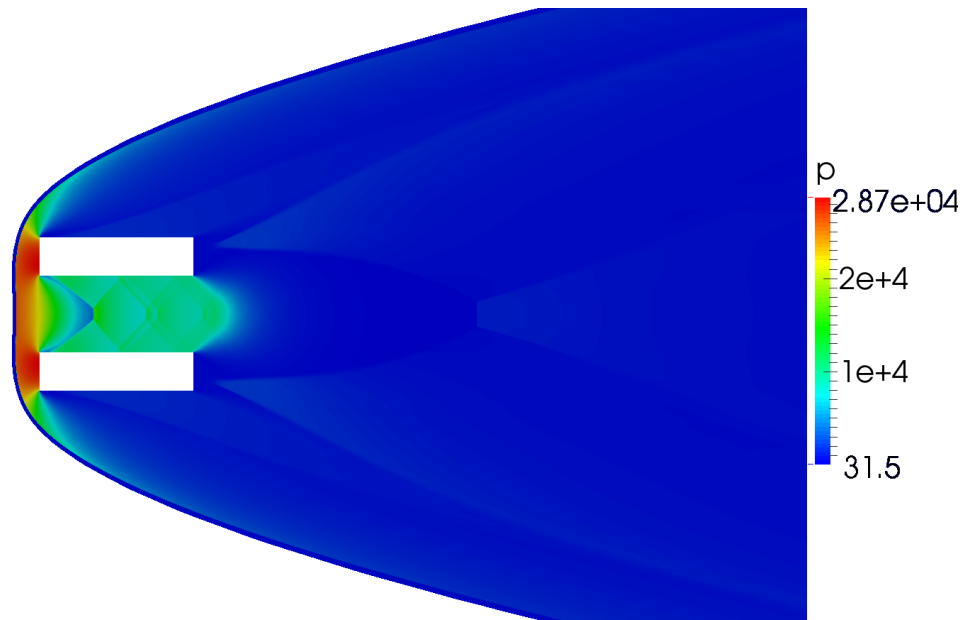


Figure 2.3: Pressure contour plot in  $Pa$  for the  $AoA = 0^\circ$  case

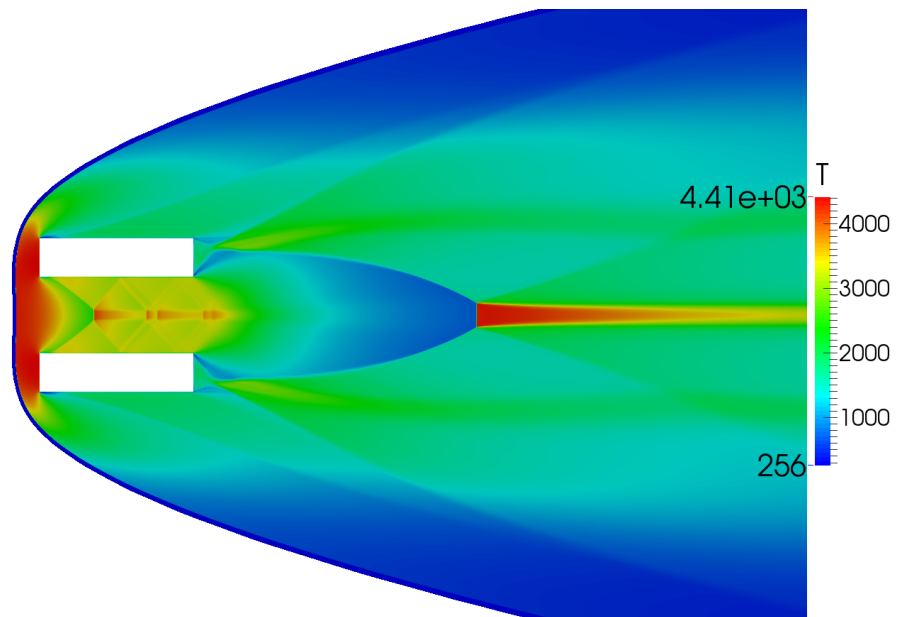


Figure 2.4: Temperature contour plot in  $K$  for the  $AoA = 0^\circ$  case, in K

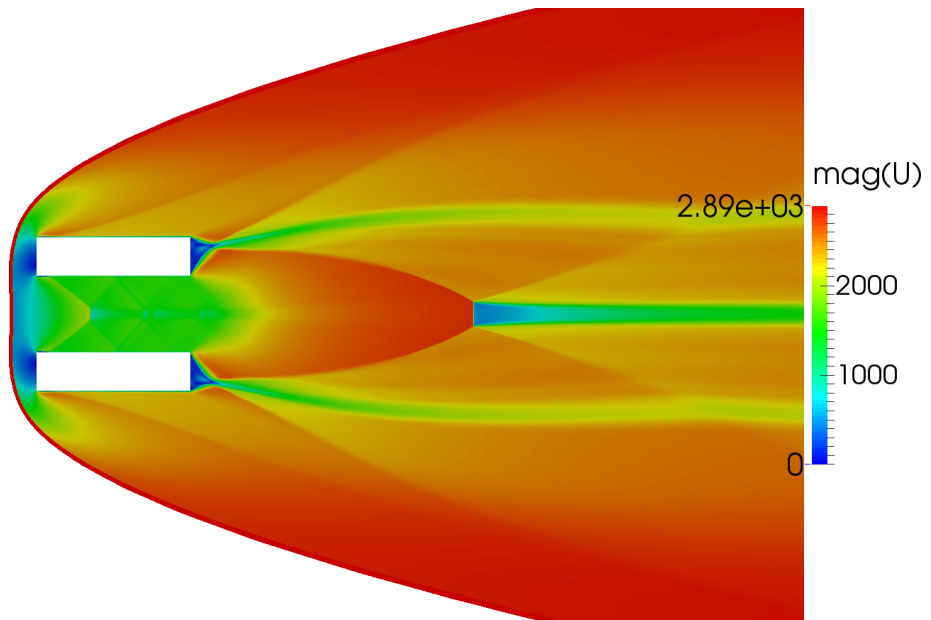


Figure 2.5: Velocity magnitude contour plot in  $m/s$  for the  $AoA = 0^\circ$  case

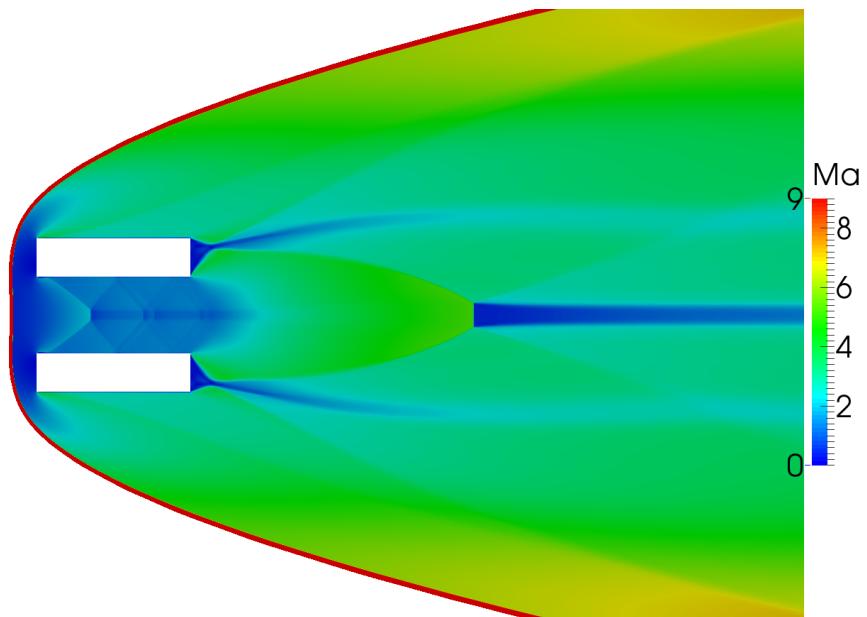


Figure 2.6: Mach number contour plot for the  $AoA = 0^\circ$  case



Figure 2.7: Schlieren visualization of the shock structure inside the cylinder

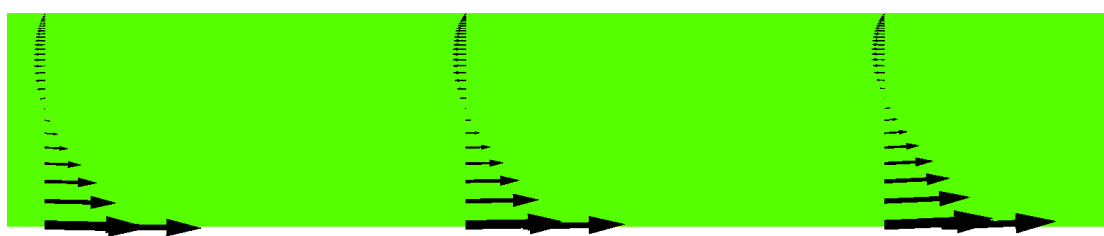


Figure 2.8: Recirculation bubble in the region of interest from Figure 2.7, with the background colour for contrast.

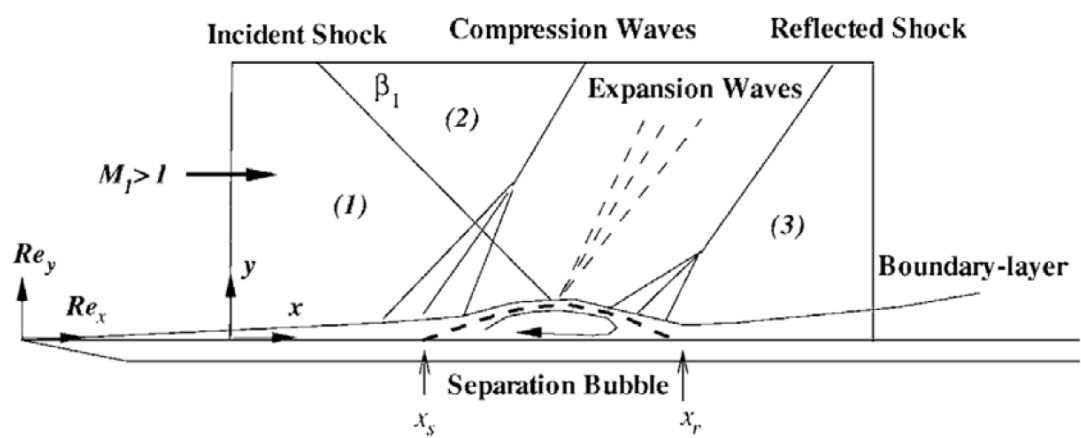


Figure 2.9: Flow features of a laminar shock impingement configuration, from [105].

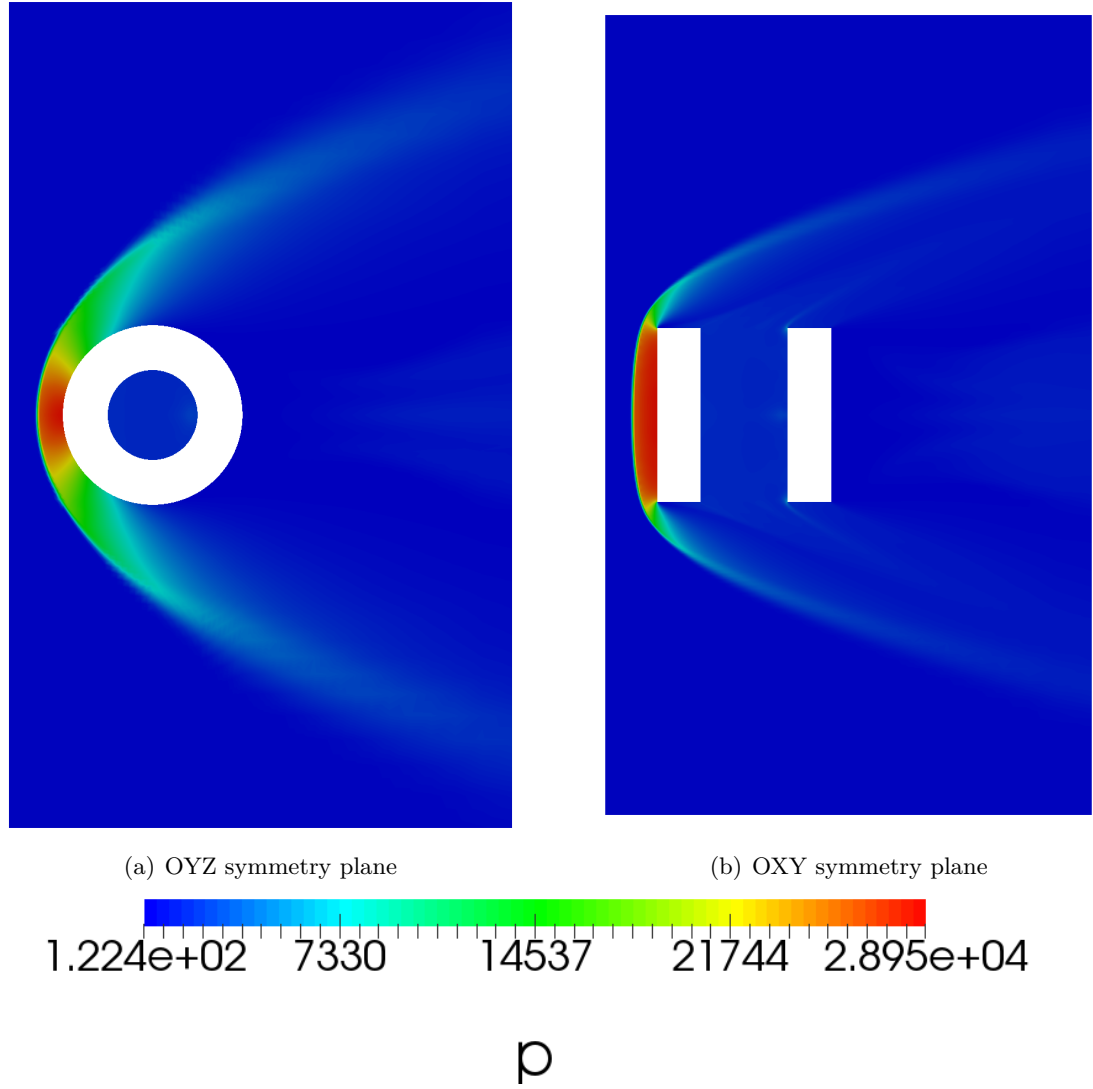


Figure 2.10: Pressure contour plots for the  $AoA = 90^\circ$  case

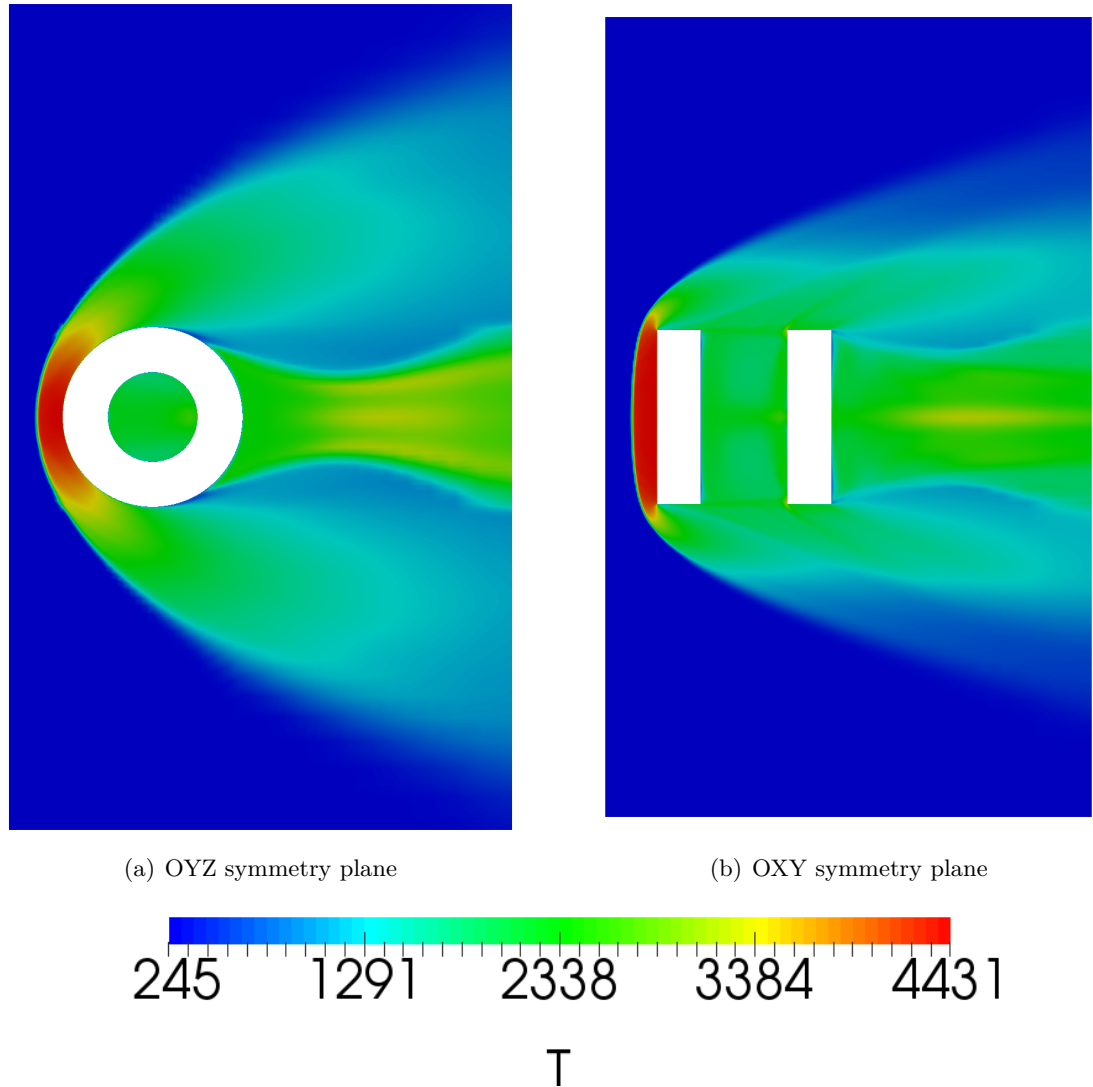


Figure 2.11: Temperature contour plots for the  $AoA = 90^\circ$  case

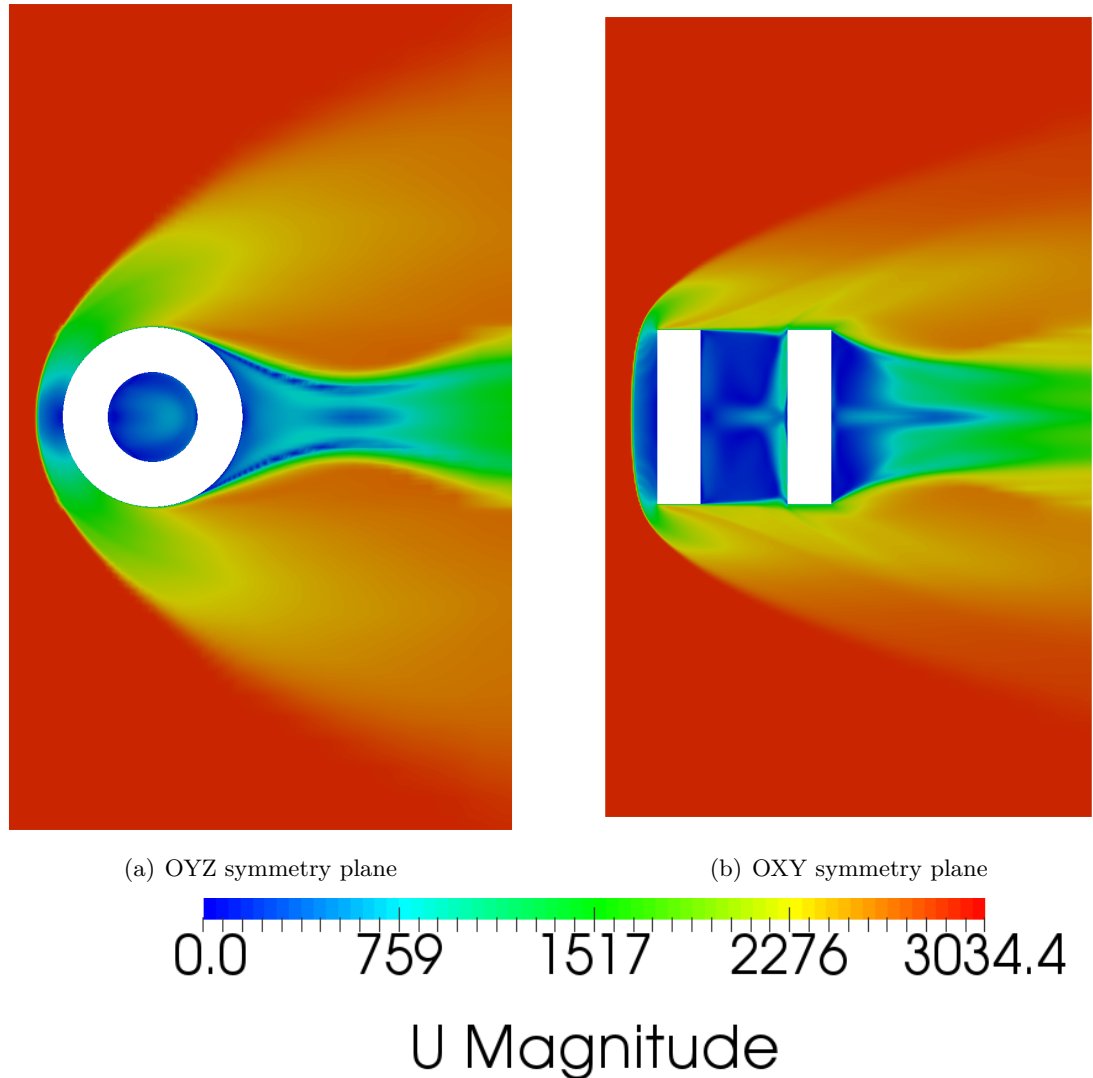


Figure 2.12: Velocity magnitude contour plots for the  $AoA = 90^\circ$  case

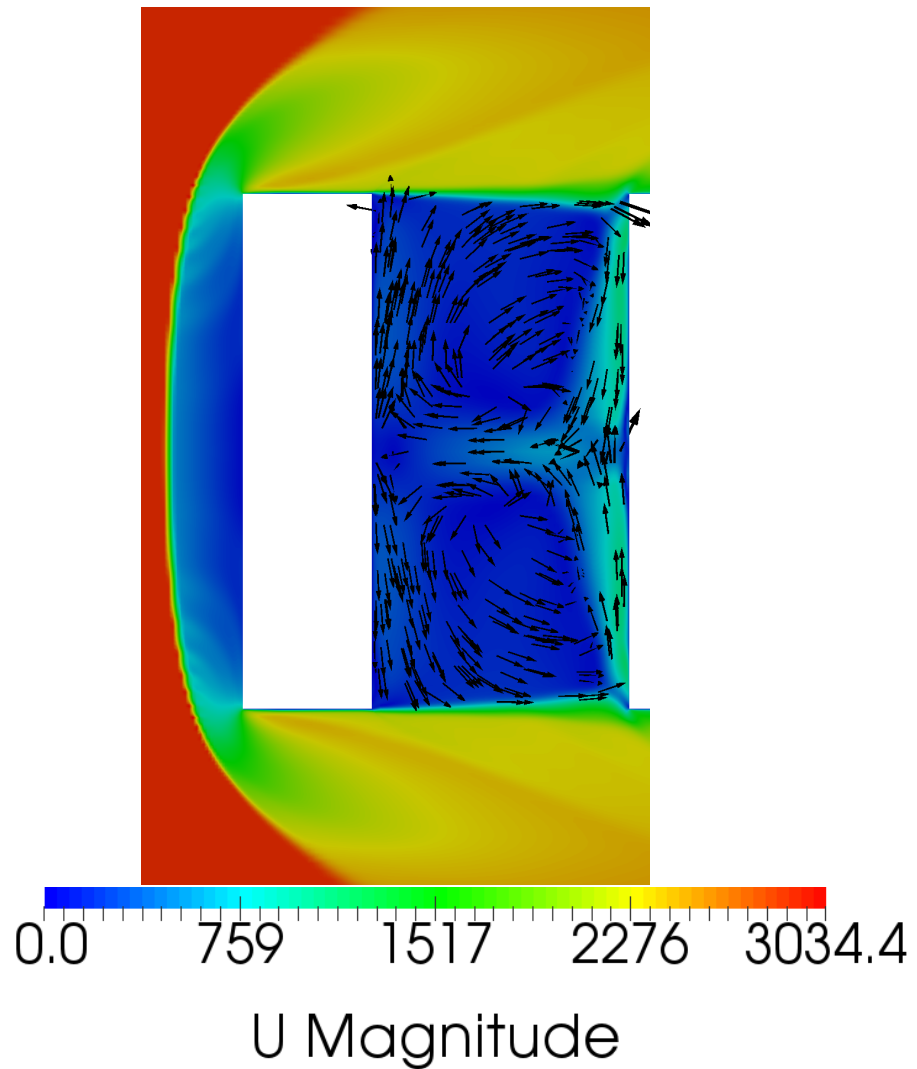


Figure 2.13: Recirculating flow inside the cylinder for the  $AoA = 90^\circ$  case, with velocity magnitude contour plot, in m/s

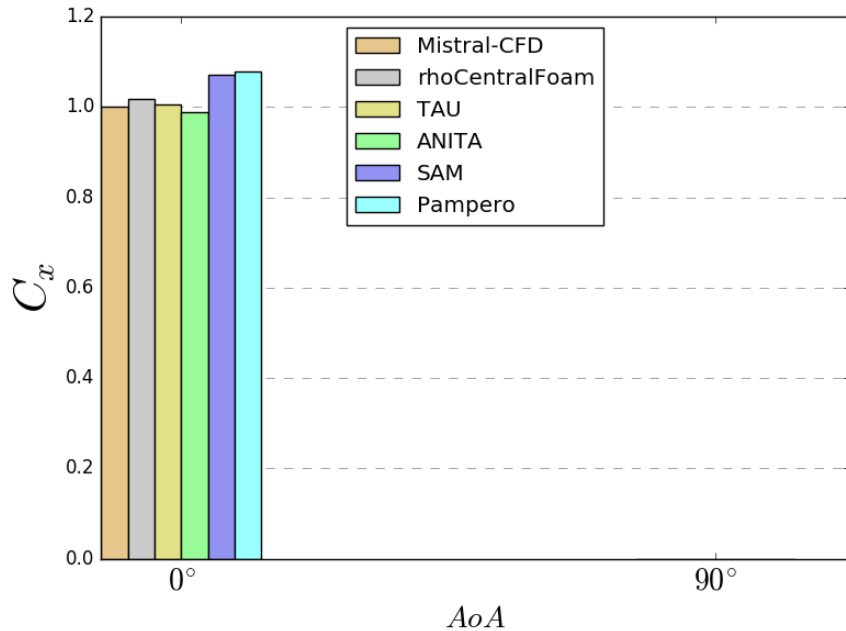


Figure 2.14: Comparison of axial force coefficients (from Ref [31])

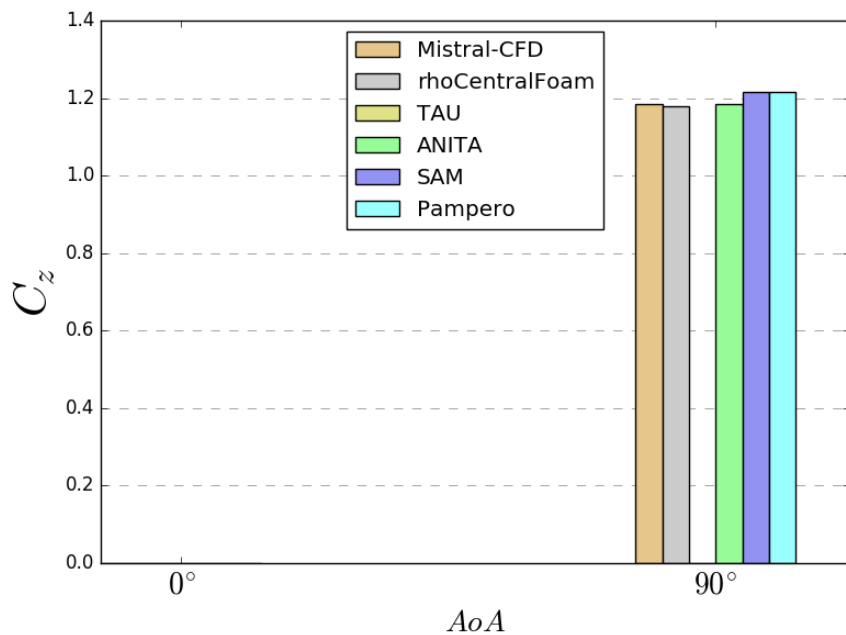


Figure 2.15: Comparison of normal force coefficients (from Ref [31])

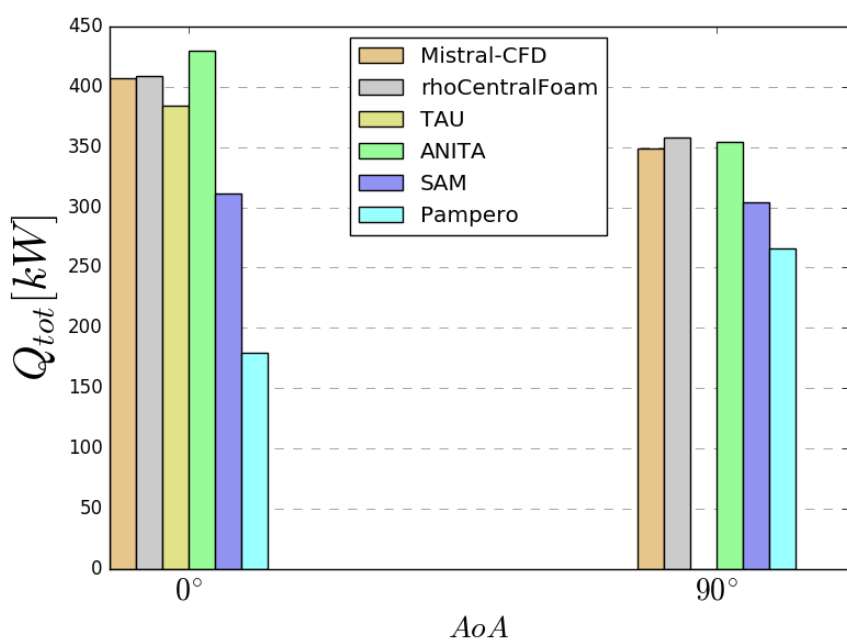


Figure 2.16: Comparison of heat fluxes (from Ref [31])

## 2.2 Tools to accelerate convergence

As can be seen from the workshop's results, the accuracy of the solver has been deemed satisfactory. However, during these simulations, *rhoCentralFoam* raised some concerns regarding the computational time required. The transient nature of the solver, while useful for unsteady simulations, proved to be an inconvenience for steady cases. Whereas with the coarse mesh for the  $AoA = 0^\circ$  case, only 66 CPU Hours were necessary till convergence, the better aligned and more refined meshes required, respectively, 173 and 321 CPU Hours, for a grand total of 560 CPU hours, about 7.5 times more than the coarse mesh. This effect would have had a heavier impact for the  $AoA = 90^\circ$  case, where the quarter symmetry coarse mesh required already 2275 CPU Hours. This lead to further code development, to incorporate some techniques that could reduce the computational expenses of the *rhoCentralFoam* solver. These techniques are local time stepping (LTS) and adaptive mesh refinement (AMR), and will be further analysed in the following subsections.

### 2.2.1 Local time stepping

LTS is a technique that can be used to speed up the convergence of a simulation towards its steady-state solution. *rhoCentralFoam* being an unsteady solver, the flow will go through a transient solution before reaching steady state. In its present form, the solver moves forward in time using the same time-step for all the cells in the computational domain. This means that, to avoid instabilities, this rate of temporal advance is limited by the cell having the smallest time-step.

Looking at the both the standard Navier-Stokes equations and the LTS equations aides to the understanding of how LTS works. Navier-Stokes equations have the form:

$$\frac{\partial \mathbf{W}}{\partial t} + \nabla \cdot \mathbf{F} = \mathbf{S} \quad (2.1)$$

where  $\mathbf{W}$  represents the conserved variables,  $\mathbf{F}$  the fluxes,  $\mathbf{S}$  the source terms, and  $t$

the time. The LTS technique solves a slightly modified version of the Navier-Stokes equations:

$$\frac{1}{a} \frac{\partial \mathbf{W}}{\partial t} + \nabla \cdot \mathbf{F} = \mathbf{S} \quad (2.2)$$

where  $a$  is an acceleration factor that depends on  $\mathbf{W}$ . For a simulation with a steady solution, the time derivative is exactly zero. Therefore, a solution of Equation 2.2 will also be a solution of Equation 2.1, independently of the value of  $a$ .

By the time these code developments were made, there was LTS implementation on OpenFOAM for some solvers. However, this was not the case for *rhoCentralFoam*. Thus, similar implementations in the OpenFOAM solver *LTSInterFoam*, and those found on Ref. [106], served as a base for the implementation of LTS on the chosen compressible solver. On this implementation, the time-step  $\Delta t$  for each cell is selected as the minimum between the time-step determined by the user-defined maximum Courant number  $C_{max}$  within the flow, and a user-defined maximum time-step  $\Delta t_{max}$ . In other words:

$$\Delta t = \min(\Delta t(C_{max}), \Delta t_{max}) \quad (2.3)$$

Once the  $\Delta t$  field is calculated using Equation 2.3, the field is then smoothed spatially, before being used for the calculation of the solution in each computational cell.

To validate the LTS procedure, a subsonic Couette flow with heat transfer, as well as a supersonic flat plate have been simulated.

### Couette flow

For the Couette flow, the upper and lower walls have a separation of 1 m, and the lateral boundaries of the computational domain were 40 cm apart, but modelled using cyclic boundary conditions. The base cell size used is 0.01 m  $\times$  0.01 m. To have different cell sizes to be able to use the LTS technique effectively, the four cells at the centre of the channel were split in half in each dimension, from these resulting 16 cells, the four in the middle were again split in half in each dimension, and so on until 11 levels of

refinement were achieved. The smallest cells has a size of approximately  $4.88 \mu\text{m} \times 4.88 \mu\text{m}$ . A depiction of the domain, including zoom-ins to observe the refinement levels, can be seen in Figure 2.17.

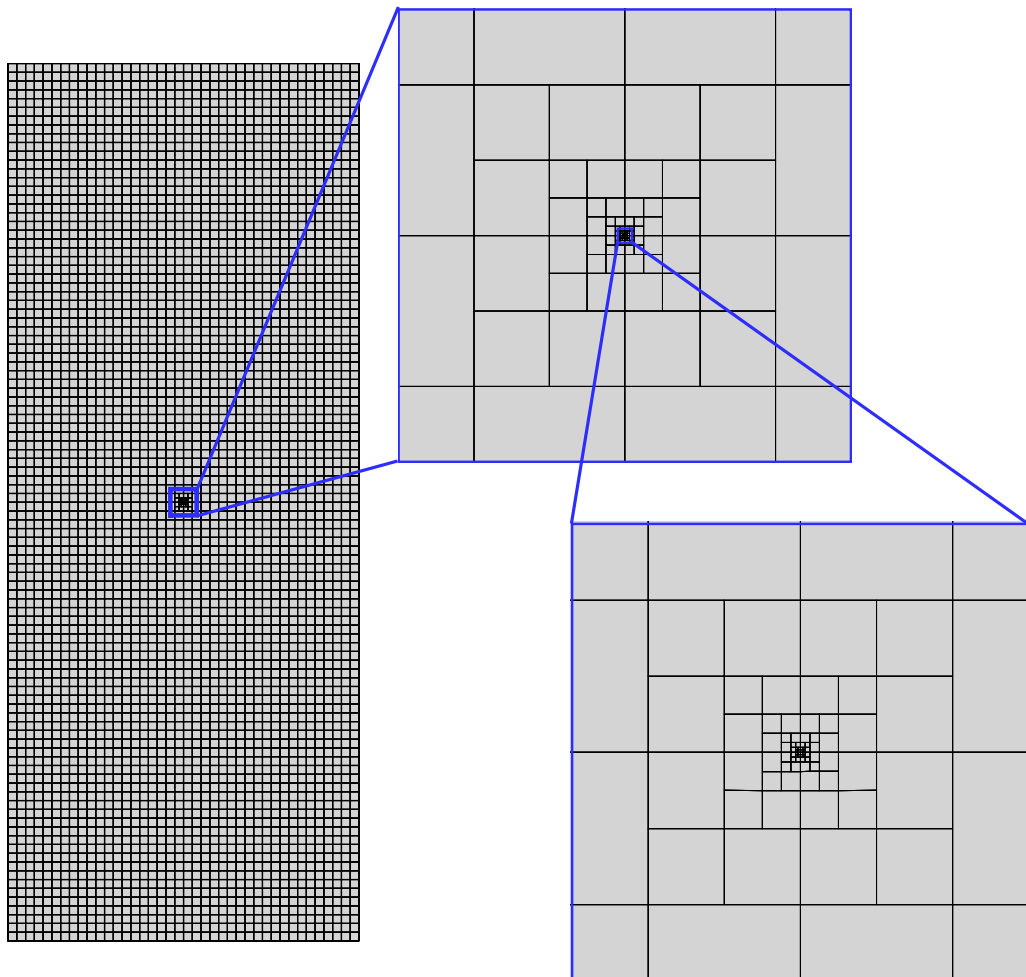


Figure 2.17: Mesh for the Couette flow test case

The fluid within the channel is air, and the initial and boundary conditions are set as can be seen in Table 2.2.

where  $u$  represents the flow speed in the  $x$ -direction,  $v$  is the flow speed in the  $y$ -direction,  $H$  is the height of the channel, and the subscripts  $TW$  and  $BW$  refer to the top and bottom walls of the channel, respectively.

	$u$	$v$	$T$	$p$
$t = 0; \forall x, y$	0 m/s	0 m/s	200 K	100 Pa
$\forall t, x; y = 0$	$u_{BW} = 0$ m/s	$v_{BW} = 0$ m/s	$T_{BW} = 200$ K	-
$\forall t, x; y = H$	$u_{TW} = 200$ m/s	$v_{TW} = 0$ m/s	$T_{TW} = 400$ K	-

Table 2.2: Initial and boundary conditions for the Couette flow test case

The maximum Courant number was set to 0.2, and the maximum allowable time-step to 1 ms.

The results obtained from the numerical simulation along the vertical centreline of the domain have been compared to the analytical solution for this flow considering constant transport properties, namely:

$$T(y) = T_{BW} + (T_{TW} - T_{BW}) \frac{y}{H} + \frac{\mu u_{TW}^2}{2\kappa} \frac{y}{H} \left(1 - \frac{y}{H}\right) \quad (2.4)$$

$$u(y) = u_{TW} \frac{y}{H} \quad (2.5)$$

$$v(y) = 0 \text{ m/s} \quad (2.6)$$

$$p(y) = \text{constant} \quad (2.7)$$

where  $\kappa$  is the thermal conductivity.

Figures 2.18 to 2.20 show how the solution progresses with respect to the number of iterations. It can be observed, the LTS solver converges to the analytical solution in much fewer iterations than the unmodified solver. Setting the convergence criterion as having a maximum relative error smaller than 1% for any variable, it takes the unmodified solver 27.5 million iterations to reach convergence, whereas only 7.5 million iterations are needed for the LTS version. The individual cell time-step is shown on Table 2.3. The time-step for the unmodified solver is the same for all the cells, thus being represented with a single value. For the LTS solver, however, the value of the minimum time-step greatly differs from the value of the maximum time-step. The bigger cells will evolve in time using these large values, thus progressing faster to the steady-state solution.

The computational time can be seen in Table 2.4 every 2.5 million iterations. From that table it can be concluded that the LTS solver employed 2.56 times less computational resources than the unmodified solver, to reach a relative error of approximately 1%.

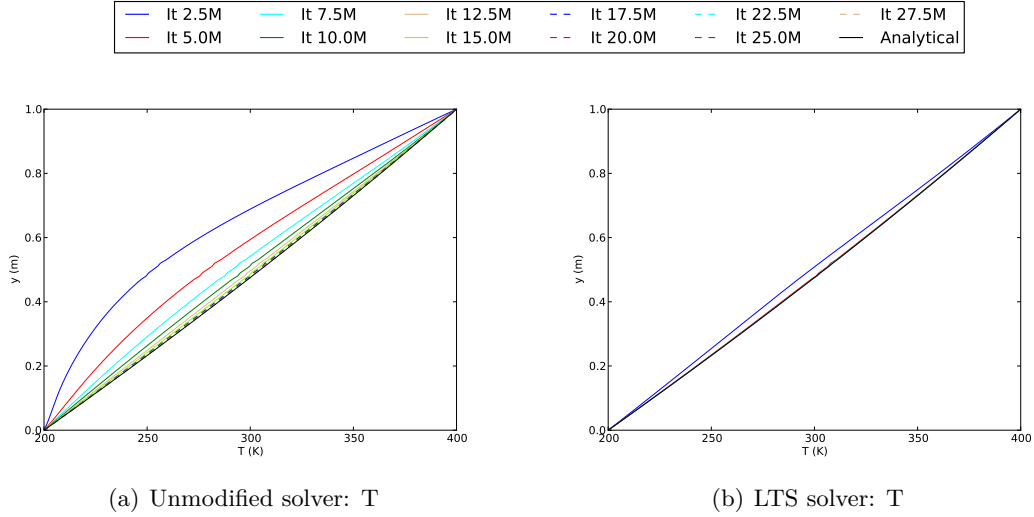


Figure 2.18: Results from the unmodified and the LTS solvers for temperature

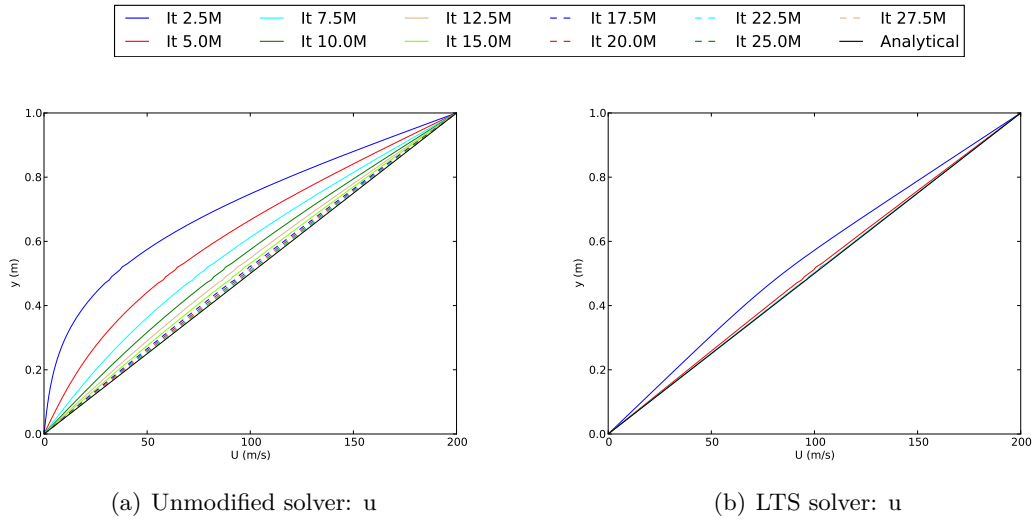
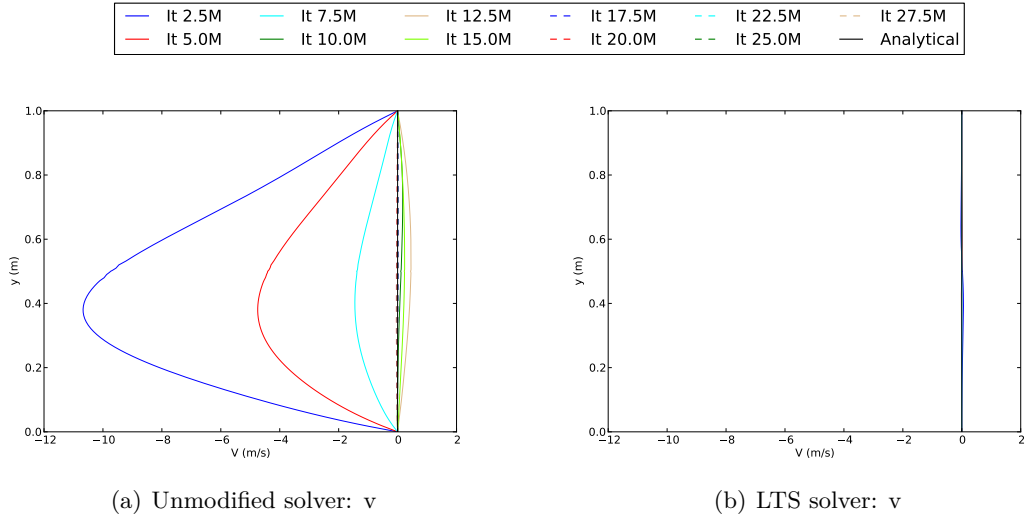


Figure 2.19: Results from the unmodified and the LTS solvers for *x*-velocity


 Figure 2.20: Results from the unmodified and the LTS solvers for  $y$ -velocity

Iteration ( $\times 10^6$ )	Unmodified	LTS	
		Min	Max
2.5	5.515 ns	20.148 ns	2.150 $\mu$ s
5	4.922 ns	1.237 ns	0.343 $\mu$ s
7.5	4.667 ns	1.233 ns	0.341 $\mu$ s
10	4.531 ns	-	-
12.5	4.522 ns	-	-
15	4.406 ns	-	-
17.5	4.378 ns	-	-
20	4.361 ns	-	-
22.5	4.351 ns	-	-
25	4.344 ns	-	-
27.5	4.340 ns	-	-

Table 2.3: Simulation time-step in each iteration level, for the unmodified and LTS solvers

Iteration ( $\times 10^6$ )	Unmodified	LTS
2.5	7h 27min	9h 21min
5	14h 56min	18h 53min
7.5	22h 37min	28h 1min
10	29h 23min	-
12.5	35h 5min	-
15	41h 13min	-
17.5	47h 13min	-
20	52h 58min	-
22.5	59h 21min	-
25	65h 30min	-
27.5	71h 42min	-

Table 2.4: Computational time required to reach each iteration level, for the unmodified and LTS solvers

### Flat plate

The test case from the supersonic plate have been taken from Ref. [107], with the intentions of both compare with experimental results, and provide a test case for which the cell refinement comes naturally. The length of the plate within the domain has been set to 0.1 m, with the domain being extended 5 mm upstream of the flat plate. The smallest cells, located at the leading edge of the plate, have a size of  $1 \mu\text{m} \times 1 \mu\text{m}$ , whereas the cell at the top right corner, which is the coarsest cell of the computational domain, has a size of approximately  $2.8 \text{ mm} \times 2.8 \text{ mm}$ . The computational domain for this test case can be seen in Figure 2.21, with the flat plate in red, and consecutive zoom levels to appreciate the refinement in detail.

The fluid for this test case is air, and the initial and boundary conditions have been set so to match the Reynolds ( $Re$ ) and Mach number to those in Ref. [107], as well as the plate to upstream temperature ratio (that is,  $Re = 500$ ,  $M_\infty = 2$ ,  $\frac{T_w}{T_\infty} = 2$ ). The upstream temperature has been set to 300K, and a reference length of 1 cm was used to calculate the Reynolds number. With these values, the initial conditions are the same as the upstream condition, these values being:  $u_\infty = 694.55 \text{ m/s}$ ,  $T_\infty = 300 \text{ K}$ ,  $p_\infty = 114.46 \text{ Pa}$ .

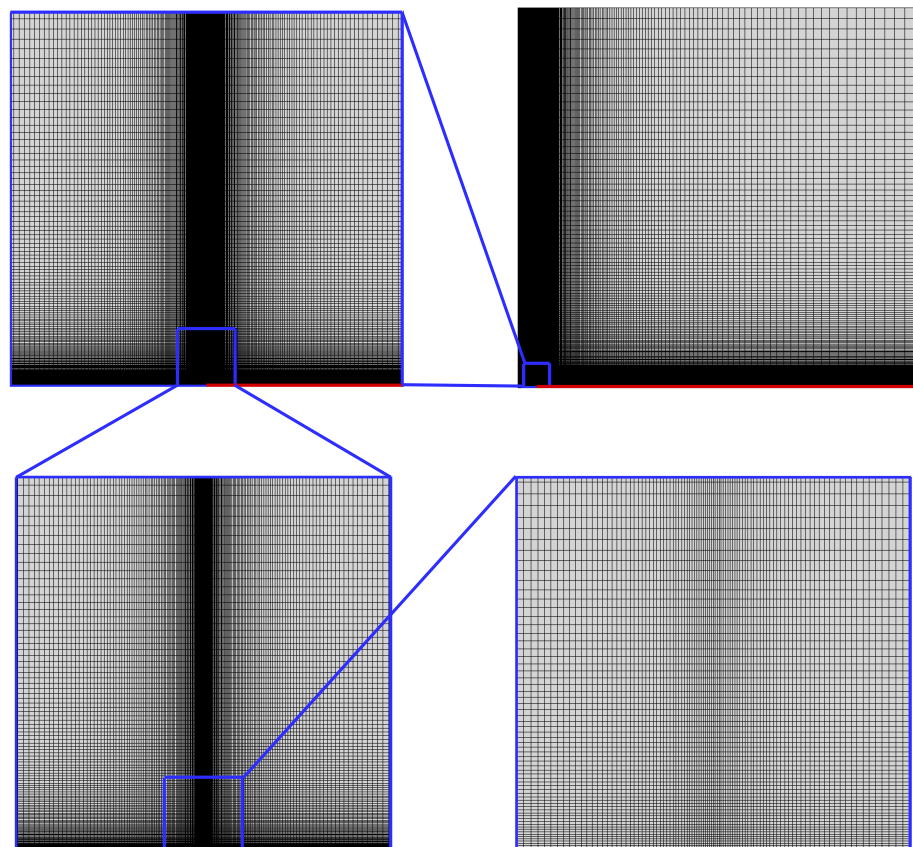


Figure 2.21: Mesh for the flat plate test case

No-slip boundary conditions are assumed at the plate. The maximum Courant number was set to 0.1, and the maximum allowable time-step had been defined as  $10\ \mu\text{s}$ .

The flow properties that will be analysed are those along the vertical line located one reference length (1 cm) behind the leading edge of the flat plate, and the simulation is considered converged when the difference between properties  $5 \times 10^4$  iterations apart is smaller than 0.01% of the upstream values. For the unmodified solver, this condition meant reaching 1.7 million iterations until convergence, whereas for the LTS version, only  $1.5 \times 10^5$  iterations were sufficient to reach a converged state. Table 2.5 shows the time needed to reach different number of iterations for this case. From this table, it can be concluded that the LTS solver achieved convergence 8.96 times faster than its unmodified counterpart. Figures 2.22 to 2.25 show how the solution progressed with the number of iterations. Comparing these figures, it can be seen that for both solvers, pressure (Figure 2.22) is the property that required the most iterations to converge. Figure 2.25 shows as well a comparison with the velocity profile that was obtained in Ref. [107].

Iteration ( $\times 1000$ )	Unmodified	LTS
50	2h 46min	3h 20min
100	5h 25min	6h 31min
150	8h 2min	9h 41min
300	15h 49min	-
600	31h 12min	-
900	46h 23min	-
1200	61h 31min	-
1500	76h 42min	-
1700	86h 49min	-

Table 2.5: Computational time required to reach each iteration level, for the unmodified and LTS solvers

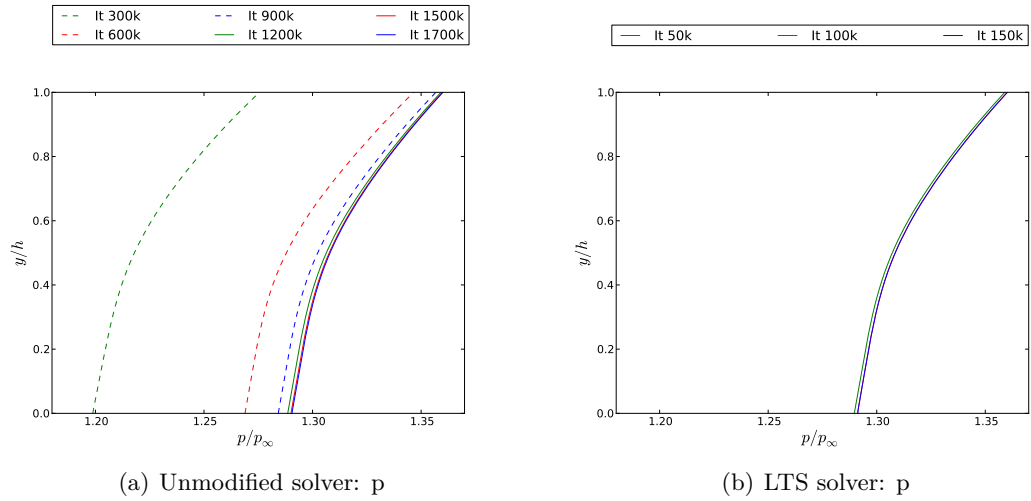


Figure 2.22: Results from the unmodified and the LTS solvers for pressure

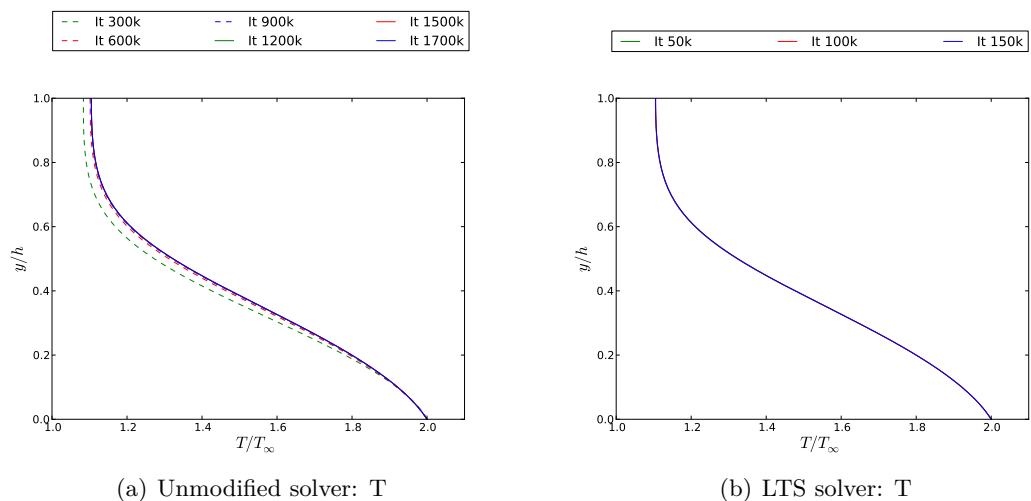
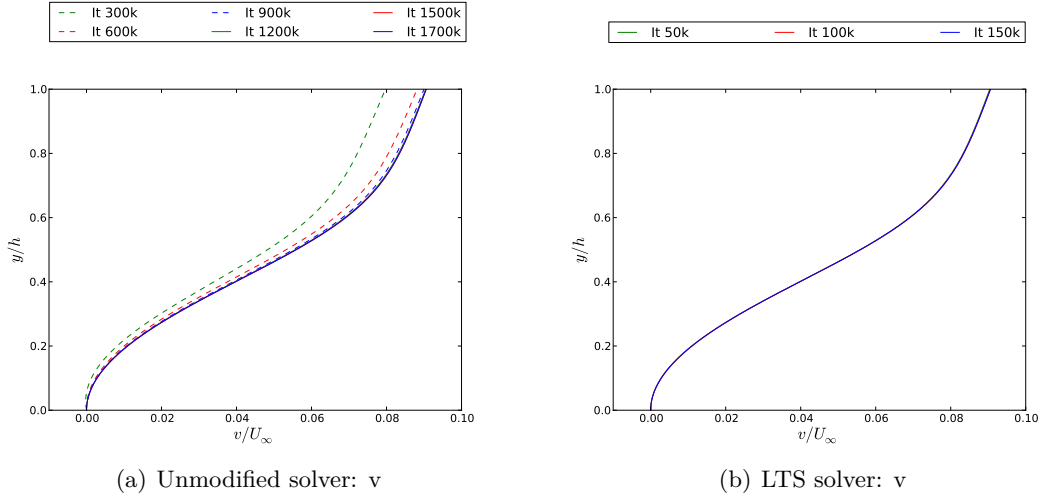
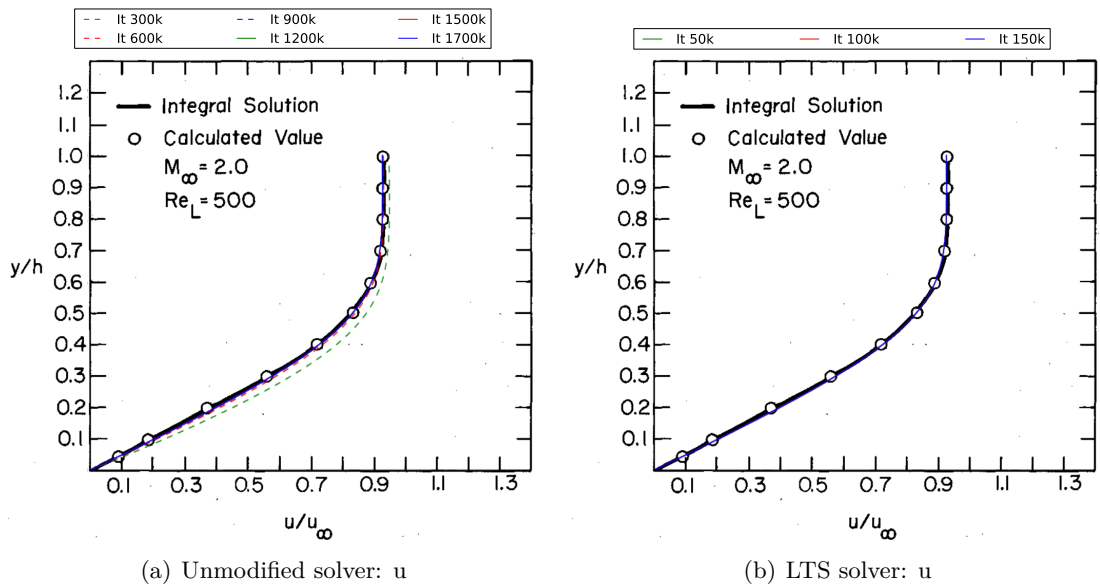


Figure 2.23: Results from the unmodified and the LTS solvers for temperature


 Figure 2.24: Results from the unmodified and the LTS solvers for  $y$ -velocity

 Figure 2.25: Numerical laminar boundary layer profiles ( $x$ -velocity) from Ref. 107 and present work, for the unmodified and LTS solvers

### 2.2.2 Adaptive mesh refinement

The second technique incorporated to *rhoCentralFoam* is AMR, which is used to improve the resolution of an existing mesh in regions of interest, thus capturing the flow properties on these portions of the domain with enhanced accuracy, without excessive increase in computational effort. The advantage of implementing this technique within *rhoCentralFoam* is that it will allow the details near shocks and other discontinuities to be captured without excessive refinement of the mesh throughout the full computational domain. Based on the implementations of this technique in the OpenFOAM solvers *interDyMFoam* and *rhoCentralDyMFoam*, the mesh is modified during the computation, to adapt to the magnitudes of interest, by refining or coarsening cells. The approach uses a tree-structure, so the maximum coarsening that can be achieved using this technique is the equivalent to the cell density of the original mesh. When refining, each hexahedral cell that has been selected is split in two along each coordinate direction, generating eight new child cells from the original parent cell. Figure 2.26 exemplifies a possible refinement/coarsening sequence that could be obtained using this method.

The algorithm followed by the AMR procedure is as follows (represented in Figure 2.27):

- Verification if mesh should be updated: The AMR only modifies the mesh at regular user-defined intervals. The process keeps going if the iteration number reaches the desired interval, and stops and proceeds with the solver iteration if it does not.
- Selection of protected cells: From all the cells, those that can't be refined are selected. In the version of OpenFOAM this code was written in, 2.3.0, protected cells are all non-hexahedral cells and all polyhedral cells that do not belong to a refinement tree.
- Selection of cells to refine: From the remaining cells, those that fulfil the user-defined conditions are selected for refinement/coarsening.
- Updating of the mesh: The selected cells are refined/coarsened.
- Mapping of fields: The macroscopic fields from the previous mesh are then

mapped to the current mesh.

- Solver step: After this refinement/coarsening process has finished, the code proceeds to the solver, using the new mesh.

To verify the implementation of the AMR technique, two test cases have been performed, the first one being the simulation of supersonic flow over a wedge. As a second simulation the Sod shock tube test case [108] was simulated to test the mesh refinement on run-time. Due to AMR producing a 3D refinement of each cell, and the two-dimensionality of these test cases, time comparison between solvers would not be informative, and therefore these test cases are mainly to show its capabilities. Future work could remove this 3D restriction on OpenFOAM's AMR procedure.

### Supersonic Wedge

In this test case, the inviscid flow at Mach 5 over a two-dimensional 30° wedge has been analysed. The initial mesh is represented in Figure 2.28.

For this simulation, the fluid used has been set so to resolve the non-dimensional problem. Thus, the initial and boundary conditions are:

$$\begin{aligned}\vec{v}(t = 0) &= 0 & M_\infty &= 5 \\ T(t = 0) &= 1 & T_\infty &= 1 \\ p(t = 0) &= 1 & p_\infty &= 1\end{aligned}$$

and slip, adiabatic wall boundaries are assumed.

As for the user-defined parameters that control the mesh adaptation, refinement is triggered when  $\|\nabla M\| > 1$ , and coarsening when  $\|\nabla M\| < 1$ . The mesh was updated every million time-steps.

In Figure 2.29 the Mach contours from different refinement levels are presented, with the meshes used for each cases superimposed. It can be observed that a higher level

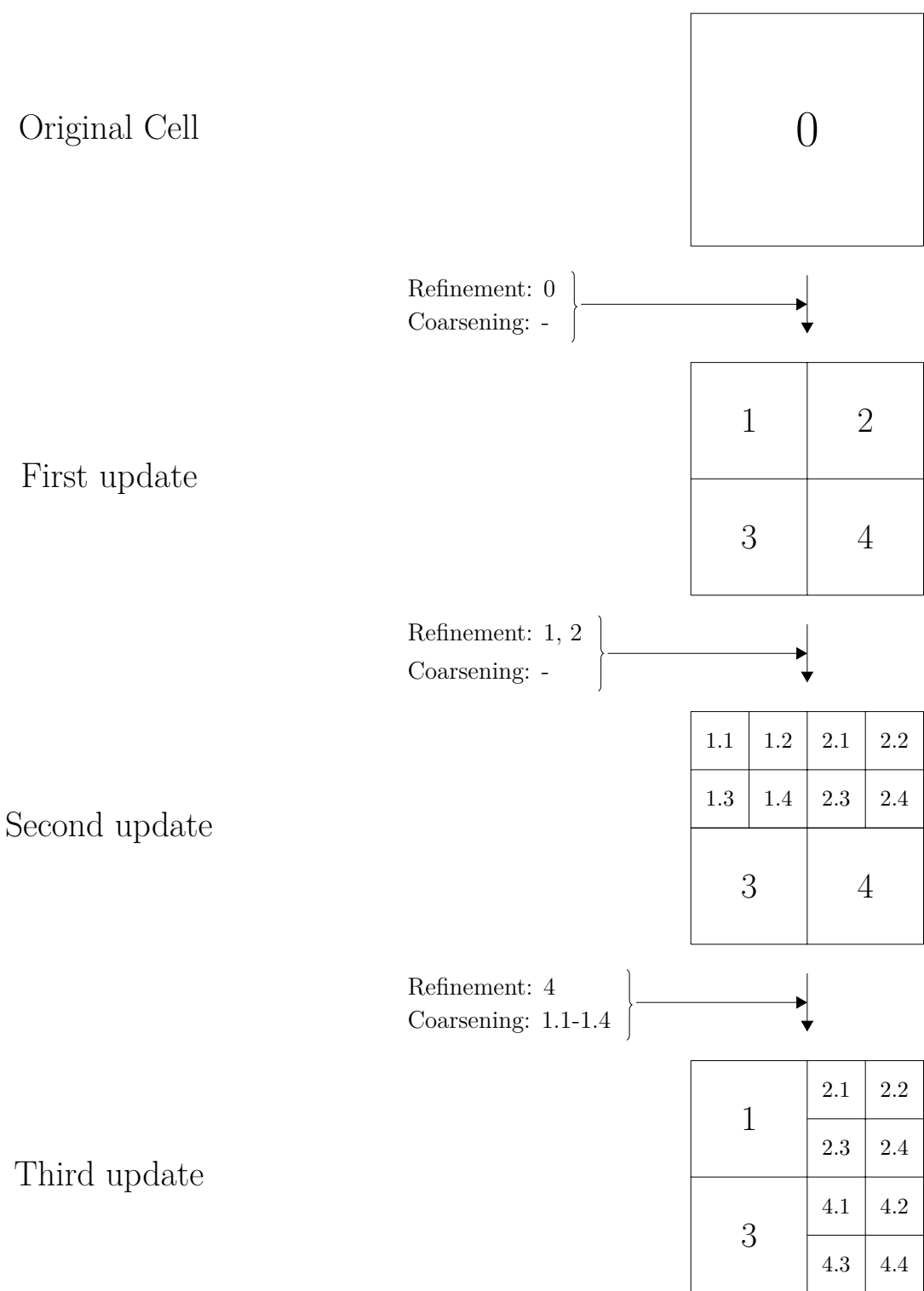


Figure 2.26: Example of a refinement/coarsening sequence

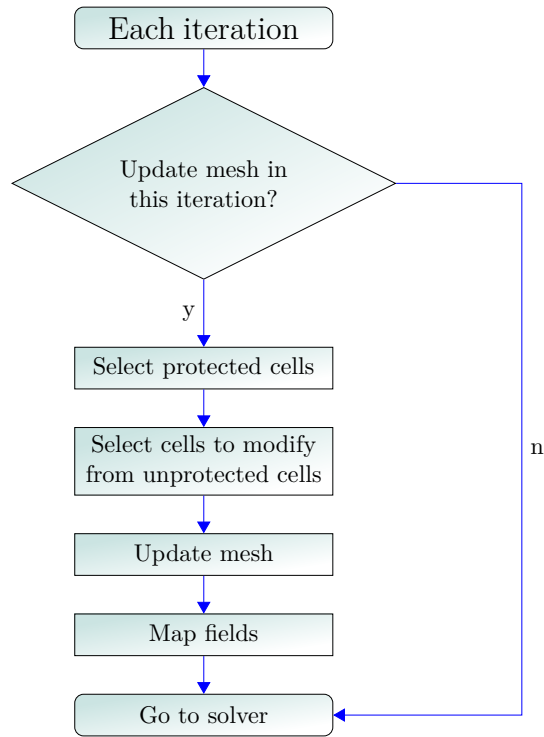


Figure 2.27: Flow chart for the AMR algorithm

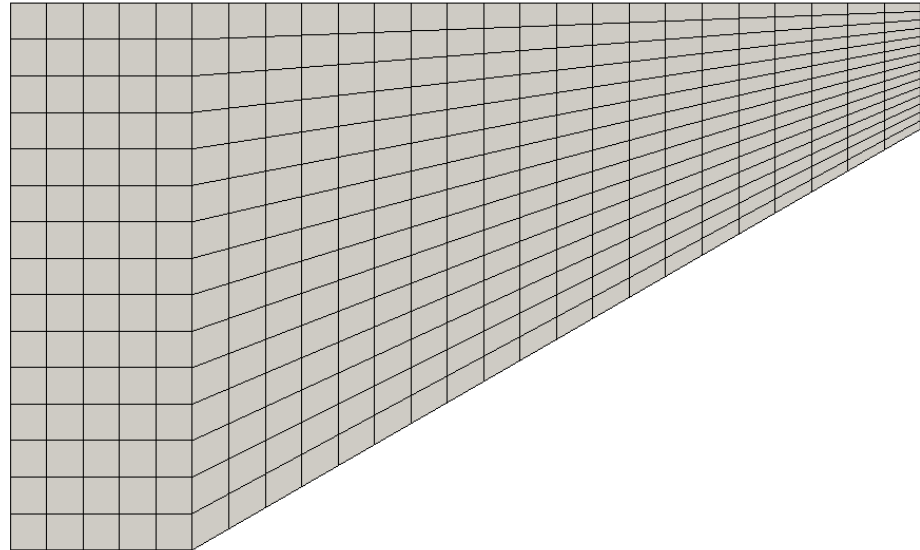


Figure 2.28: Initial mesh for the supersonic wedge test case

of refinement returns a better defined shock wave. Figure 2.30 shows that the shock wave position is captured with higher accuracy when increasing refinement levels, as the analytical position of the shock is superimposed with the previously shown contour plots. This analytical solution is given by:

$$\tan \delta = \frac{2}{\tan \theta} \frac{M_\infty^2 \sin^2 \theta - 1}{M_\infty^2 (\gamma + \cos 2\theta) + 2} \quad (2.8)$$

where  $\delta$  is the angle between the geometry and the direction of the freestream,  $\theta$  is the angle between the shock wave and the direction of the freestream, and  $\gamma$  is the ratio of specific heats.

In Figure 2.31, results from the upper boundary for pressure, temperature and Mach number are shown, reinforcing the critical role of cell refinement in the proximities of the shock.

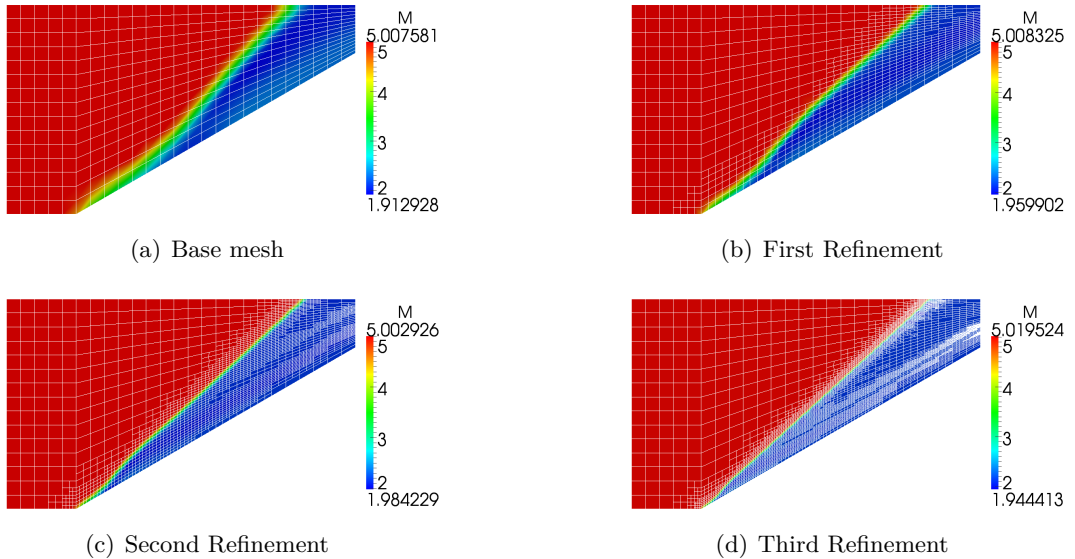


Figure 2.29: Mach number contour plots for different refinement levels

### Sod shock tube

Sod shock tube is a common case for compressible solvers. The initial macroscopic

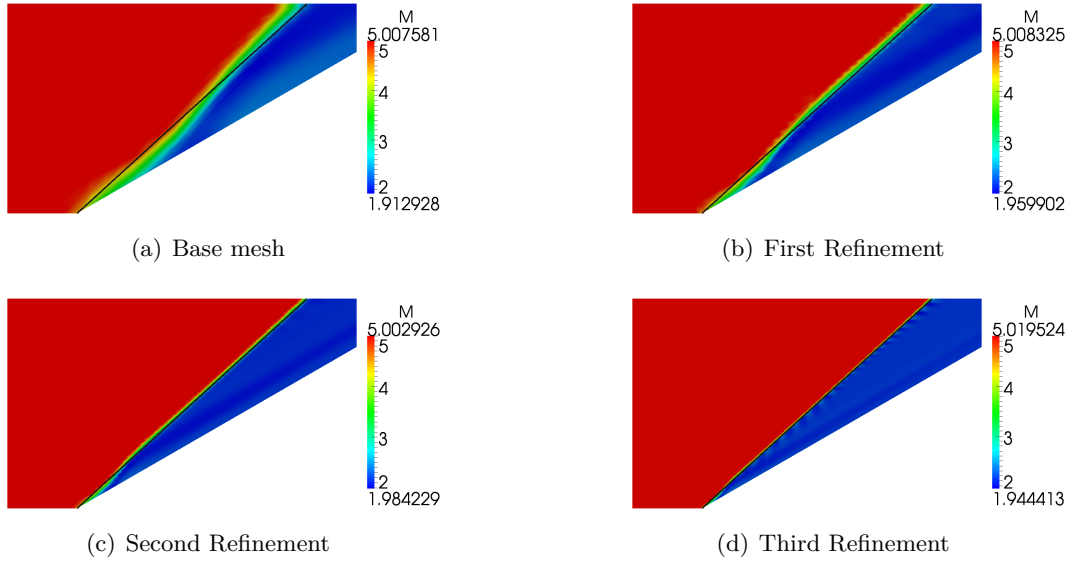


Figure 2.30: Comparison between Mach contour plots and analytical position (line in black) of the shock wave for different refinement levels

properties on the left side of the shock tube are different from the ones on the right side, leading to compression and expansion waves. The initial mesh for this study is presented in Figure 2.32.

In a similar fashion to the supersonic wedge, the fluid used for the simulation has been set up so to resolve the non-dimensional problem. This leads to the following initial conditions:

$$\begin{aligned}
 u(x/L < 0, t = 0) &= u_l = 0 & u(x/L > 0, t = 0) &= u_r = 0 \\
 p(x/L < 0, t = 0) &= p_l = 1 & p(x/L > 0, t = 0) &= p_r = 0.1 \\
 \rho(x/L < 0, t = 0) &= \rho_l = 1 & \rho(x/L > 0, t = 0) &= \rho_r = 0.125
 \end{aligned}$$

where the center of the shock tube is considered the origin of coordinates,  $\rho$  represents the density of the fluid, and the subscripts  $l$  and  $r$  refer to the left and right half of the shock tube, respectively.

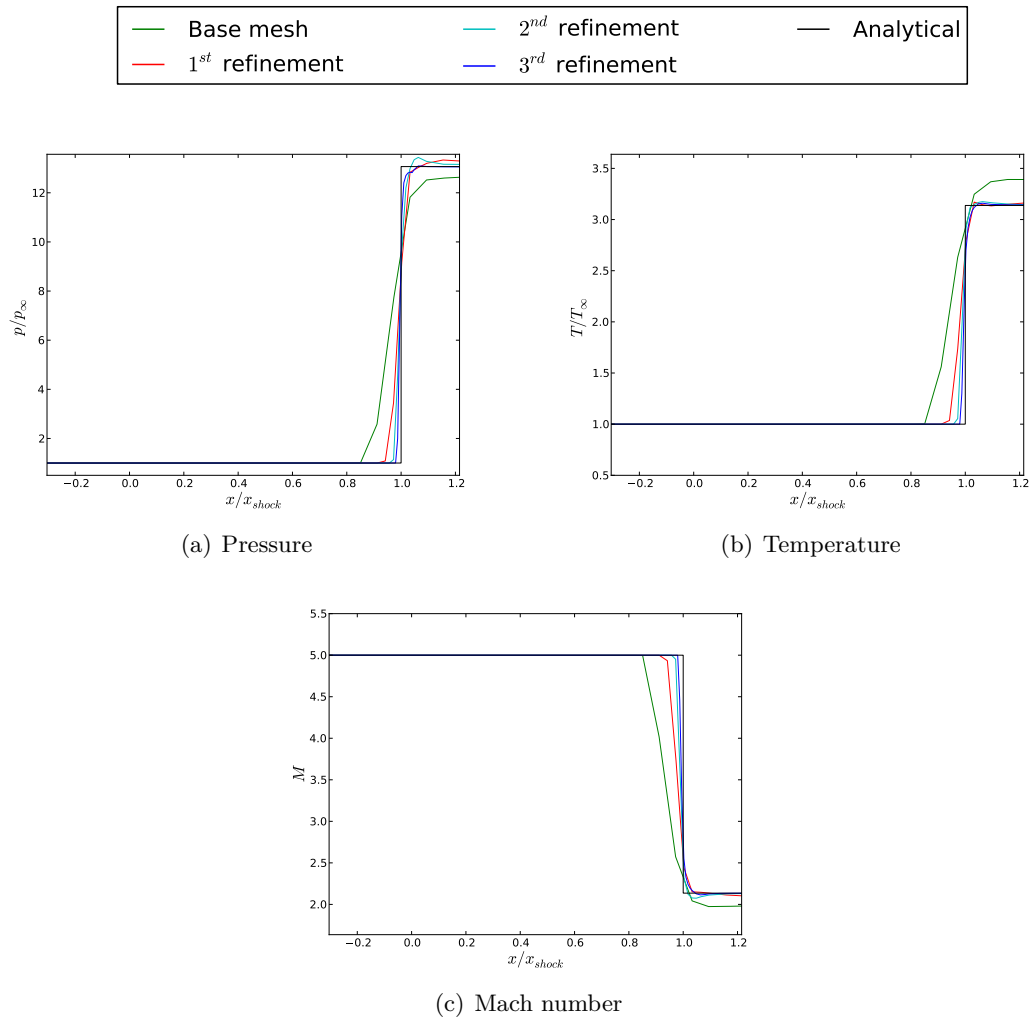


Figure 2.31: Solution comparison for the initial and refined meshes

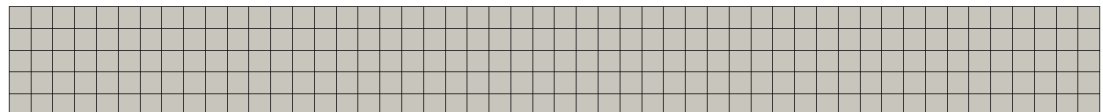


Figure 2.32: Initial mesh for the shock tube test case

For this test case, two different refinement/coarsening criteria have been compared. For the first criterion, the mesh has been refined when  $\left\| \frac{\nabla p}{p} \right\| > 1$  and coarsened when  $\left\| \frac{\nabla p}{p} \right\| < 0.5$ . For the second one, mesh refinement was instigated when  $\left\| \frac{\nabla \rho}{\rho} \right\| > 1$ , and coarsening when  $\left\| \frac{\nabla \rho}{\rho} \right\| < 0.5$ . As the compression and expansion waves are non-stationary, the mesh has been updated every five time-steps.

In Figure 2.33, density contour plots for both refinement/coarsening criteria can be seen, as well as the meshes themselves, for different times. Both the shock and rarefaction wave can be correctly captured by both criteria, therefore resolving them with higher accuracy than with the original mesh, as the cell resolution increases near these discontinuities. However, the  $\frac{\nabla p}{p}$  criterion is unable to capture the density discontinuity, not modifying the mesh and therefore resolving this contact discontinuity with poor accuracy, as compared with the  $\frac{\nabla \rho}{\rho}$  criteria, which is in fact able to recognise the need of a finer mesh. The effect of the mesh refinement or lack thereof can be seen in Figure 2.34, where the analytical solution for this shock tube is compared with the results obtained. As mentioned before, the lack of refinement on the contact discontinuity for the  $\frac{\nabla p}{p}$  criterion is due to the fact that this type of discontinuity is only present for density, whereas it is not present for pressure, making it invisible to the pressure criterion. This phenomenon shows the importance of selecting a refinement criterion that would suit the problem at hand.

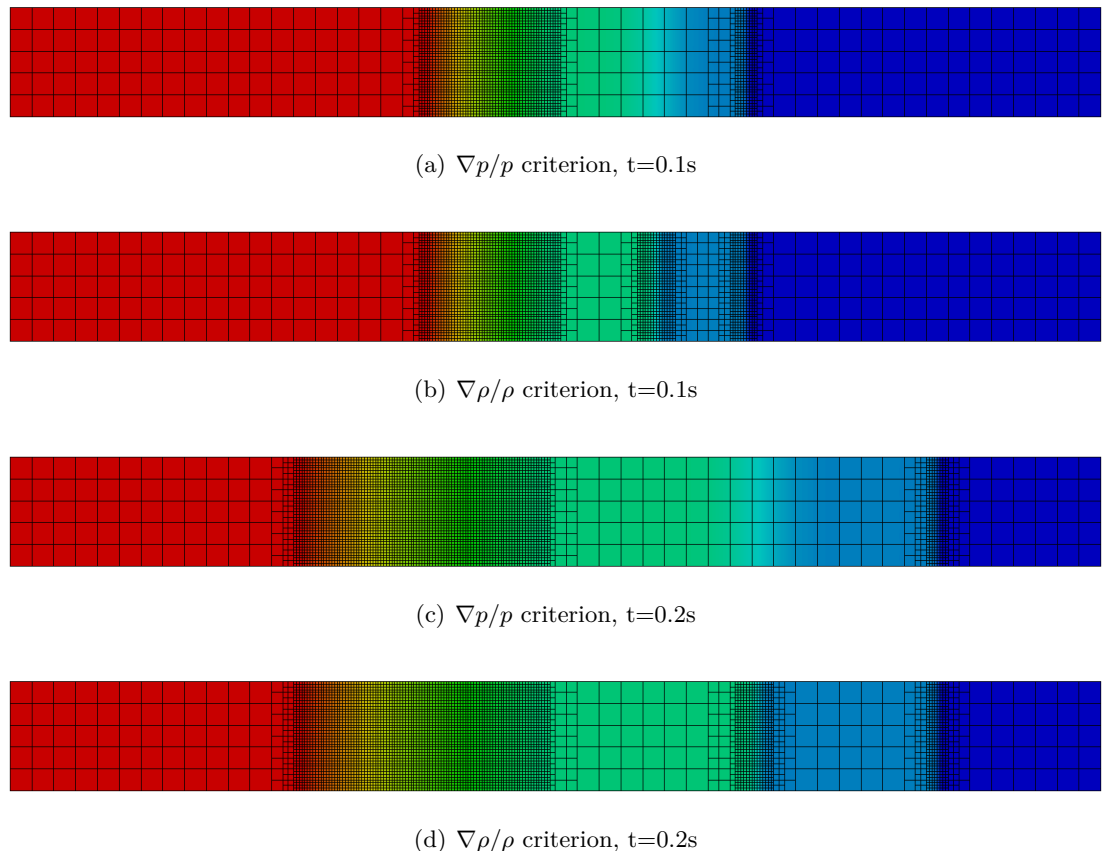


Figure 2.33: Density contour plots for the different refinement criteria, for  $t=0.1$  s and  $t=0.2$  s.

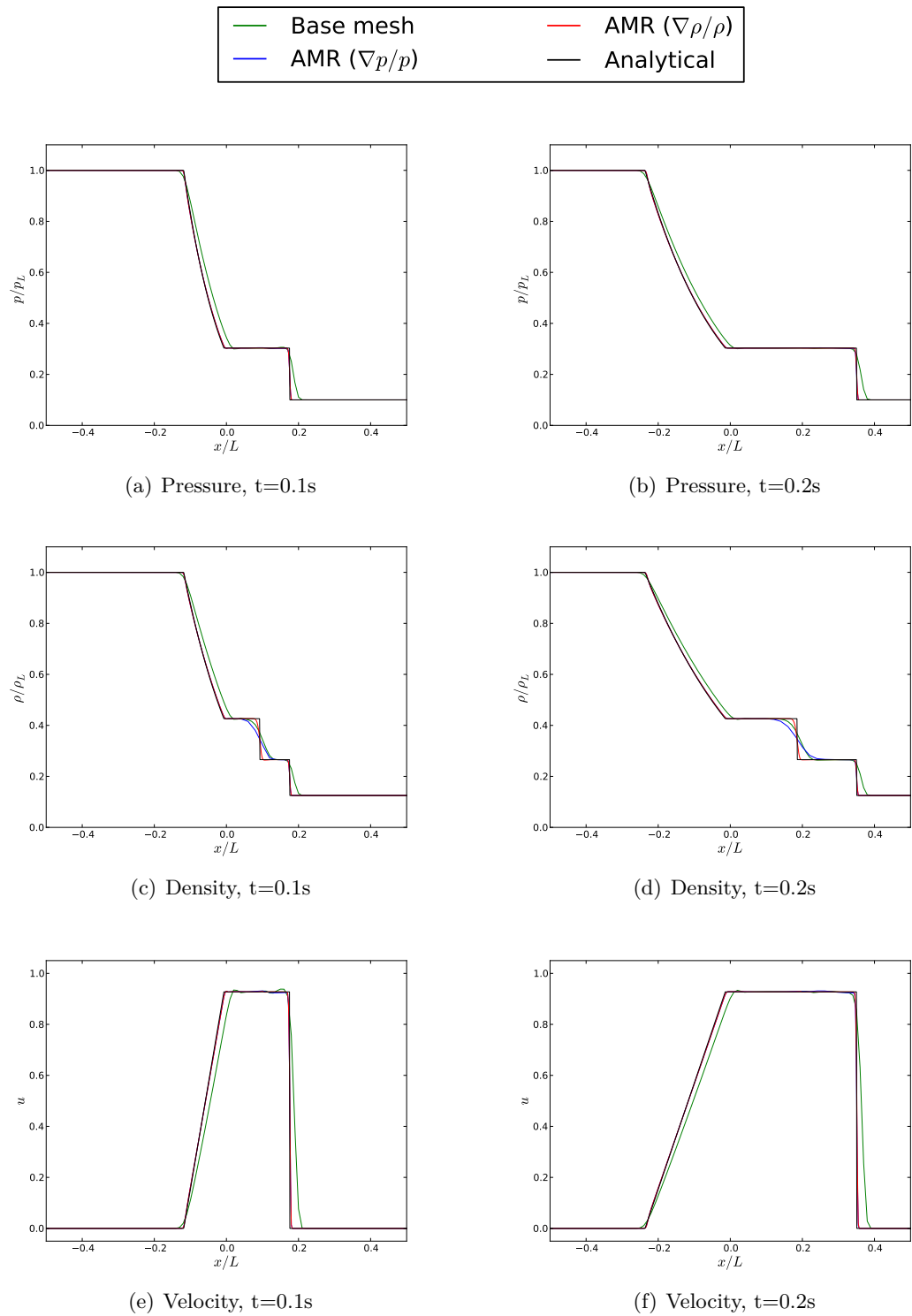


Figure 2.34: Solution comparison for initial and refined meshes, for  $t=0.1$  s and  $t=0.2$  s.

# Chapter 3

## OpenFOAM solvers for the hybrid code

It has been established that several aspects need to be considered to properly represent the particular physics of hypersonic flows. The models required by a CFD solver to be able to capture these features, and their specific implementation in the continuum solver *hy2Foam* apt for these flow conditions are detailed in section 3.1, with the main differences with *rhoCentralFoam* separated in two main formulations, two-temperature modelling and multispecies, and further explained in subsections 3.1.1 and 3.1.2. Section 3.2 describes the DSMC method in more detail, including the number density range in which this method can be applied, as well as the fundamental principles in which the method is based upon. The treatment of boundary conditions, collisions, chemical reactions, and distribution functions within the solver *dsmcFoam* are then explored in subsections 3.2.1, 3.2.2, 3.2.3, and 3.2.4 respectively.

### 3.1 CFD and *hy2Foam*

The first aspect of consideration for the CFD portion of the hybrid is the conditions the continuum solver must adhere to, to be able to capture the correct and complex physics of reentry. First of all, the solver must be able to capture the essential physics

of high speed flows, the shock waves, accurately. Moreover, the code must be capable of modelling gas properties accurately for a wide range of temperatures. In addition, it should be feasible to simulate not only multiple species, but also the possible chemical reactions that could be present due to the aforementioned temperature range. Again as a consequence of the temperatures that can be achieved during reentry, it is of special importance to be able to model the non-equilibrium that may appear as the vibrational and electronic modes of the gas molecules become excited.

*rhoCentralFoam* has shown to adequately meet the first two requirements. However, it lacks the capabilities to simulate multiple species, chemical reactions, or thermal non-equilibrium. To solve this problem, *hy2Foam* was developed at Strathclyde University. Based on the chemical models present in *reactingFoam*, and the Godunov-type solvers of *rhoCentralFoam*, this solver provides the aforementioned capabilities that are fundamental for hypersonic applications. The most important characteristics for the purpose of this thesis will now be summarised, with an in-depth description provided on Ref. [8].

### 3.1.1 Two-temperature model

First of all, the solver includes translational, rotational, and vibrational energy modes, represented by a translational-rotational (from now on, transrotational) and a vibrational temperature. The idea behind this two-temperature model is that the time required to achieve translational-rotational equilibrium is usually small when compared to the time for translational-vibrational equilibrium, therefore it can be assumed that the translational and rotational temperatures are always in equilibrium, and thus a transrotational temperature is sufficient to represent both. This multi-temperature approach leads to the definition of certain gas properties. Translational, rotational and vibrational energies can be defined as:

$$e_{tra} = \frac{3}{2}R_g T_{tra} \quad (3.1)$$

$$e_{rot} = \frac{\zeta_{rot}}{2} R_g T_{rot} \quad (3.2)$$

$$e_{vib} = R_g \frac{\theta_{vib}}{\exp\left(\frac{\theta_{vib}}{T_{vib}}\right) - 1} \quad (3.3)$$

where  $e$  represents the energy per unit mass,  $R_g$  is the specific gas constant,  $\zeta$  the degrees of freedom of a particular energy mode,  $\theta_{vib}$  is the characteristic vibrational temperature, and the subscript  $vib$  indicates vibrational properties.

From these energies, the heat capacity at constant volume,  $C_v$ , can be defined as  $C_{v,j} = \frac{\partial e_j}{\partial T_j}$  where  $j$  represents any of the energy modes. This results in:

$$C_{v,tra} = \frac{3}{2} R_g \quad (3.4)$$

$$C_{v,rot} = \frac{\zeta_{rot}}{2} R_g \quad (3.5)$$

$$C_{v,vib} = R_g \frac{(\theta_{vib}/T_{vib})^2 \exp\left(\frac{\theta_{vib}}{T_{vib}}\right)}{\left(\exp\left(\frac{\theta_{vib}}{T_{vib}}\right) - 1\right)^2} \quad (3.6)$$

and finally, restricting the previous expressions to a two temperature formulation:

$$T_{tra} = T_{rot} = T_{t-r} \quad (3.7)$$

$$e_{t-r} = e_{tra} + e_{rot} = \frac{3 + \zeta_{rot}}{2} R_g T_{t-r} \quad (3.8)$$

$$C_{v,t-r} = C_{v,tra} + C_{v,rot} = \frac{3 + \zeta_{rot}}{2} R_g \quad (3.9)$$

where the subscript  $t - r$  refers to transrotational quantities.

In addition to the expressions for the heat capacities and energies, the transport properties of the gas need to be defined. To be consistent with DSMC parameters, the variable hard sphere (VHS) model [109, 110] has been used, leading to the following definitions:

$$\mu = \mu_{ref} \left( \frac{T_{t-r}}{T_{ref}} \right)^\omega \quad (3.10)$$

$$\kappa_{t-r} = \frac{5}{2} C_{v,tra} \mu + C_{v,rot} \mu = \frac{15 + 2\zeta_{rot}}{4} R_g \mu \quad (3.11)$$

$$\kappa_{vib} = C_{v,vib} \mu \quad (3.12)$$

where  $\kappa$  is the thermal conductivity,  $\omega$  is the temperature exponent of the coefficient of viscosity, and the subscript *ref* indicates reference values.

Furthermore, the two-temperature model requires an additional equation to deal with the conservation of vibrational energy. This results in the following set of equations:

$$\frac{\partial \rho}{\partial t} + \nabla \cdot (\rho \vec{v}) = 0 \quad (3.13)$$

$$\frac{\partial (\rho \vec{v})}{\partial t} + \nabla \cdot (\rho \vec{v} \otimes \vec{v}) = -\nabla p + \nabla \cdot \tau \quad (3.14)$$

$$\frac{\partial (\rho e_{vib})}{\partial t} + \nabla \cdot (\rho e_{vib} \vec{v}) = Q_{v-t} - \nabla \cdot \vec{q}_{vib} \quad (3.15)$$

$$\frac{\partial (\rho e_{tot})}{\partial t} + \nabla \cdot (\rho e_{tot} \vec{v}) = -\nabla \cdot (p \vec{v}) + \nabla \cdot (\tau \cdot \vec{v}) - \nabla \cdot \vec{q}_{t-r} - \nabla \cdot \vec{q}_{vib} \quad (3.16)$$

where Equations 3.13, 3.14, 3.15, and 3.16 are, respectively, the continuity, momentum, vibrational energy, and internal energy equations for a single species fluid.  $\rho$  is the density,  $e_{tot} = e_{t-r} + e_v + \frac{1}{2} (\vec{v} \cdot \vec{v})$  is the internal energy per unit mass,  $\tau$  is the viscous stress tensor,  $\vec{q}$  is the heat flux vector, and  $Q_{v-t}$  represents the exchange between the transrotational and vibrational energy modes. In *hy2Foam* this energy exchange term is dictated by the Landau-Teller equation [111], and uses a relaxation time evaluated using the Millikan and White correlation [112] and Park's correction factor [113]. The viscous stress tensor and the heat flux vector can be written as:

$$\tau = \mu \left( \nabla \vec{v} + (\nabla \vec{v})^T \right) + (\lambda + \mu_b) (\nabla \cdot v) \mathbf{I} \quad (3.17)$$

$$\vec{q} = -\kappa \nabla T \quad (3.18)$$

where  $\lambda$  is the second coefficient of viscosity,  $\mu_b$  is the bulk viscosity, and the superscript *T* represents the transpose of a tensor. In this work, Stokes' hypothesis will be

assumed, resulting in  $\lambda = -\frac{2}{3}\mu; \mu_b = 0$ .

### 3.1.2 Multispecies

The second most important addition within *hy2Foam* is the possibility of using multiple species during the simulations. To be able to include this multispecies modelling, some new properties need to be defined, as well as the mixing rules used for the transport properties from the previous subsection. It is important to notice that, whereas *hy2Foam* allows for the utilisation of electronic energy and ions, none of these types of species have been taken into consideration for the present work.

### Diffusive fluxes

The first magnitude that need to be defined is the mass diffusion. This is done by calculating the diffusive fluxes of each species,  $\vec{\mathcal{J}}$ , using the following expression:

$$\vec{\mathcal{J}}_s = \vec{\mathcal{I}}_s - Y_s \sum_r \vec{\mathcal{I}}_r \quad (3.19)$$

with

$$\vec{\mathcal{I}}_s = -\rho \mathcal{D}_s \frac{m_s}{m} \vec{G}_s \quad (3.20)$$

and

$$\vec{G}_s = \nabla X_s + (X_s - Y_s) \frac{\nabla p}{p} + K_{T,s} \frac{\nabla T}{T} - \frac{1}{p} \left( \rho_s \vec{F}_s - Y_s \sum_r \rho_r \vec{F}_r \right) \quad (3.21)$$

where  $Y$  is the mass fraction,  $X$  is the molar fraction,  $m_s$  is the mass of one particle of specie s,  $m = \sum_r \rho_r/n$  is the average mass of one particle of the mixture,  $n$  is the number density of the mixture,  $\mathcal{D}_s$  is the effective diffusion coefficient of species  $s$ ,  $K_T$  is related to the species thermal diffusion coefficients,  $\vec{F}$  is the body force per unit mass acting on the flow, and the subscripts  $s$  or  $r$  refers to the species. In the present work, the thermal diffusion coefficients, as well as the body forces per unit mass will

be ignored.

In addition to the diffusion models presented in Ref. [8], the Self Consistent Effective Binary Diffusion (SCEBD) approximation [114] was implemented. For this model, the effective diffusion coefficients are calculated as:

$$\mathcal{D}_s = \left(1 - \frac{w_s}{w}\right) \left(\sum_{r \neq s} \frac{X_r}{\mathcal{D}_{s,r}}\right)^{-1} \quad (3.22)$$

with

$$w_s = \frac{\rho_s}{\sqrt{\mathcal{M}_s}} \quad (3.23)$$

and

$$w = \sum_r \frac{\rho_r}{\sqrt{\mathcal{M}_r}} \quad (3.24)$$

where  $\mathcal{M}$  is the molecular weight, and  $\mathcal{D}_{s,r}$  is the binary diffusion coefficient for species s and r, which can be modelled using collision integrals as follows:

$$\mathcal{D}_{s,r} = \frac{3k_B T_{t-r}}{16nm_{s,r}^* \Omega_{s,r}^{(1,1)}} \quad (3.25)$$

where  $k_B$  is Boltzmann constant,  $m_{s,r}^* = \frac{m_r m_s}{m_r + m_s}$  is the reduced mass of species s and r, and  $\Omega_{s,r}^{(1,1)}$  is a collision integral [115]. For the VHS model, this collision integral can be expressed as:

$$\Omega_{s,r}^{(1,1)}|_{VHS} = \frac{\pi}{2} d_{s,r-ref}^2 \left(\frac{k_B T_{t-r}}{2\pi m_{s,r}^*}\right)^{1/2} \left(\frac{T_{ref}}{T_{t-r}}\right)^{\omega_{s,r}-1/2} \frac{\Gamma(7/2 - \omega_{s,r})}{\Gamma(5/2 - \omega_{s,r})} \quad (3.26)$$

where  $d_{s,ref}$  is the reference diameter of a particle of species s and  $\Gamma$  is the Gamma function. The values of  $d_{s,r-ref}$  and  $\omega_{s,r}$  are calculated as follows, to be consistent with the DSMC solver.

$$d_{s,r-ref} = \frac{1}{2} (d_{s,ref} + d_{r,ref}) \quad (3.27)$$

$$\omega_{s,r} = \frac{1}{2} (\omega_s + \omega_r) \quad (3.28)$$

### Mixing rule

Having defined the diffusive fluxes, what is left is to select a mixing rule for the transport properties. *hy2Foam* includes different mixing rules, but for this work only Wilke's [116] mixing rule will be considered. Using this, both the viscosity and transrotational thermal conductivity are defined as

$$\mu = \sum_s \frac{\mu_s X_s}{\phi_s} \quad (3.29)$$

$$\kappa_{t-r} = \sum_s \frac{\kappa_{s,t-r} X_s}{\phi_s} \quad (3.30)$$

with

$$\phi_s = X_s + \sum_{r \neq s} X_r \left[ 1 + \sqrt{\frac{\mu_s}{\mu_r}} \left( \frac{\mathcal{M}_r}{\mathcal{M}_s} \right)^{1/4} \right]^2 \left[ \sqrt{8 \left( 1 + \frac{\mathcal{M}_s}{\mathcal{M}_r} \right)} \right]^{-1} \quad (3.31)$$

### Equations

Using the diffusive fluxes and the mixing rule described above, the continuum equations become

$$\frac{\partial \rho}{\partial t} + \nabla \cdot (\rho \vec{v}) = 0 \quad (3.32)$$

$$\frac{\partial \rho_s}{\partial t} + \nabla \cdot (\rho_s \vec{v}) = \dot{\omega}_s - \nabla \cdot \vec{\mathcal{J}}_s \quad (3.33)$$

$$\frac{\partial (\rho \vec{v})}{\partial t} + \nabla \cdot (\rho \vec{v} \otimes \vec{v}) = -\nabla p + \nabla \cdot \tau \quad (3.34)$$

$$\frac{\partial (\rho_s e_{s,vib})}{\partial t} + \nabla \cdot (\rho_s e_{s,vib} \vec{v}) = \dot{\omega}_{s,vib} - \nabla \cdot \vec{q}_{s,vib} - \nabla \cdot (e_{s,vib} \vec{\mathcal{J}}_s) \quad (3.35)$$

$$\frac{\partial (\rho e_{tot})}{\partial t} + \nabla \cdot (\rho e_{tot} \vec{v}) = -\nabla \cdot (p \vec{v}) + \nabla \cdot (\tau \cdot \vec{v}) - \nabla \cdot \vec{q}_{t-r} - \sum_s \nabla \cdot \vec{q}_{s,vib} - \sum_s \nabla \cdot (h_{tot,s} \vec{\mathcal{J}}_s) \quad (3.36)$$

where Equations 3.32, 3.33, 3.34, 3.35, and 3.36 are, respectively, the continuity, species conservation, momentum, vibrational energy and internal energy equations for multi-species fluids.  $\dot{\omega}_s$  is the net source of species  $s$  due to chemical reactions,  $\dot{\omega}_{s,vib}$  is the net vibrational energy production,  $h_{tot}$  is the total enthalpy per unit mass, Equation 3.33 is solved for each species whereas Equation 3.35 is solved for each of the species that

are molecules, and the magnitudes with an  $s$  subscript refer to magnitudes of species  $s$ , whereas magnitudes lacking this subscript refer to the properties of the mixture. The total enthalpy is defined as

$$h_{tot,s} = e_{s,t-r} + e_{s,vib} + \frac{1}{2} (\vec{v} \cdot \vec{v}) + R_g T_{s,t-r} \quad (3.37)$$

$\dot{\omega}_s$  is calculated using the reactions sources of all the reactions species  $s$  takes part, as specified in Ref. [117], and  $\dot{\omega}_{s,vib} = Q_{s,v-t} + Q_{s,v-v} + Q_{s,v-c}$ , where  $Q_{s,v-v}$  is the vibrational-vibrational energy transfer between different species, modelled according to Ref. [118, 119], and  $Q_{s,v-c}$  is the energy added to or removed from the system due to chemical reactions, modelled using the Park TTv model [120, 121].

### Wall boundary conditions

The classic treatment of boundary conditions for continuum solvers is the no-slip condition, where the velocity and temperature of the fluid match those at the wall.

To be able to take into account the rarefaction of the flow these boundary conditions need to be modified in consequence, as this will imply that the number of gas-surface interaction events becomes insufficient to guarantee this equilibrium between wall and fluid properties. As such, slip boundary conditions are employed.

Maxwellian velocity slip [122] and Smoluchowski temperature jump [123] boundary conditions are the most common when treating with a single-species gas. For a gas mixture, these boundary conditions can also be derived [124]. The velocity slip condition results in

$$u = u_{wall} + \frac{2 - \sigma}{\sigma} \lambda \frac{\partial u}{\partial n} + \frac{3}{4} \frac{\mu}{\rho T_{t-r}} \frac{\partial T_{t-r}}{\partial x} \quad (3.38)$$

where  $\sigma$  is the tangential-momentum-accommodation coefficient,  $\lambda$  is the mean free path of the gas mixture, and  $n$  and  $x$  are the normal and tangential components of a coordinate system centred at the point of the wall taken into consideration, and with the normal pointing into the fluid.

After some modifications to include the vibrational energy mode (see Appendix A) the energy boundary conditions become

$$e_{t-r} = e_{t-r,wall} + \frac{2-\alpha}{\alpha} \frac{2\gamma}{\gamma+1} \frac{\lambda}{Pr} \frac{\partial e_{t-r}}{\partial n} \quad (3.39)$$

$$e_{s,vib} = e_{s,vib,wall} + \frac{2-\alpha_s}{\alpha_s} \frac{2}{\gamma_s+1} \lambda \frac{\partial e_{s,vib}}{\partial n} \quad (3.40)$$

where  $\alpha$  is the thermal-accommodation coefficient,  $\gamma = \frac{C_{p,t-r}}{C_{v,t-r}}$  is the ratio of specific heats, and  $Pr = \frac{\mu C_{p,t-r}}{\kappa_{t-r}}$  is the Prandtl number. It is important to note that, because *hy2Foam* solves the Navier-Stokes equations for energy, and not temperature, the boundary conditions needed should be entered in terms of the energy. Whereas this difference is not important for single-temperature models due to the linear relation between the energy and temperature, the same cannot be said when the vibrational temperature is taken into account.

## 3.2 DSMC and *dsmcFoam*

DSMC is a stochastic, particle-based method used to compute and analyse rarefied gas flows. It is a fairly new numerical model, having been proposed in 1963 [125]. However, it has grown into one of the preferred methods for the simulation of nonequilibrium gas flows that require the molecular nature of the gas to be taken into consideration [126]. In this aspect, the particle-based formulation of this method inherently captures the physics of hypersonic flows, and thus no specific new formulations needed to be added to *dsmcFoam* to properly represent the characteristic of this regime. In spite of the physics to be captured properly, the treatment of different distribution functions to initialise the gas properties has been included in this work, to be able to start a DSMC simulation from a non-equilibrium state.

First of all, it is important to identify the range of applicability of the DSMC method. This can be determined by the ratio  $\delta/d$ , where  $\delta = n^{-1/3}$  is the mean molec-

ular spacing and  $d$  is the effective molecular diameter of the gas. When  $\delta/d \gg 1$ , the molecules occupy only a very small fraction of the space, and thus most of these molecules will move outside the range of influence of the others. Furthermore, it is extremely likely that when they do collide it would only be between pairs of molecules. In addition, these collisions occur over time scales much shorter than the mean collision time of the flow, which is the mean time between collisions by any specific molecule, and thus can be considered instantaneous. When this  $\delta/d \gg 1$  condition is fulfilled, the flow regime is called dilute gas, and it is where the DSMC method can be applied [9]. For air at standard conditions, the dilute gas assumptions can be considered valid for  $\delta/d > 7$  [126].

DSMC is based on three main characteristics of dilute gases. First, that the movement of molecules on time scales comparable to the mean collision time can be considered as free flight without interaction. Secondly, that the impact parameters of colliding molecules do not present any inherent bias, and do not need to be deterministically simulated. Finally, that despite there being a massive number of molecules per cubic mean free path, the simulation of only a small fraction of them is required for an accurate representation of the flow [126]. Based on these properties, a simulation is performed using computational particles, also called simulators, each of which represents a large number of real atoms/molecules. Good DSMC practice dictates that a cell should contain a minimum of 20 computational particles, and that the time-step of the simulation should be smaller than the minimum between the mean collision time and the mean residence time, defined as the mean time it takes a particle to traverse a cell [8]. DSMC has been proven to return the exact solution to the Boltzmann equation when the number of particles tends to infinity, and the time-step and cell size tend to zero [127].

The DSMC algorithm starts by filling the domain with simulators, whose properties are generated at random according to a suitable distribution, generally an equilibrium distribution. During each time-step afterwards, the simulators are first moved ballis-

tically at their velocities, including the generation of new particles at boundaries and any interaction with these boundaries that needs to be taken into consideration (see subsection 3.2.1). After the movement stage collisions between particles are performed (see subsection 3.2.2). Finally, the microscopic state of the particles are used to recover the macroscopic flow variables, which are averaged over a certain number of iterations to reduce the scattering that is present in these simulations.

### 3.2.1 Boundary Conditions

For the simulations included in this work, four types of boundaries are considered besides symmetry and cyclic boundaries. First of all, the inlet patch, where new simulators are inserted from at each time-step, and all simulators that cross this boundary are deleted. The second type is an outflow boundary, which functions as a vacuum, deleting all the simulators that cross it and is valid for Mach number greater than 2 [9]. The remaining boundary types are used on walls, and are used to model both specular and fully diffuse reflections respectively. The specular wall patch works in the same manner as a symmetry boundary, with the simulators being reflected without change in energies and with the component of the velocity normal to the wall being the opposite of the normal component of the velocity prior to the simulator-surface interaction. On the fully diffuse wall patch the energies and velocity of the simulators are replaced by values randomly sampled from an equilibrium distribution with the same temperature as the wall and moving at its same speed.

### 3.2.2 Collisions

There are different methods to handle the collisions between simulators, *dsmcFoam* uses the No Time Counter (NTC) model [9,37]. In this model, the number of collisions to be tested per cell is defined before starting to compute the collisions. Once this number is determined, pairs of particles are randomly selected, and then tested using an acceptance-rejection procedure, until the previously calculated number of collision

attempts is fulfilled.

The collision process itself requires the modelisation of the collision cross section of the molecules. Among the possible models, in this work the variable hard sphere (VHS) model will be used, to be consistent with the implementation on *hy2Foam*. In addition, the collisions can be elastic, that is with no energy exchange, or inelastic, where energy is exchanged between translational and internal modes. The internal energy is modelled in *dsmcFoam* using the rigid rotator and the harmonic oscillator models [9] for rotational and vibrational energy respectively. The harmonic oscillator model states that the vibrational energy can only take discrete quantum levels [128,129].

The Larsen-Borgnakke (L-B) model [130] is used for the energy exchange, employing the quantum L-B procedure [59,131] for the vibrational energy. *dsmcFoam* uses Bird's particle selection permitting double relaxation method [9]. In this method, during a collision between particles P and Q, the energy is exchanged between the relative translational energy and the vibrational energy of particle P is tested for inelastic collision first. Then, the energy exchange between the remaining relative translational energy and the rotational energy of the same particle. Energy exchanges with particle Q are tested for inelastic collisions afterwards.

The inelastic collision tests are done using a probability that depends on the collision number,  $Z$ , defined as the average number of collisions required to reach equilibrium between the desired energy mode and the translational energy. The quantum L-B model provides an expression for  $Z_{vib}$  that depends on properties of the species, whereas for  $Z_{rot}$  it has been observed that 5 is a reasonable approximation for engineering applications [62].

The expression for the vibrational collision number that the quantum L-B model

provides is [59] :

$$Z_{vib}(T) = \left(\frac{\theta_d}{T}\right)^\omega \left[ Z_{ref} \left(\frac{\theta_d}{T_{Z_{ref}}}\right)^{-\omega} \right]^{\left[(\theta_d/T)^{\frac{1}{3}} - 1\right]/\left[\left(\theta_d/T_{Z_{ref}}\right)^{\frac{1}{3}} - 1\right]} \quad (3.41)$$

where  $\theta_d$  is the characteristic dissociation temperature,  $T_{Z_{ref}}$  is a reference temperature usually taken to be the same as  $\theta_{vib}$ , and  $Z_{ref}$  is the vibrational collision number at  $T_{Z_{ref}}$  following the expression:

$$Z_{ref} = \left(\frac{C_1}{T_{Z_{ref}}^\omega}\right) \exp\left(C_2 T_{Z_{ref}}^{-1/3}\right) \quad (3.42)$$

where  $C_1$  and  $C_2$  are constants that can be found in Ref [9].

### 3.2.3 Chemical reactions

Among the different chemistry models used in DSMC, the most common is the Total Collision Energy (TCE) model [38]. The reaction probabilities of this model, which depend on the collision energy of each collision pair, are linked to the coefficients of the Arrhenius rate model, that depend on the macroscopic temperature. As such, this method relies on the availability of experimental data, making it a highly phenomenological model. Another possibility is the more recent quantum-kinetic (Q-K) chemical model [131], built upon the quantum L-B model, and it is the model used by *dsmcFoam*. The Q-K model uses molecular-level chemistry, and mainly requires fundamental properties [132].

For each accepted collision, the possible reactions for the pair of simulators are tested, from most to less likely, using an acceptance-rejection method that involves the reaction's probabilities. If multiple possible reactions have the same probability, the algorithm would pick one of them randomly. Ignoring the presence of ions, only dissociation and exchange reactions can be observed, and are described as follows [8].

### Dissociation

A dissociation reaction has the form  $AB + C \rightarrow A + B + C$ , where AB is formed by atoms A and B, and C is a reactant partner. The collision energy is calculated as in the vibrational collision phase of the L-B collision, that is, the sum of the relative translational energy of the pair AB-C and the vibrational energy of the molecule AB. If this collision energy is greater than the dissociation energy of the molecule AB, then the probability of this reaction is set to 1. When the dissociation takes place, the molecule AB is deleted and A and B are introduced. The dissociation energy is then removed from the energy balance and the remaining energy is redistributed between all three particles.

### Exchange

An exchange reaction has the form  $AB + C \rightarrow AC + B$ , where AB is formed by atoms A and B, and C is a reactant partner that has to be an atom as well. In this case, the probability of the reaction takes the form

$$P_{exchange} = \frac{(e_{coll} - e_a)^{\frac{3}{2} - \omega_{AB-C}}}{\sum_i^{i_{max}} (e_{coll} - e_{vib,AB,i})^{\frac{3}{2} - \omega_{AB-C}}} \quad (3.43)$$

where  $e_{coll}$  is the collision energy,  $e_a$  is the activation energy of the exchange reaction,  $i$  represents a vibrational energy level,  $i_{max}$  being the maximum level available to the molecule [53].

#### 3.2.4 Distribution functions

The initialisation of the DSMC particles is a quite important part of the simulation. Depending on the case of study, an incorrect initialisation could provide the flow with the wrong momentum and energy, resulting in incorrect results, despite every other part of the code to be functioning as it should. Equilibrium and near-equilibrium distributions for atoms and molecules are detailed as follows. The near-equilibrium

Chapman-Enskog and Generalised Chapman-Enskog distributions can be helpful to initialise DSMC particles from an already converged first approximation of the solution, e.g. from a CFD simulation.

## Atoms

For atoms there are no internal degrees of freedom, and thus the properties of the particle can be characterised by a distribution function that only depends on the thermal velocity  $\vec{c}$ . The thermal velocity is defined as  $\vec{c} = \vec{c}_p - \vec{v}$ , where  $\vec{c}_p$  is the velocity of the particle and  $\vec{v}$  is the macroscopic velocity. The velocity distribution function (VDF),  $f(\vec{c})$ , is defined as the fraction of molecules located, in velocity space, at position  $\vec{c}$  and within an element of volume  $d\vec{c}$  [9].

**Equilibrium distribution** The most widely used VDF is the equilibrium or Maxwellian distribution,  $f^{(0)}(\vec{c})$ , and it is the distribution function found when the flow is spatially homogeneous. The Maxwellian distribution function for a gas of species  $s$  has the form

$$f_s^{(0)}(\vec{c}) = \sqrt{\left(\frac{m_s}{2\pi k_B T_{tra}}\right)^3} \exp\left(-\frac{m_s}{2k_B T_{tra}} \vec{c} \cdot \vec{c}\right) = \frac{\beta_s^3}{\pi^{3/2}} \exp\left(-\beta_s^2 \vec{c} \cdot \vec{c}\right) \quad (3.44)$$

where  $\beta_s = \sqrt{\frac{m_s}{2k_B T_{tra}}}$  is the inverse of the most probable speed of species  $s$  at temperature  $T_{tra}$ . Integrating this VDF over two of the thermal velocity components, the VDF for the remaining component can be calculated. For instance

$$f_s^{(0)}(c_x) = \int_{c_y \rightarrow -\infty}^{c_y \rightarrow \infty} \int_{c_z \rightarrow -\infty}^{c_z \rightarrow \infty} f_s^{(0)}(\vec{c}) dc_y dc_z = \frac{\beta_s}{\sqrt{\pi}} \exp\left(-\beta_s^2 c_x^2\right) \quad (3.45)$$

where  $c_x$ ,  $c_y$ , and  $c_z$  are the thermal velocity components in the  $x$ ,  $y$ , and  $z$  directions respectively. Similar formulas can be obtained for  $f_s^{(0)}(c_y)$  and  $f_s^{(0)}(c_z)$ . To initialise a particle, each thermal velocity component can be obtained by sampling from its distribution function, resulting in [126]

$$c_i = \frac{1}{\beta_s} \sin(2\pi \mathcal{R}_1) \sqrt{-\ln(\mathcal{R}_2)} \quad (3.46)$$

where  $i = x, y$ , or  $z$ , and  $\mathcal{R}_1 \neq \mathcal{R}_2$  are two random numbers between 0 and 1. The particle velocity is then initialised as  $\vec{c}_p = \vec{c} + \vec{v}$ .

**Chapman-Enskog distribution** For simulations of interest, the flow will not be spatially homogeneous. Whereas it is possible to initialise the flow properties using a Maxwellian distribution and proceed with the simulation until the flow reaches a non-homogeneous state, it may be interesting to initialise the flow under other initial conditions. This is possible in near-equilibrium conditions, that is, when the perturbations from equilibrium are small. In this scenario, the VDF is called a Chapman-Enskog distribution,  $f^{(1)}(\vec{c})$ , and can be expressed as [115]

$$f^{(1)}(\vec{c}) = f^{(0)}(\vec{c})\Gamma_{CE}(\vec{c}) \quad (3.47)$$

where  $\Gamma_{CE}(\vec{c})$  is the Chapman-Enskog perturbation function, defined as

$$\Gamma_{CE}(\vec{c}) = 1 + \left( \hat{\vec{q}}_{tra} \cdot \vec{\mathcal{C}} \right) \left( \frac{2}{5} \vec{\mathcal{C}} \cdot \vec{\mathcal{C}} - 1 \right) - \left( \vec{\mathcal{C}} \cdot \hat{\tau} \cdot \vec{\mathcal{C}} \right) \quad (3.48)$$

where  $\vec{\mathcal{C}} = \beta \vec{c}$ , and the non-dimensional translational heat flux vector  $\hat{\vec{q}}_{tra}$ , and viscous stress tensor  $\hat{\tau}$  are used for convenience and are defined as

$$\hat{\vec{q}}_{tra} = \frac{2\beta}{p} \vec{q}_{tra} \quad (3.49)$$

$$\hat{\tau} = \frac{\tau}{p} \quad (3.50)$$

Particle properties can be generated from the Chapman-Enskog distribution using the following acceptance-rejection algorithm [67]:

1. Compute the parameters  $A$  and  $B$ , where  $A = 1+30B$  and  $B = \max \left( \|\hat{\vec{q}}_{tra}\|, \|\hat{\tau}\| \right)$ .  
If  $B > 0.2$ , the flow cannot be considered in near-equilibrium, and therefore the use of this distribution is not recommended.
2. Generate  $\vec{\mathcal{C}}$  from the Maxwellian distribution.
3. Accept  $\vec{\mathcal{C}}$  if  $A\mathcal{R} \leq \Gamma_{CE}(\vec{c})$ , where  $\mathcal{R}$  is a random number between 0 and 1.  
Otherwise, go back to 2.

4. Set the particle velocity  $\vec{c}_p = \vec{v} + \vec{\mathcal{C}}/\beta$ .

It is important to note that this VDF does not take into account the effects of diffusion, and is therefore recommended for single species only.

## Molecules

When dealing with molecules, internal energy modes need to be considered. For this reason, the distribution function depends not only on the thermal velocity, but also on the rotational and vibrational energies,  $\epsilon_{rot}$  and  $\epsilon_{vib}$ , and takes the form  $f(\vec{c}, \epsilon_{rot}, \epsilon_{vib})$ .

**Equilibrium distribution** The distribution function of particles of species  $s$  for a spatially homogeneous flow, also called Maxwell-Boltzmann distribution,  $f_s^{(0)}(\vec{c}, \epsilon_{rot}, \epsilon_{vib})$ , can be written as [9, 129]

$$f_s^{(0)}(\vec{c}, \epsilon_{rot}, \epsilon_{vib}) = f_s^{(0)}(\vec{c}) f_{s,rot}^{(0)}(\epsilon_{rot}) f_{s,vib}^{(0)}(\epsilon_{vib}) \quad (3.51)$$

$$f_{s,rot}^{(0)}(\epsilon_{rot}) = \frac{1}{k_B T_{rot}} \frac{1}{\Gamma(\zeta_{rot}/2)} \left( \frac{\epsilon_{rot}}{k_B T_{rot}} \right)^{\zeta_{rot}/2-1} \exp \left( -\frac{\epsilon_{rot}}{k_B T_{rot}} \right) \quad (3.52)$$

$$f_{s,vib}^{(0)}(\epsilon_{vib}) = \left[ 1 - \exp \left( -\frac{\theta_{vib}}{T_{vib}} \right) \right] \exp \left( -\frac{\epsilon_{vib}}{k_B T_{vib}} \right) \sum_{i=0}^{\infty} \delta(\epsilon_{vib} - ik_B \theta_{vib}) \quad (3.53)$$

where  $\delta(x - x_0)$  is the Dirac delta function. The main focus on this work are the most common molecular components of air, for which  $\zeta_{rot} = 2$ , and therefore

$$f_{s,rot}^{(0)}(\epsilon_{rot}) = \frac{1}{k_B T_{rot}} \exp \left( -\frac{\epsilon_{rot}}{k_B T_{rot}} \right) \quad (3.54)$$

Particle properties can be sampled with the following algorithm:

1. Generate the particle velocity in the same manner as in the atom equilibrium distribution.
2. Generate the rotational energy  $\epsilon_{rot}$  by sampling it from its distribution, with an acceptance-rejection procedure if  $\zeta_{rot} \neq 2$ . If  $\zeta_{rot} = 2$ , it can be shown that a random sample of rotational energy can be obtained as  $\epsilon_{rot} = -\ln(\mathcal{R})k_B T_{rot}$ ,

where  $\mathcal{R}$  is a random number between 0 and 1 [126].

3. Generate the vibrational energy from its distribution. It can be shown that a random sample of vibrational energy can be obtained as  $\epsilon_{vib} = k_B \theta_{vib} i_{vib}$  where  $i_{vib} = \text{floor} \left[ -\ln(\mathcal{R}) \left( \frac{T_{vib}}{\theta_{vib}} \right) \right]$ , where  $\mathcal{R}$  is a random number between 0 and 1 [126].

**Generalised Chapman-Enskog distribution** Similarly than with atoms, in near-equilibrium conditions it is possible to derive a distribution function. This function is called a Generalised Chapman-Enskog distribution,  $f^{(1)}(\vec{c}, \epsilon_{rot}, \epsilon_{vib})$ , and can be expressed for species  $s$  as [77]

$$f_s^{(1)}(\vec{c}, \epsilon_{rot}, \epsilon_{vib}) = f_s^{(0)}(\vec{c}, \epsilon_{rot}, \epsilon_{vib}) \Gamma_{GCE,s}(\vec{c}, \epsilon_{rot}, \epsilon_{vib}) \quad (3.55)$$

where  $\Gamma_{GCE}(\vec{c}, \epsilon_{rot}, \epsilon_{vib})$  is the generalised Chapman-Enskog perturbation function, defined as

$$\begin{aligned} \Gamma_{GCE,s}(\vec{c}, \epsilon_{rot}, \epsilon_{vib}) = & 1 + 2\vec{\mathcal{D}}_s \cdot \vec{\mathcal{C}} + \left( \hat{\vec{q}}_{tra} \cdot \vec{\mathcal{C}} \right) \left( \frac{2}{5} \vec{\mathcal{C}} \cdot \vec{\mathcal{C}} - 1 \right) + \\ & + \left( \hat{\vec{q}}_{rot,s} \cdot \vec{\mathcal{C}} \right) (\epsilon_{rot} - \langle \epsilon_{rot,s} \rangle) + \left( \hat{\vec{q}}_{vib,s} \cdot \vec{\mathcal{C}} \right) (\epsilon_{vib} - \langle \epsilon_{vib,s} \rangle) - \left( \vec{\mathcal{C}} \cdot \hat{\tau} \cdot \vec{\mathcal{C}} \right) \end{aligned} \quad (3.56)$$

where  $\vec{\mathcal{D}}_s = \frac{\beta_s}{\rho_s} \vec{\mathcal{J}}_s$  is the scaled diffusion flux for species  $s$ ,  $\hat{\vec{q}}_{i,s} = \frac{2\beta_s}{\rho C_{v,s,i} T_i} \vec{q}_{i,s}$  is the scaled heat flux vector for energy mode  $i$  of species  $s$ ,  $\epsilon_i = \frac{\epsilon_i}{k_B T_i}$  is the scaled energy of mode  $i$ , and  $\langle \epsilon_{rot,s} \rangle = 1$  and  $\langle \epsilon_{vib,s} \rangle = \frac{\theta_{vib,s}}{T_{vib}} [\exp(\theta_{vib,s}/T_{vib}) - 1]^{-1}$  are the average rotational and vibrational energies respectively. A particle can be initialised using this distribution by using the following algorithm for an acceptance-rejection method [77]:

1. Compute  $B = \max \left( \|\vec{\mathcal{D}}\|, \|\hat{\vec{q}}_{tra}\|, \|\hat{\vec{q}}_{rot,s}\|, \|\hat{\vec{q}}_{vib,s}\|, \|\hat{\tau}\| \right)$  and  $A = 1 + 30B$ . If  $B > 0.2$ , the flow cannot be considered in near-equilibrium, and therefore the use of this distribution is not recommended.
2. Compute the average scaled energies  $\langle \epsilon_{rot,s} \rangle$  and  $\langle \epsilon_{vib,s} \rangle$ .
3. Generate  $\vec{\mathcal{C}}$ ,  $\epsilon_{rot}$ , and  $\epsilon_{vib}$  from the Maxwell-Boltzmann distribution.
4. Accept  $\vec{\mathcal{C}}$ ,  $\epsilon_{rot}$ , and  $\epsilon_{vib}$  if  $A\mathcal{R} \leq \Gamma_{GCE,s}(\vec{c}, \epsilon_{rot}, \epsilon_{vib})$ , where  $\mathcal{R}$  is a random number between 0 and 1. Otherwise, go back to 3.
5. Set the particle properties  $\vec{c}_p = \vec{v} + \vec{\mathcal{C}}/\beta_s$ ,  $\epsilon_{rot} = \epsilon_{rot} k_B T_{rot}$ , and  $\epsilon_{vib} = \epsilon_{vib} k_B T_{vib}$ .

### Distribution comparison

For illustrative purposes, Figure 3.1 shows the Maxwell-Boltzmann, Chapman-Enskog, and Generalised Chapman-Enskog distribution functions for one velocity component on a vibrationless  $N_2$  configuration with heat transfer. As the complete difference between distributions cannot be fully observed in this plot, Figure 3.2 show the perturbation functions for the same configuration instead.

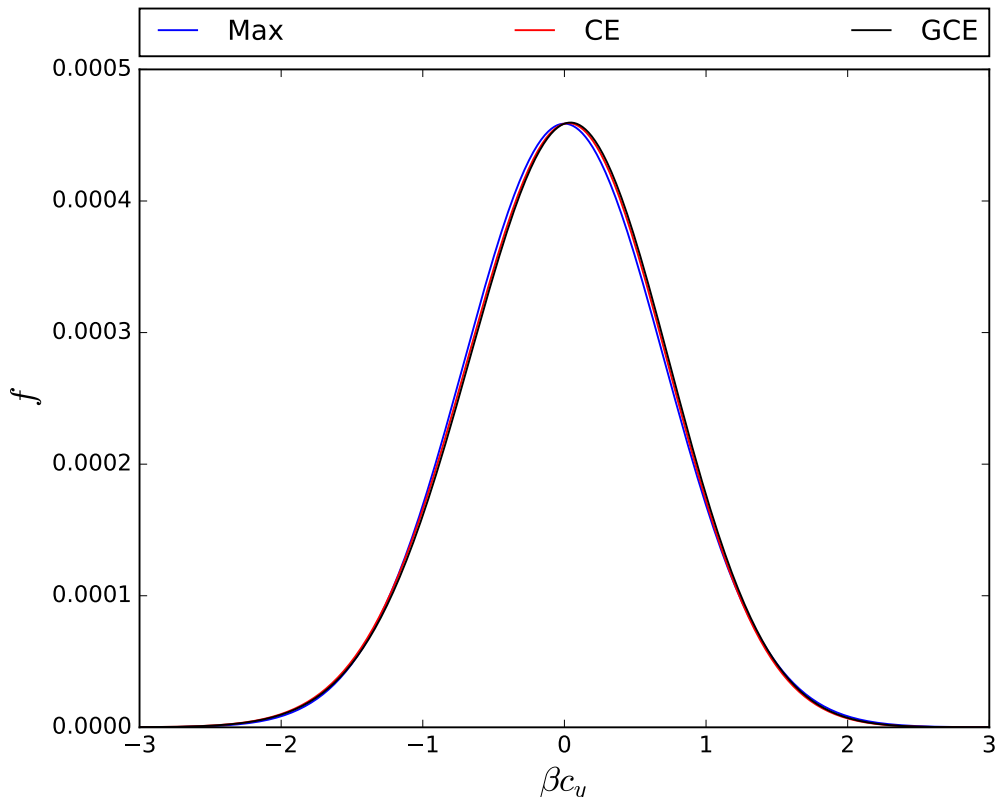


Figure 3.1: Maxwell-Boltzmann (Max), Chapman-Enskog (CE), and Generalised Chapman-Enskog (GCE) distribution functions comparison

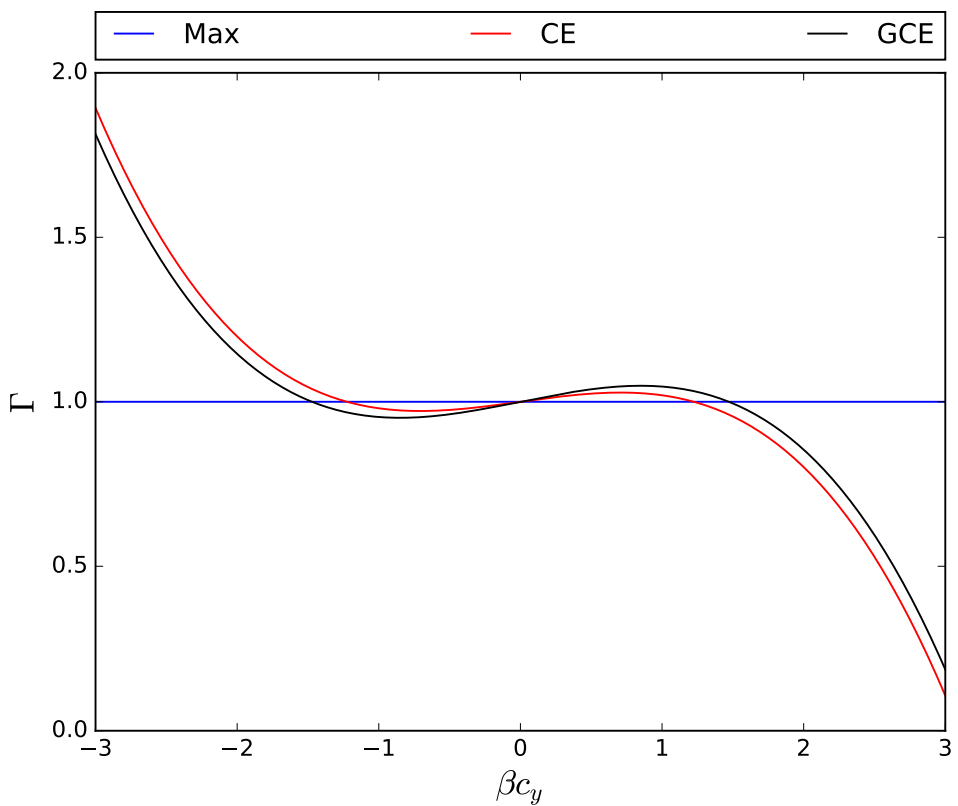


Figure 3.2: Maxwell-Boltzmann (Max), Chapman-Enskog (CE), and Generalised Chapman-Enskog (GCE) perturbation functions comparison

# Chapter 4

## *hyperFoam*

A hybrid CFD-DSMC solver has been created within OpenFOAM, using the CFD solver *hy2Foam* and the DSMC solver *dsmcFoam*, both of which fulfil the required conditions for hypersonic flows, and can therefore be used when dealing with the reentry of spacecraft. The characteristics of this new solver, *hyperFoam*, will be discussed in Section 4.1. In Section 4.2, a Couette flow with heat transfer will be simulated for different gases, comparing the results from both *hy2Foam* and *hyperFoam* with the solution from *dsmcFoam*, to show how they compare in terms of accuracy.

### 4.1 Characteristics

In Chapter 1 the two aspects that need to be considered before a hybrid scheme can be successfully implemented were introduced.

First of all, the breakdown parameter is fundamental to determine in which regions of the domain the validity of the continuum hypothesis can be brought into question. Several criteria can be used to determine this breakdown parameter, and the most common have already been mentioned in Chapter 1.

Bird's parameter  $P$  [66] represents the ratio between the Lagrangian mean free path

and the density scale length, and can be defined for steady flows as

$$P = \frac{\lambda}{\rho} \sqrt{\frac{m}{2k_B T_{tra}}} \|\vec{v} \cdot \nabla \rho\| \quad (4.1)$$

and the flow regime is not considered continuum anymore when  $P > 0.04$  [66, 133].

The Chapman-Enskog parameter  $\Gamma_{CE}$  [67] is an accurate predictor of the validity of continuum conditions. This function, however, proves to be difficult to evaluate, as it depends on the thermal velocity of particles, and therefore a different parameter  $B$  is used. As mentioned in Chapter 3, this parameter is defined as

$$B = \max (\|\hat{\vec{q}}_{tra}\|, \|\hat{\tau}\|) \quad (4.2)$$

but can be generalised to include multiple energy modes and species diffusion to [77]

$$B = \max (\|\vec{\mathcal{D}}\|, \|\hat{\vec{q}}_{tra}\|, \|\hat{\vec{q}}_{rot}\|, \|\hat{\vec{q}}_{vib}\|, \|\hat{\tau}\|) \quad (4.3)$$

where  $B > 0.2$  can be used as the breakdown criterion [133] if the continuum regime is treated employing high-order equations. For traditional Navier-Stokes continuum solvers, the breakdown criteria should be set to  $B > 0.1$  [77].

The Knudsen number  $Kn = \lambda/L$  gives a reasonable first approximation on the dominant regime of the domain. However, it does not consider some local effects that can affect greatly the flow properties. Boyd's Gradient-Length-Local Knudsen number  $Kn_{GLL}$  [68] solves this issue by taking into consideration the variation of macroscopic properties on a local level, and it is defined as

$$Kn_{GLL,Q} = \lambda \left\| \frac{\nabla Q}{Q} \right\| \quad (4.4)$$

where  $Q$  represents a macroscopic property such as density, pressure, or temperature. A breakdown criterion of  $Kn_{GLL} > 0.05$  has been established for this parameter as suitable for most engineering applications [68, 133].

In *hyperFoam*, an amalgamation of two criteria has been adopted as the breakdown parameter,  $Kn_{breakdown}$ . This combination consists of both the Gradient-Length-Local Knudsen number, and the modified Chapman-Enskog parameter, resulting in

$$Kn_{breakdown} = \max(Kn_{GLL,\rho}, Kn_{GLL,T}, Kn_{GLL,\|\vec{v}\|}, 0.5B) \quad (4.5)$$

where  $Kn_{GLL,\|\vec{v}\|} = \lambda \frac{\|\nabla\|\vec{v}\|\|}{\max(\|\vec{v}\|, a)}$ , and  $a = \sqrt{\gamma k_B T_{t-r}/m}$  is the speed of sound at temperature  $T_{t-r}$ , to avoid problems when in low-speed areas of the flow [48]. The factor 0.5 is included for the modified Chapman-Enskog parameter so that both criteria have the same breakdown threshold of 0.05. Originally, *hyperFoam* used the  $Kn_{GLL}$  criterion only, but it was modified to increase the accuracy in the results at walls (see Chapter 5).

The second factor to take into account is the mechanism to transfer information between the rarefied and the continuum regions. As explained in Chapter 1 the two most common methods are the flux-based method, in which each solver dictates the flux of properties that enter the other solver's domain through the interface, and the state-based method, in which the domains of both solvers are extended a few additional cells, where the macroscopic properties are fixed by the solution of the other solver. The most significant difference between the two is the number of samples  $N$  required to obtain a comparable level of scattering error in the DSMC solution, which behaves as:

$$error_{flux} \approx error_{state} \implies N_{flux} \propto \frac{N_{state}}{Kn^2} \quad (4.6)$$

As applications requiring the use of *hyperFoam* will have a low  $Kn$  on the regions near the interface, state-based coupling has been adopted to radically reduce the number of samples required until the scattering error of the DSMC solution is acceptable to use as the macroscopic state for a CFD simulation.

With both breakdown criterion and information transfer method defined, the algorithm for the *hyperFoam* solver can then be established, as follows:

1. Initialise the simulation by using a previous CFD solution to calculate the breakdown parameter and determine the continuum and rarefied domains and their buffer regions.
2. Progress the solution in the DSMC domain using the CFD solution in the buffer cells of the rarefied domain.
3. Progress the solution in the CFD domain using the macroscopic results from the previous DSMC solution in the buffer cells of the continuum domain.
4. End the simulation if the final time has been reached. Otherwise, go back to 2.

Each of these steps will be elaborated in the following subsections.

#### 4.1.1 Determination of the continuum and rarefied domains

As with other hybrid solvers, *hyperFoam* requires an initial approximation of the solution, which is better described by the results of a CFD simulation of the flow using the same geometry and mesh as the ones to be employed by *hyperFoam*. Using the macroscopic fields obtained from this simulation, the breakdown parameter is then calculated and the domains for each of the solvers are identified.

For the rarefied solver, the purely rarefied region, from now denoted as DSMC region, is formed by all the cells that exceed the value specified by the breakdown criterion. The buffer region for this rarefied domain is then generated, separated in two, following a user-defined number of layers for each. Assuming that the CFD solution is not accurate enough, and hence the hybrid solver is needed, the macroscopic values on the continuum domain are at an incorrect state. Although the effect of these ill-posed boundary conditions on the DSMC solution seems to be small, a possible way to ensure that the DSMC particles evolve to the right solution is to enforce the CFD solution some cells away from the continuum-rarefied interface instead of immediately adjacent to it, and letting the particles evolve naturally from there onwards using the DSMC method [70]. The part of the buffer region where the particles are generated by enforcing the CFD solution is called outer buffer region, whereas the part where

## Chapter 4. *hyperFoam*

particles evolve according to the DSMC method is called inner buffer region.

The inner buffer region is adjacent to the rarefied region, and must be formed by as many layers of cells as specified by the user. Increasing the number of layers in this buffer region would result in better interface properties provided by the DSMC solver [83]. However, having more layers also implies increasing the computational expenses. A compromise value of 5 has been found to be acceptable for this solver.

The outer buffer region is then formed by as many layers as defined by the user, and it is directly in contact with the inner buffer region but not with the DSMC region. A minimum of 2 layers is recommended for the outer buffer region [83], as increasing the number of outer buffer layers decreases the information loss from particles that should enter the inner buffer region directly from the continuum region. Similar to the inner buffer region, however, adding layers will require more computational resources. For the present work, a value of 5 layers has been adopted as a compromise.

If there are not enough layers between two DSMC cells for the specified number of buffer layers, the buffer cells belonging to these incomplete layers become DSMC cells instead. Finally, all of the cells that are not part of any of these three regions belong to the continuum region, or CFD region onwards.

This process has been represented step by step in Figure 4.1, for a case with 3 and 2 layers for the inner buffer and the outer buffer regions respectively.

For the continuum solver, the purely continuum region is formed by all inner buffer, outer buffer and CFD regions previously described. For the purpose of simplicity, the whole DSMC region is used as the buffer region of the continuum domain instead of defining new regions to represent these buffer cells.

Once these aforementioned four regions have been defined, the global simulation time  $t_{hybrid}$  is set to 0, and the solution can progress using the DSMC solver to update the results.

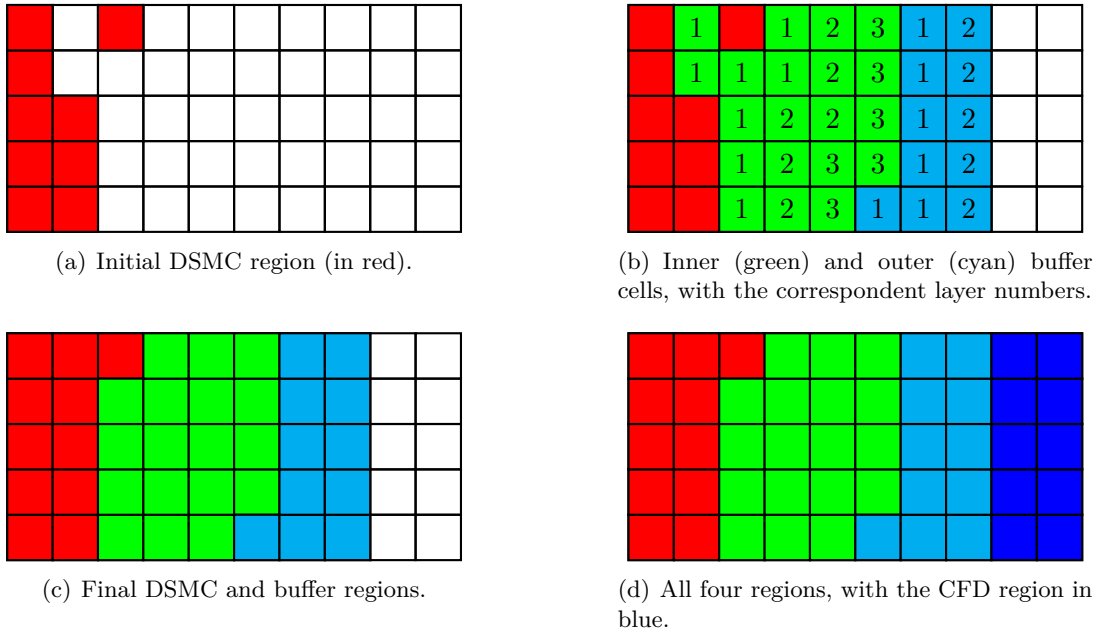


Figure 4.1: Determination of the different domains for the hybrid solver.

#### 4.1.2 Progression of the solution using the DSMC solver

To progress with the DSMC simulation the mesh first needs to be populated by particles. These particles are created in the DSMC, inner buffer, and outer buffer regions using the CFD fields (transrotational and vibrational temperatures, partial and total densities, velocity, diffusion, shear stress, and heat transfer) to initialise the particle properties via a generalised Chapman-Enskog distribution. The method to generate this distribution has, however, a minor modification with respect to the one shown in subsection 3.2.4. It can be assumed that on the range of application of *hyperFoam*,  $T_{tra} \approx T_{rot}$ , therefore the definitions of  $\varepsilon_{rot}$  and  $\langle \varepsilon_{rot,s} \rangle$  can be changed as follows [77]:

- $\varepsilon_{rot} = \epsilon_{rot}/k_B T_{tra}$
- $\langle \varepsilon_{rot,s} \rangle = T_{rot}/T_{tra}$

Once the particles have been initialised, they proceed to move and collide, and new particles are added at the corresponding boundaries, as per usual on a regular DSMC step. The difference with regular DSMC behaviour is that the solution should have

the same macroscopic state on the non-rarefied cells that the CFD solution imposes. To do that, after moving, colliding and adding new particles, all of those simulators that are located within the outer buffer and CFD regions are eliminated, and particles are created and initialised again in the outer buffer region. This process, from now on referred to as resetting the particles, will occur after each regular DSMC step and represent the coupling between the previous CFD state and the actual DSMC simulation, as indicated by state-based coupling, and will result in the same average state for both in the outer buffer region.

As specified in subsection 4.1.1 the particles in the inner buffer region are not reset, but are left to the normal evolution of the DSMC procedure. A representation of the particle resetting process can be seen in Figure 4.2.

Combined, regular DSMC evolution and particle resetting continue until the prescribed time for coupling back with CFD,  $\Delta t_{hybrid}$ , is reached. This time is defined by a user-defined number of DSMC steps  $\Delta t_{DSMC}$ , such that  $\Delta t_{hybrid} = n_{steps} \Delta t_{DSMC}$ , with a recommended minimum value of  $n_{steps,min} = 5000$ . However, the number of time-steps required to reduce significantly the scattering of the macroscopic fields is in most of the simulations case dependent. Hadjiconstantinou [69], derived expressions that link the fluctuations of the macroscopic properties with their averaged value. These expressions can be used to get an estimation on the  $n_{steps}$  necessary to reduce the scattering error to an acceptable level.

The sampling of the simulators through these time-steps provide the macroscopic state that will be used in the buffer region of the continuum solver.

#### 4.1.3 Progression of the solution using the CFD solver

For the solver to update its continuum solution, the values of the CFD fields on the DSMC region start by being replaced by the DSMC solution recently obtained. The DSMC solver will return translational, rotational, and vibrational temperatures, partial

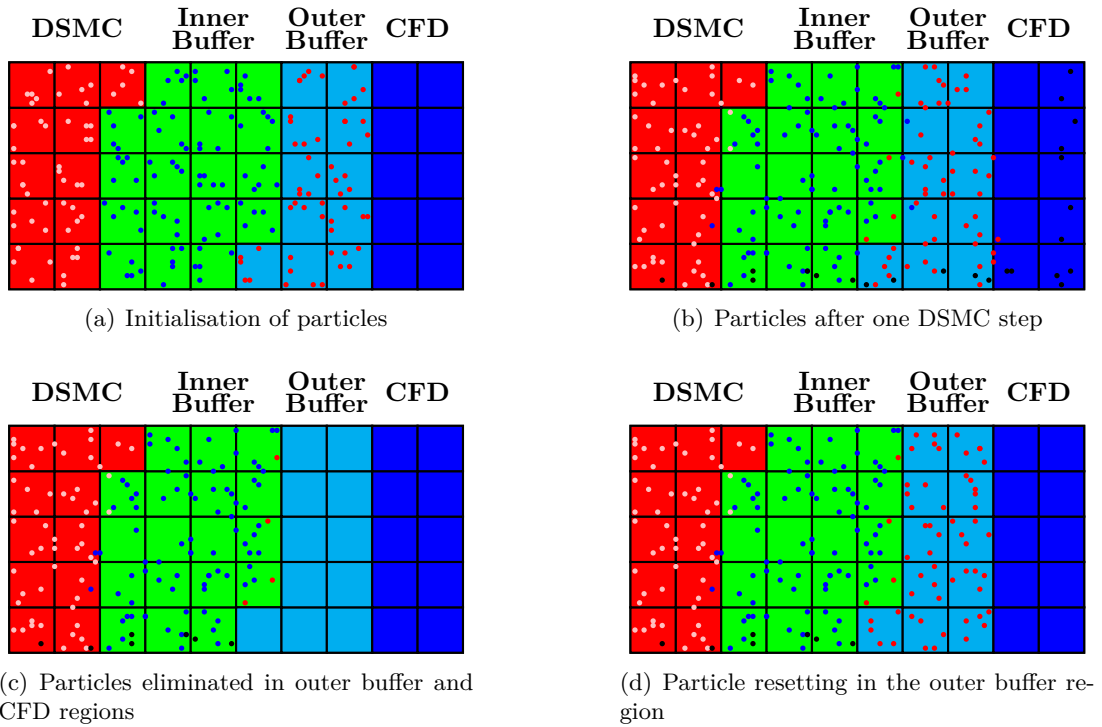


Figure 4.2: Particle progression with the DSMC solver. The particle colour indicates only the region where the particle originates from: pink if the particle started in the DSMC region, blue if in the inner buffer region, red if in the outer buffer region, and black if the particle was generated at the boundaries.

and total densities, and velocities. Most of the DSMC fields can be directly transferred into their respective CFD counterpart. However, the transrotational temperature will be calculated from the translational and rotational temperature as follows [9]:

$$T_{t-r}^{CFD} = \frac{3T_{tra}^{DSMC} + \zeta_{rot} T_{rot}^{DSMC}}{3 + \zeta_{rot}} \quad (4.7)$$

The continuum solver then advances the simulation by one time-step, and the DSMC solution is imposed again on the cells of the DSMC region. This process, from now on called resetting the CFD fields, then continues until the time for coupling back with DSMC is reached. The simulated time between couplings is again  $\Delta t_{hybrid}$ , but the continuum solver will evolve at its own time-step  $\Delta t_{CFD}$ , and could even use the local time-stepping technique from Chapter 2 to benefit from a faster convergence.

#### 4.1.4 Check for final time

After each CFD-DSMC cycle,  $t_{hybrid}$  increases by  $\Delta t_{hybrid}$ . If the final simulation time  $t_{final}$  is such that  $t_{final} > t_{hybrid}$ , a new hybrid cycle starts. For this new cycle, the CFD results obtained from the previous cycle can be used to recalculate the breakdown parameter if desired, updating the continuum and rarefied domains accordingly. If on the other hand  $t_{final} \leq t_{hybrid}$ , the simulation is considered completed.

## 4.2 Validation with a Couette Flow

To test the capabilities of *hyperFoam* in a simple yet concise manner, different configurations for a Couette flow have simulated and then compared with the initial CFD solution from *hy2Foam* and the DSMC results from *dsmcFoam*.

In a Couette flow the properties of a fluid at rest are modified by a moving wall that transfers momentum into the domain, and thus the departure from equilibrium due to gradients of the velocity can be perfectly represented. Adding heat transfer in the form

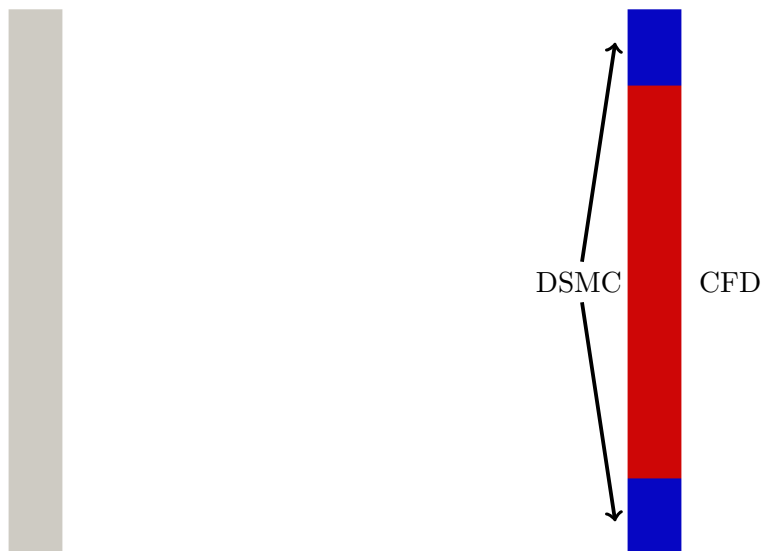
of different temperatures at the channel walls adds gradients of temperature as causes of non-equilibrium, and thus increases the complexity of the simulation. To fully assess the suitability of the hybrid solver for this relatively simple test case, different gases have been considered in increasing complexity. The domain of the simulation has been defined as a horizontal channel, with the upper and lower walls separated by 1 m. The left and right boundaries of the domain have been established as cyclic boundaries, so that fluid leaving through one of them enters through the other. The temperature of the bottom wall was set at 2000 K while the top wall had a temperature of 3000 K, to generate a significant temperature difference. According to similar test cases, the non-equilibrium originates from the Knudsen layer near the walls, and thus the DSMC domain has been established as 15% of the domain next to each of the walls, as suggested by those test cases [83, 134]. Fixing these domains independently of flow properties may affect the number of simulators required for the hybrid solver and thus its total computational requirements. For this reason, the accuracy of the solution, but not the computational requirements, are the subject to study for the Couette flow. The CFD domain, that includes the two buffers and the CFD region, is the region in between the two DSMC regions. The domain, boundary conditions, and CFD and DSMC domains can be seen in Figure 4.3.

The initial temperature for all the species has been set to 2000 K, and the density of each has been chosen so that the body-length Knudsen number  $Kn_{BL}$  is 0.05, to have the gas near non-equilibrium conditions. Unless otherwise stated, the generalised Chapman-Enskog distribution is used for the creation of the simulators. In addition, the LTS technique has been used for the CFD portion of the all the simulations.

#### 4.2.1 Argon

Argon (*Ar*) has no internal degrees of freedom, as it is a monoatomic gas. This results in only translational energy, making monoatomic gases the simplest gas to consider. Figures 4.4 and 4.5 show the comparison between the CFD, DSMC, and hybrid

$$T_1 = 3000K; U_1 = 300m/s$$



$$T_0 = 2000K; U_0 = 0$$

a) Couette flow domain and boundary conditions

b) CFD and DSMC zones

Figure 4.3: Boundary conditions and zones for the Couette flow

results for the translational temperature and velocity respectively. On both figures it can be observed that the hybrid solver manage to adapt the solution so it resembles the DSMC results with greater accuracy than the CFD results.

In addition, a study of the importance of the distribution used while resetting the particles can be seen in Figures 4.6 and 4.7. An equilibrium distribution (*Max* in the plots) provides inaccurate particle properties thus causing the disparity in the results. For the other two distributions, due to the fact that Ar possess no internal degrees of freedom, the Generalised Chapman-Enskog distribution (*GCE*) collapses into the standard Chapman-Enskog distribution (*CE*), and therefore both provide the same results.

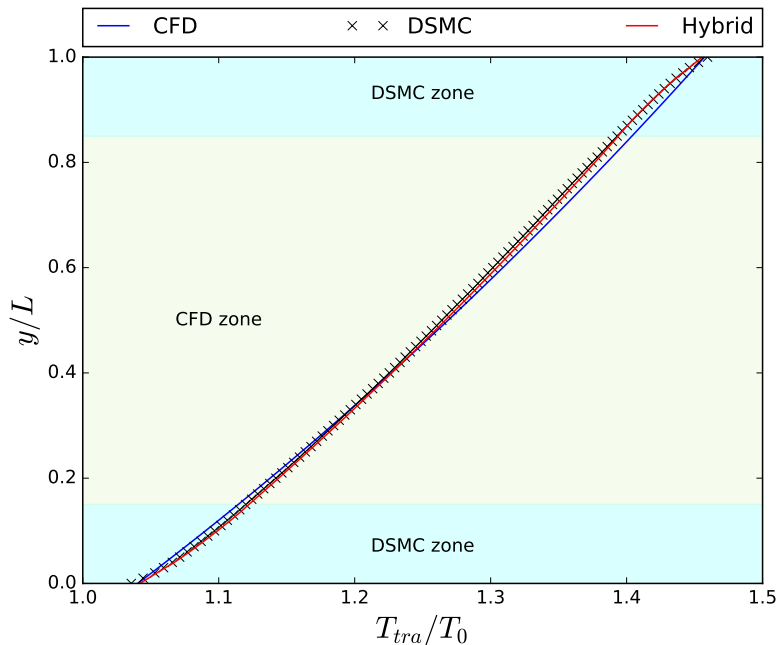


Figure 4.4: Translational temperature comparison, for Ar

#### 4.2.2 Vibrationless Nitrogen

The next step is to simulate a gas with translational and rotational energy. For the continuum solver this wouldn't represent much of a difference, as two-temperature models treat translational and rotational temperatures as one and the same. But the

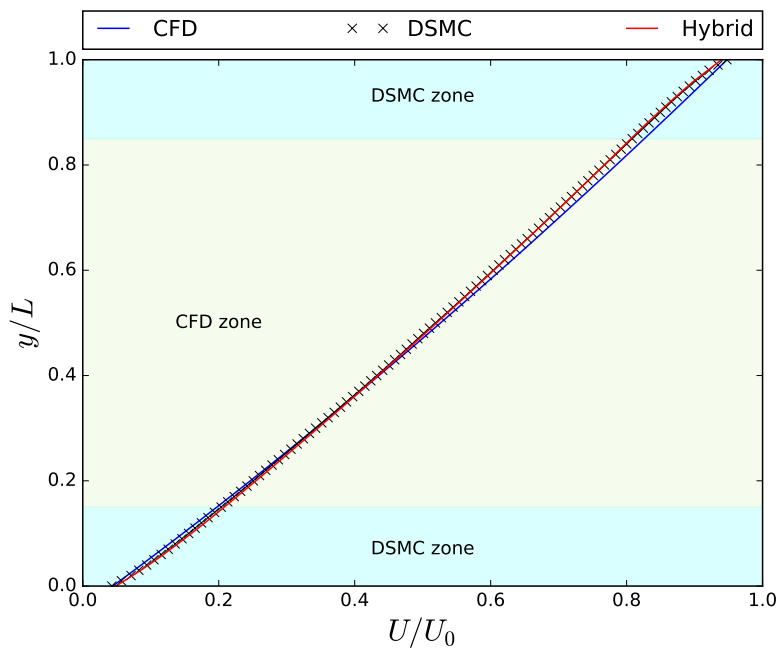


Figure 4.5: Velocity comparison, for  $Ar$

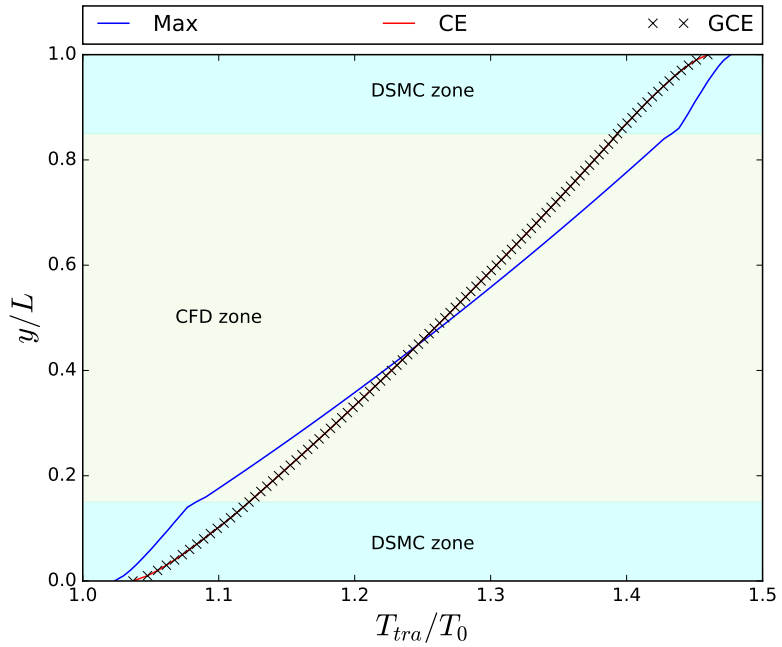


Figure 4.6: Influence of different distributions in the translational temperature, for  $Ar$

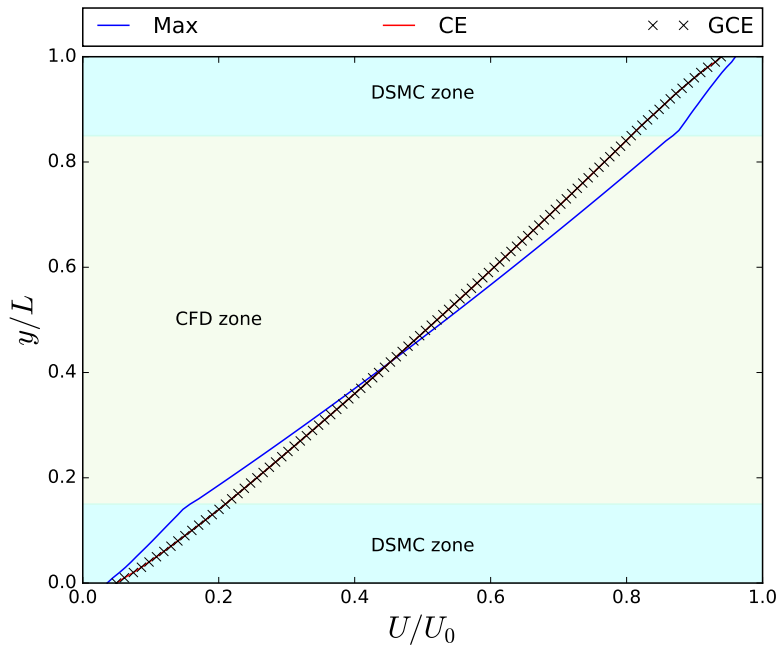


Figure 4.7: Influence of different distributions in the velocity, for  $Ar$

particle solver does distinguish between the two temperatures and as such this needs to be taken into account when sending information into the continuum solver. However, it is not possible to have a real fluid with rotational degrees of freedom that at the same time present no vibrational energy. Therefore, a fictitious gas must be used for this test. This is a simple task to do computationally, and  $N_2$  has been chosen for this test case due to it being the predominant component of air.

The results from the three solvers for transrotational temperature and velocity can be observed in Figures 4.8 and 4.9 respectively. The hybrid solver continues to approximate to the DSMC solution better than the CFD solution, meaning that the coupling between DSMC translational and rotational temperatures and CFD transrotational temperature has been successfully implemented.

Another study was performed using the equilibrium, Chapman-Enskog, and generalised Chapman-Enskog distributions for this case. It can be observed in Figure 4.10 that the results for transrotational temperature based on a Chapman-Enskog distribution differs slightly from the results based on a Generalised Chapman-Enskog distribu-

tion. This difference is due to the fact that whereas the Chapman-Enskog distribution includes the departure from equilibrium due to translational temperature gradients, it does not take into account the effects of the rotational temperature. Figure 4.11 shows that both the CE and GCE distributions provide the same results for velocity, as both distributions consider the effects of the velocity gradients on the departure from equilibrium. The equilibrium distribution does not capture any of this phenomena and thus the results it provides are quite inaccurate.

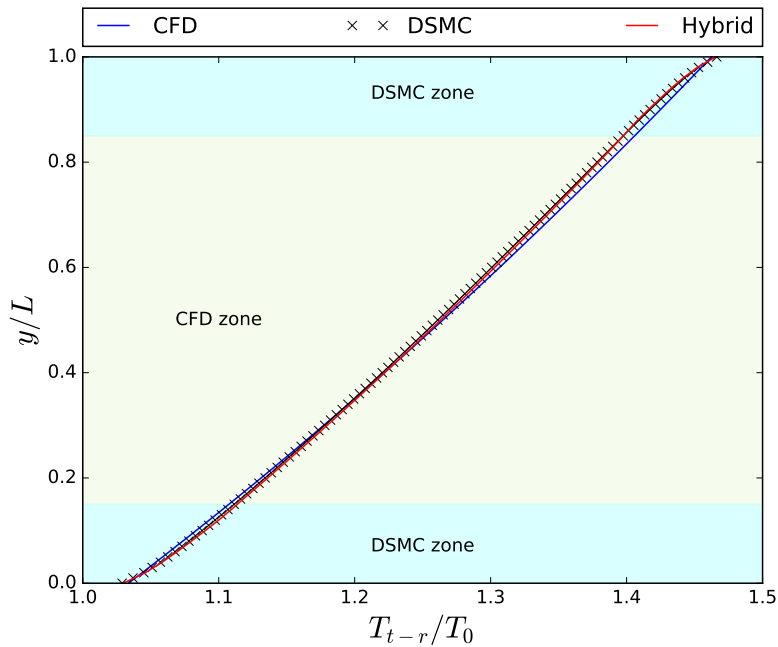


Figure 4.8: Transrotational temperature comparison, for vibrationless  $N_2$

### 4.2.3 Molecular Nitrogen

The simplest scenario where the gas under consideration has all three energy modes active is obtained using diatomic gases.  $N_2$  has been chosen as an example due to its predominance in air. The inclusion of a vibrational temperature test both the two-temperature capabilities of the continuum solver as well as the coupling mechanism between all energy modes. Good agreement can be seen between the hybrid and DSMC results for transrotational and vibrational temperatures, as well as velocities, on Figures 4.12 to 4.14.

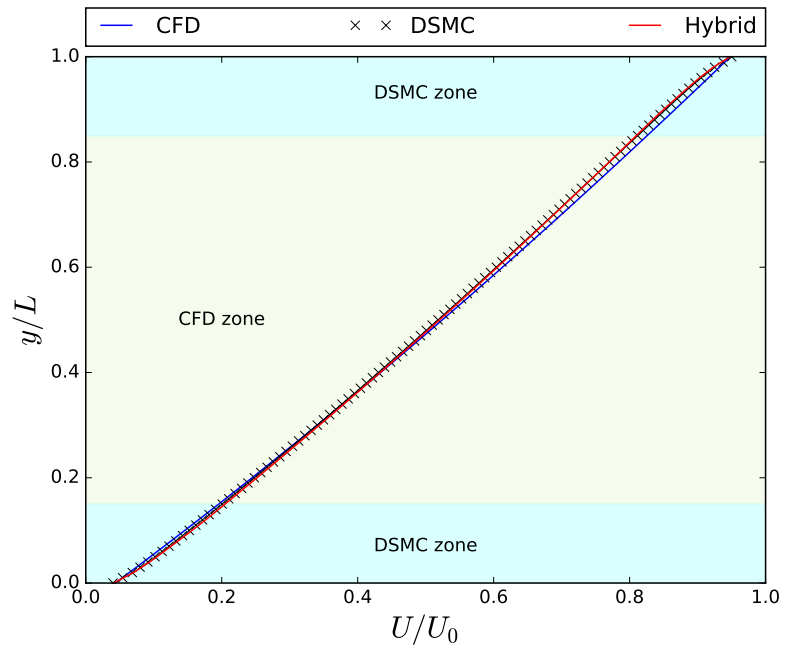


Figure 4.9: Velocity comparison, for vibrationless  $N_2$

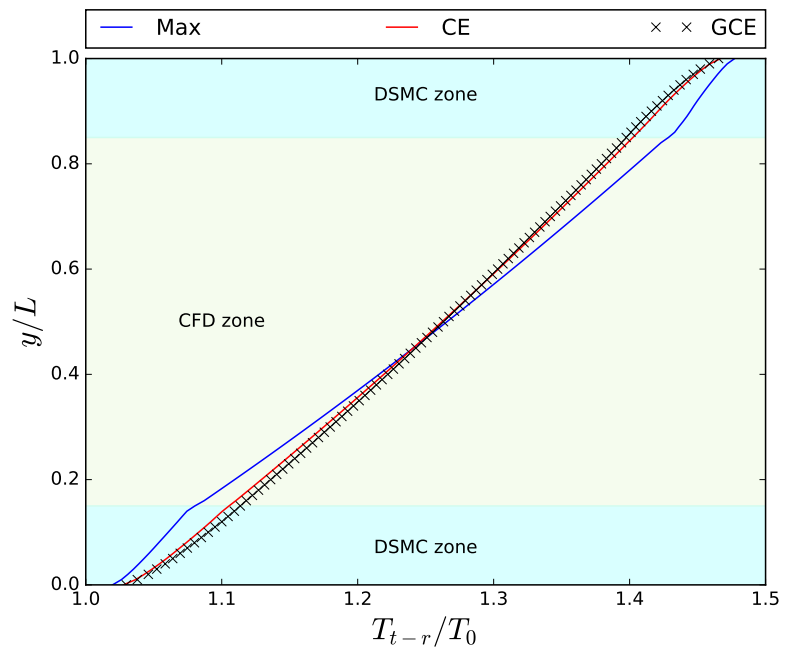


Figure 4.10: Influence of different distributions in the transrotational temperature, for vibrationless  $N_2$

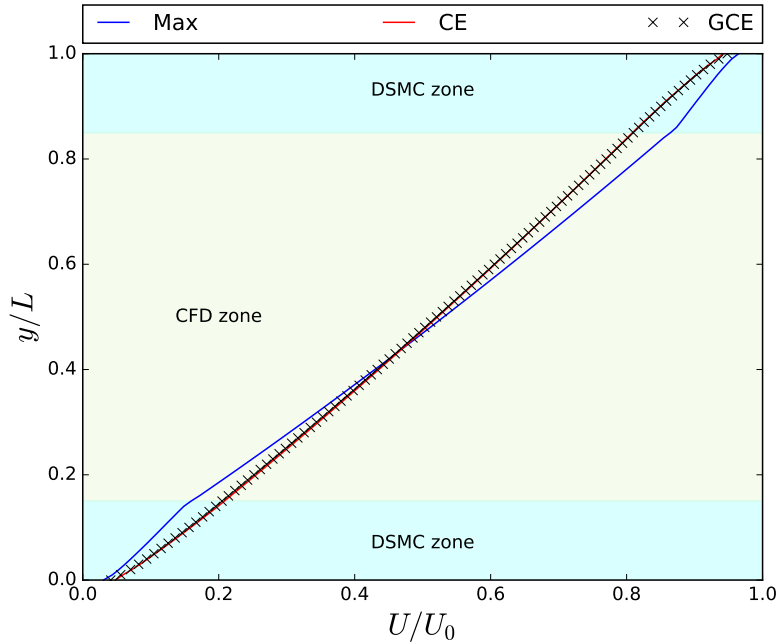


Figure 4.11: Influence of different distributions in the velocity, for vibrationless  $N_2$

A distribution comparison can be seen in Figures 4.15 to 4.17. This case presents the same trend for transrotational temperature and velocity as the vibrationless  $N_2$  case. For the vibrational temperature comparison, both the standard Chapman-Enskog and the equilibrium distributions don't include vibrational temperature in their formulations, and thus both results are similar and compare poorly with the Generalised Chapman-Enskog distribution results.

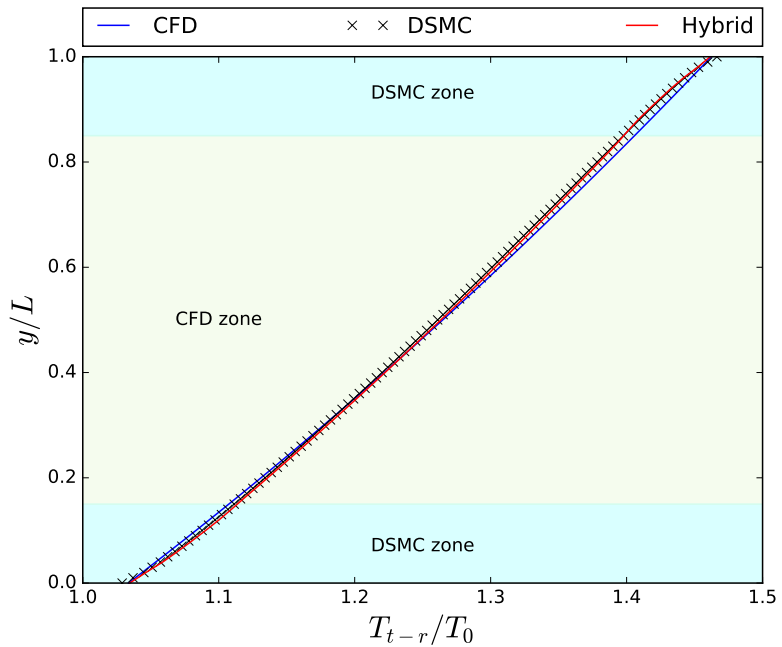


Figure 4.12: Transrotational temperature comparison, for  $N_2$

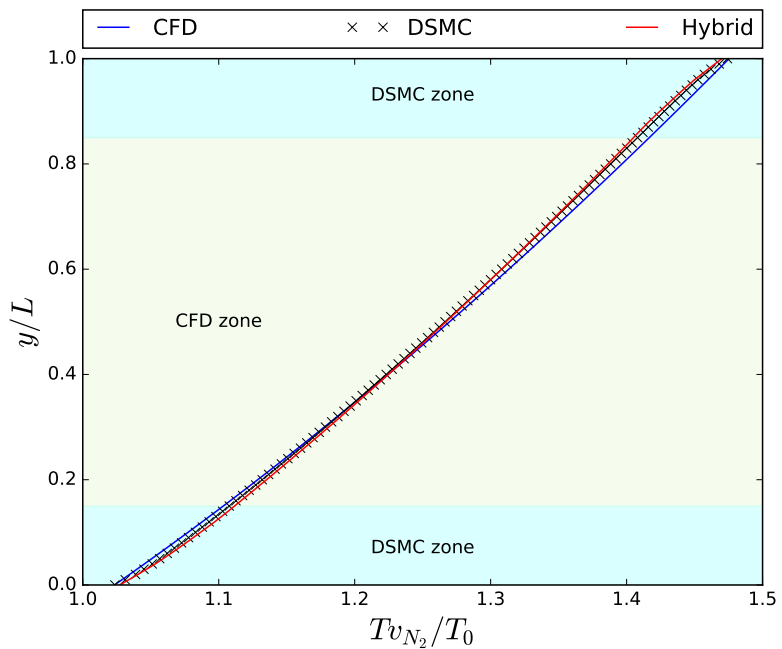


Figure 4.13: Vibrational temperature comparison, for  $N_2$

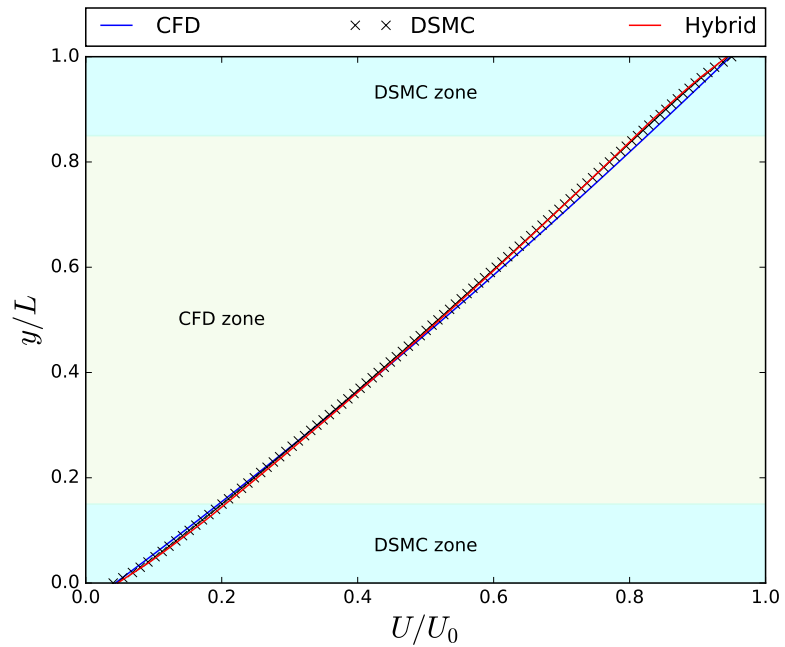


Figure 4.14: Velocity comparison, for  $N_2$

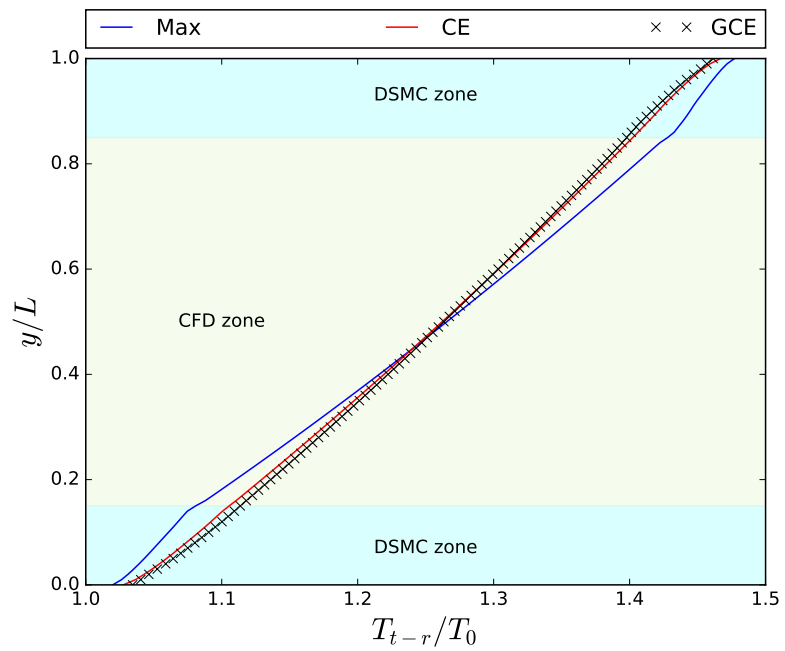


Figure 4.15: Influence of different distributions in the transrotational temperature, for  $N_2$

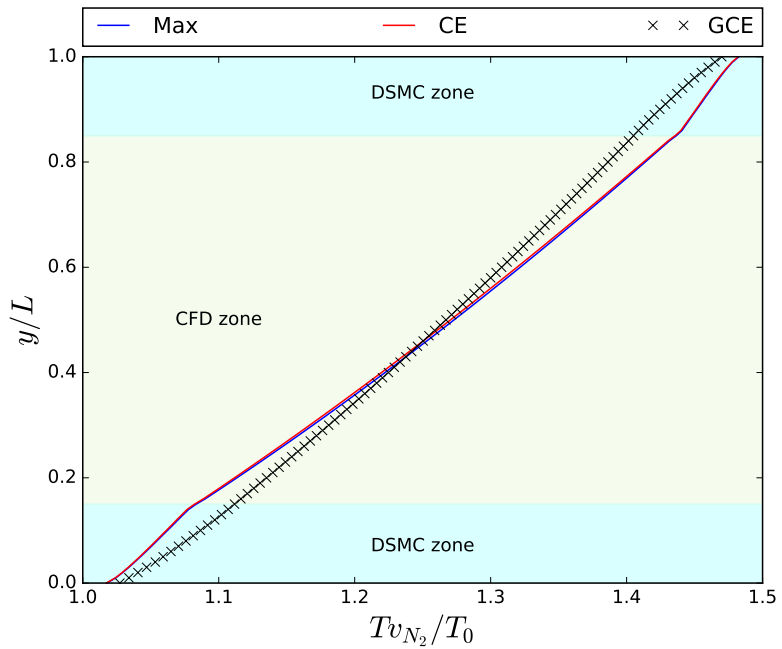


Figure 4.16: Influence of different distributions in the vibrational temperature, for  $N_2$

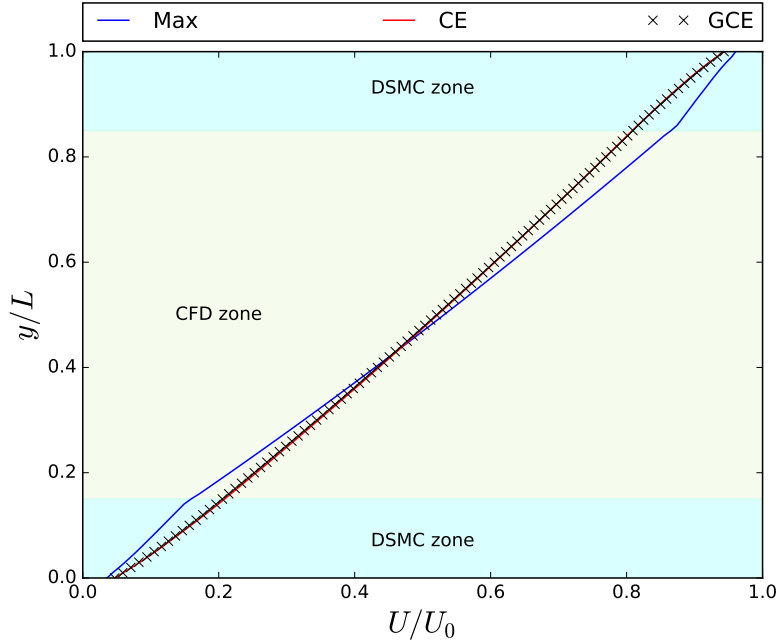


Figure 4.17: Influence of different distributions in the velocity, for  $N_2$

#### 4.2.4 Argon mixture

Similarly to single-species gases, the simulation of multi-species gas mixtures has been performed in increasing complexity. The simplest possible two-species case is again a monoatomic gas, and thus *Ar* has been used again. This artificial *Ar – Ar* test case, in which both species possess the exact same properties, allow for the test of the effects of the diffusion fluxes only. As the results provided by the three solvers should in theory be the same as the single-species simulations, any difference in them should come from the diffusive fluxes. Comparison between the three solvers for translational temperature and velocity can be seen in Figures 4.18 and 4.19. Figures 4.20 and 4.21 show the number density of each species. It can be seen that that the hybrid profiles differ slightly from the DSMC results. The CFD fluxes do not take into account the diffusion due to the temperature gradient, and thus the macroscopic state used to reset the particles at the frontier of the rarefied domain is not completely accurate. Nonetheless, the multispecies results are still within reasonable agreement with respect to the DSMC results. This can also be observed in Figures 4.22 and 4.23, where the results from the single-species, multispecies, and DSMC simulations are compared, with small differences between each other.

#### 4.2.5 Atomic Nitrogen and Oxygen

Atomic nitrogen and oxygen provide a different example of a multispecies gas mixture that lacks internal degrees of freedom. This mixture, that consists of 75% of *N*, 25% of *O* in number of molecules, show reasonable agreement concerning translational temperature and velocity, as can be seen in Figures 4.24 and 4.25. Figures 4.26 and 4.27 show the number density for *N* and *O* respectively, where some disagreement on the number density of *O* can be observed, especially at the top of the channel. This disagreement, however, represent a small percentage on the DSMC solution, and thus the accuracy on the other quantities are not extremely affected.

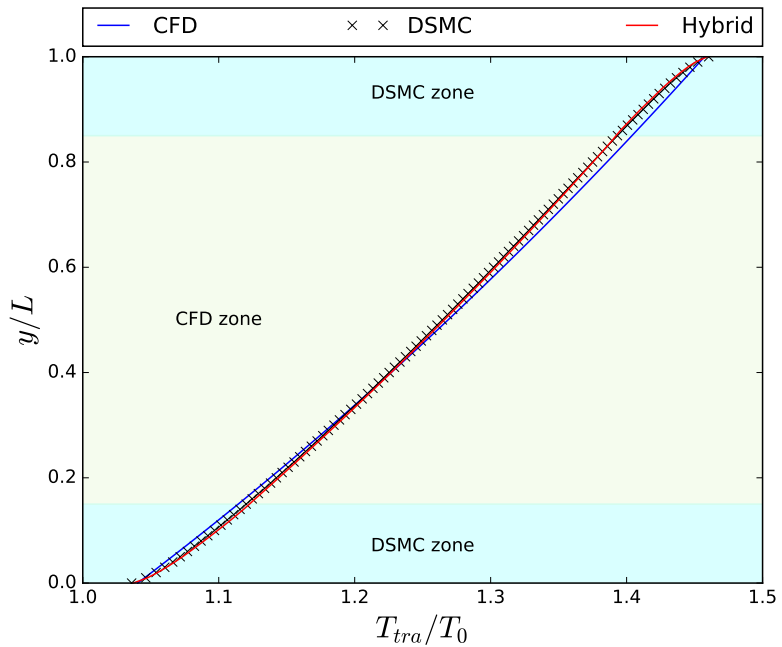


Figure 4.18: Translational temperature comparison, for an  $Ar - Ar$  mixture

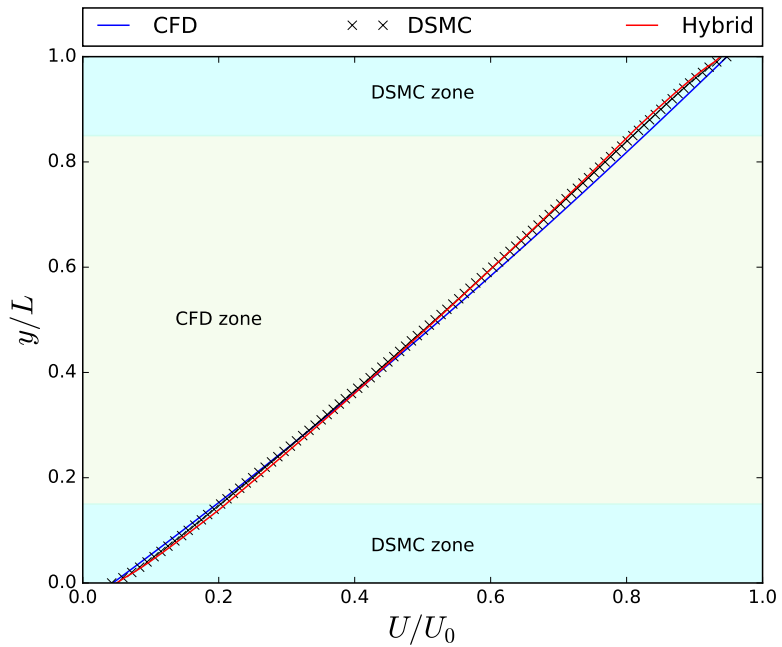


Figure 4.19: Velocity comparison, for an  $Ar - Ar$  mixture

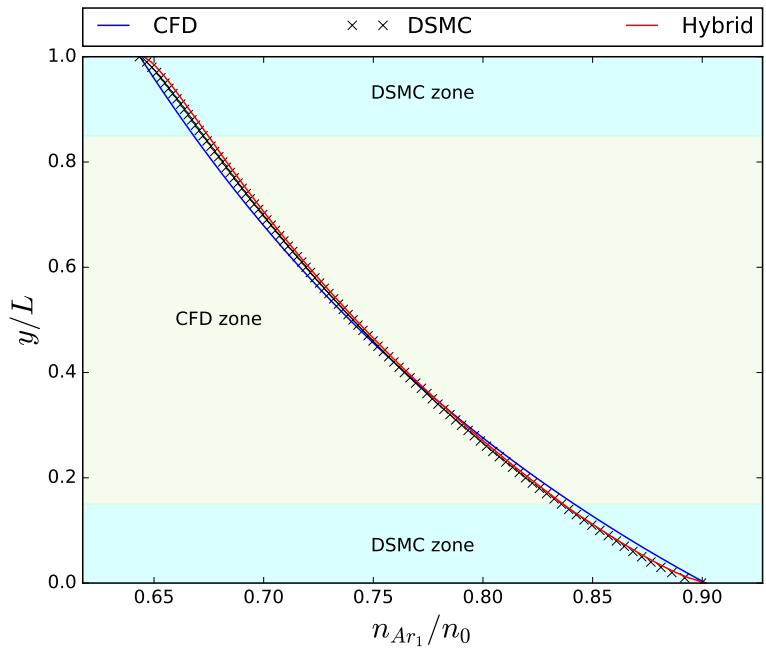


Figure 4.20: Number density comparison, for an  $Ar - Ar$  mixture,  $Ar_1$

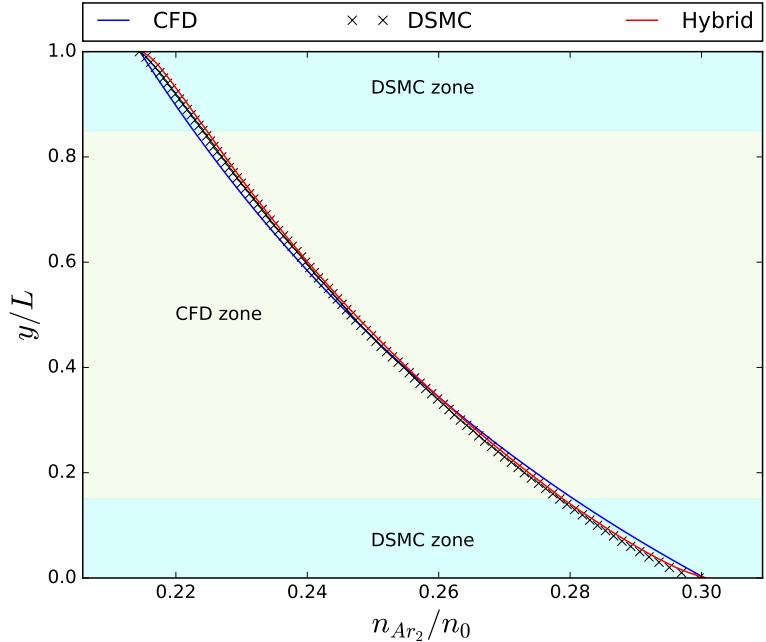


Figure 4.21: Number density comparison, for an  $Ar - Ar$  mixture,  $Ar_2$

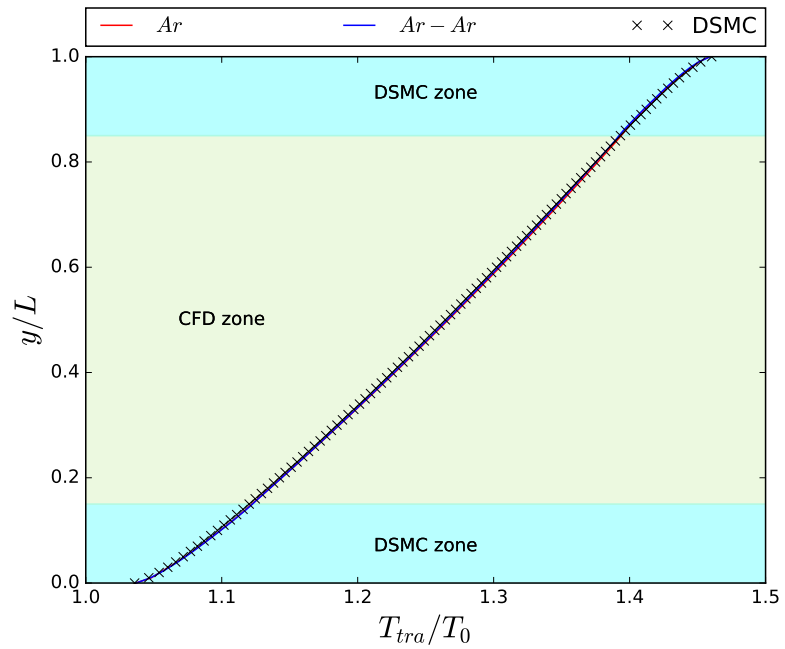


Figure 4.22: Comparison between *Ar* and *Ar – Ar* gas mixture, for translational temperature

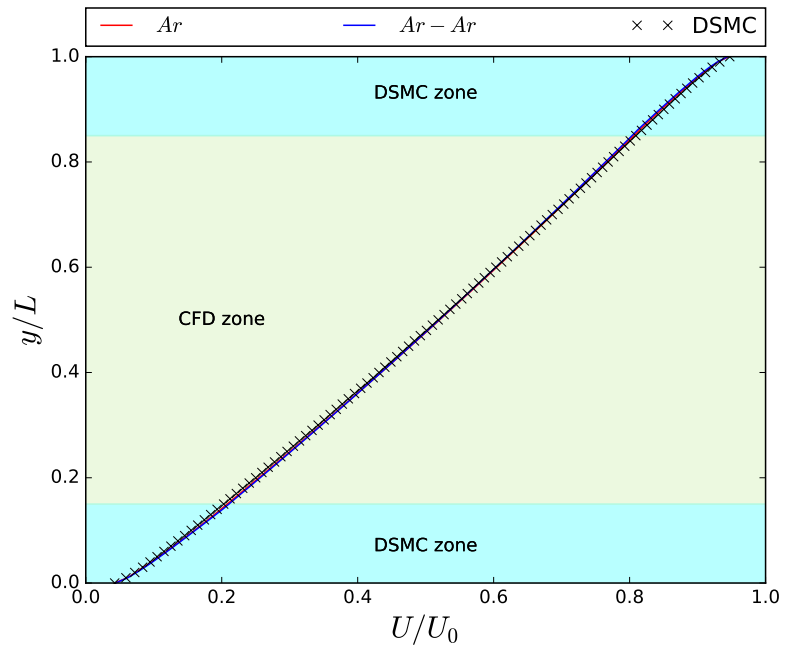


Figure 4.23: Comparison between *Ar* and *Ar – Ar* gas mixture, for velocity

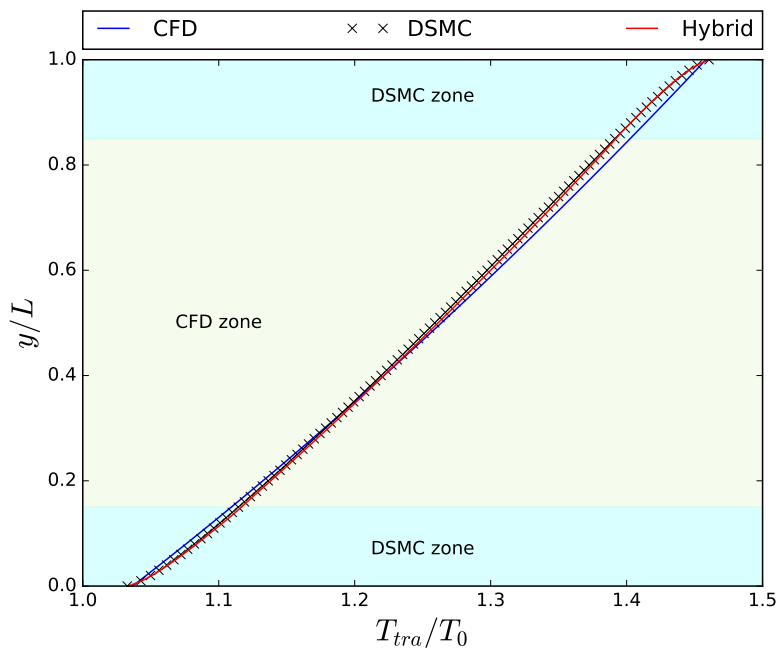


Figure 4.24: Translational temperature comparison, for a  $N - O$  mixture

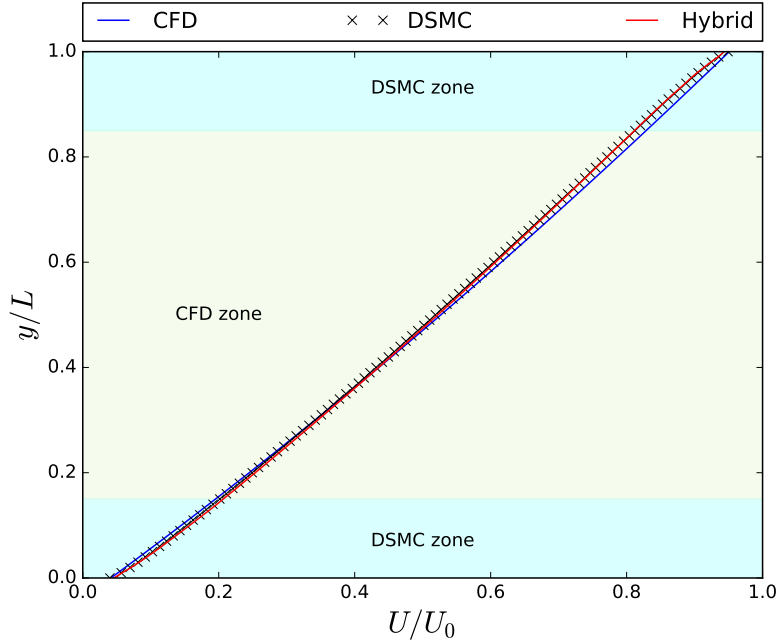


Figure 4.25: Velocity comparison, for a  $N - O$  mixture

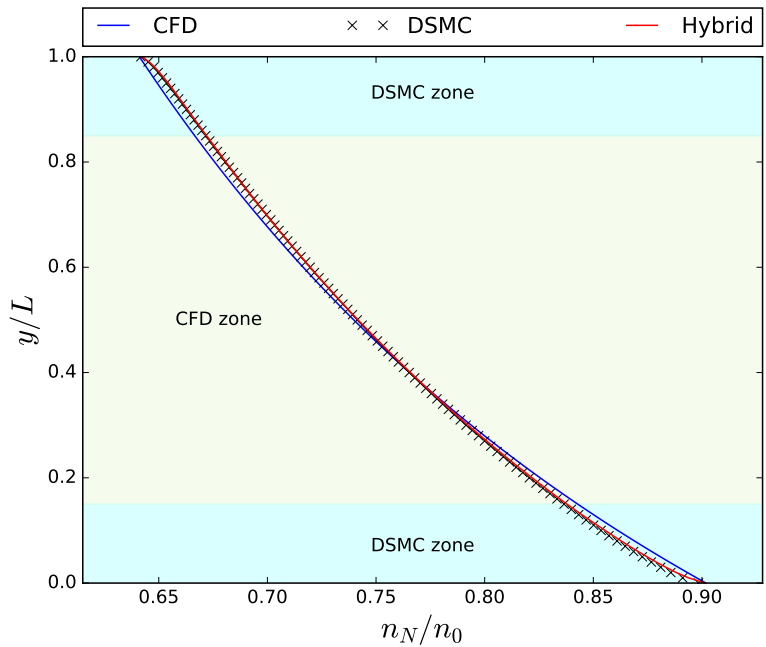


Figure 4.26: Number density comparison, for a  $N - O$  mixture,  $N$

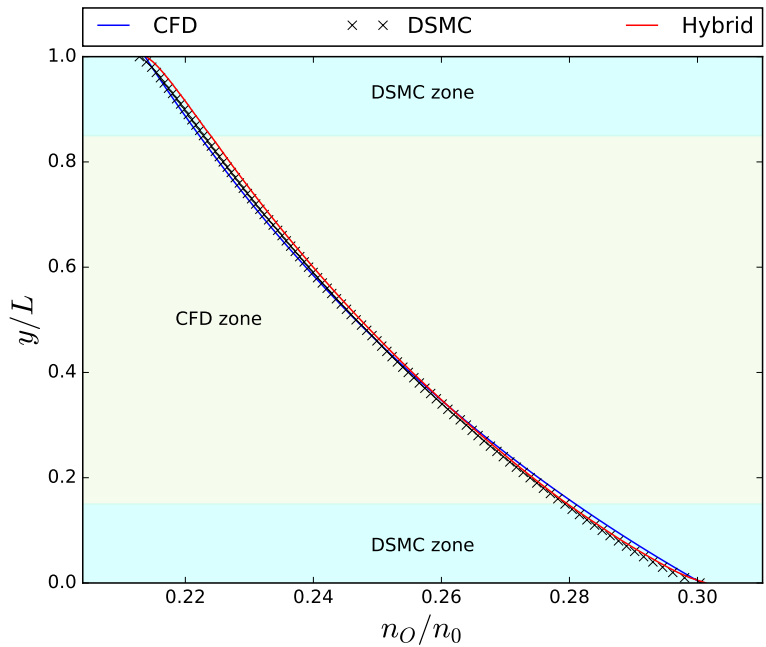


Figure 4.27: Number density comparison, for a  $N - O$  mixture,  $O$

#### 4.2.6 Vibrationless Nitrogen and Oxygen

A vibrationless mixture of two diatomic molecules has also been simulated, using  $N_2$  and  $O_2$  in 79% and 21% respectively, as they are found in air. Transrotational temperature and velocity results from the hybrid solver agree fairly well with the solution obtained by *dsmcFoam*, and this can be seen in Figures 4.28 and 4.29. Good agreement can also be seen in the number density plots in Figures 4.30 and 4.31.

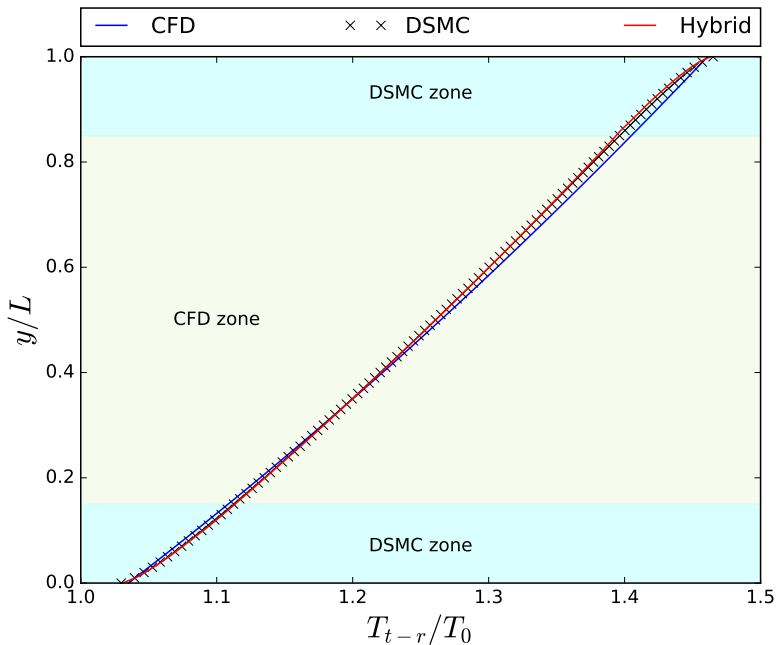


Figure 4.28: Transrotational temperature comparison, for a vibrationless  $N_2 - O_2$  mixture

#### 4.2.7 Molecular Nitrogen and Oxygen

As the last test case for the Couette flow, a  $N_2 - O_2$  gas mixture has been simulated, with the same 79% – 21% configuration as with the vibrationless case. Good correspondence can be seen between the hybrid and DSMC solver for transrotational and vibrational temperatures, as well as velocity, as can be seen in Figures 4.32 to 4.35. Taking a look at the number density comparisons in Figures 4.36 and 4.37, it can be seen that whereas the number density of  $N_2$  for the hybrid solver is sufficiently accurate

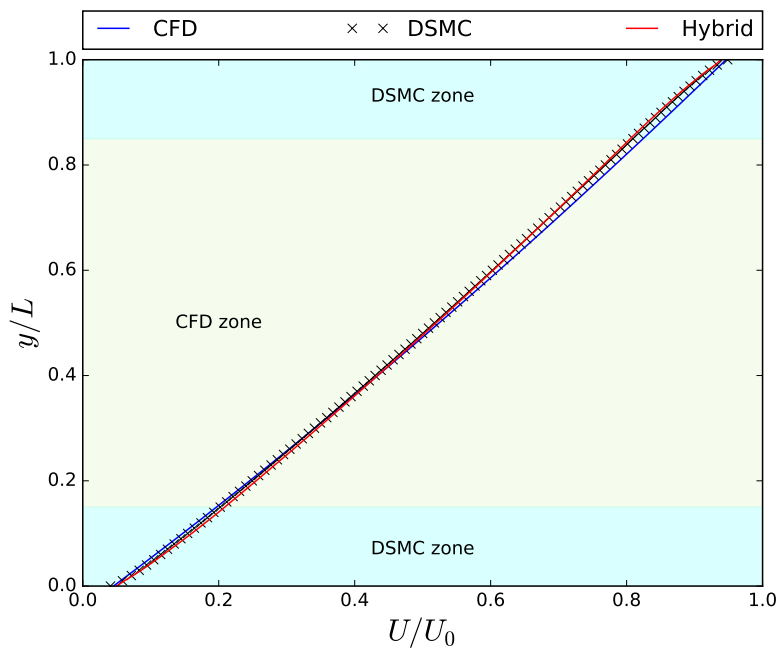


Figure 4.29: Velocity comparison, for a vibrationless  $N_2 - O_2$  mixture

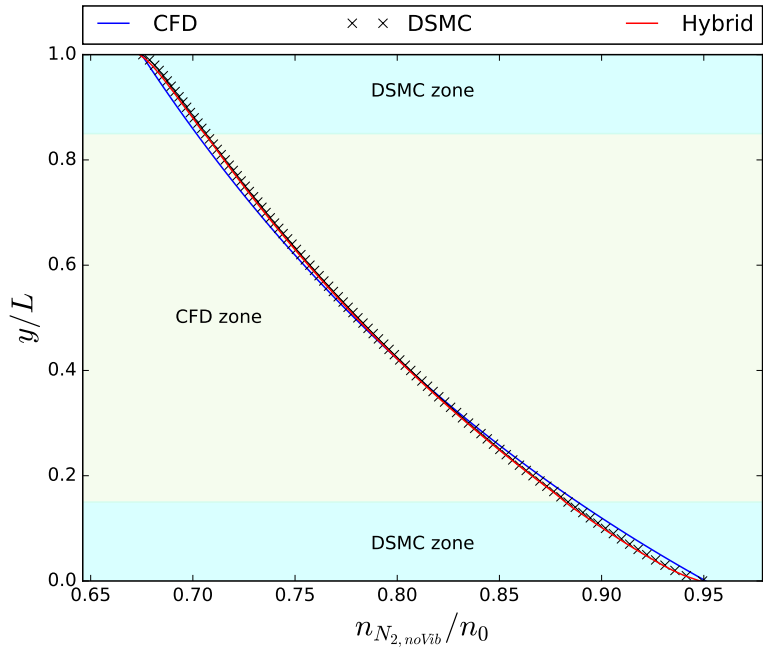


Figure 4.30: Number density comparison, for a vibrationless  $N_2 - O_2$  mixture,  $N_2$

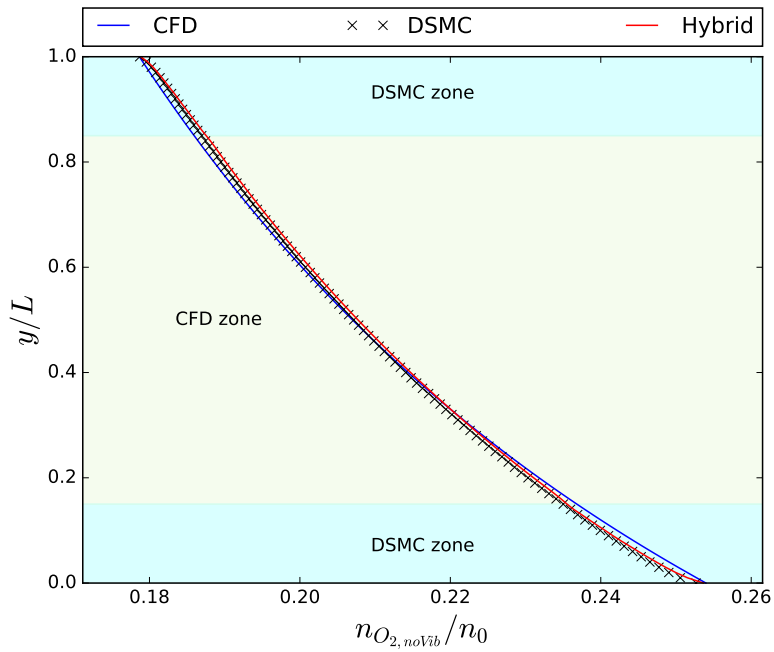


Figure 4.31: Number density comparison, for a vibrationless  $N_2 - O_2$  mixture,  $O_2$

with respect to the DSMC results, the  $O_2$  profile differs from the DSMC number density plot more than usual. The fact that this difference can be identified in this case but not in the vibrationless  $N_2 - O_2$  mixture indicates that this may have to do with how the solvers model the vibrational temperature and the translational-vibrational temperature exchanges. The quantum Q-K model from DSMC and the Millikan-White-Park CFD model are not completely consistent with each other. As such, it is expected that a new implementation that matches both CFD and DSMC energy transfer more accurately can reduce, or even negate, these effects. For this reason, vibrationless simulations are still of interest, and will be included in the hypersonic cylinder test cases.

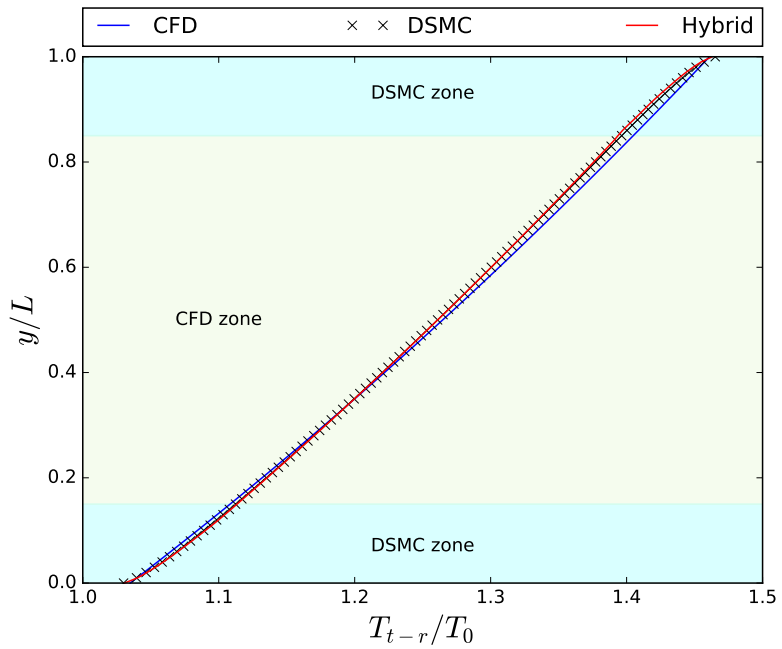


Figure 4.32: Transrotational temperature comparison, for a  $N_2 - O_2$  mixture

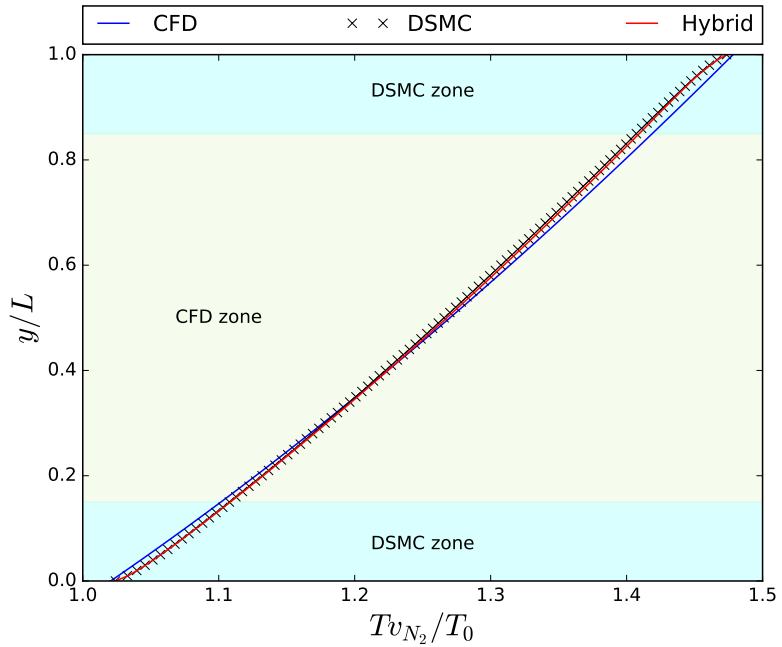


Figure 4.33: Vibrational temperature comparison, for a  $N_2 - O_2$  mixture,  $N_2$

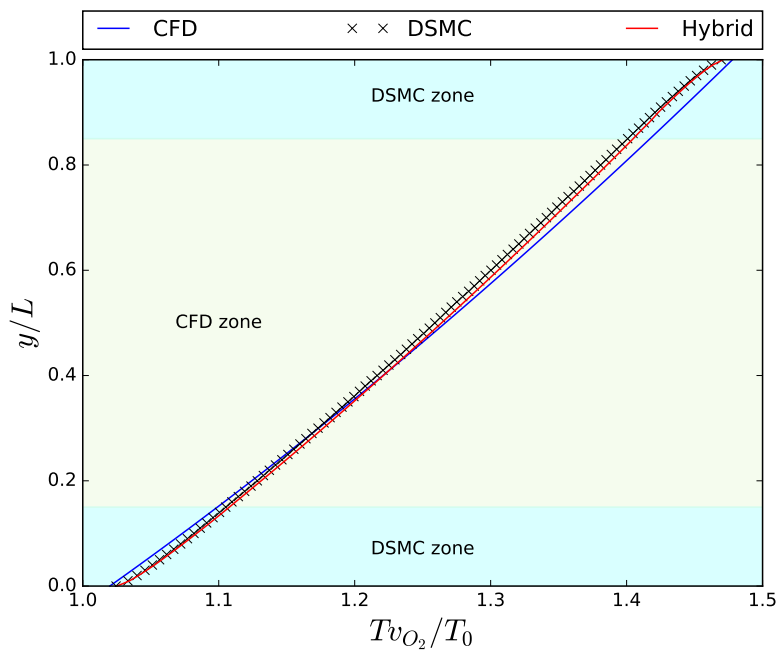


Figure 4.34: Vibrational temperature comparison, for a  $N_2 - O_2$  mixture,  $O_2$

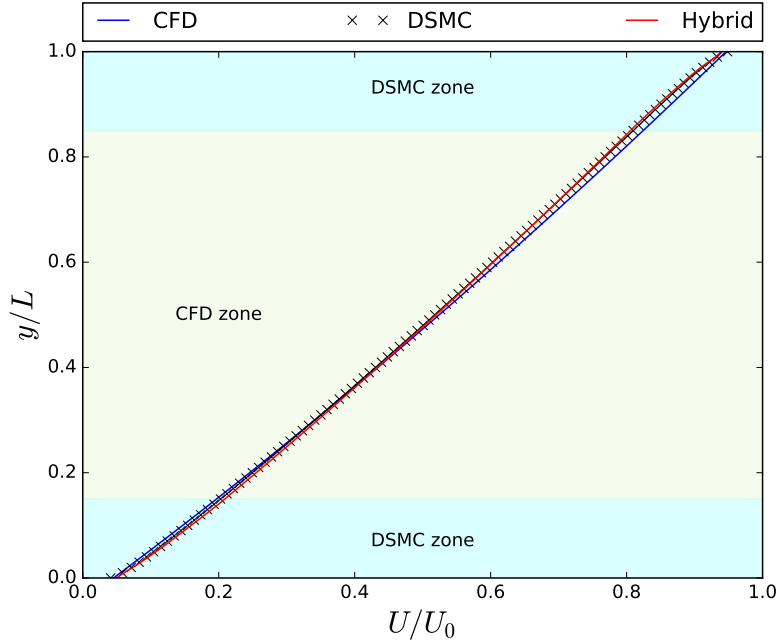


Figure 4.35: Velocity comparison, for a  $N_2 - O_2$  mixture

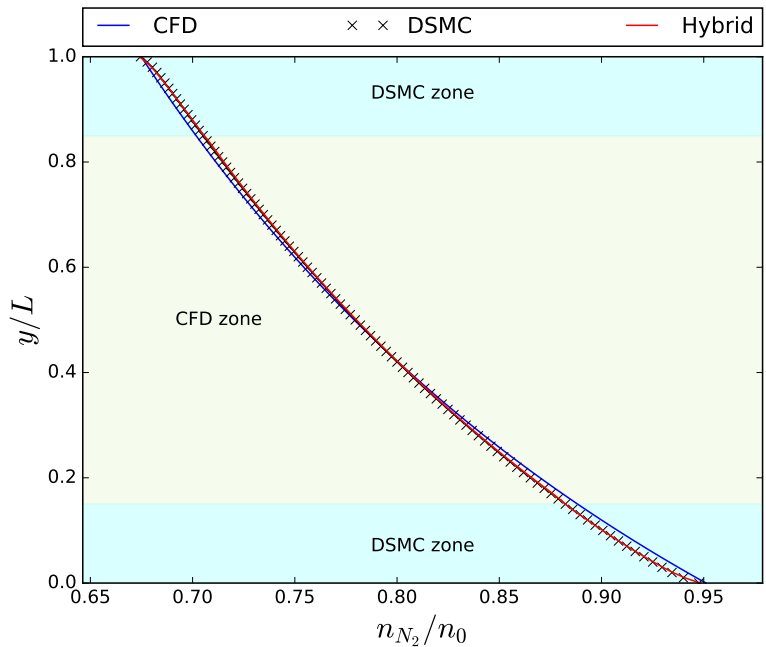


Figure 4.36: Number density comparison, for a  $N_2 - O_2$  mixture,  $N_2$

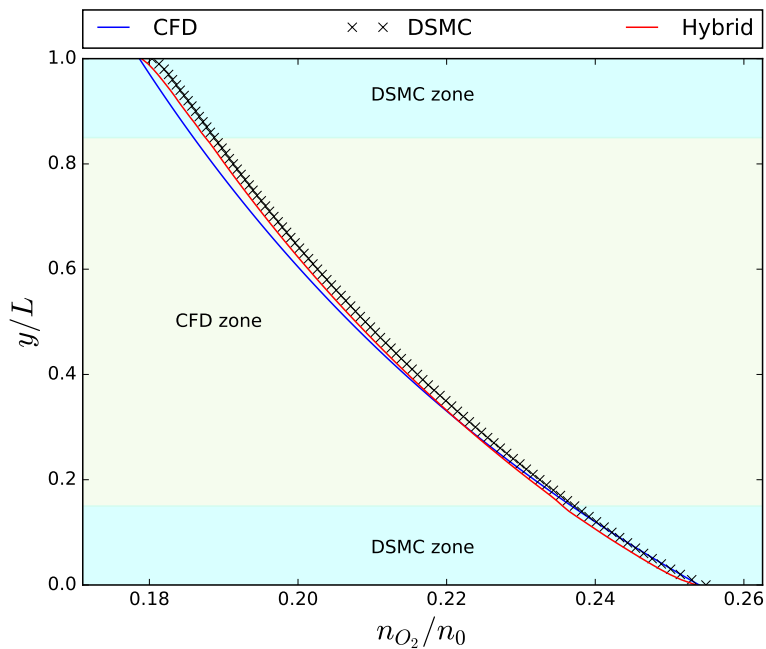


Figure 4.37: Number density comparison, for a  $N_2 - O_2$  mixture,  $O_2$

# Chapter 5

## Hypersonic cylinder

Further validation is required in order to assess the full capabilities of the hybrid solver, both in terms of accuracy and computational time. A hypersonic cylinder has been included for this purpose. This simulation takes into account not only a shock wave which thickness heavily depends on the local mean free path, but also a Knudsen layer around the cylinder that can provide the wrong surface properties if it is not properly captured. Finally, the correct capture of the properties in the wake region is of great importance, as this would affect any other object downstream. Section 5.1 establishes the computational domain of the simulation, common to all of the configurations. Section 5.2 details the results of a simulation with vibrationless  $N_2$ , which would be the simplest case in this analysis. Section 5.3 shows the effects of having a multispecies gas mixture on the simulation. Both species lack vibrational capabilities for simplicity. Finally, in Section 5.4 the effects of vibrational energy modes are studied by using molecular  $O_2$  as the gas species.

### 5.1 Computational domain

The domain of the simulation has been defined in the proximity of a cylinder with a 0.04 cm radius. Only the top half of the domain needs to be considered, thanks to the symmetry of the geometry and initial and boundary conditions. Whereas the exact

values of the boundary conditions are case dependent, and will be detailed in each of them, all of these test cases present a similar configuration that can be seen in Figure 5.1.

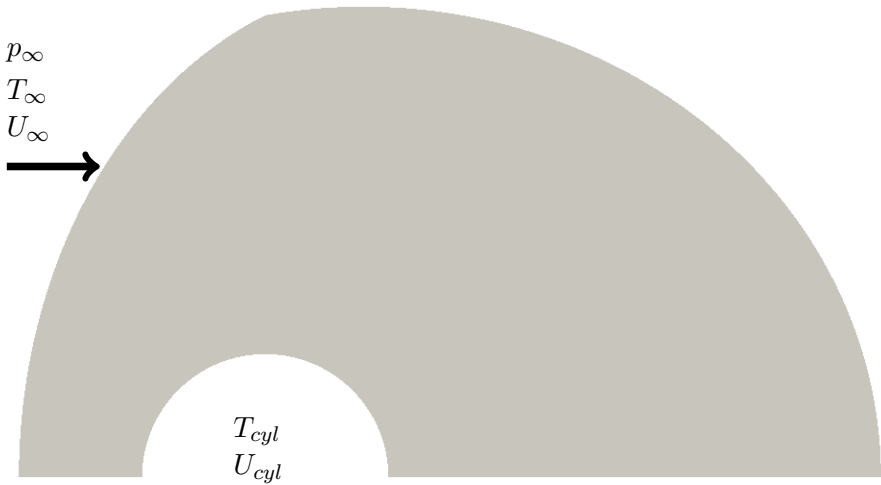


Figure 5.1: Hypersonic cylinder domain and boundary conditions

## 5.2 Vibrationless $N_2$

This test case has been taken from Ref. [47], case **M6**. The gas used for this simulation is nitrogen, without considering energy transfer to vibrational modes. The freestream flow travels at Mach 6, with a temperature of 217.45 K and a number density of  $1.61 \cdot 10^{21}$  particles/m<sup>3</sup>. These conditions translate to a pressure of 4.8336 Pa, a velocity of 1803.9 m/s, and a Knudsen number based on the cylinder diameter of 0.01, using the VHS model for the mean free path. The cylinder wall is stationary and at a fixed temperature of 500 K.

Initially,  $Kn_{GLL}$  had been the breakdown criterion used for the identification of the different domains. However, due to some poor results in the cylinder surface, the  $Kn_{breakdown}$  criterion was also studied. At present, the hybrid solver lacks an algorithm that would allow for a reasonably inexpensive update of the domains. For this

reason, results using these two breakdown criteria are analysed without recalculating the initial domain partitions. Nonetheless, this simulation has also been performed using the  $Kn_{breakdown}$  criterion on the final DSMC solution to identify the different domains (called  $Kn_{DSMC}$  from now own), as a proof of concept for when the updating algorithm is properly implemented. Regardless of how the domains had been determined for these three hybrid simulations, all of them have been initialised using the results from the CFD simulations. The different domains can be seen in Figure 5.2. On the left, the  $Kn_{GLL}$  and  $Kn_{breakdown}$  domains are compared, and it can be observed that for the  $Kn_{GLL}$  criterion only a few cells around the cylinder are considered to be in non-equilibrium, specially near the stagnation point. In addition, a great portion of the wake is also identified as continuum using the  $Kn_{GLL}$  criterion. On the right half of figure 5.2, the  $Kn_{breakdown}$  criterion domain decomposition is compared with the domains obtained from  $Kn_{DSMC}$ . Whereas  $Kn_{GLL}$  and  $Kn_{breakdown}$  portray a similar determination of non-equilibrium cells in the shock region, the  $Kn_{DSMC}$  non-equilibrium cells at the shock is quite wider than the DSMC domain the other two generate. This is mainly due to the difference between translational and rotational temperatures in the DSMC solution. Schwartzenruber recommends to also consider a cell as belonging to the DSMC domain when the translational temperature is at least 1% higher than the rotational temperature [47]. These temperatures are calculated as one and the same in the CFD solver, therefore the  $Kn_{GLL}$  and  $Kn_{breakdown}$  criteria cannot identify a priori any new cells using this new condition. The difference in CFD and DSMC regions between these three domain decompositions is responsible for the difference in the results that will be seen in the following Figures.

Figures 5.3 to 5.5 show a contour plot comparison between the CFD and hybrid solvers (top half of the image) with the DSMC results (bottom half), for pressure, transrotational temperature, and velocity. The isocontour lines show a big difference between the CFD and DSMC results, as expected. Regarding the hybrid solver solutions,  $Kn_{breakdown}$  appears to have better agreement with the DSMC solution than  $Kn_{GLL}$  in the near-wake region, but seems to behave slightly worse after the shock.

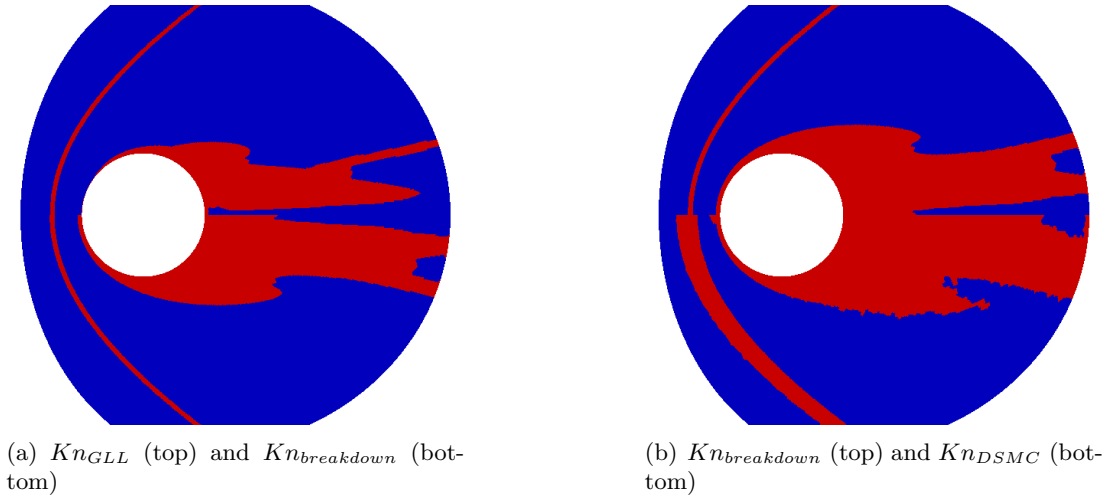


Figure 5.2: Hypersonic cylinder CFD (in blue) and DSMC (in red) zones for different criteria,  $N_2$  case.

The CFD and the aforementioned hybrid solutions all fail to fully capture the thickening of the shock due to rarefied effects and thus the contour lines before the shock do not match those from the DSMC solution. On the other hand, hybrid results from the  $Kn_{DSMC}$  case show a great agreement with the DSMC solution, which indicates that with the right domain decomposition the quality of the hybrid results is comparable to those from the DSMC simulation.

Figures 5.6 to 5.8 show the density, transrotational temperature, and velocity comparison between the solvers along the stagnation line. The rarefied regions for the three hybrid cases are also indicated. Whereas the DSMC region is bigger for the  $Kn_{breakdown}$  case, a greater error than the  $Kn_{GLL}$  case can be distinguished, specially on the temperature plot, in the CFD region between the shock and near-body DSMC regions, although better concordance can be seen in the near-body region for the former case. The DSMC domain for the  $Kn_{breakdown}$  simulation extends longer near the cylinder, and thus the hybrid solution follows the DSMC results with better agreement in this area. However, as the  $Kn_{DSMC}$  domains show, the continuum-rarefied interface for the  $Kn_{breakdown}$  scenario is located still in what should be part of the DSMC region, so the continuum solver is unable to accurately predict the behaviour in what should be a non-

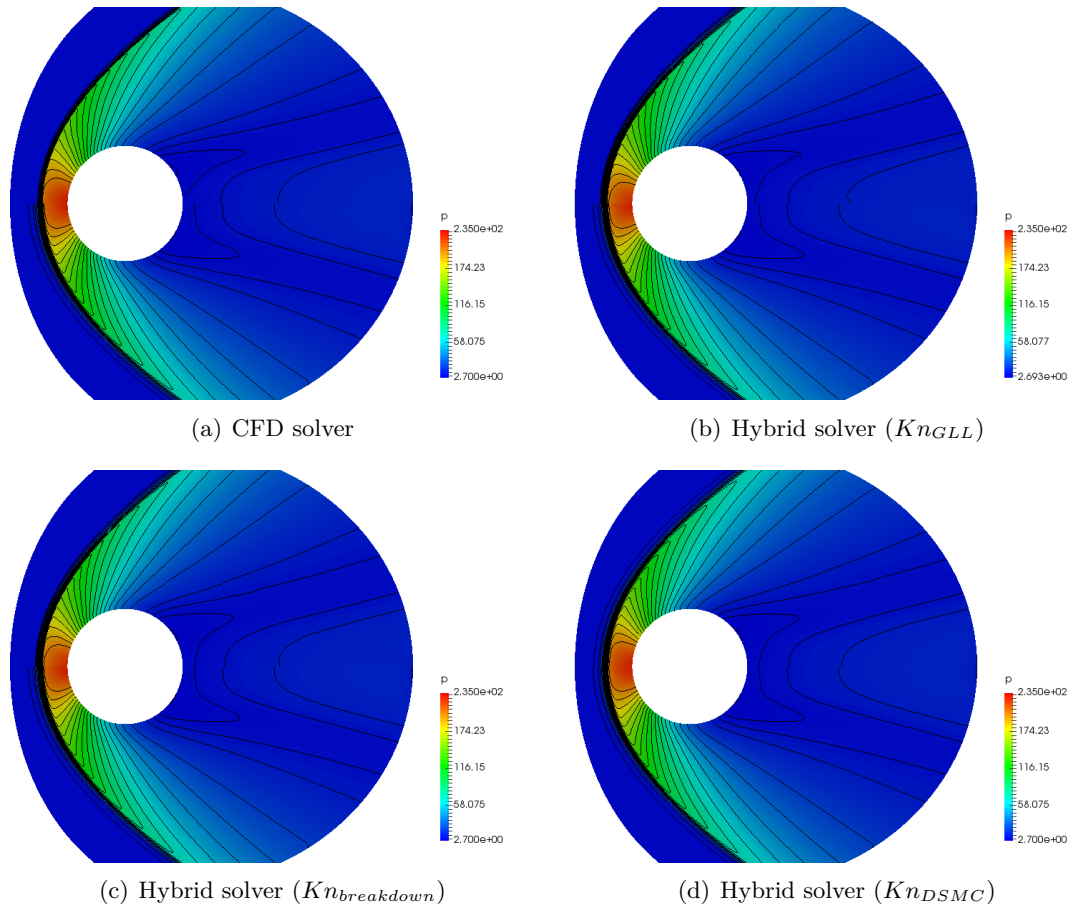


Figure 5.3: Pressure contour comparison, in  $Pa$ , between the DSMC solver (bottom half) and other solvers (top half),  $N_2$  case.

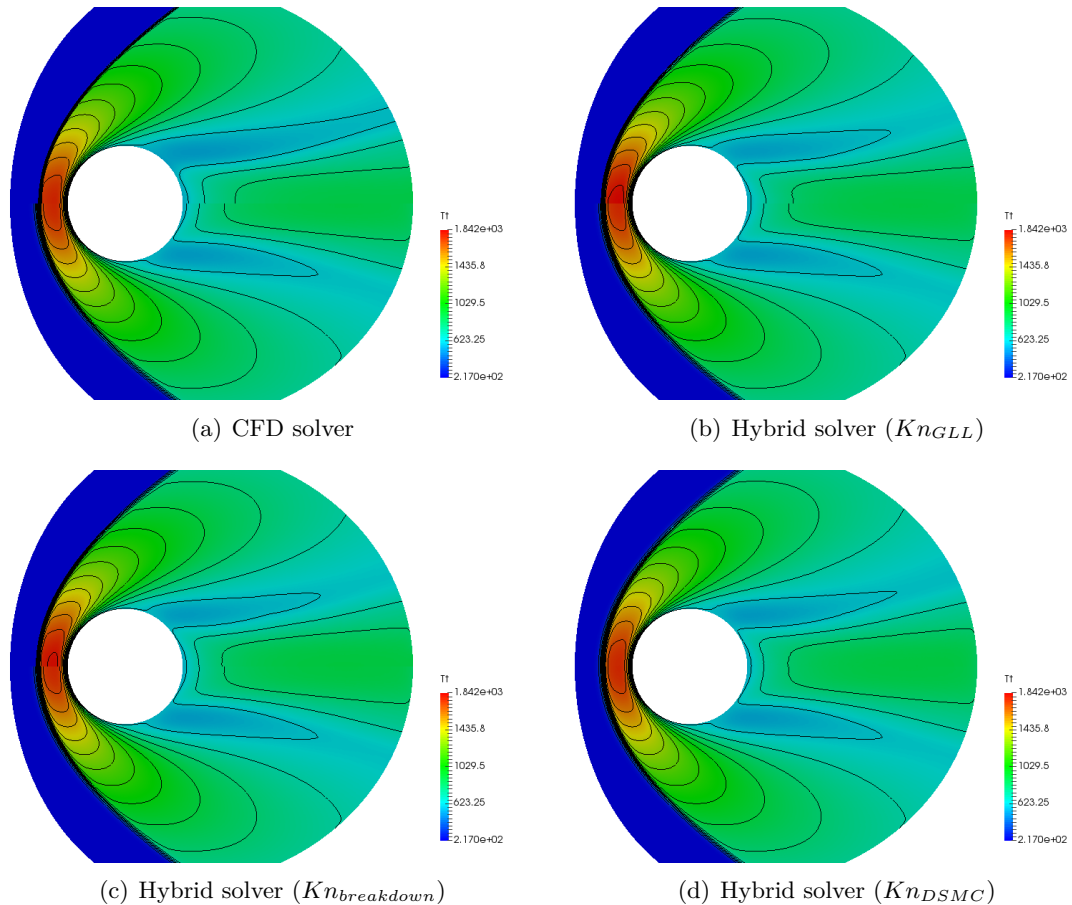


Figure 5.4: Transrotational temperature contour comparison, in  $K$ , between the DSMC solver (bottom half) and other solvers (top half),  $N_2$  case.

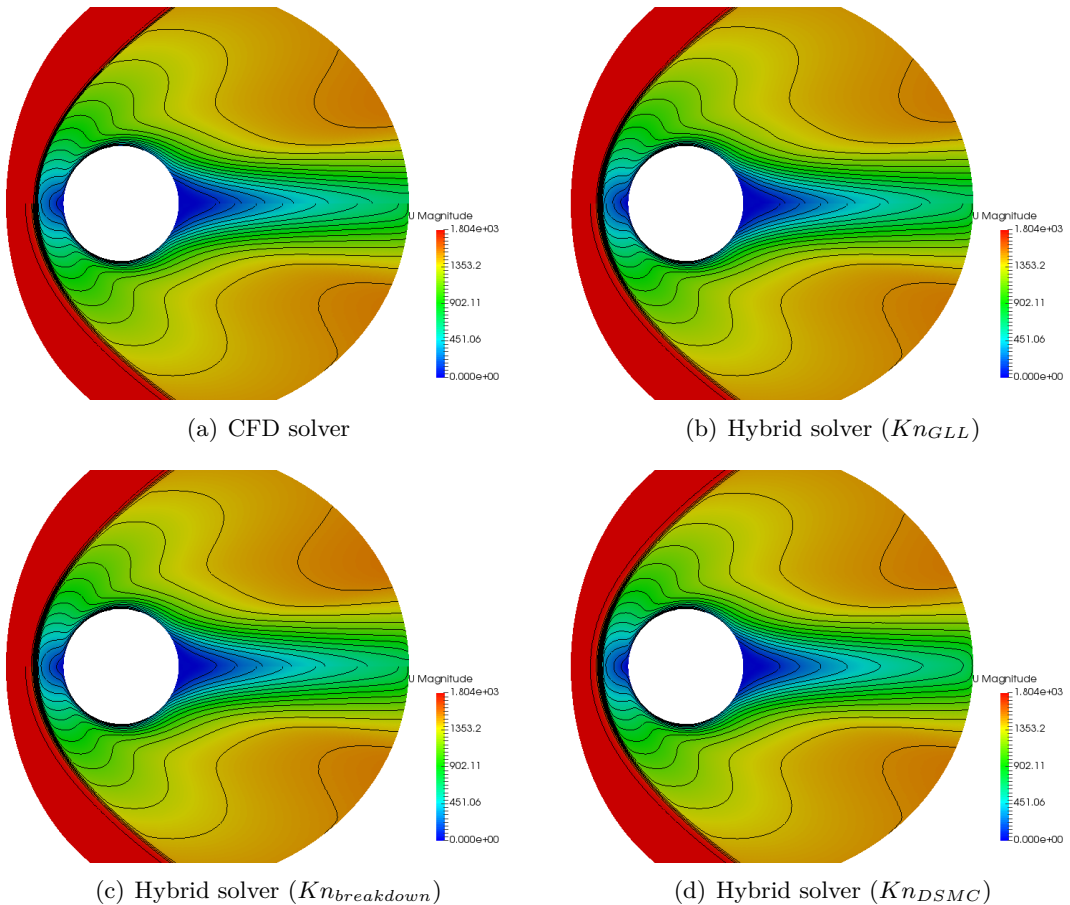


Figure 5.5: Velocity magnitude contour comparison, in  $m/s$ , between the DSMC solver (bottom half) and other solvers (top half),  $N_2$  case.

equilibrium region, leading to this error. The CFD solver, on the other hand, returns by itself a reasonable solution in that region. This is why the  $Kn_{GLL}$  case, presenting only a handful of non-equilibrium cells at the cylinder boundary, has a wider area to adapt this CFD solution and provide more accurate post-shock estimations. The effect that a misplaced interface can have on the global solution have been previously observed specially on 1D shockwaves [47]. When the regions are correctly determined and thus the interfaces are located in an equilibrium region, the continuum and rarefied solvers reach the same value with similar gradients and thus the hybrid solution match the DSMC solution almost perfectly, as can be observed from the  $Kn_{DSMC}$  case.

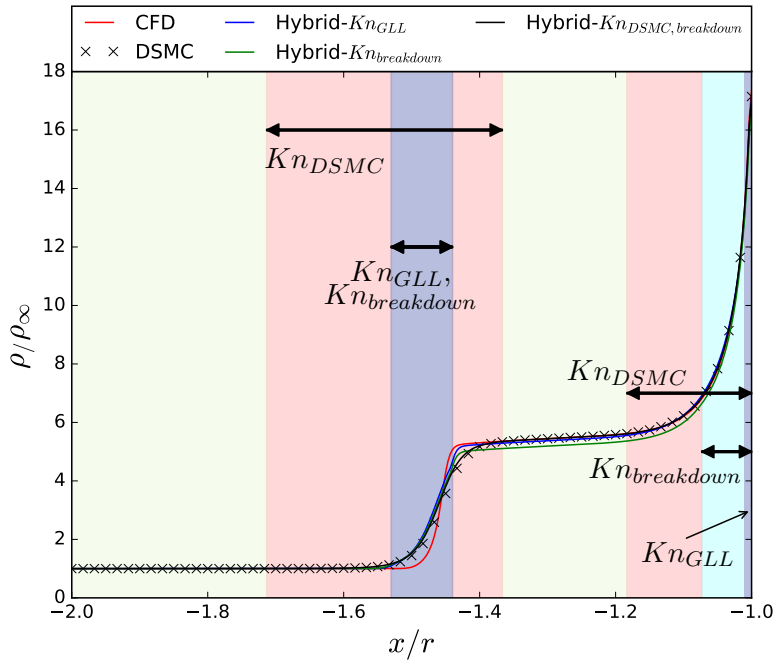


Figure 5.6: Density plot along the stagnation line,  $N_2$  case.

The accuracy of the different solvers in the wake along the symmetry plane can be observed in Figures 5.9 to 5.11, where density, temperature and velocity are compared. Similarly to the region near the stagnation point, the  $Kn_{breakdown}$  case present a wider rarefied domain just after the cylinder. This case presents more accurate results than the  $Kn_{GLL}$  case when compared to the DSMC values while in this region. After it,

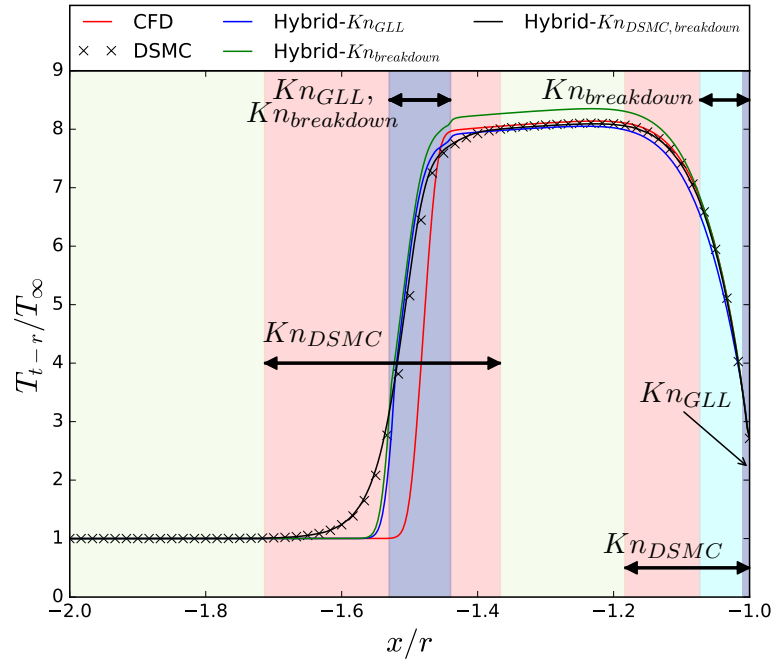


Figure 5.7: Transrotational temperature plot along the stagnation line,  $N_2$  case.

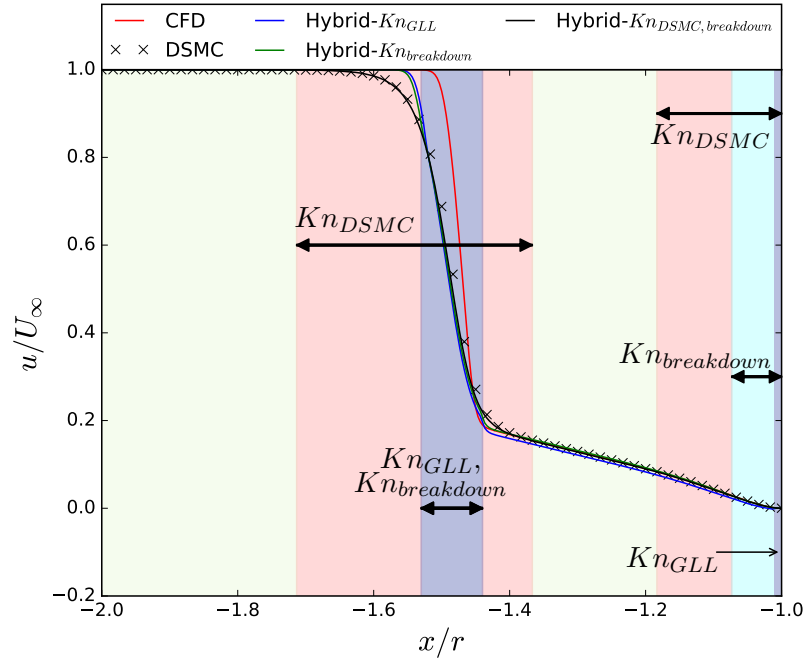


Figure 5.8: Velocity plot along the stagnation line,  $N_2$  case.

however, the  $Kn_{breakdown}$  separates from the DSMC solution. It can be appreciated that in this continuum portion of the domain, whereas the  $Kn_{GLL}$  criterion follows the DSMC profile more closely for density, it is  $Kn_{breakdown}$  which matches better for temperature, and both behave similarly for velocity. On the other hand, the hybrid solution using the  $Kn_{DSMC}$  criterion matches the DSMC solution with great precision. It is important to note the sudden change in properties at the end of the domain for both the DSMC and the  $Kn_{DSMC}$  solutions, which occurs due to the vacuum boundary condition. As the Mach number in this region should be around 1.1, some simulators should still enter the domain from that boundary, and failure to take these particles into account lead to the shown results. However, this region is far enough away and does not influence the results near the cylinder. This phenomenon will be found in the other cases as well.

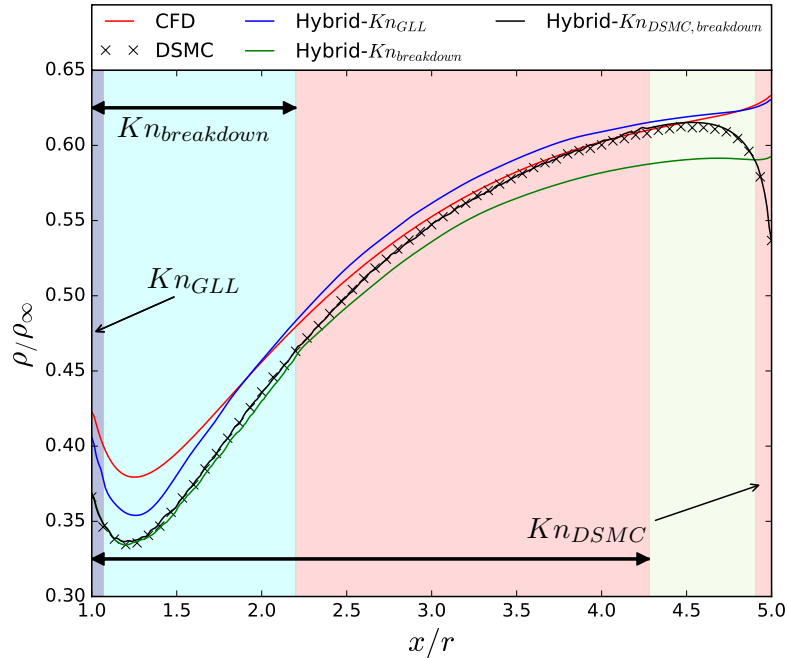


Figure 5.9: Density plot along the symmetry plane, in the wake.  $N_2$  case.

To finish the accuracy comparisons, results at the surface of the cylinder can be seen in Figures 5.12 to 5.16, where all of the cylinder belongs to the DSMC region. In partic-

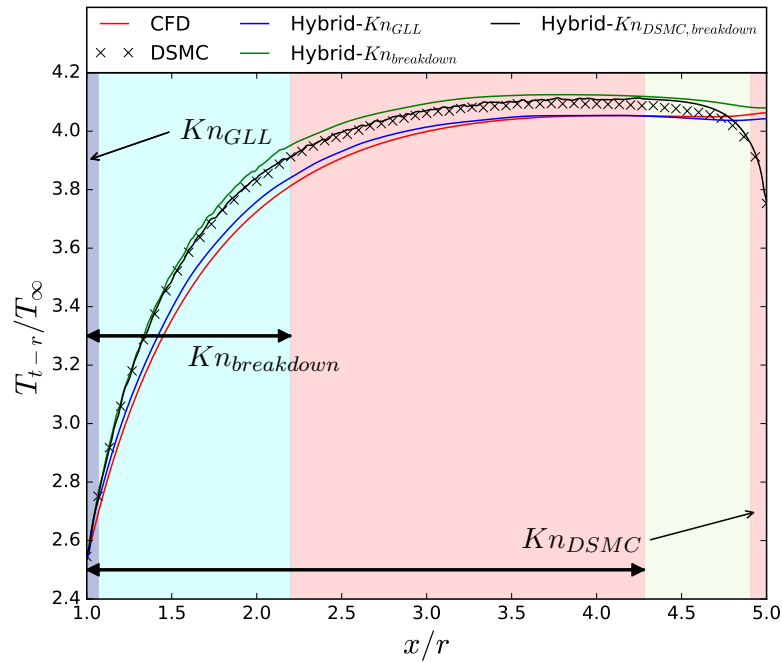


Figure 5.10: Transrotational temperature plot along the symmetry plane, in the wake.  $N_2$  case.

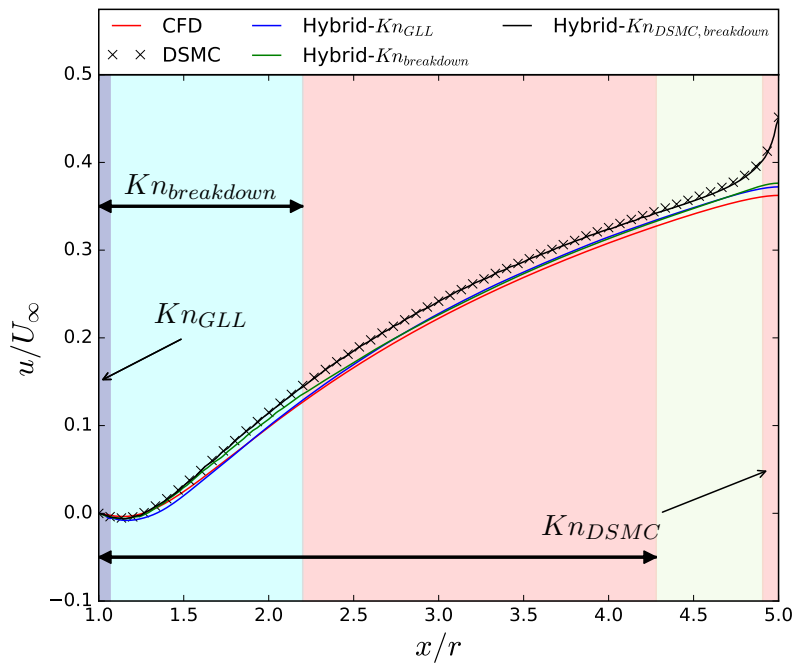


Figure 5.11: Velocity plot along the symmetry plane, in the wake.  $N_2$  case.

ular, Figures 5.12 and 5.13 show the accuracy of the slip conditions. It can be observed that both the temperature jump and the velocity slip cannot be accurately represented for this phenomenon. The hybrid solution on the other hand matches significantly well with the DSMC plots for all three cases, showing that due to this Knudsen layer next to the body the results are better captured when considering non-equilibrium effects. Figures 5.14 to 5.16 show the pressure ( $c_p$ ), friction( $c_f$ ), and heat transfer ( $c_q$ ) coefficients respectively. Both  $Kn_{GLL}$  and  $Kn_{breakdown}$  behave similarly for these three magnitudes as well, underpredicting the  $c_p$  at the stagnation point and overpredicting the  $c_q$  in the same location. It is important to note that the  $Kn_{GLL}$  case presents a higher error on the  $c_q$ , whereas the  $Kn_{breakdown}$  error is comparable to the CFD solution. Further along on the cylinder and away from the stagnation point, both hybrid cases match the DSMC profiles quite well. Following the same behaviour that has been observed so far, the  $Kn_{DSMC}$  case show the most accurate results. One fundamental observation, however, is that the CFD solver show quite reasonable agreement for  $c_p$  and  $c_q$ .

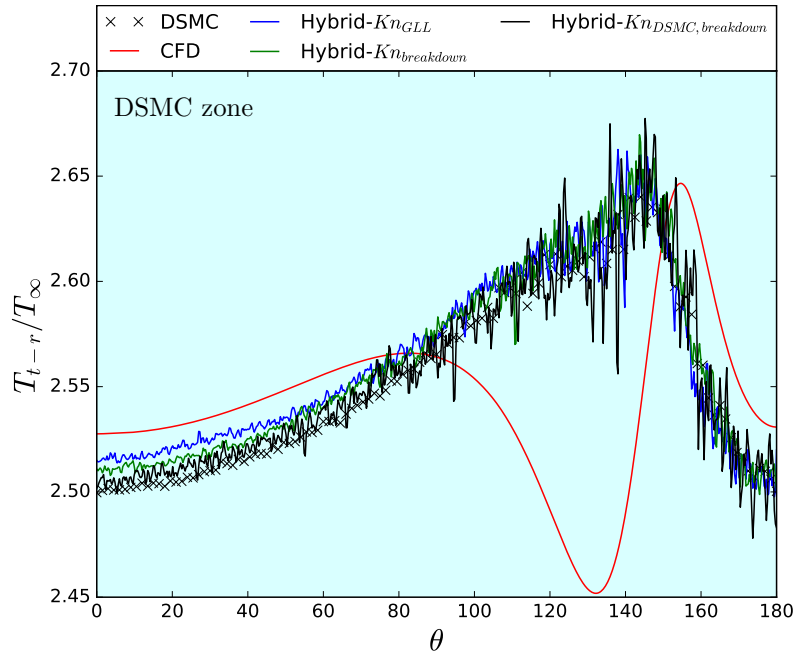
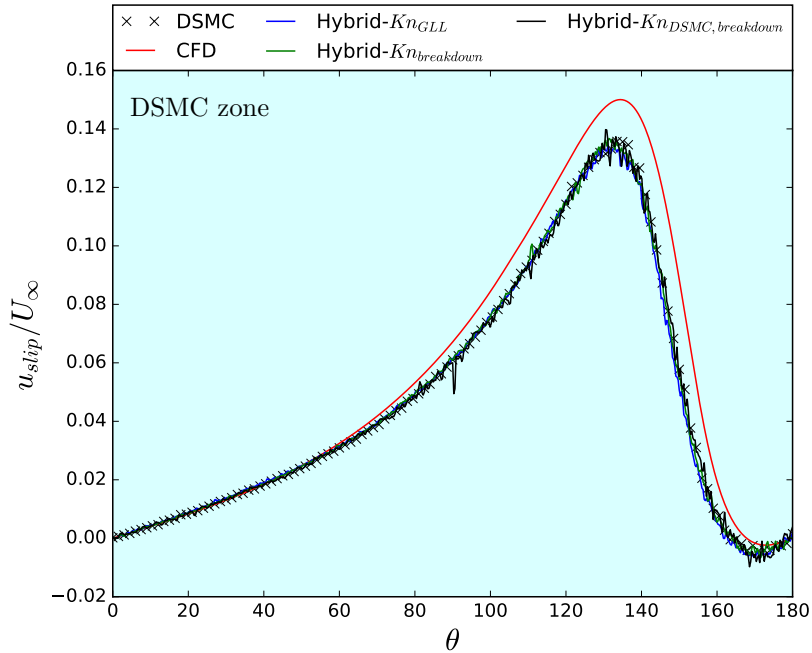


Figure 5.12: Transrotational temperature plot along the cylinder surface,  $N_2$  case.


 Figure 5.13: Slip velocity plot along the cylinder surface,  $N_2$  case.

Finally, Table 5.1 shows the computational resources needed for all the solvers. It is important to note that the individual time per iteration has been obtained by using the average for a 10-iteration simulation using a single processor. In addition, the final times for the hybrid cases include the time of the CFD simulation as well, which provides the initial state for the hybrid algorithm. As expected, the CFD solutions are significantly faster than the DSMC approach due to its multiple simplifications. For the hybrid cases, it can be seen that the speedup decreases accordingly to the size of the DSMC domain, from a value of 2.51 for the  $Kn_{GLL}$  case to a still reasonable but not as good 1.8 for the  $Kn_{DSMC}$  criterion. It would be expected, however, that during a run-time domain modification simulation, the DSMC region would be increasing in size from the initial domain from  $Kn_{breakdown}$  to the final domains of  $Kn_{DSMC}$ , which would situate the speedup between the 1.8 and 2.27 values obtained during this study.

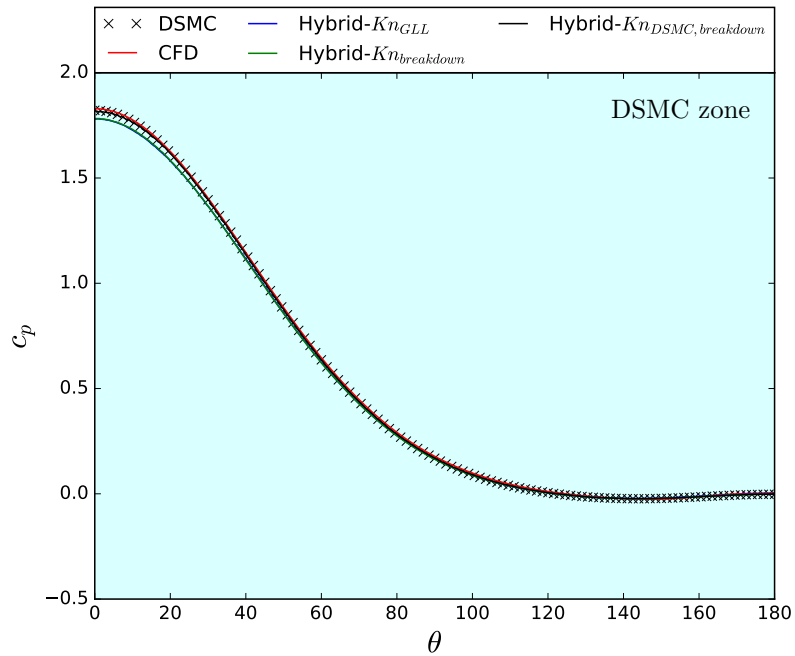


Figure 5.14: Pressure coefficient plot along the cylinder surface,  $N_2$  case.

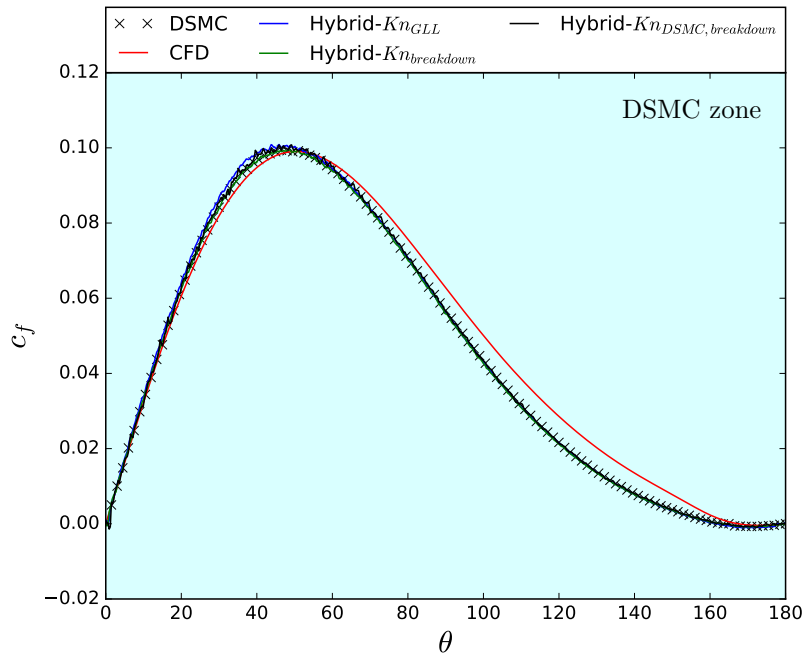
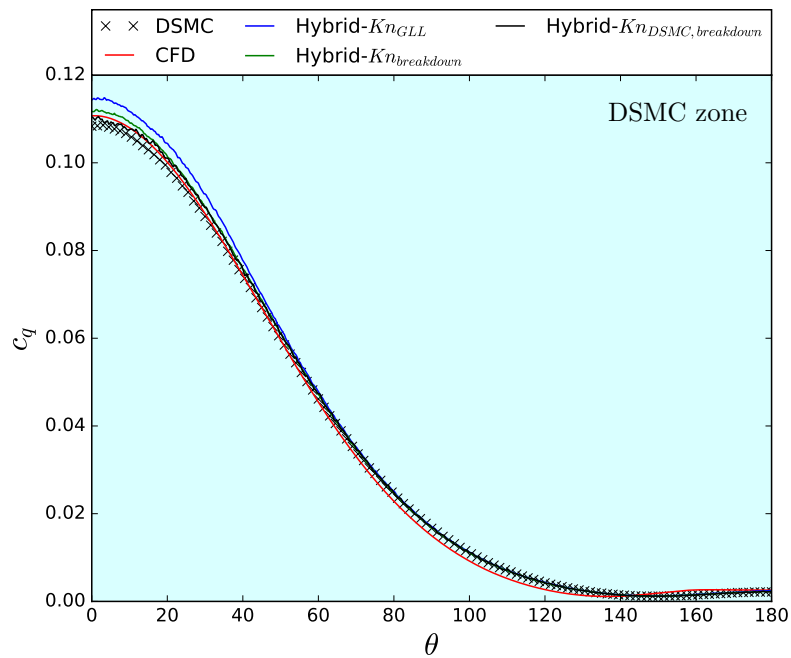


Figure 5.15: Friction coefficient plot along the cylinder surface,  $N_2$  case.


 Figure 5.16: Heat transfer coefficient plot along the cylinder surface,  $N_2$  case.

	DSMC	CFD	Hybrid					
			$Kn_{GLL}$		$Kn_{breakdown}$		$Kn_{DSMC}$	
			CFD	DSMC	CFD	DSMC	CFD	DSMC
Seconds per it.	4.2525	0.8950	1.3750	1.1725	1.4325	1.3363	1.4425	1.8243
n° it.	$1 \cdot 10^6$	$2 \cdot 10^5$	$2.5 \cdot 10^5$	$1 \cdot 10^6$	$2.5 \cdot 10^5$	$1 \cdot 10^6$	$2.5 \cdot 10^5$	$1 \cdot 10^6$
Total time	1181h 15min	49h 43min	470h 54min		520h 13min		656h 55min	
Speedup	-	23.76	2.51		2.27		1.80	

 Table 5.1: Time comparison among the different solvers,  $N_2$  case

### 5.3 Vibrationless $N_2 - O_2$

The idea behind this test case is to analyse the multispecies capabilities of *hyperFoam*. The gas used for this simulation is a mixture of 29%  $O_2$ , 71%  $N_2$  to try to emulate air, without considering energy transfer to vibrational modes. Keeping the same freestream temperature, total number density, and velocity of 217.45 K,  $1.61 \cdot 10^{21}$  m<sup>-3</sup>, and 1803.9 m/s respectively, this returns a freestream Mach number of 6.09, less than a 1.5% increase from the  $N_2$  test case. Finally, the cylinder wall keeps its temperature and velocity of 500 K and 0 m/s respectively.

Similarly to the previous test case, the results from the domain decomposition for both  $Kn_{GLL}$  and  $Kn_{breakdown}$  criteria have been studied. These domains can be seen in Figure 5.17. In the same fashion than with the  $N_2$  case, the  $Kn_{breakdown}$  criterion identify more rarefied cells in the near-cylinder area than the  $Kn_{GLL}$  criteria, as well as in the wake, which will again be reflected in the results.

Figures 5.18 to 5.20 show the contour plot comparison for pressure, transrotational temperature, and velocity respectively. Following a similar trend, the solution in the wake are better represented by the  $Kn_{breakdown}$ , whereas the post-shock region is more accurately calculated using the  $Kn_{GLL}$  criterion. It can also be appreciated that neither of these two hybrid solutions, nor the CFD simulation, is capable of fully capturing the shock wave thickening, as neither of the hybrids cases extend enough their rarefied domains upstream of the shock.

The plots along the stagnation line, Figures 5.21 to 5.24, again show the better agreement for  $Kn_{breakdown}$  in the rarefied regions, but poor continuation of these results in the in-between continuum region, where both the CFD and the  $Kn_{GLL}$ -based hybrid solutions return a smaller error when compared with DSMC.

The  $Kn_{breakdown}$  region shows remarkable results in the rarefied region of the wake,

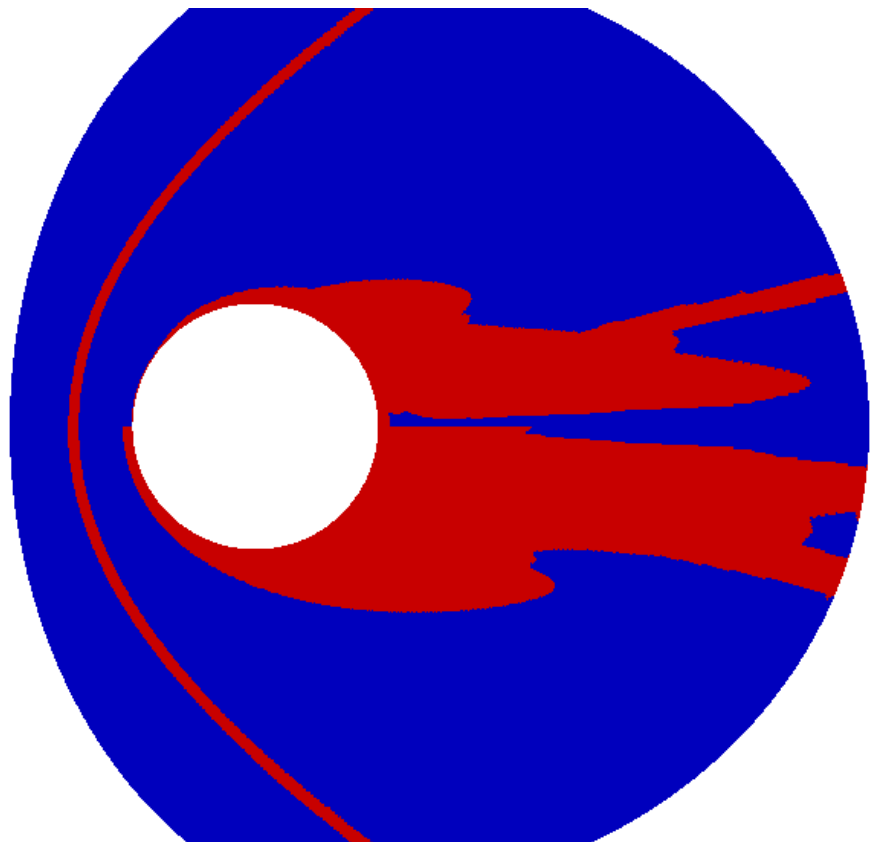


Figure 5.17: Hypersonic cylinder zones using  $Kn_{GLL}$  (top) and  $Kn_{breakdown}$  (bottom) as criteria,  $N_2 - O_2$  case.

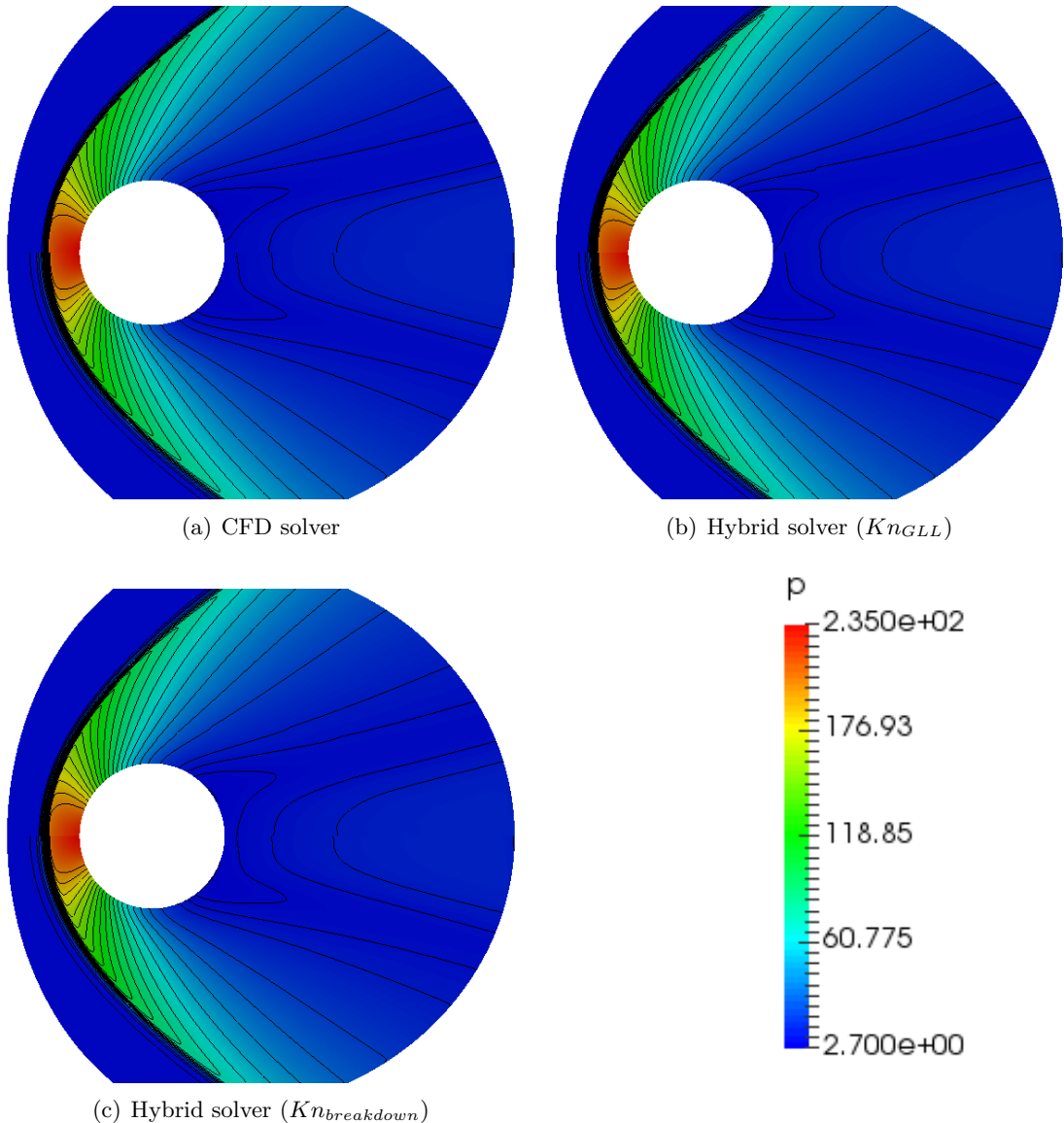


Figure 5.18: Pressure contour comparison, in  $Pa$ , between the DSMC solver (bottom half) and other solvers (top half),  $N_2 - O_2$  case.

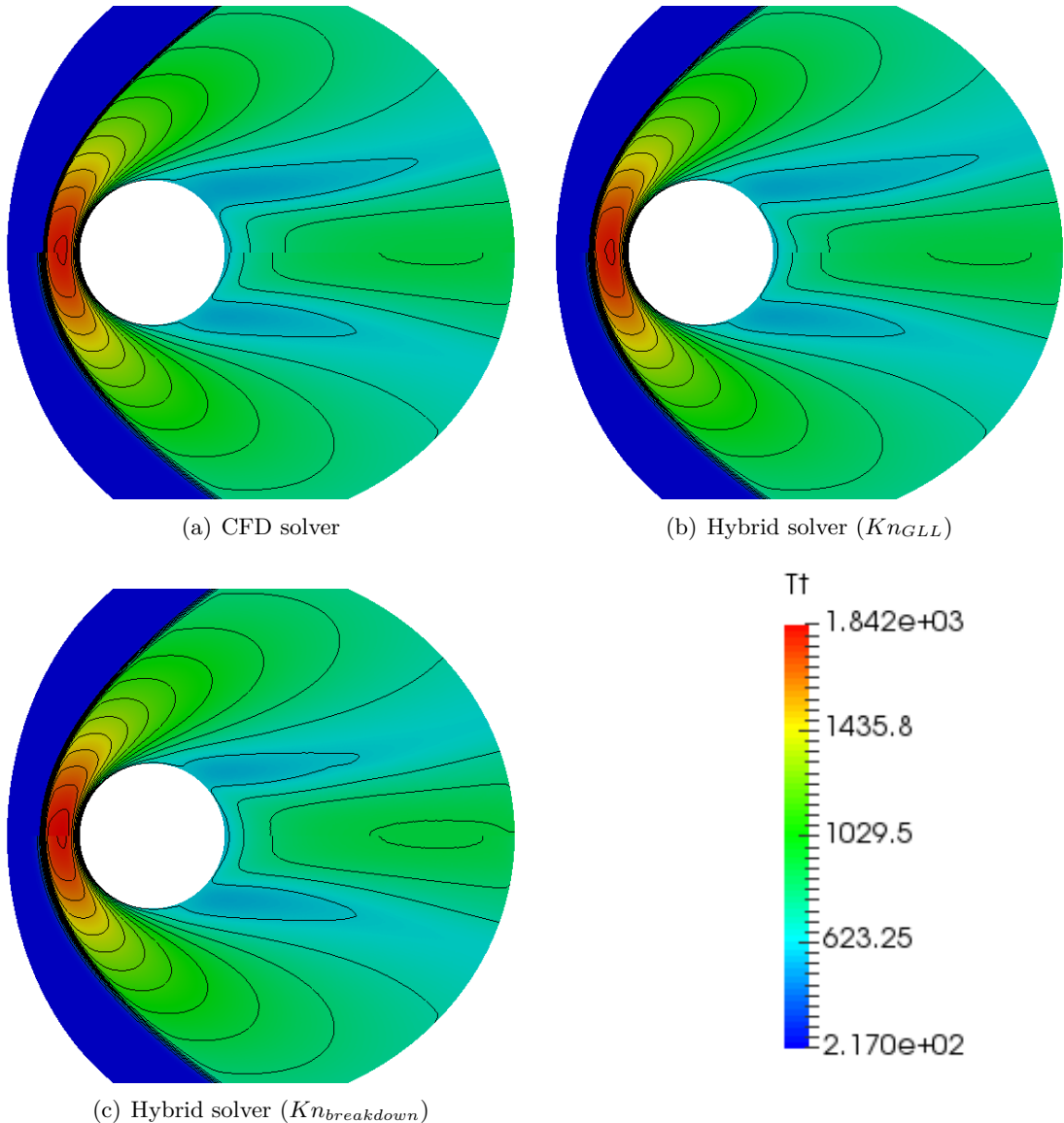


Figure 5.19: Transrotational temperature contour comparison, in  $K$ , between the DSMC solver (bottom half) and other solvers (top half),  $N_2 - O_2$  case.

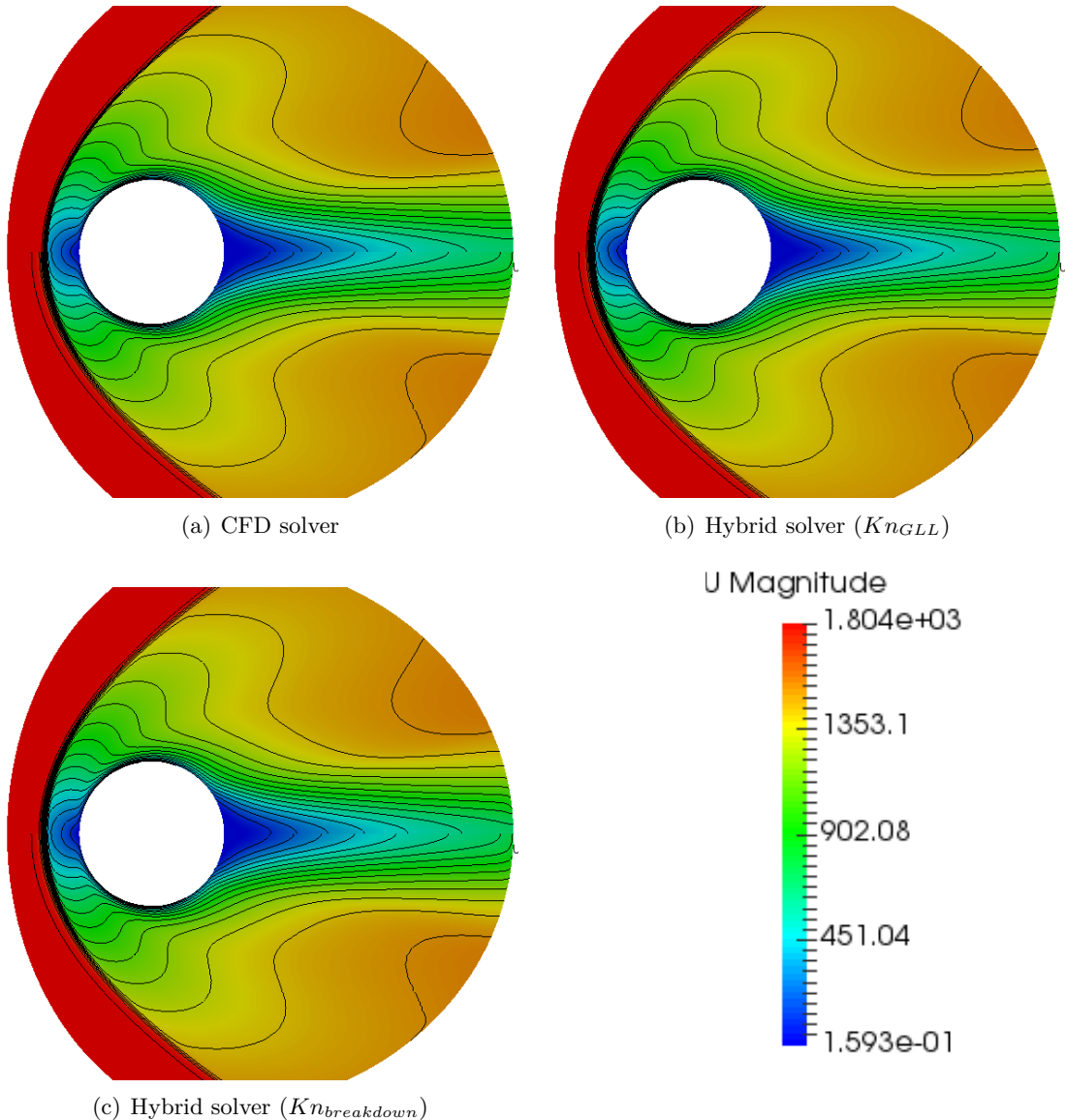


Figure 5.20: Velocity magnitude contour comparison, in  $m/s$ , between the DSMC solver (bottom half) and other solvers (top half),  $N_2 - O_2$  case.

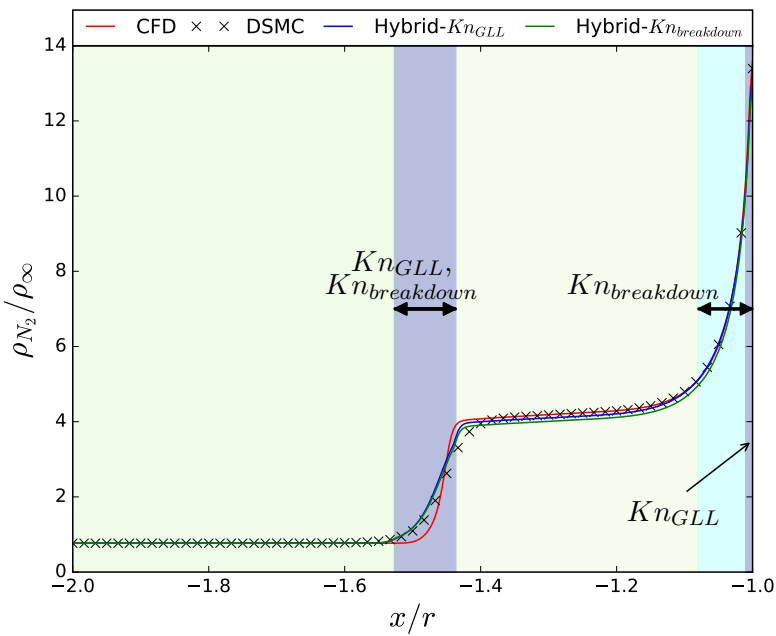


Figure 5.21:  $N_2$  density plot along the stagnation line,  $N_2 - O_2$  case.

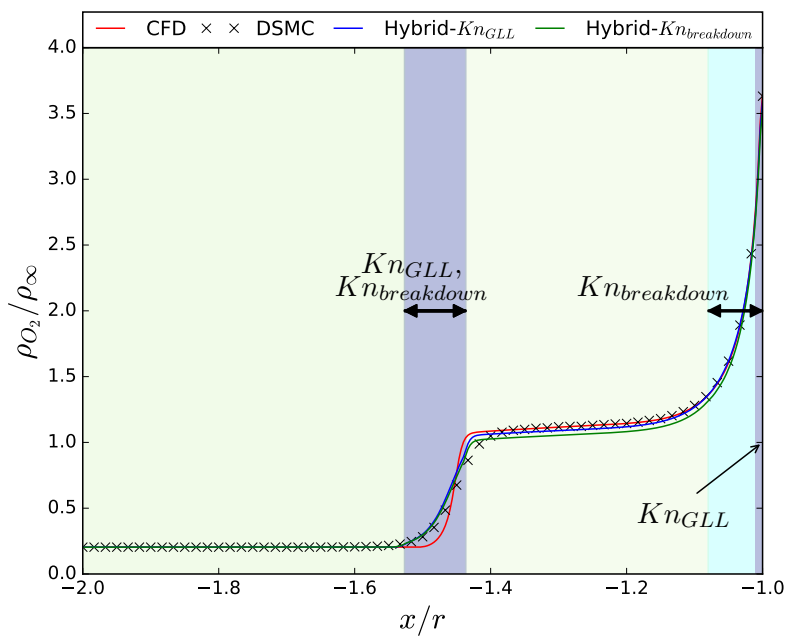


Figure 5.22:  $O_2$  density plot along the stagnation line,  $N_2 - O_2$  case.

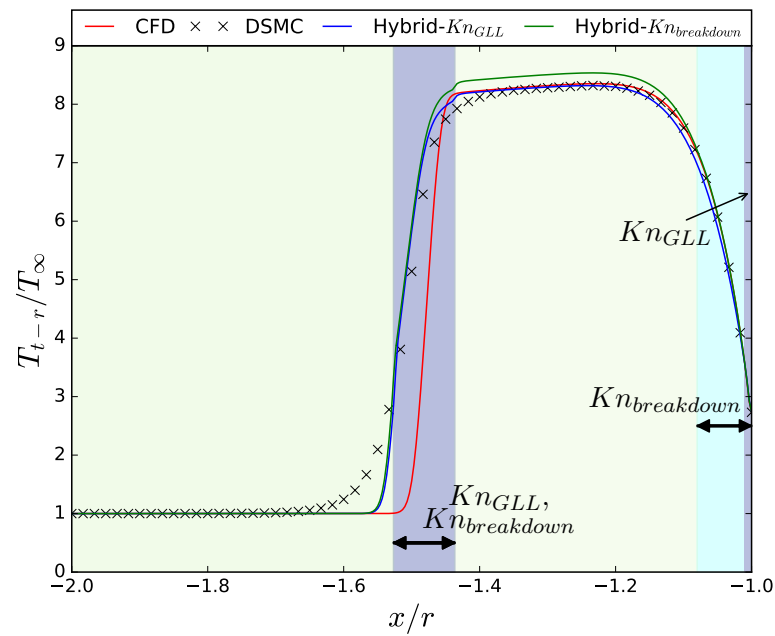


Figure 5.23: Transrotational temperature plot along the stagnation line,  $N_2 - O_2$  case.

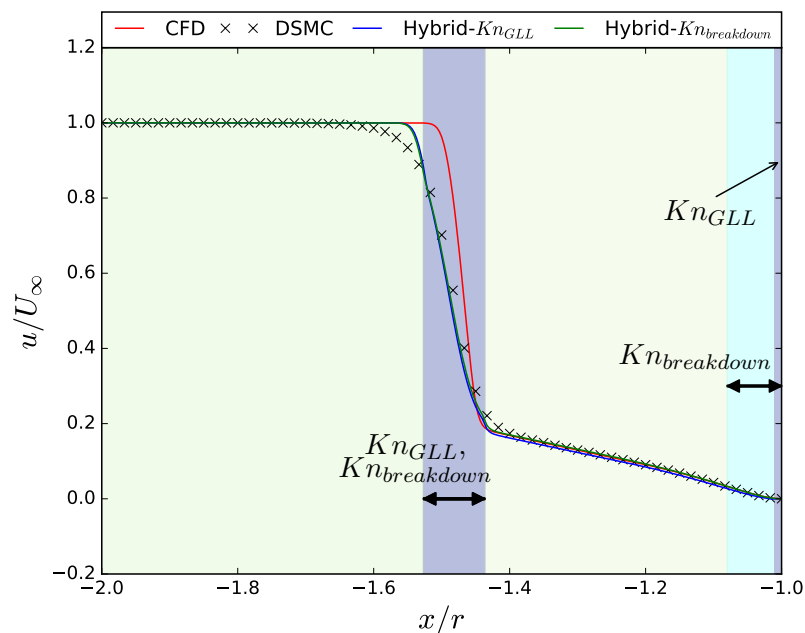


Figure 5.24: Velocity plot along the stagnation line.

as can be seen in Figures 5.25 to 5.28. Past this region, the accuracy of the different solvers can be observed to be property dependent, showing that for both densities  $Kn_{GLL}$  provides the most accurate solution, whereas for the transrotational temperature it is the  $Kn_{breakdown}$  solution, and comparable results between both criteria for velocity.

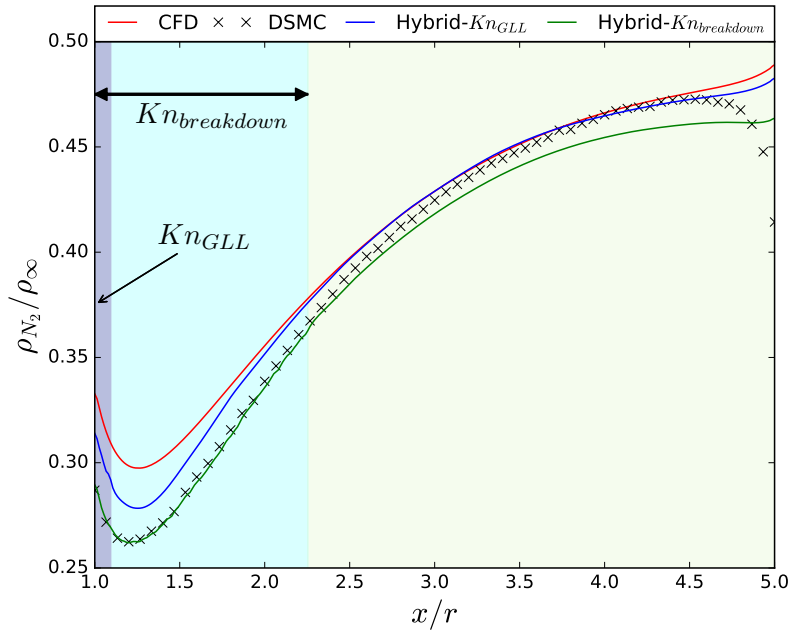


Figure 5.25:  $N_2$  density plot along the symmetry plane, in the wake.  $N_2 - O_2$  case.

For the surface properties, both solvers provide with a similarly accurate solution when compared to the DSMC results for transrotational temperature and velocity, as can be seen in Figures 5.29 and 5.30, where the CFD solver is unable to capture the right velocity slip, and more notoriously, the temperature jump. Regarding the pressure, friction, and heat transfer coefficients, the  $Kn_{GLL}$  solution shows better agreement for  $c_p$ , whereas  $Kn_{breakdown}$  match the DSMC solution for  $c_f$  and  $c_q$  respectively. As with the  $N_2$  case, CFD results for  $c_p$ ,  $c_f$ , and  $c_q$  are a suitable first approximation to the real value of these magnitudes.

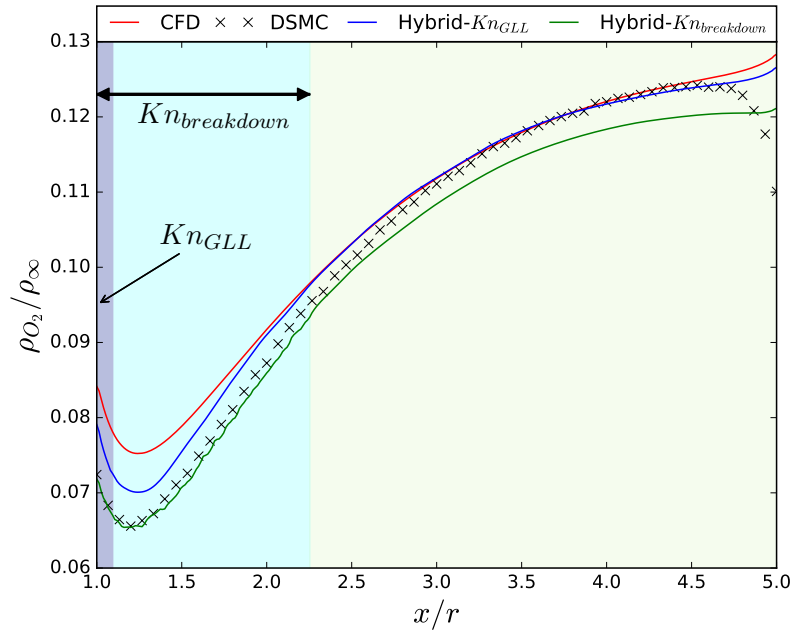


Figure 5.26:  $O_2$  density plot along the symmetry plane, in the wake.  $N_2 - O_2$  case.

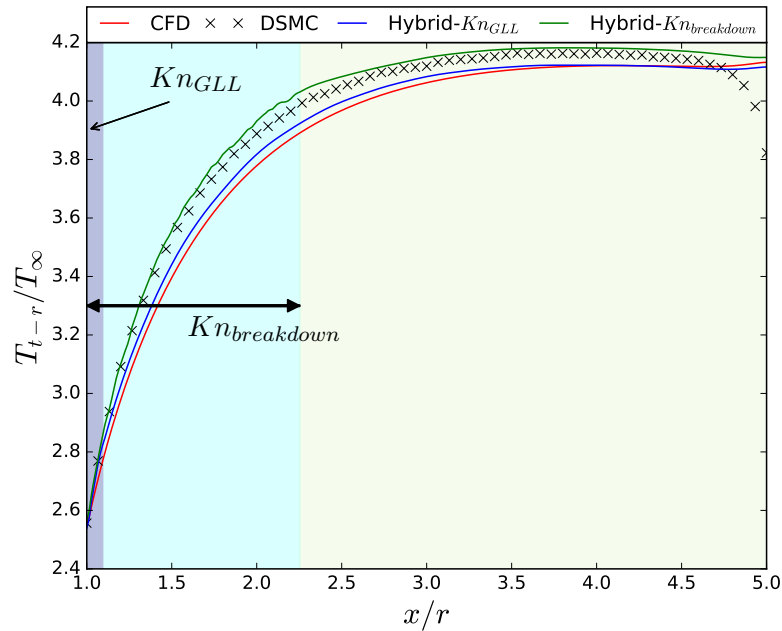


Figure 5.27: Transrotational temperature plot along the symmetry plane, in the wake.  $N_2 - O_2$  case.

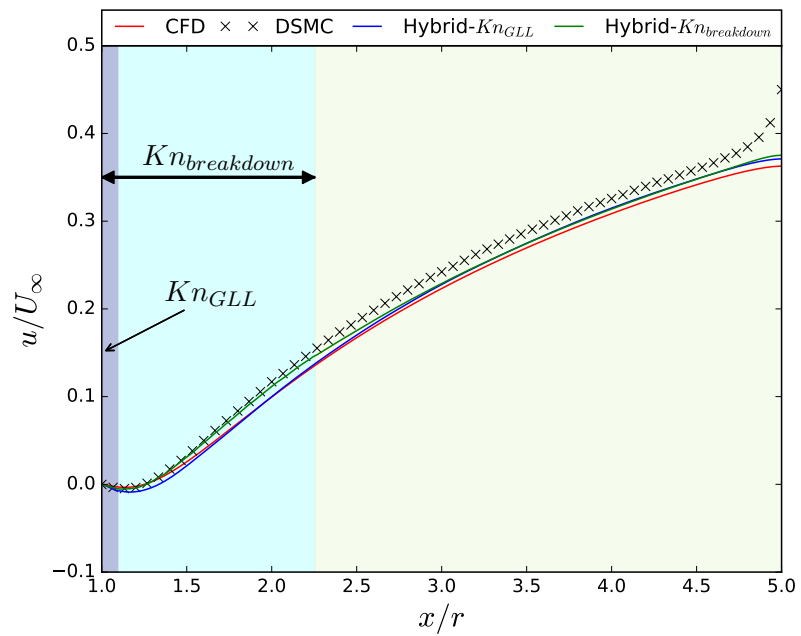


Figure 5.28: Velocity plot along the symmetry plane, in the wake.  $N_2 - O_2$  case.

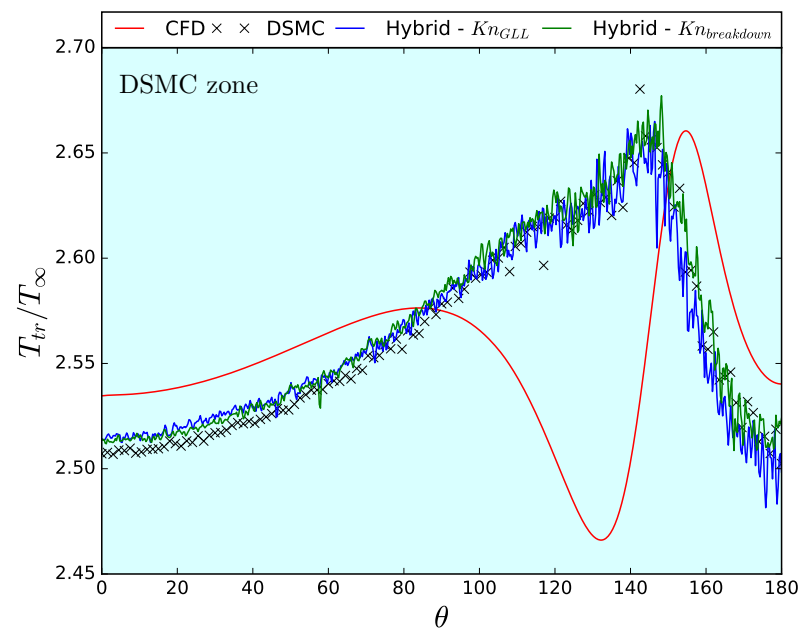


Figure 5.29: Transrotational temperature plot along the cylinder surface,  $N_2 - O_2$  case.

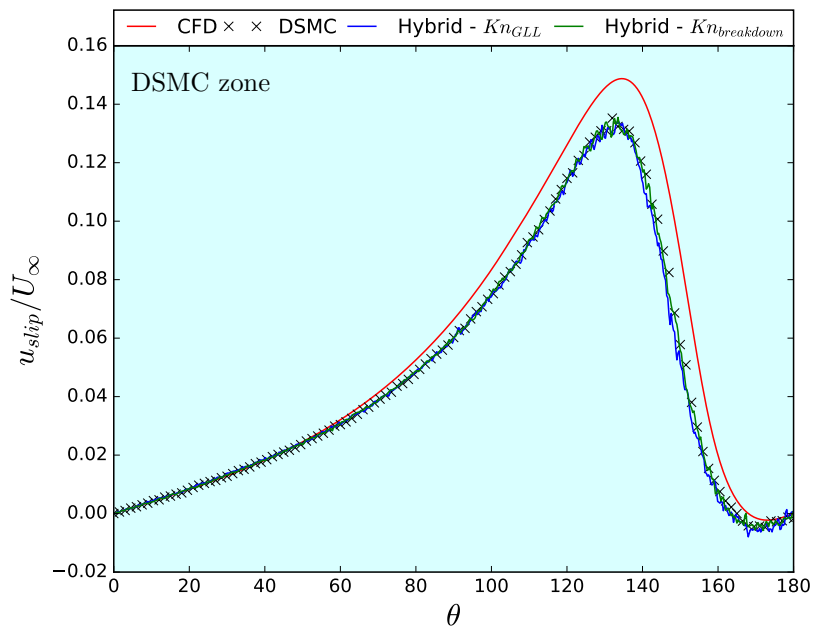


Figure 5.30: Slip velocity plot along the cylinder surface,  $N_2 - O_2$  case.

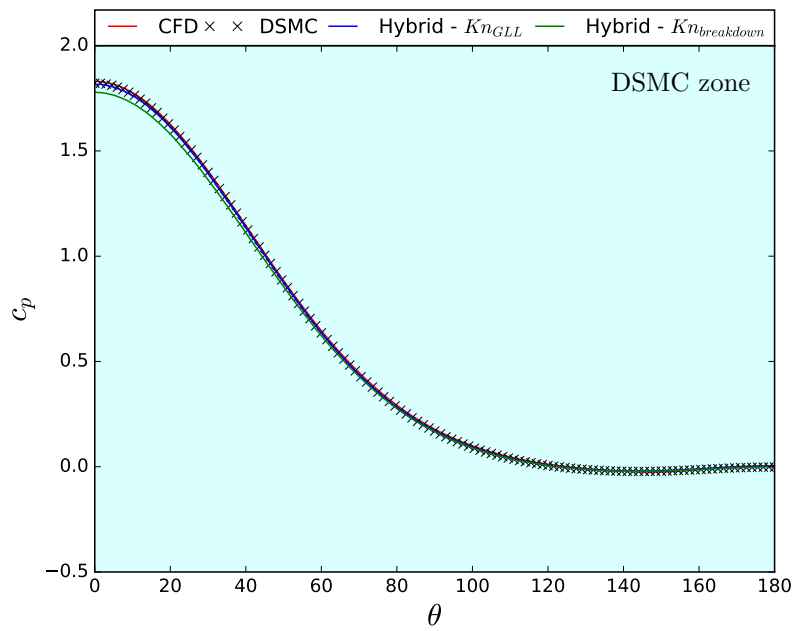


Figure 5.31: Pressure coefficient plot along the cylinder surface,  $N_2 - O_2$  case.

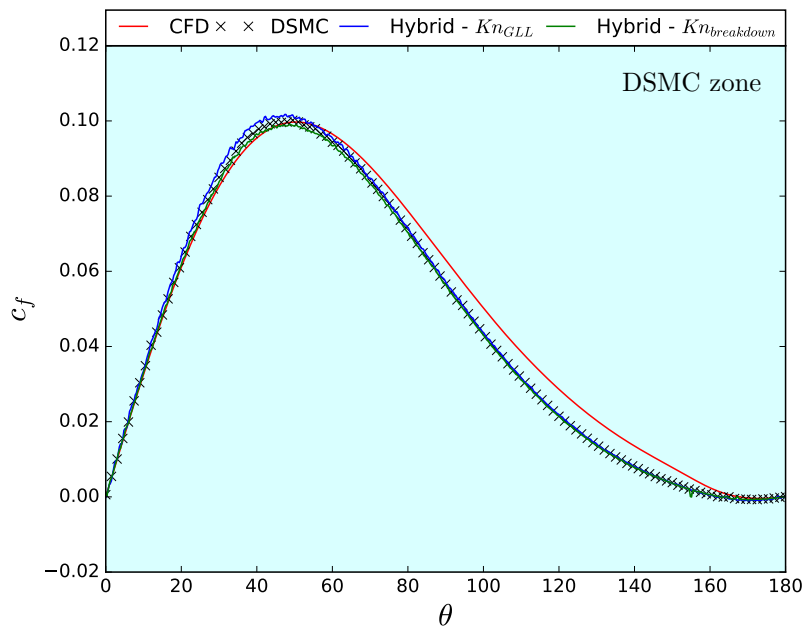


Figure 5.32: Friction coefficient plot along the cylinder surface,  $N_2 - O_2$  case.

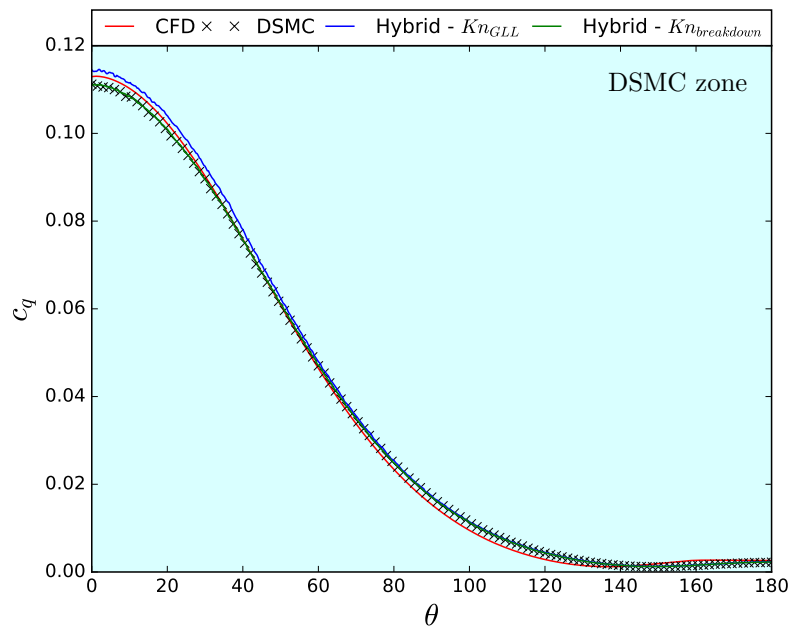


Figure 5.33: Heat transfer coefficient plot along the cylinder surface,  $N_2 - O_2$  case.

The time comparison for the  $N_2 - O_2$  case on Table 5.2 shows a major difference to the  $N_2$  case previously analysed: The DSMC solution takes up to 4.33 times more. The reason for this increment in time is due to an increase in the number of simulators. To decrease the scatter of the simulations, good DSMC practice require more than the minimum of 2.17 particles on average found on one cell, that would be obtained by keeping the same real-particle-to-simulator equivalence. To obtain low scatter on the results for the  $O_2$  species, this equivalence was modified, increasing the number of simulators by a factor of 4.76, which in turn increased the total number of the simulated particles by a similar ratio. The increase in computational time for the CFD solver is due to the addition of a second species and therefore the inclusion of new equations to solve. However, this increase is by a factor of 2.2, about half of the increase in computational resources due to DSMC particles. For this reason, the CFD solver sees an impressive speedup when compared to DSMC, albeit the lack of accuracy of the solution. Unfortunately, for the hybrid solver this multispecies test case increases the sizes of the DSMC domains for both  $Kn_{GLL}$  and  $Kn_{breakdown}$  criteria, increasing the DSMC time per iteration to an even higher factor. On the other hand, the CFD time per iteration is also increased to more than 2.2 times due to the new cells that require resetting. For these reasons, the speedup of the hybrid solver drops when compared to those of the  $N_2$  case. However, a speedup of 1.83 for the  $Kn_{breakdown}$  simulation is more than an acceptable result.

	DSMC	CFD	Hybrid			
			$Kn_{GLL}$		$Kn_{breakdown}$	
			CFD	DSMC	CFD	DSMC
Seconds per it.	18.436	1.940	3.226	6.964	3.269	8.875
nº it.	$1 \cdot 10^6$	$2 \cdot 10^5$	$2.5 \cdot 10^5$	$1 \cdot 10^6$	$2.5 \cdot 10^5$	$1 \cdot 10^6$
Total time	5121h 7min	107h 47min	2266h 15min		2800h 5min	
Speedup	-	47.5	2.26		1.83	

 Table 5.2: Time comparison among the different solvers,  $N_2 - O_2$  case

## 5.4 Molecular $O_2$

To be able to test the vibrational capabilities, a new single species test case was simulated. The gas used for this simulation is oxygen, due to its lower characteristic vibrational temperature. However, the temperatures achieved with the previous test cases are too low to obtain accurate vibrational temperature estimations within a reasonable computational time. For this reason, the temperatures for this simulation are set to 869.8 K for the freestream flow and 2000 K at the cylinder wall, which is exactly four times those temperatures of the  $N_2$  test case. The flow still travels at Mach 6, which results in a freestream velocity of 3375.5 m/s. The pressure has been chosen so that the freestream mean free path remains in the order of 0.01, giving a value of 21 Pa.

Similarly to the previous test cases, the results from the domain decomposition for both  $Kn_{GLL}$  and  $Kn_{breakdown}$  criteria have been studied. However, for this test case all cells where the vibrational temperature was higher than the transrotational temperature were included into the DSMC domain. The reason for this new imposition is the fact that in these conditions the CFD model for vibrational-translational energy transfer provides a relaxation rate quite different than that of the quantum Larsen-Borgnakke model [8]. These domains can be seen in Figure 5.34. Keeping the same trend as the previous cases, the  $Kn_{breakdown}$  criterion identify more rarefied cells in the near-cylinder area than the  $Kn_{GLL}$  criteria. In addition, the wake region of the  $Kn_{breakdown}$  criterion becomes almost entirely rarefied, due to the new temperature condition.

Figures 5.35 to 5.38 show the contour plot comparison for pressure, transrotational and vibrational temperatures, and velocity. For the pressure it seems that the  $Kn_{GLL}$  case provides with a better approximation of the DSMC solution. Nonetheless it is the  $Kn_{breakdown}$  case the one that follows the DSMC contour lines of velocity and transrotational temperature more precisely. Despite the agreement on these properties, none of the hybrid cases nor the CFD solution seem to come close to the DSMC results for

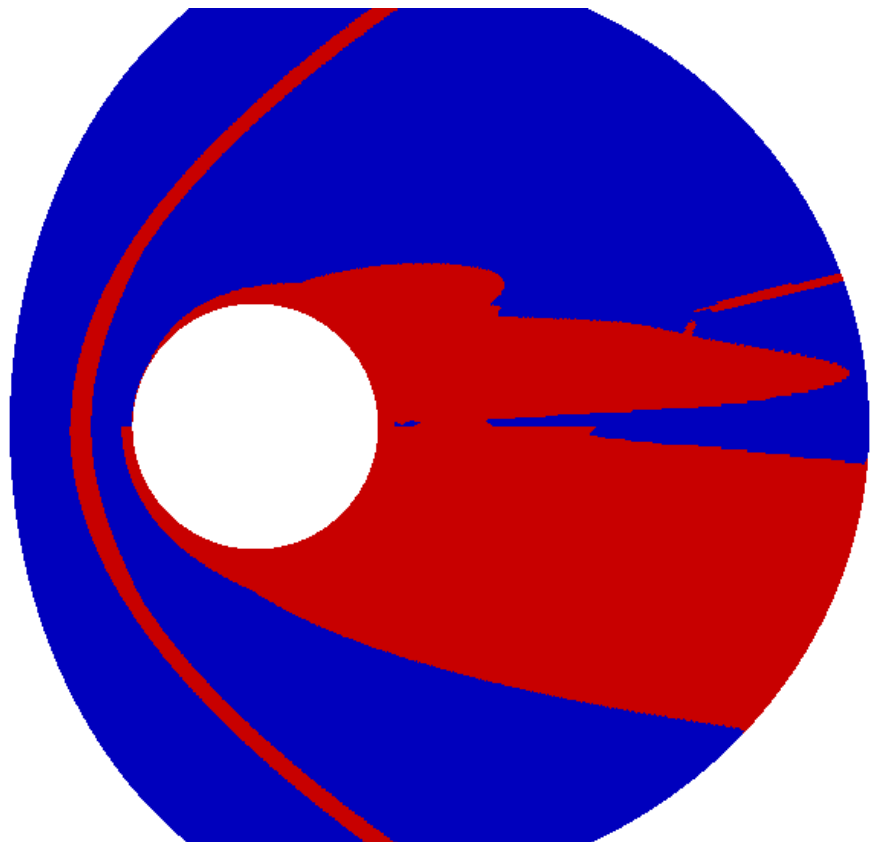


Figure 5.34: Hypersonic cylinder CFD (in blue) and DSMC (in red) zones using  $Kn_{GLL}$  (top) and  $Kn_{breakdown}$  (bottom) as criteria,  $O_2$  case.

the vibrational temperature. The reason for this is the evident disagreement between the CFD and DSMC results. The DSMC solver is capable of returning a more accurate solution when the initial CFD state is slightly inaccurate, as have been shown in the previous cases. However, for this simulation the error from the CFD solver is quite significant and *hyperFoam* cannot overcome it, and therefore returns a solution far from the expected DSMC values.

Figures 5.39 to 5.42 continue to show the vibrational temperature error along the stagnation line. Whereas the position of the shock can be identified in some of the plots, it can be observed especially on the density and velocity plots that this position have been translated downstream. Figure 5.41 shows the vibrational temperature plot. Whereas there is quite good agreement between the hybrid and DSMC solutions on the near-shock rarefied domain, the vibrational energy is overestimated in the post-shock continuum region, which translates in a similar behaviour for the vibrational temperature itself. Besides these two effects, the behaviour of the hybrid solutions is similar to that of the vibrationless  $N_2$  and  $N_2 - O_2$  cases, with quite good agreement on the near-cylinder rarefied domain for the  $Kn_{breakdown}$ , followed by a too-steep gradient for the transrotational temperature which is therefore overestimated in this post-shock region.

The results in the wake region for the  $O_2$  simulations, which can be seen in Figures 5.43 to 5.46, vary from what have been seen in previous cases. First of all, it can be observed that the  $Kn_{GLL}$  criterion now returns two rarefied zones along this line, instead of only one as previously seen. This helps the  $Kn_{GLL}$  solution to keep good accuracy further down the wake. In addition, it can be observed that the  $Kn_{breakdown}$  criterion is less accurate for the density along the wake than the  $Kn_{GLL}$  criterion, and that neither of the solvers match the DSMC results regarding the vibrational temperature.

Figures 5.47 to 5.52 show the results along the cylinder. It can be seen in Figures 5.47 and 5.49 that the hybrid solver matches the transrotational temperature and ve-

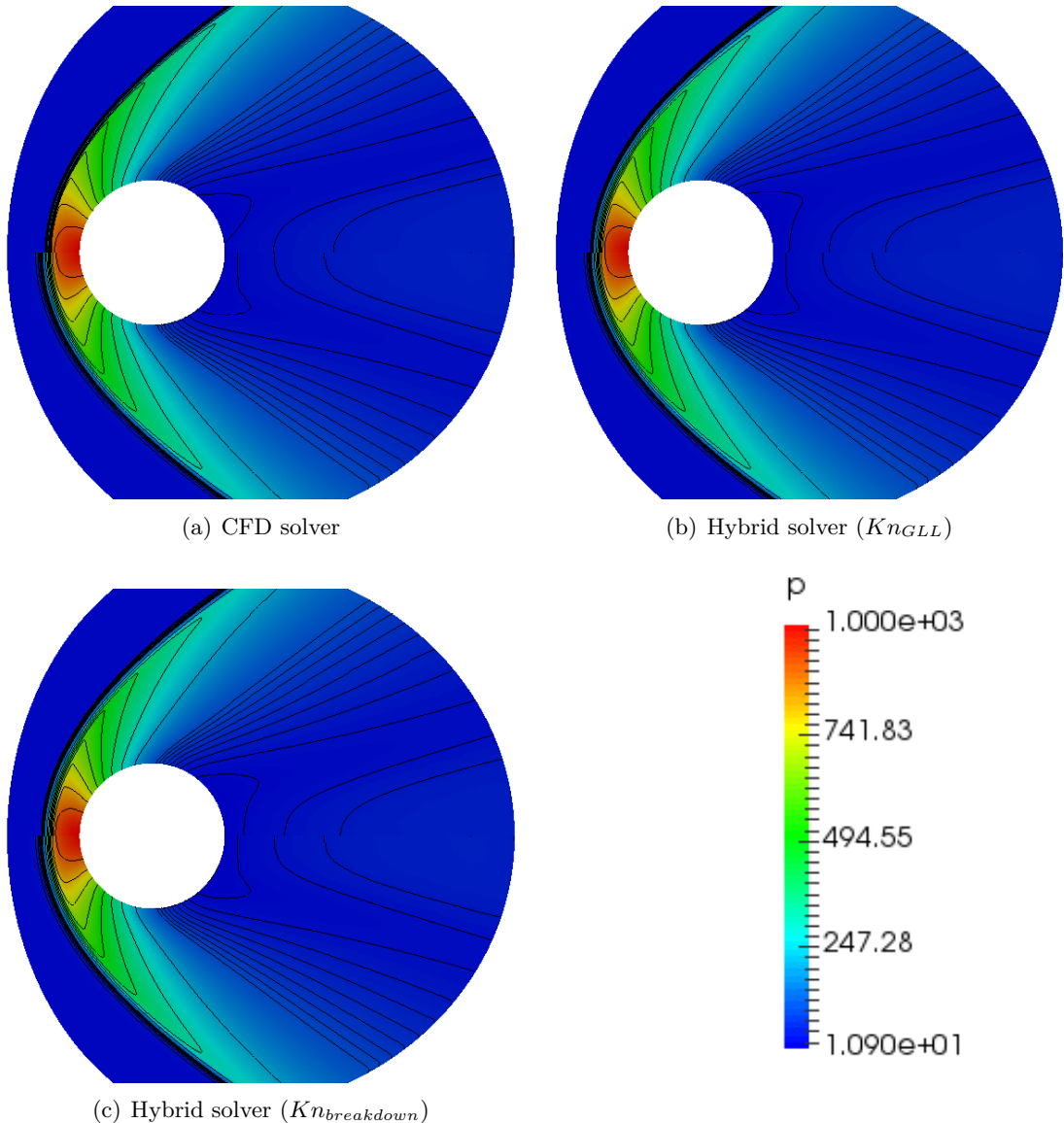


Figure 5.35: Pressure contour comparison, in  $Pa$ , between the DSMC solver (bottom half) and other solvers (top half).  $O_2$  case.

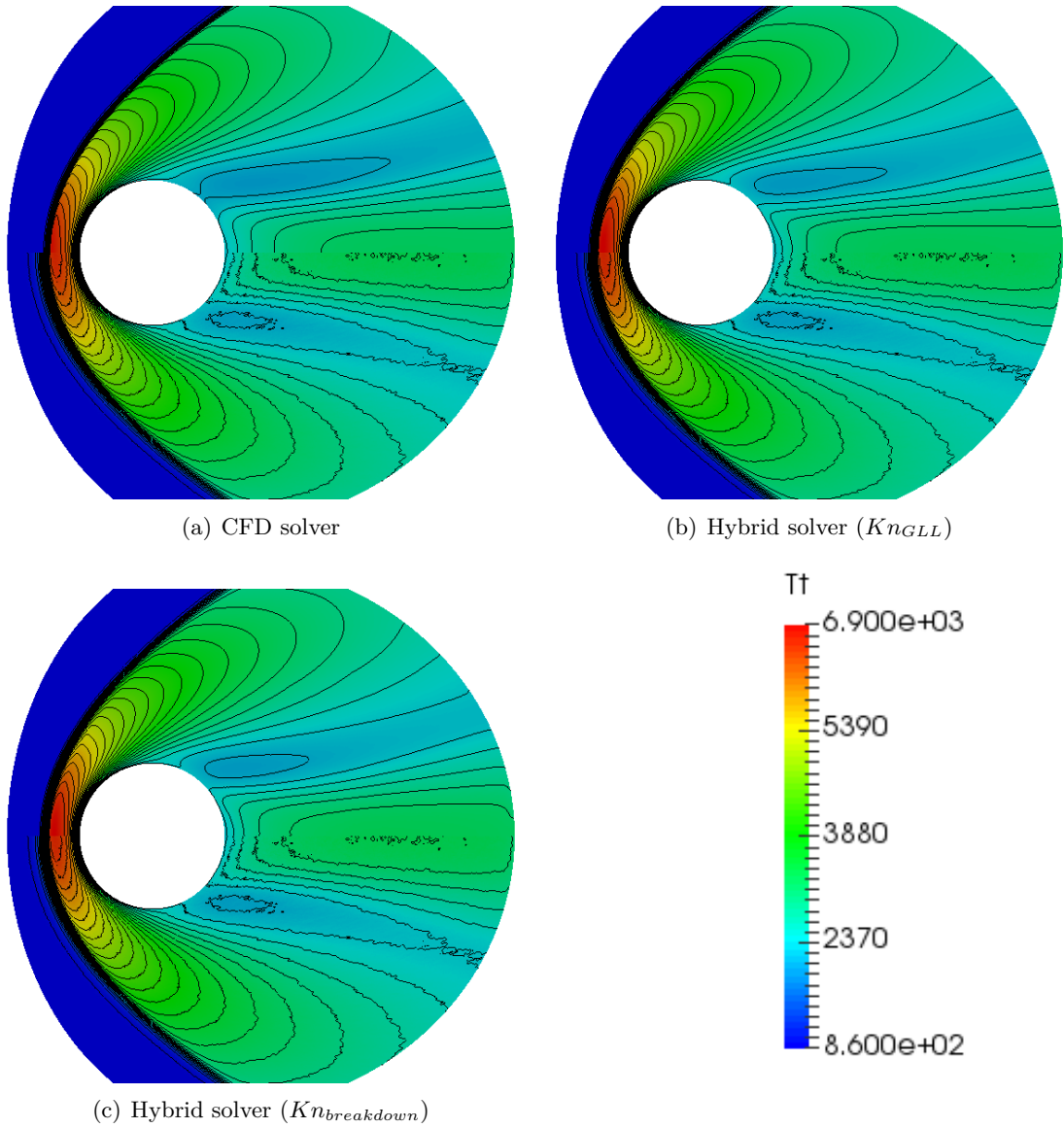


Figure 5.36: Transrotational temperature contour comparison, in  $K$ , between the DSMC solver (bottom half) and other solvers (top half),  $O_2$  case.

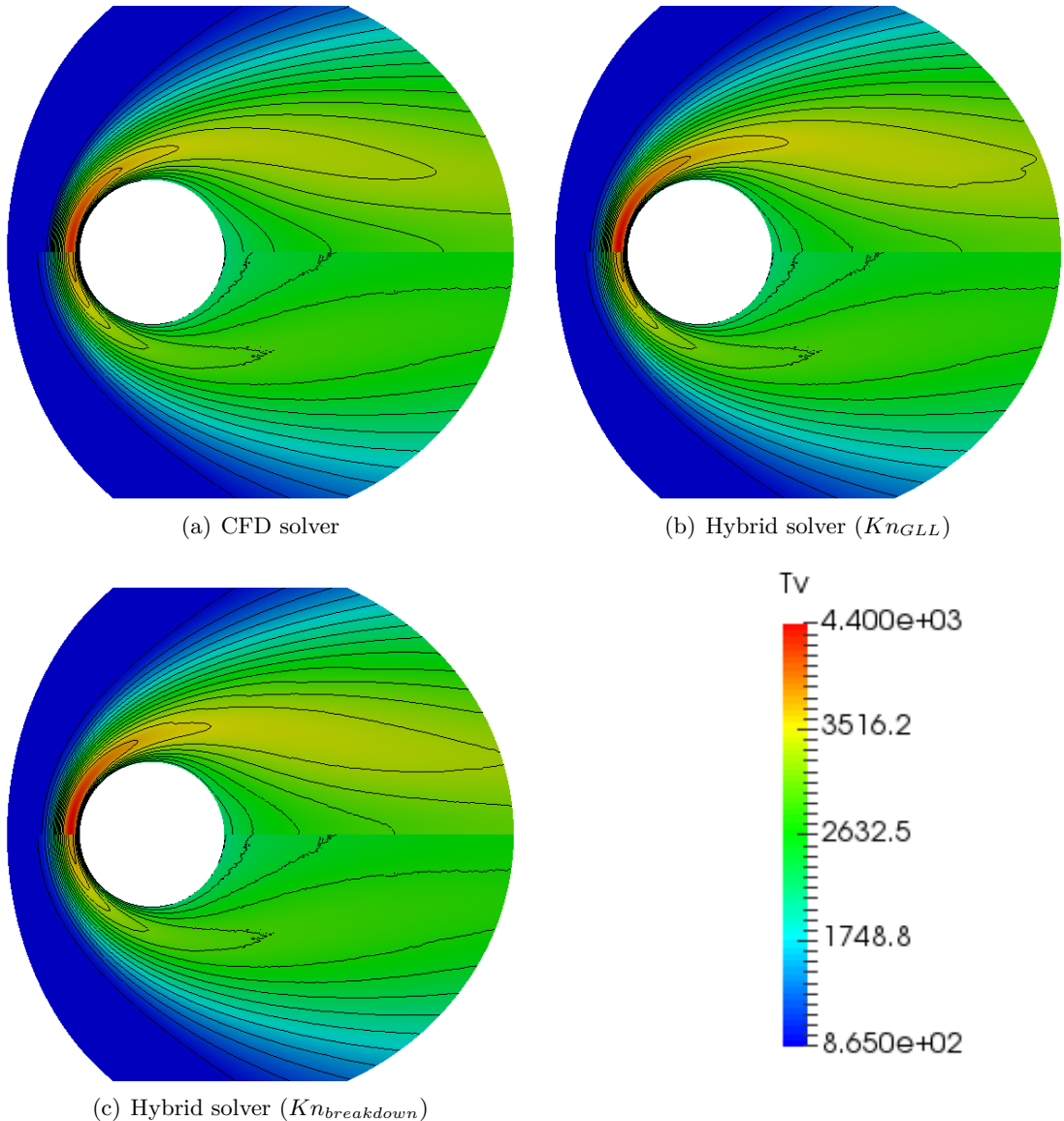


Figure 5.37: Vibrational temperature contour comparison, in  $K$ , between the DSMC solver (bottom half) and other solvers (top half),  $O_2$  case.

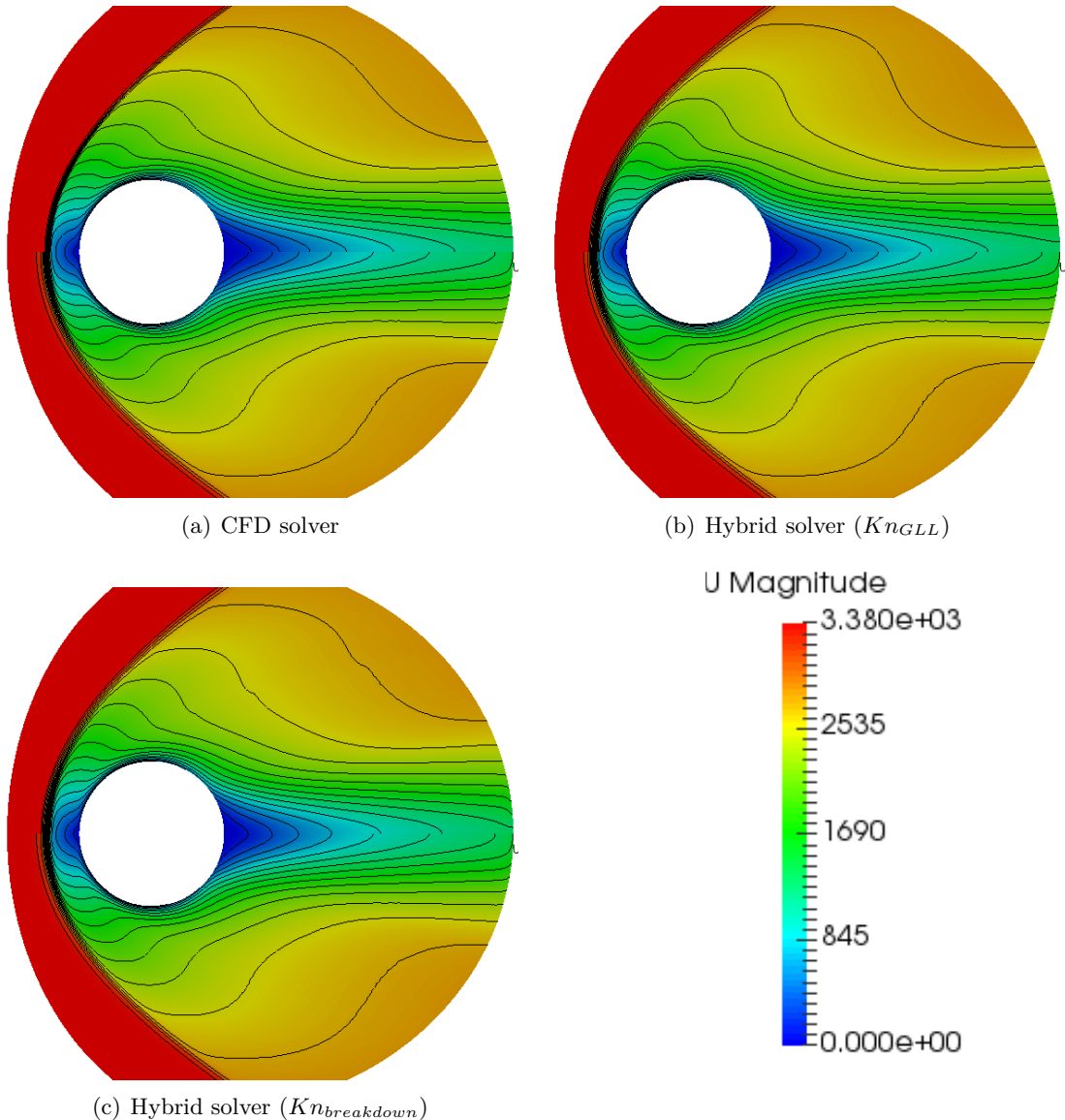


Figure 5.38: Velocity magnitude contour comparison, in  $m/s$ , between the DSMC solver (bottom half) and other solvers (top half),  $O_2$  case.

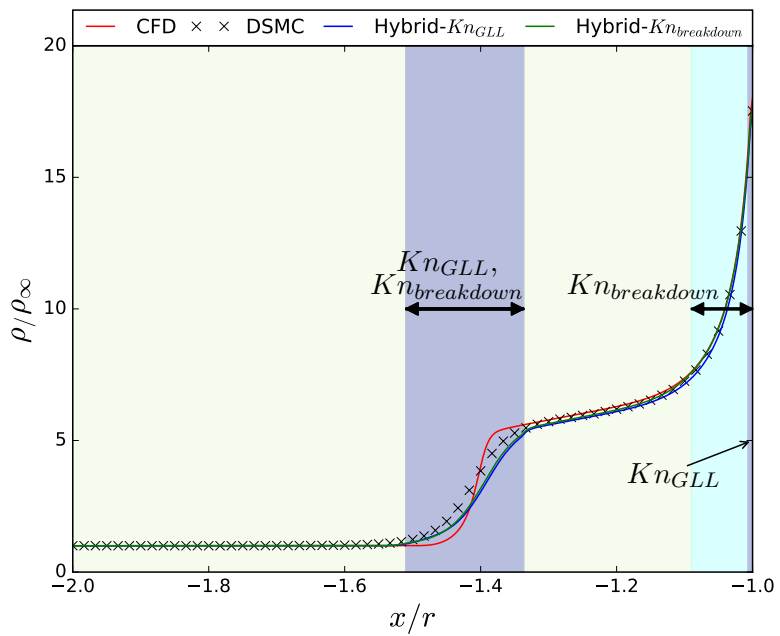


Figure 5.39: Density plot along the stagnation line,  $O_2$  case.

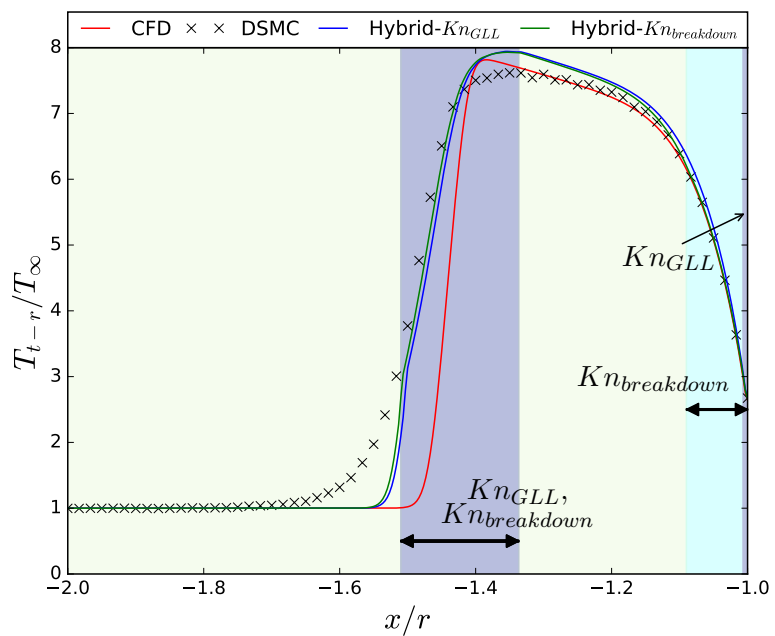


Figure 5.40: Transrotational temperature plot along the stagnation line,  $O_2$  case.

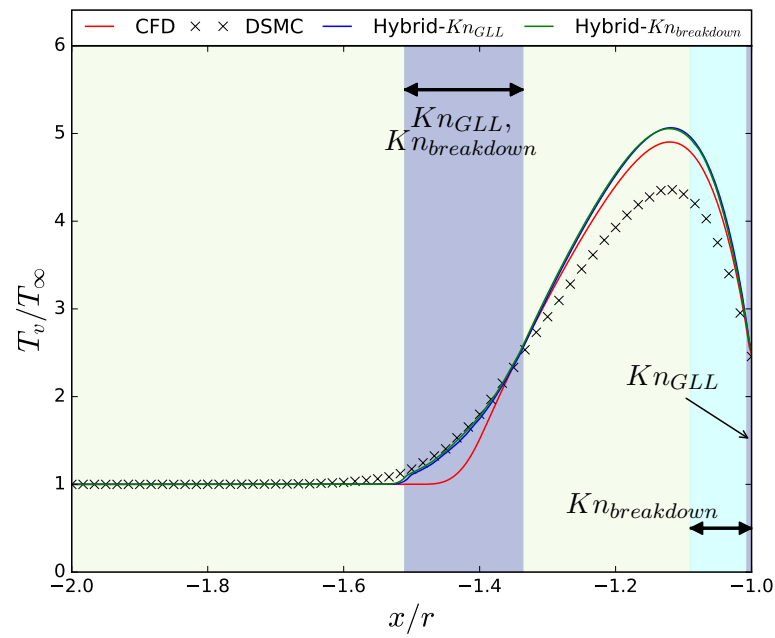


Figure 5.41: Vibrational temperature plot along the stagnation line,  $O_2$  case.

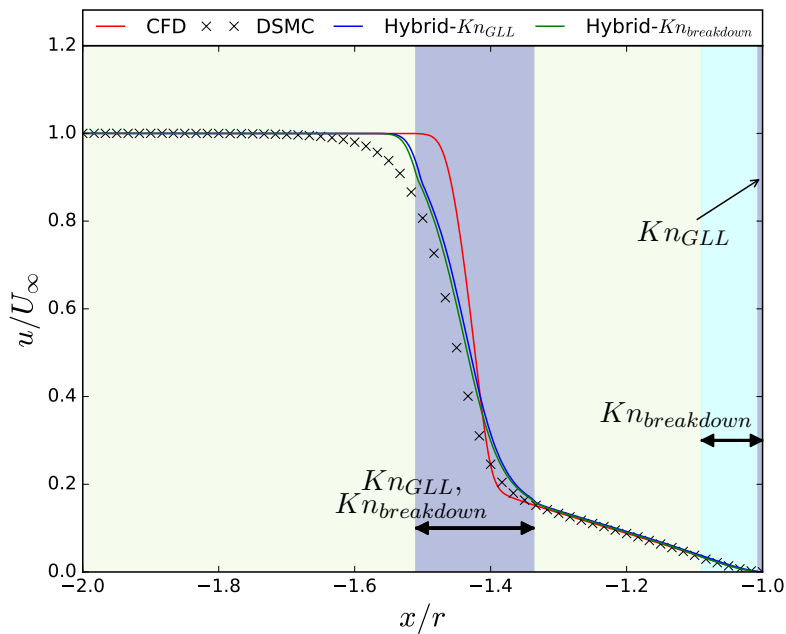


Figure 5.42: Velocity plot along the stagnation line,  $O_2$  case.

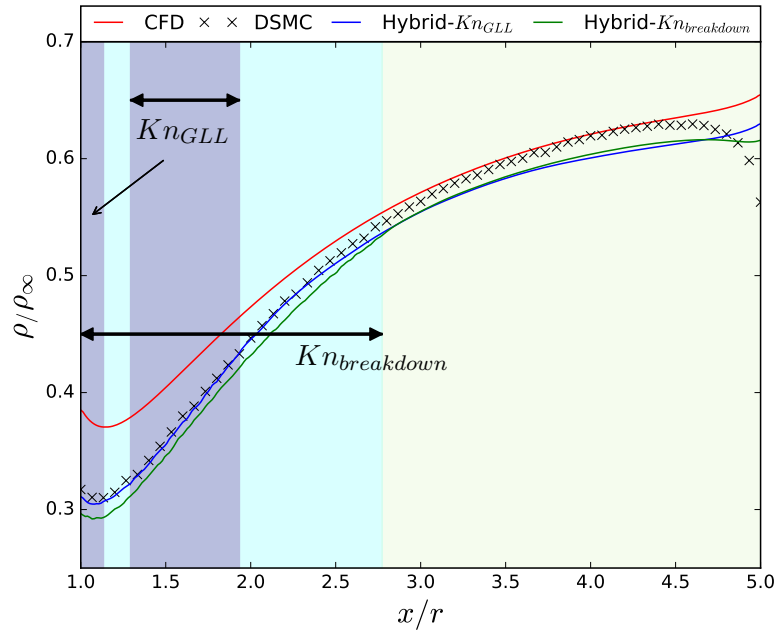


Figure 5.43: Density plot along the symmetry plane, in the wake.  $O_2$  case.

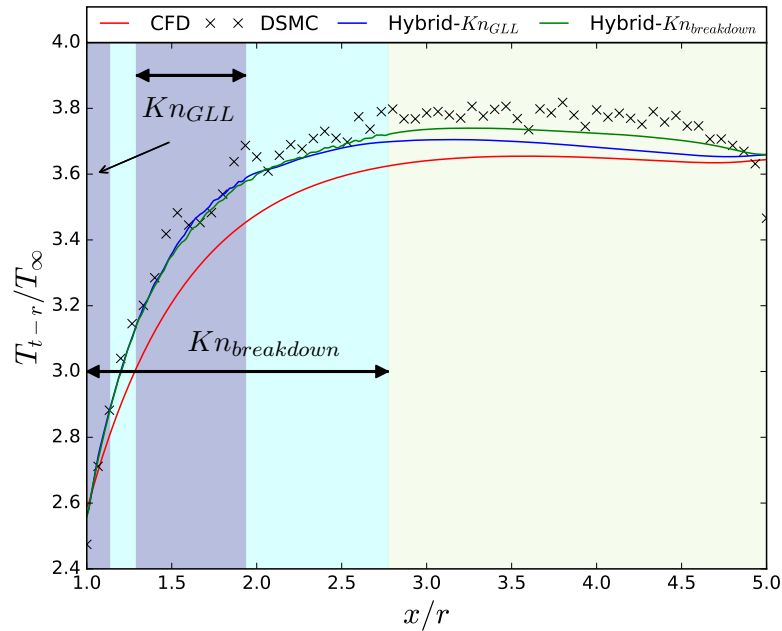


Figure 5.44: Transrotational temperature plot along the symmetry plane, in the wake.  $O_2$  case

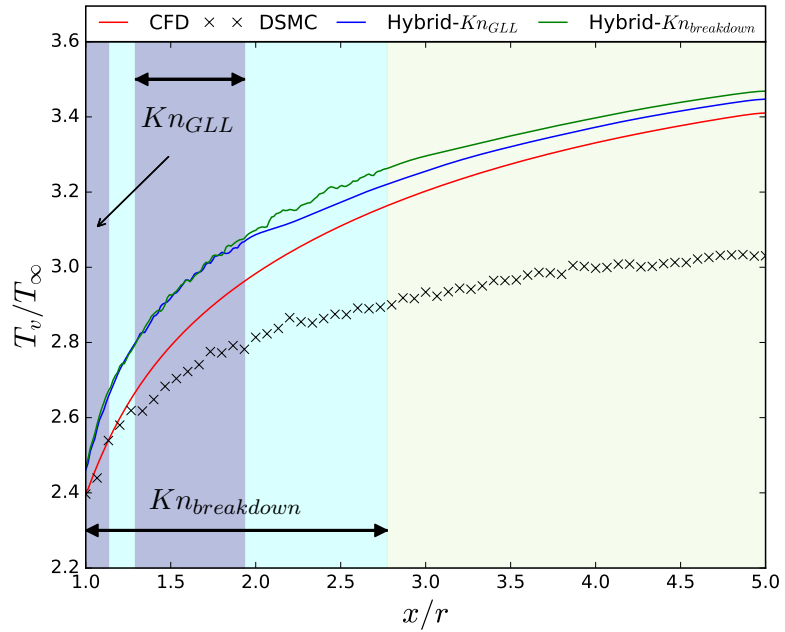


Figure 5.45: Vibrational temperature plot along the symmetry plane, in the wake.  $O_2$  case

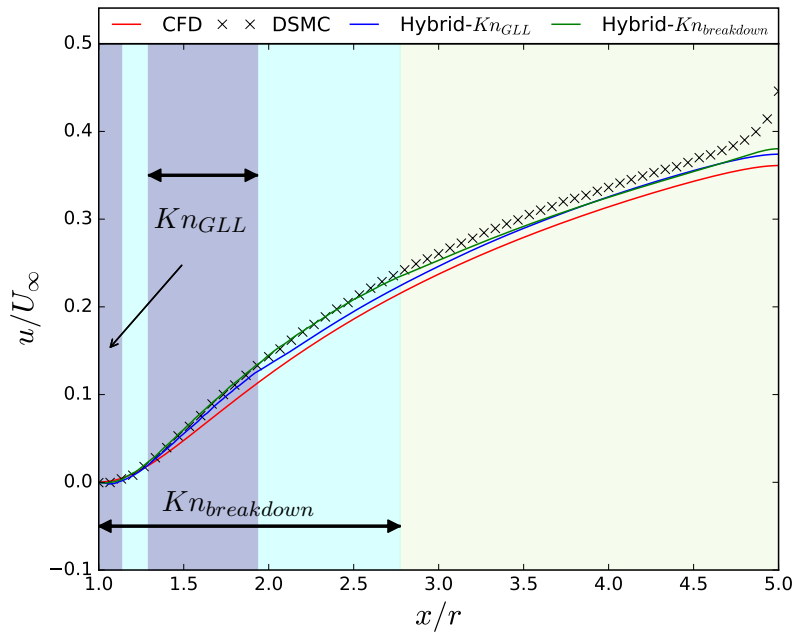


Figure 5.46: Velocity plot along the symmetry plane, in the wake.  $O_2$  case.

locity quite well when compared to the DSMC results. For vibrational temperature, however, the trend seen so far continues and *hyperFoam* is unable to approach the right solution. Finally, for the pressure, friction, and heat transfer coefficients, it can be seen that all the cases follow the same trend as before, where the hybrid using the *Kn<sub>GLL</sub>* criterion matches well except for the  $c_q$ , whereas the *Kn<sub>breakdown</sub>* matches reasonable well in all, and the CFD solver provided a quite good approximation for these quantities. It is important to notice that even with a more significant disagreement on the vibrational temperature values, these coefficients are found to be quite similar to the previous cases. The error in terms of vibrational energy is quite small in comparison with the energy transferred at the wall, returning a less inaccurate measure for the heat transfer.

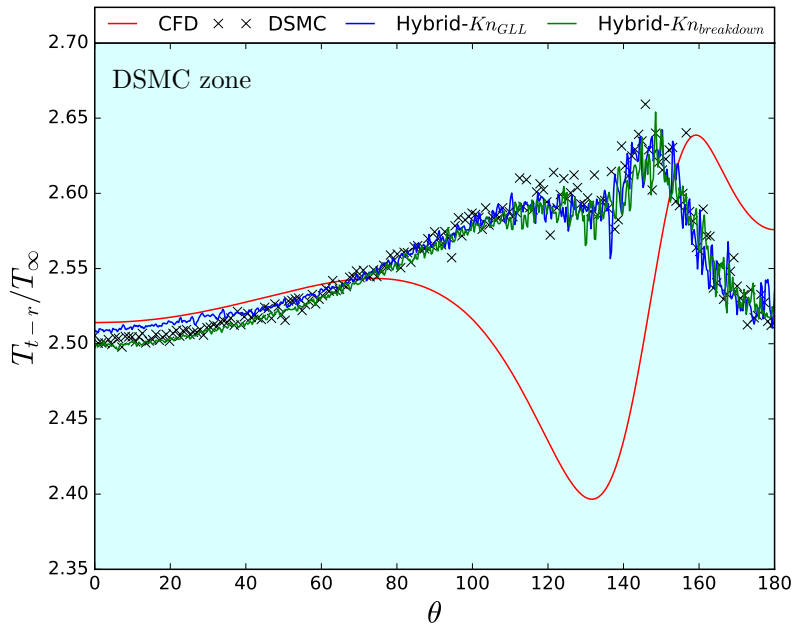


Figure 5.47: Transrotational temperature plot along the cylinder surface,  $O_2$  case.

The computational time required by the simulation behaves similarly, regardless of the accuracy of the solution. However, the effects of the new temperature condition for the calculation of the domains are evident. Whereas the CFD speedup is similar to

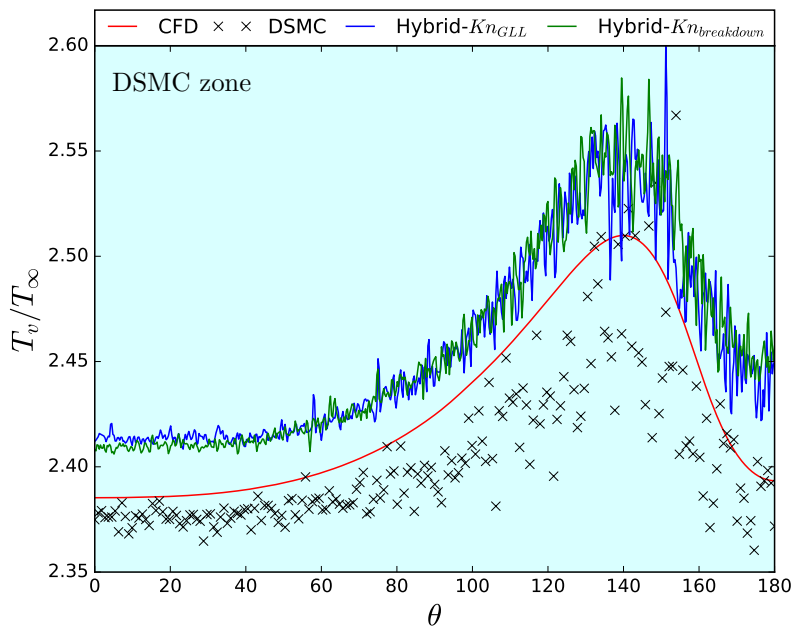


Figure 5.48: Vibrational temperature plot along the cylinder surface,  $O_2$  case.

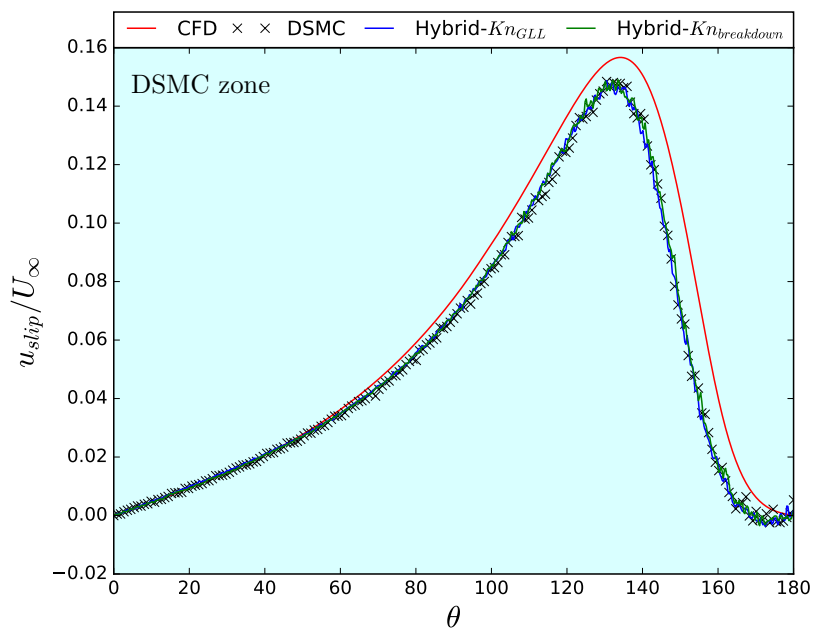


Figure 5.49: Slip velocity plot along the cylinder surface,  $O_2$  case.

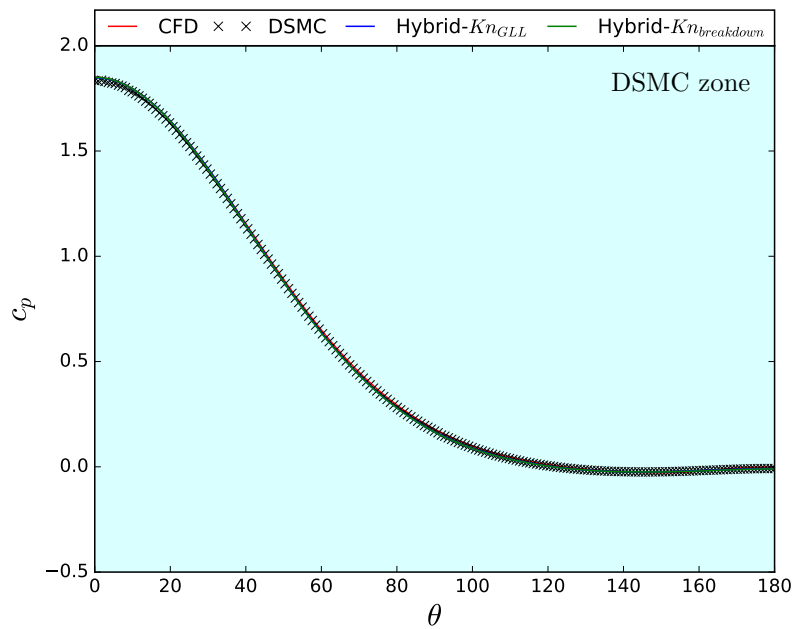


Figure 5.50: Pressure coefficient plot along the cylinder surface,  $O_2$  case.

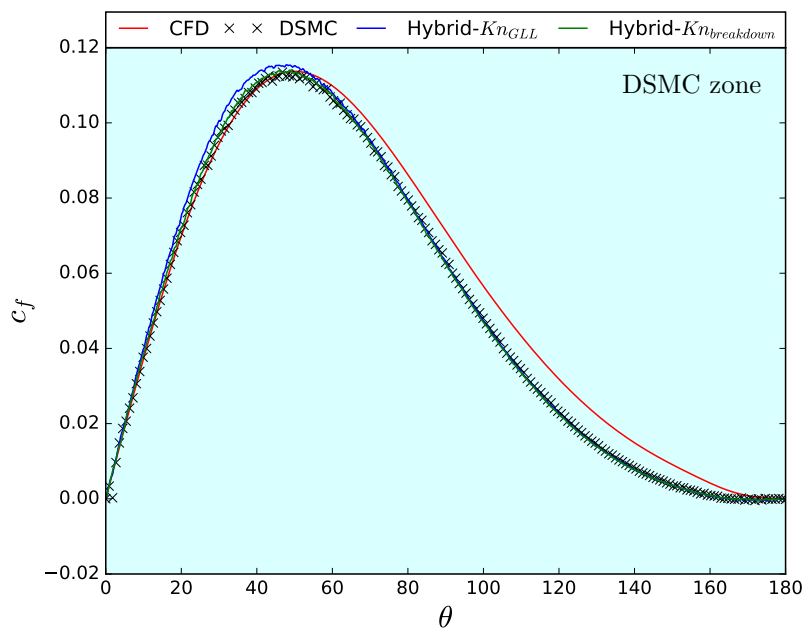
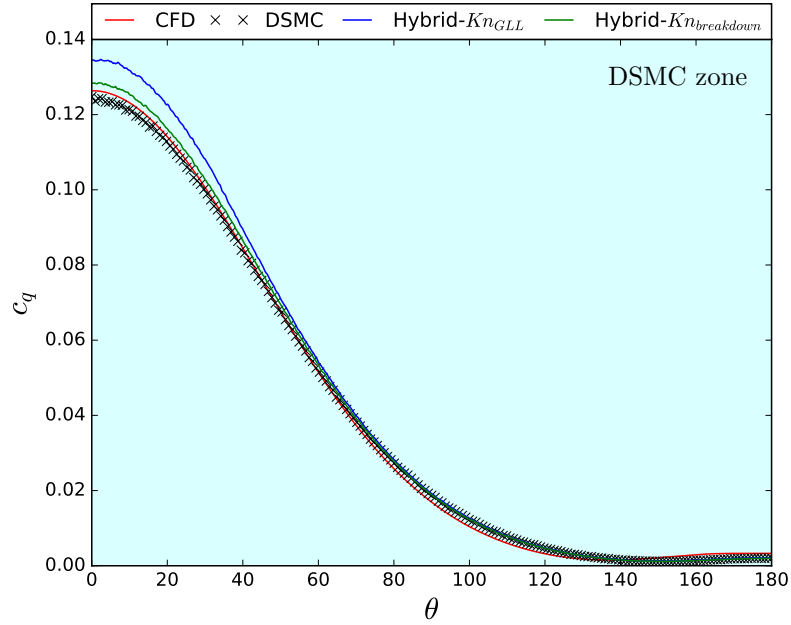


Figure 5.51: Friction coefficient plot along the cylinder surface,  $O_2$  case.


 Figure 5.52: Heat transfer coefficient plot along the cylinder surface,  $O_2$  case.

that of the  $N_2$  case, the hybrid speedup drops from 2.51 and 2.27 on the  $N_2$  case for  $Kn_{GLL}$  and  $Kn_{breakdown}$  respectively to 2.16 and 1.5.

	DSMC	CFD	Hybrid			
			$Kn_{GLL}$		$Kn_{breakdown}$	
			CFD	DSMC	CFD	DSMC
Seconds per it.	5.6563	1.1523	2.5230	1.7550	2.6738	2.8714
n° it.	$1 \cdot 10^6$	$2 \cdot 10^5$	$2.5 \cdot 10^5$	$1 \cdot 10^6$	$2.5 \cdot 10^5$	$1 \cdot 10^6$
Total time	1571h 12min	64h 1min	726h 45min		1047h 19min	
Speedup	-	24.5	2.16		1.5	

 Table 5.3: Time comparison among the different solvers,  $O_2$  case

# Chapter 6

## Conclusions

A new CFD-DSMC hybrid code has been developed for the open-source framework OpenFOAM. This code, called *hyperFoam*, uses a mixture between Boyd's Gradient-Length-Local Knudsen number  $Kn_{GLL}$  and Stephani's multispecies modified Chapman-Enskog parameter  $B$  to distinguish between continuum and rarefied portions of the domain, which are then solved using a CFD and DSMC solver respectively. *hyperFoam* takes advantage of the capabilities of the recently developed *hy2Foam* solver to simulate the continuum cells of the domain, that allow for multispecies simulations and two-temperature models. In addition, the hybrid code borrows from the widely employed *dsmcFoam* solver to calculate the solution in the rarefied parts of the domain. State-based coupling is used between both type of domains, generating particles in the vicinity of the DSMC domain using a Generalised Chapman-Enskog distribution, and using the averaged DSMC-generated macroscopic fields as the state of the continuum variables for the cells surrounding the CFD domain.

The first step towards accomplishing the objectives was conducted in Chapter 2, where the suitability of *rhoCentralFoam* for hypersonic test cases was analysed, comparing its results with other state-of-the-art solvers such as DLR-TAU. This analysis also led to the implementation of two techniques, local time stepping (LTS) and adaptive mesh refinement (AMR), to accelerate the convergence for the simulations performed with *rhoCentralFoam*. These two techniques proved effective for the cases studied in

this work. Consequently, LTS and AMR were also incorporated into *hy2Foam* during its development and thus used as well for the hybrid simulations. Even with a very conservative time-step chosen for the LTS method during the hybrid solver simulations, the coupling time would be reached with less than a tenth of the iterations required if LTS was not used.

The most important aspect of this research was included in Chapter 4, where the full details for the methods and algorithm of *hyperFoam* are explained. Later in the chapter the hybrid solver displayed satisfactory results for cases of different complexities for the Couette flow with heat transfer simulations. In Chapter 5 the more complex hypersonic cylinder test case was studied. It was observed that a continuum vibrational model that is consistent with the quantum Larsen-Borgnakke procedure from the rarefied solver is needed to obtain a better agreement between the CFD and DSMC results, specially on cases with high temperatures. As these two solutions are quite different from each other, a hybrid that employs both methods will not reach a good approximation of the real solution. In addition, with the vibrationless  $N_2$  cylinder case it could be observed that an algorithm to change the continuum and rarefied domains while the solution is evolving would greatly improve the overall results of the hybrid solver. However, even without a zone modification algorithm, the use of both the  $Kn_{GLL}$  and  $B$  parameters to distinguish between continuum and rarefied zones, the  $Kn_{breakdown}$  criterion, proved to provide accurate approximations for the real solution.

## 6.1 Future work

Further test cases should be analysed with *hyperFoam*, the final goal being the simulation of a real spacecraft during reentry. To reach this point, new capabilities would need to be implemented into the solver. This opens new lines for future research, some of which are:

- automatic  $n_{steps}$  calculation: using Hadjiconstantinou's relations, an automatic

## Chapter 6. Conclusions

estimation of  $n_{cases}$  could be calculated and imposed to the simulation.

- energy exchange: new continuum models for the transfer between different energy modes would need to be developed to capture the same behaviour for the vibrational energy exchange as the quantum Larsen-Borgnakke energy distribution procedures.
- chemical reactions: once the modelling of vibrational energy rates match, simulations with chemical reactions could be performed.
- automatic domain recalculation: state-of-the-art sampling methodologies would need to be introduced to be able to diminish the number of iterations required to efficiently adapt the rarefied domain at run-time.
- unsteady simulations: a new treatment of the time-steps of each of the individual solvers could be employed to combine the intrinsic unsteady capabilities of *hy2Foam* with an unsteady variant of *dsmcFoam* to allow for the simulation of full reentry trajectories.

## Appendix A

# Derivation of the temperature-jump conditions

Using Zahmatkesh *et al.* derivation [124], but including vibrational energies on the formulation, it can be obtained that

$$E_i = \frac{1}{4} \sum_s \left[ \rho_s \bar{v} \frac{\gamma_s + 1}{2} (e_{t-r} + e_{s,vib}) \right] + \frac{1}{2\rho} \sum_s \left[ \rho_s \left( \kappa_{s,t-r} \frac{\partial T_{t-r}}{\partial n} + \kappa_{s,vib} \frac{\partial T_{s,vib}}{\partial n} \right) \right] \quad (\text{A.1})$$

$$E_w = \frac{1}{4} \sum_s \left[ \rho_s \bar{v} \frac{\gamma_s + 1}{2} (e_{t-r,wall} + e_{s,vib,wall}) \right] \quad (\text{A.2})$$

$$E_i - E_r = \frac{1}{\rho} \sum_s \left[ \rho_s \left( \kappa_{s,t-r} \frac{\partial T_{t-r}}{\partial n} + \kappa_{s,vib} \frac{\partial T_{s,vib}}{\partial n} \right) \right] \quad (\text{A.3})$$

$$\alpha = \frac{E_i - E_r}{E_i - E_w} \quad (\text{A.4})$$

where  $E_i$  is the energy flux of the incoming molecules,  $E_w$  is the energy flux of the reflected molecules assumed to be at the wall temperature,  $E_r$  is the energy flux of the reflected molecules,  $\alpha$  is the thermal-accommodation coefficient, and  $\bar{v}$  is the mean velocity of the gas mixture. It can be considered as a first approximation that

$$\frac{1}{\rho} \sum_s \left[ \rho_s \left( \kappa_{s,t-r} \frac{\partial T_{t-r}}{\partial n} \right) \right] \approx \kappa_{t-r} \frac{\partial T_{t-r}}{\partial n} \quad (\text{A.5})$$

## Appendix A. Derivation of the temperature-jump conditions

resulting in the following equation for the energy at the boundary

$$\begin{aligned} \sum_s \left( \rho_s \bar{v} \frac{\gamma_s + 1}{2} \right) (e_{t-r} - e_{t-r,wall}) + \sum_s \left( \rho_s \bar{v} \frac{\gamma_s + 1}{2} \right) (e_{s,vib} - e_{s,vib,wall}) = \\ = 2 \frac{2-\alpha}{\alpha} \kappa_{t-r} \frac{\partial T_{t-r}}{\partial n} + 2 \frac{2-\alpha}{\rho \alpha} \sum_s \left( \rho_s \kappa_{s,vib} \frac{\partial T_{s,vib}}{\partial n} \right) \quad (\text{A.6}) \end{aligned}$$

A further simplification is to assume that the terms that depend on the transrotational temperature and the vibrational temperature of each species are decoupled, resulting in the following sets of equations:

$$\left( \sum_s \rho_s \bar{v} \frac{\gamma_s + 1}{2} \right) (e_{t-r} - e_{t-r,wall}) = 2 \frac{2-\alpha}{\alpha} \kappa_{t-r} \frac{\partial T_{t-r}}{\partial n} \quad (\text{A.7})$$

$$\rho_s \bar{v} \frac{\gamma_s + 1}{2} (e_{s,vib} - e_{s,vib,wall}) = 2 \frac{2-\alpha}{\alpha} \frac{\rho_s}{\rho} \kappa_{s,vib} \frac{\partial T_{s,vib}}{\partial n} \quad (\text{A.8})$$

for all species  $s$ .

Taking into account that  $Pr = \frac{\mu C_{p,t-r}}{\kappa_{t-r}}$ ,  $\gamma = \frac{C_{p,t-r}}{C_{v,t-r}}$ , and approximating  $\sum_s (\rho_s \gamma_s) \approx \rho \gamma$ , Equation A.7 can be rewritten as

$$e_{t-r} - e_{t-r,wall} = \frac{2-\alpha}{\alpha} \frac{2\gamma}{\gamma+1} \frac{2\mu}{Pr \rho \bar{v}} C_{v,t-r} \frac{\partial T_{t-r}}{\partial n} \quad (\text{A.9})$$

On the other hand, considering that  $\kappa_{vib} = \mu C_{v,vib}$ , Equation A.8 results in

$$e_{s,vib} - e_{s,vib,wall} = \frac{2-\alpha}{\alpha} \frac{2}{\gamma_s + 1} \frac{2\mu}{\rho \bar{v}} C_{v,vib,s} \frac{\partial T_{s,vib}}{\partial n} \quad (\text{A.10})$$

The partial derivatives of the energies and their respective temperatures can be related as follows

$$\frac{\partial e_{t-r}}{\partial n} = \frac{de_{t,r}}{dT_{t-r}} \frac{\partial T_{t-r}}{\partial n} = C_{v,t-r} \frac{\partial T_{t-r}}{\partial n} \quad (\text{A.11})$$

$$\frac{\partial e_{vib}}{\partial n} = \frac{de_{vib}}{dT_{vib}} \frac{\partial T_{vib}}{\partial n} = C_{v,vib} \frac{\partial T_{vib}}{\partial n} \quad (\text{A.12})$$

Using several kinetic relations [124] and the relations from Equations A.11 and A.12, the final form of the boundary conditions for transrotational and vibrational energies

## Appendix A. Derivation of the temperature-jump conditions

can be obtained:

$$e_{t-r} - e_{t-r,wall} = \frac{2-\alpha}{\alpha} \frac{2\gamma}{\gamma+1} \frac{\lambda}{Pr} \frac{\partial e_{t-r}}{\partial n} \quad (\text{A.13})$$

$$e_{s,vib} - e_{s,vib,wall} = \frac{2-\alpha}{\alpha} \frac{2}{\gamma_s+1} \lambda \frac{\partial e_{s,vib}}{\partial n} \quad (\text{A.14})$$

# Bibliography

- [1] E. Blancillain and G. Gallic. HIKARI: Paving the Way towards High Speed Air Transport. In *20th AIAA International Space Planes and Hypersonic Systems and Technologies Conference*. Glasgow, UK, 6–9 July 2015.
- [2] A. Mack and J. Steelant. FAST20XX: First Progress on European Future High-Altitude High-Speed Transport. In *17th AIAA International Space Planes and Hypersonic Systems and Technologies Conference*. California, USA, 11–14 April 2011.
- [3] M. Sippel, T. Schwanekamp, O. Trivailo, A. Kopp, C. Bauer, and N. Garbers. SpaceLiner Technical Progress and Mission Definition. In *20th AIAA International Space Planes and Hypersonic Systems and Technologies Conference*. Glasgow, UK, 6–9 July 2015.
- [4] R. Wuilbercq, F. Pescetelli, A. Mogavero, E. Minisci, and R. E. Brown. Robust Multidisciplinary Design and Optimisation of a Reusable Launch Vehicle. In *19th AIAA International Space Planes and Hypersonic Systems and Technologies Conference*. Georgia, USA, 16–20 June 2014.
- [5] J. Moss, K. Boyles, and F. Greene. Orion Aerodynamics for Hypersonic Free Molecular to Continuum Conditions. In *14th AIAA/AHI International Space Planes and Hypersonic System and Technologies Conference*. Canberra, Australia, 6–9 November 2006.
- [6] T. P. Wadhams, A. M. Cassady, M. MacLean, and M. S. Holden. Experimental Studies of the Aero thermal Characteristics of the Project Orion CEV Heat

## Bibliography

- Shield in High Speed Transitional and Turbulent Flows. In *47th AIAA Aerospace Sciences Meeting and Exhibit*. Florida, USA, 5–8 January 2009.
- [7] A. M. Feldick, M. F. Modest, D. A. Levin, P. Gnoffo, and C. O. Johnston. Examination of Coupled Continuum Fluid Dynamics and Radiation in Hypersonic Simulations. In *AIAA Aerospace Sciences Meeting*, number Paper 2009-0475, 2009.
- [8] V. Casseau. *An Open-Source CFD Solver for Planetary Entry*. PhD thesis, University of Strathclyde, 2017.
- [9] G. A. Bird. *Molecular Gas Dynamics and the Direct Simulation of Gas Flows*. Oxford Science Publications, 1994.
- [10] G. Abbate, B. J. Thijssse, and C. R. Kleijn. Coupled Navier-Stokes/DSMC Method for Transient and Steady-State Gas Flows. In *7th International Conference on Computational Science*. Beijing, China, 27–30 May 2007.
- [11] P. Gnoffo. An Upwind-Biased, Point-Implicit Relaxation Algorithm for Viscous, Compressible Perfect-Gas Flows. Technical Report 2953, NASA, 1990.
- [12] M. Wright, G. Candler, and D. Bose. Data-Parallel Line Relaxation Method of the Navier-Stokes Equations. *AIAA Journal*, 36(9):1603–1609, 1998.
- [13] H. Lüdeke, J. Oswald, J. M. A. Longo, F. Thivet, J. Hylkema, M. Spel, and W. Dieudonne. DLR-ONERA Accurate CFD Support for the Pre-X Project. In *6th International Symposium on Launcher Technologies*. Munich, Germany, November 8–11 2005.
- [14] T. Langener. ESA’s Activities Using TAU Within the Field of Aerothermodynamics and Propulsion Analysis. In *TAU User Meeting 2011*. DLR Braunschweig, Germany, October 18–19 2011.
- [15] L. C. Scalabrin and I. D. Boyd. Development of an Unstructured Navier-Stokes Solver for Hypersonic Nonequilibrium Aerothermodynamics. In *38th AIAA Thermophysics Conference*. Toronto, Canada, 6–9 June 2005.

## Bibliography

- [16] L. C. Scalabrin and I. D. Boyd. Numerical Simulation of Weakly Ionized Hypersonic Flow for Reentry Configurations. In *9th AIAA/ASME Joint Thermophysics and Heat Transfer Conference*. California, USA, 5–8 June 2006.
- [17] P. Gnoffo. Computational Aerothermodynamic Design Issues for Hypersonic Vehicles. *Journal of Spacecraft and Rockets*, 36(1):21–43, 1999.
- [18] C. Johnston. *Nonequilibrium Shock-Layer Radiative Heating for Earth and Titan Entry*. PhD thesis, Virginia Polytechnic Institute and State University, 2006.
- [19] C. Johnston, B. R. Hollis, and K. Sutton. Radiative Heating Methodology for the Huygens Probe. *Journal of Spacecraft and Rockets*, 44(5):993–1002, 2007.
- [20] P. A. Gnoffo, W. K. James, and S. J. Alter. Multiblock Analysis for Shuttle Orbiter Re-entry Heating from Mach 24 to Mach 12. *Journal of Spacecraft and Rockets*, 31(3), 1994.
- [21] NASA. Report of Columbia Accident Investigation Board, August 2003.
- [22] R. Upadhyay, P. T. Bauman, R. Stogner, K. W. Schulz, and O. Ezekoye. Steady-State Ablation Model Coupling with Hypersonic Flow. In *48th AIAA Aerospace Sciences Meeting Including New Horizons Forum and Aerospace Exposition*. Florida, USA, 4–7 January 2010.
- [23] C. Park. Calculation of Nonequilibrium Radiation in AOTV Flight Regimes. Technical Report AIAA 84-0306, January 1984.
- [24] E. E. Whiting, C. PArk, Y. Liu, J. O. Arnold, and J. A. Paterson. *NEQAIR96, Nonequilibrium and Equilibrium Radiative Transport and Spectra Program: User's Manual*, 1996.
- [25] M. Wright, M. Loomis, and P. Papadopoulos. Aerothermal Analysis of the Project Fire II Afterbody Flow. In *35th AIAA Thermophysics Conference*. California, USA, 11–14 June 2001.

## Bibliography

- [26] M. Wright, D. Prabhu, and E. R. Martinez. Analysis of Afterbody Heating Rates on the Apollo Command Modules, Part 1: AS-202. In *37th AIAA Thermophysics Conference*. Oregon, USA, 28 June – 1 July 2004.
- [27] S. A. Berry, T. J. Horvath, A. M. Cassady, B. S. Kirk, K. C. Wang, and A. J. Hyatt. Boundary Layer Transition Results from STS-114. In *9th AIAA/ASME Joint Thermophysics and Heat Transfer Conference*, number AIAA 2006-2922, 2006.
- [28] OpenFOAM official website, the OpenFOAM Foundation, accessed: 15 June 2016. URL <http://www.openfoam.org/>.
- [29] C. J. Greenshields, H. G. Weller, L. Gasparini, and J. M. Reese. Implementation of Semi Discrete, Non-Staggered Central Schemes in a Colocated, Polyhedral, Finite Volume Framework, for High-Speed Viscous Flows. *International Journal for Numerical Methods in Fluids*, 63:1–21, 2010.
- [30] L. F. Gutiérrez Marcantoni, J. P. Tamagno, and S. A. Elaskar. High Speed Flow Simulation Using OpenFOAM. *Mecánica Computacional*, 31:2939–2959, 2012.
- [31] S. Martin, R. Vincent, and P. Bastien. First Spacecraft Demise Workshop-Test Case Description and Results. In *8th European Symposium on Aerothermodynamics for Space Vehicles*. Lisbon, Portugal, 2–6 March 2015.
- [32] V. Casseau, T. J. Scanlon, and R. E. Brown. Development of a Two-Temperature Open-Source CFD Model for Hypersonic Reacting Flows. In *20th AIAA International Space Planes and Hypersonic Systems and Technologies Conference*, number Paper Number 3637. Glasgow, UK, 6–9 July 2015.
- [33] V. Casseau, T. J. Scanlon, B. John, D. R. Emerson, and R. E. Brown. Hypersonic Simulations using Open-Source CFD and DSMC Solvers. In *30th International Symposium on Rarefied Gas Dynamics*, number Paper Number 2828. Victoria, Canada, 10–15 July 2016.

## Bibliography

- [34] V. Casseau, D. E. R. Espinoza, T. J. Scanlon, and R. E. Brown. A Two-Temperature Open-Source CFD Model for Hypersonic Reacting Flows, Part Two: Multi-dimensional Analysis. *Aerospace*, 3(4), 2016.
- [35] S. Dietrich and I. D. Boyd. A Scalar Optimized Parallel Implementation of the DSMC Method. Number AIAA Paper 1994-0355, 1994.
- [36] S. Dietrich and I. D. Boyd. Scalar and Parallel Optimized Implementation of the Direct Simulation Monte Carlo Method. *Journal of Computational Physics*, 126 (4):328–342, 1996.
- [37] G. A. Bird. Perception of Numerical Methods in Rarefied Gas Dynamics. *Progress in Astronautics and Aeronautics*, 118:211–226, 1989.
- [38] G. A. Bird. Simulation of Multi-Dimensional and Chemically Reacting Flows (Past Space Shuttle Orbiter). In *Proceedings of the 11th International Symposium on Rarefied Gas Dynamics*, pages 365–388, 1979.
- [39] A. Danckert and H. Legge. Experimental and Computational Wake Structure Study for a Wide-Angle Cone. *Journal of Spacecraft and Rockets*, 33(4), 1996.
- [40] J. M. Burt and I. D. Boyd. High Altitude Plume Simulations for a Solid Propellant Rocket. *AIAA Journal*, 42(12):2872–2884, 2007.
- [41] A. J. Lofthouse, L. C. Scalabrin, and I. D. Boyd. Velocity Slip and Temperature Jump in Hypersonic Aerothermodynamics. *Journal of Thermophysics and Heat Transfer*, 22(1):38–49, 2008.
- [42] J. F. Padilla and I. D. Boyd. Assessment of gas-surface interaction models for computation of rarefied hypersonic flow. *Journal of Thermophysics and Heat Transfer*, 23(1):96–105, 2009.
- [43] K. C. Kannenberg and I. D. Boyd. Three-Dimensional Monte Carlo Simulations of Plume Impingement. *Journal of Thermophysics and Heat Transfer*, 13(2):226–235, 1999.

## Bibliography

- [44] Q. Sun, C. Cai, and I. D. Boyd. Computational Analysis of High-Altitude Ionization Gauge Flight Measurements. *Journal of Spacecraft and Rockets*, 43(1):186–193, 2006.
- [45] C. K. Birdsall and A. B. Langdon. *Plasma Physics Via Particle Simulation*. Adam Hilger, 1991.
- [46] Y. Choi, M. Keidar, and I. D. Boyd. Particle Simulation of Plume Flows From an Anode-Layer Hall Thruster. *Journal of Propulsion and Power*, 24(3):554–561, 2008.
- [47] T. E. Schwartzenruber, L. C. Scalabrin, and I. D. Boyd. A Modular Particle-Continuum Numerical Method for Hypersonic Non-Equilibrium Gas Flows. *Journal of Computational Physics*, 225(1):1159–1174, 2007.
- [48] T. E. Schwartzenruber, L. C. Scalabrin, and I. D. Boyd. Hybrid Particle-Continuum Simulations of Nonequilibrium Hypersonic Blunt-Body Flowfields. *Journal of Thermophysics and Heat Transfer*, 22(1):29–37, 2008.
- [49] T. E. Schwartzenruber, L. C. Scalabrin, and I. D. Boyd. Multiscale Particle-Continuum Simulations of Hypersonic Flow Over a Planetary Probe. *Journal of Spacecraft and Rockets*, 45(6):1196–1206, 2008.
- [50] T. E. Schwartzenruber, L. C. Scalabrin, and I. D. Boyd. Hybrid Particle Continuum Simulations of Hypersonic Flow Over a Hollow-Cylinder-Flare Geometry. *AIAA Journal*, 46(8):2086–2095, 2008.
- [51] G. J. LeBeau. A Parallel Implementation of the Direct Simulation Monte Carlo Method. *Computer Methods in Applied Mechanics and Engineering*, 174:319–337, 1999.
- [52] P. I. Larsen and C. Borgnakke. Statistical Collision Model for Simulating Polyatomic Gas with Restricted Energy Exchange. In *Proceedings of the 9th International Symposium on Rarefied Gas Dynamics*, volume 1, 1974.
- [53] G. A. Bird. *The DSMC Method*. 2013.

## Bibliography

- [54] D. S. Liechty. State-to-State Internal Energy Relaxation Following the Quantum-Kinetic Model in DSMC. In *44th AIAA Fluid Dynamics Conference*. Georgia, USA, 16–20 June 2014.
- [55] J. N. Moss, R. C. Blanchard, R. G. Wilmoth, and R. D. Braun. Mars Pathfinder Rarefied Aerodynamics: Computations and Measurements. *Journal of Spacecraft and Rockets*, 36:330–339, 1999.
- [56] R. G. Wilmoth, D. F. G. Rault, F. M. Cheatwood, W. C. Engelund, and R. W. Shane. Rarefied Aerothermodynamic Prediction for Mars Global Surveyor. *Journal of Spacecraft and Rockets*, 36:314–322, 1999.
- [57] G. J. LeBeau and F. E. Lumpkin III. Application Highlights of the DSMC Analysis Code (DAC) Software for Simulating Rarefied Flows. *Computer Methods in Applied Mechanics and Engineering*, 191:595–609, 2001.
- [58] T. J. Scanlon, E. Roohi, C. White, M. Darbandi, and J. M. Reese. An Open Source, Parallel DSMC Code for Rarefied Gas Flows in Arbitrary Geometries. *Computers & Fluids*, 39(10):2078–2089, 2010.
- [59] T. J. Scanlon, C. White, M. K. Borg, R. C. Palharini, E. Farbar, I. D. Boyd, J. M. Reese, and R. E. Brown. Open-Source Direct Simulation Monte Carlo Chemistry Modeling for Hypersonic Flows. *AIAA Journal*, 53(6):1670–1680, 2015.
- [60] Github repository of the *dsmcFoamPlus* solver, 2016. URL <https://github.com/MicroNanoFlows/OpenFOAM-2.4.0-MNF/tree-devel-craig>.
- [61] C. White, M. K. Borg, T. J. Scanlon, S. M. Longshaw, B. John, D. R. Emerson, and J. M. Reese. dsmcFoam+: An OpenFOAM based direct simulation Monte Carlo solver. *Computer Physics Communications*, 224:22–43, 2018.
- [62] R. C. Palharini. *Atmospheric Reentry Modelling Using an Open-Source DSMC Code*. PhD thesis, University of Strathclyde, 2014.

## Bibliography

- [63] R. C. Palharini and J. L. F. Azevedo. Assessment of Rarefaction Effects on the SARA Capsule. In *30th International Symposium on Rarefied Gas Dynamics*. Victoria, Canada, 10–15 July 2016.
- [64] T. J. Scanlon, C. White, and R. C. Palharini. Simulation of Satellite Re-entry Using the Direct Simulation Monte Carlo (DSMC) Method. Presented at the Final Stardust Conference held at ESA ESTEC, Noordwijk, The Netherlands, 31 October – 4 November 2016.
- [65] C. White, T. J. Scanlon, J. A. Merrifield, K. Kontis, T. Langener, and J. Alves. Numerical and Experimental Capabilities for Studying Rocket Plume-Regolith Interactions. In *30th International Symposium on Rarefied Gas Dynamics*. Victoria, Canada, 10–15 July 2016.
- [66] G. A. Bird. Breakdown of Translational and Rotational Equilibrium in Gaseous Expansions. *AIAA Journal*, 8(11):1998–2003, 1970.
- [67] A. L. Garcia and B. J. Alder. Generation of the Chapman-Enskog Distribution. *Journal of Computational Physics*, 140:66–70, 1998.
- [68] I. D. Boyd, G. Chen, and G. V. Candler. Predicting Failure of the Continuum Fluid Equations in Transitional Hypersonic Flows. *Physics of Fluids*, 7:210–219, 1995.
- [69] N. G. Hadjiconstantinou, A. L. Garcia, M. Z. Bazant, and G. He. Statistical Error in Particle Simulations of Hydrodynamic Phenomena. *Journal of Computational Physics*, 187:274–297, 2003.
- [70] T. E. Schwartzentruber and I. D. Boyd. Detailed Analysis of a Hybrid CFD-DSMC Method for Hypersonic Non-Equilibrium Flows. In *38th AIAA Tehrmophysics Conference*. Toronto, Canada, 6–9 June 2005.
- [71] D. B. Hash and H. A. Hassan. A Decoupled DSMC/Navier-Stokes Analysis of a Transitional Flow Experiment. In *34th AIAA Aerospace Sciences Meeting and Exhibit*, number AIAA Paper 96-0353. Nevada, USA, January 1996.

## Bibliography

- [72] D. B. Hash and H. A. Hassan. Assessment of Schemes for Coupling Monte Carlo and Navier-Stokes Solution Methods. *Journal of Thermophysics and Heat Transfer*, 10:242–249, 1996.
- [73] J. D. George and I. D. Boyd. Simulation of Nozzle Plume Flows Using a Combined CFD-DSMC Approach. In *33rd Thermophysics Conference*. Virginia, USA, 28 June – 1 July 1999.
- [74] J.-F. Bourgat, P. Le Tallec, and M. D. Tidriri. Coupling Boltzmann and Navier-Stokes Equations by Friction. *Journal of Computational Physics*, 127:227–245, 1996.
- [75] D. C. Wadsworth and D. A. Erwin. One-Dimensional Hybrid Continuum/Particle Simulation Approach for Rarefied Hypersonic Flows. In *5th AIAA/ASME Joint Thermophysics and Heat Transfer Conference*. Seattle, USA, 18–20 June 1990.
- [76] D. C. Wadsworth and D. A. Erwin. One-Dimensional Hybrid Continuum/Particle Approach for Rarefied Flows. In *23rd AIAA Plasmadynamics and Lasers Conference*, number AIAA Paper 92-2975. Tennessee, USA, July 1992.
- [77] K. A. Stephani. *Development of a Hybrid DSMC/CFD Method for Hypersonic Boundary Layer Flow over Discrete Surface Roughness*. PhD thesis, The University of Texas at Austin, 2012.
- [78] R. Roveda, D. B. Goldstein, and P. L. Varghese. Hybrid Euler/Particle Approach for Continuum/Rarefied Flows. *Journal of Spacecraft and Rockets*, 35(3):258–265, 1998.
- [79] R. Roveda, D. B. Goldstein, and P. L. Varghese. Hybrid Euler/Direct Simulation Monte Carlo Calculation of Unsteady Slit Flow. *Journal of Spacecraft and Rockets*, 37(6):753–760, 2000.
- [80] A. L. Garcia, J. B. Bell, and W. Y. Crutchfield. Adaptive Mesh and Algorithm Refinement Using Direct Simulation Monte Carlo. *Journal of Computational Physics*, 154:134–155, 1999.

## Bibliography

- [81] H. S. Wijesinghe, R. D. Hornung, A. L. Garcia, and N. G. Hadjiconstantinou. Three-Dimensional Continuum-Atomistic Simulation for Multiscale Hydrodynamics. *Journal of Fluids Engineering*, 126(5):768–776, 2004.
- [82] H. A. Carlson, R. Roveda, I. D. Boyd, and G. V. Candler. A Hybrid CFD-DSMC Method of Modeling Continuum-Rarefied Flows. In *42nd AIAA Aerospace Sciences Meeting and Exhibit*, number AIAA Paper 2004–1180, 2004.
- [83] Q. Sun, I. D. Boyd, and G. V. Candler. A Hybrid Continuum/Particle Approach for Modeling Subsonic, Rarefied Gas Flows. *Journal of Computational Physics*, 194:256–277, 2004.
- [84] T. R. Deschenes, T. D. Holman, and I. D. Boyd. Effects of Rotational Energy Relaxation in a Modular Particle-Continuum Method. *Journal of Thermophysics and Heat Transfer*, 25(2):218–227, 2011.
- [85] T. R. Deschenes and I. D. Boyd. Extension of a Modular Particle-Continuum Method to vibrationally excited, hypersonic flows. *AIAA Journal*, 49(9):1951–1959, 2011.
- [86] A. M. Verhoff and I. D. Boyd. Extension of a Hybrid Particle-Continuum Method for a Mixture of Chemical Species. *AIP Conference Proceedings*, (1501):342–349, 2012.
- [87] G. Abbate, B. J. Thijssse, and C. R. Kleijn. Multi-scale Modelling of the Two-Dimensional Flow Dynamics in a Stationary Supersonic Hot Gas Expansion. In *8th International Conference on Computational Science*. Kraków, Poland, 23–25 June 2008.
- [88] J.-S. Wu, Y.-Y. Lian, G. ChenG. Chen. P. Koomullil, and K.-C. Tseng. Development and Verification of a Coupled DSMC-NS Scheme Using Unstructured Mesh. *Journal of Computational Physics*, 219(2):579–607, 2006.

## Bibliography

- [89] Y.-Y. Lian, G. Chen, K.-C. Tseng, J.-S. Wu, B. Wu, and L. Yang. Improved Parallelized Hybrid DSMC-NS Method. *Computers and Fluids*, 45(1):254–260, 2011.
- [90] M. Darbandi and E. Roohi. A Hybrid DSMC/Navier-Stokes Frame to Solve Mixed Rarefied/Nonrarefied Hypersonic Flows over Nano-Plate and Micro-Cylinder. *International Journal for Numerical Methods in Fluids*, 72:937–966, 2013.
- [91] K. Gott. *A Hybrid CFD-DSMC Model Designed to Simulate Rapidly Rarefying Flow Fields and Its Application To Physical Vapor Deposition*. PhD thesis, The Pennsylvania State University, 2015.
- [92] D. B. Spalding S. V. Patankar. A Calculation Procedure for Heat, Mass, and Momentum Transfer in Three-Dimensional Parabolic Flows. *International Journal of Heat and Mass Transfer*, 15(10):1787–1806, 1972.
- [93] E. F. Toro. *Riemann Solvers and Numerical Methods for Fluid Dynamics*. Springer, 1997.
- [94] A. Kurganov and E. Tadmor. New High-Resolution Central Schemes for Nonlinear Conservation Laws and Convection-Diffusion Equations. *Journal of Computational Physics*, 160(1):241–282, 2000.
- [95] A. Kurganov, S. Noelle, and G. Petrova. Semi-Discrete Central-Upwind Schemes for Hyperbolic Conservation Laws and Hamilton-Jacobi Equations. *SIAM Journal on Scientific Computing*, 23:707–740, 2000.
- [96] M.-S. Liou and C. F. Steffen Jr. A new flux splitting scheme. *Journal of Computational Physics*, 107:23–39, 1993.
- [97] E. F. Toro, M. Spruce, and W. Speares. Restoration of the contact surface in the hll-riemann solver. *Shock Waves*, 4:25–34, 1994.
- [98] P. L. Roe and J. Pike. Efficient construction and utilisation of approximate riemann solutions. In *Computing Methods in Applied Science and Engineering*. North-Holland, 1984.

## Bibliography

- [99] A. Lucas-Serrano, J. A. Font, J. M. Ibáñez, and J. M. Martí. Assessment of a High-Resolution Central Scheme for the Solution of the Relativistic Hydrodynamics Equations. *Astronomy & Physics*, 428:703–715, 2004.
- [100] S. Jaisankar and S. V. Raghurama Rao. A Central Rankine-Hugoniot Solver for Hyperbolic Conservation Laws. *Journal of Computational Physics*, 228(3):770–798, 2009.
- [101] M. Pandolfi and D. D'Ambrosio. Numerical Instabilities in Upwind Methods: Anayisis and Cures for the “Carbuncle” Phenomenon. *Journal of Computational Physics*, 166:271–301, 2001.
- [102] W. Sutherland. The Viscosity of Gases and Molecular Force. *Philosophical Magazine, Series 5*, 36:507–531, 1893.
- [103] C. Geuzaine. Gmsh: a Three-Dimensional Finite Element Mesh Generator with Built-In Pre- and Post-Processing Facilities. *International Journal for Numerical Methods in Engineering*, 79(11):1309–1331, 2009.
- [104] D. A. Saunders, S. Yoon, and J. W. Michael. An Approach to Shock Envelope Grid Tailoring and Its Effect on Reentry Vehicle Solutions. In *45th AIAA Aerospace Science Meeting and Exhibit*, January 2007.
- [105] N. Sandham. Shock-Wave/Boundary-Layer Interactions. In *NATO Research and Technology Organisation (RTO) - Educational Notes Paper*, number RTO-EN-AVT-195-5, 2011.
- [106] [www.cfd-online.com](http://www.cfd-online.com).
- [107] H. A. Berman, J. D. Anderson, Jr., and J. P. Drummond. Supersonic Flow over a Rearward Facing Step with Transverse Nonreacting Hydrogen Injection. *AIAA Journal*, 21(12):1707–1713, 1983.
- [108] G. A. Sod. A Survey of Several Finite Difference Methods for Systems of Nonlinear Hyperbolic Conservation Laws. *Journal of Computational Physics*, 27:1–31, 1978.

## Bibliography

- [109] G. A. Bird. Monte Carlo Simulation in an Engineering Context. In S. S. Fisher, editor, *Progress in Astronautics and Aeronautics*, pages 239–255. New York, USA, 1981.
- [110] G. A. Bird. Definition of Mean Free Path for Real Gases. *Physics of Fluids*, 26: 3222–3223, 1983.
- [111] L. Landau and E. Teller. On the Theory of Sound Dispersion. *Physikalische Zeitschrift der Sowjetunion*, 10(34), 1936.
- [112] R. C. Millikan and D. R. White. Systematics of Vibrational Relaxation. *The Journal of Chemical Physics*, 39(12):3209–3213, 1963.
- [113] C. Park. *Nonequilibrium Hypersonic Aerothermodynamic*. Wiley International, 1990.
- [114] J. D. Ramshaw and C. H. Chang. Friction-Weighted Self-Consistent Effective Binary Diffusion Approximation. *Journal of Non-Equilibrium Thermodynamics*, 23:223–232, 1996.
- [115] S. Chapman and T. G. Cowling. *The Mathematical Theory of Non-Uniform Gases*. Cambridge University Press, 1952.
- [116] C. R. Wilke. A Viscosity Equation for Gas Mixtures. *Journal of Chemical Physics*, 18(4):517–519, 1950.
- [117] R. Brun. *Introduction to Reactive Gas Dynamics*. Oxford University Press, 2009.
- [118] O. Knab, H.-H. Frühauf, and S. Jonas. Multiple Temperature Descriptions of Reaction Rate Constants with Regard to Consistent Chemical Vibrational Coupling. Technical Report AIAA 92-2947, July 1992.
- [119] O. Knab, H.-H. Frühauf, and E. W. Messerschmid. Theory and Validation of the Physically Consistent Coupled Vibration-Chemistry-Vibration Model. *Journal of Thermophysics and Heat Transfer*, 9(2):219–226, 1995.

## Bibliography

- [120] P. A. Gnoffo, R. Gupta, and J. L. Shinn. Conservation Equations and Physical Models for Hypersonic Air Flows in Thermal and Chemical Nonequilibrium. Technical Report NASA-2867, 1989.
- [121] L. Scalabrin. *Numerical Simulation of Weakly Ionized Hypersonic Flow over Reentry Capsules*. PhD thesis, The University of Michigan, 2007.
- [122] J. C. Maxwell. On Stresses in Rarefied Gases Arising from Inequalities of Temperature. *Philosophical Transactions of the Royal Society of London*, 170:231–256, 1879.
- [123] M. von Smoluchowski. Ueber Wärmeleitung in Verdünnten Gasen. *Annalen der Physik und Chemie*, 64:101–130, 1898.
- [124] I. Zahmatkesh, M. M. Alishahi, and H. Emdad. New Velocity-Slip and Temperature-Jump Boundary Conditions for Navier-Stokes Computation of Gas Mixture Flows in Microgeometries. *Mechanics Research Communications*, 38: 417–424, 2011.
- [125] G. A. Bird. Approach to Translational Equilibrium in a Rigid Sphere Gas. *Physics of Fluids*, 6:1518–1519, 1963.
- [126] I. D. Boyd and T. E. Schwartzentruber. *Nonequilibrium Gas Dynamics and Molecular Simulation*. Cambridge University Press, 2017.
- [127] W. Wagner. A convergence Proof for Bird’s Direct Simulation Monte Carlo Method for the Boltzmann Equation. *Journal of Statistical Physics*, 66(3):1011–1044, 1992.
- [128] B. L. Haas, J. D. McDonald, and L. Dagum. Models of Thermal Relaxation Mechanics for Particle Simulations. *Journal of Computational Physics*, 107(2): 348–358, 1993.
- [129] F. Bergemann and I. D. Boyd. New Discrete Vibrational Energy Model for the Direct Simulation Monte Carlo Method. *Progress in Astronautics and Aeronautics*, 158:174, 1994.

## Bibliography

- [130] C. Borgnakke and P. S. Larsen. Statistical Collision Model for Monte Carlo Simulation of Polyatomic Gas Mixture. *Journal of Computational Physics*, 18: 405–420, 1975.
- [131] G. A. Bird. The Q-K Model for Gas-Phase Chemical Reaction Rates. *Physics of Fluids*, 23(106101), 2011.
- [132] M. A. Gallis, R. B. Bond, and J. R. Torczynski. A Kinetic-Theory Approach for Computing Chemical-Reaction Rates in Upper-Atmosphere Hypersonic Flows. *Journal of Chemical Physics*, 131(12):124311, 2009.
- [133] I. D. Boyd. Predicting Breakdown of the Continuum Equations Under Rarefied Flow Conditions. In *23rd International Symposium on Rarefied Gas Dynamics*. Whistler, Canada, 20–25 July 2002.
- [134] D. A. Lockerby, J. M. Reese, and H. Struchtrup. Switching Criteria for Hybrid Rarefied Gas Flow Solvers. In *Proceedings of the Royal Society A*, volume 465, pages 1581–1598, 2009.